Elastic Instabilities and Structural Responses of β-SiC Under Stress

by

Meijie Tang

Submitted to the Department of Nuclear Engineering
in partial fulfillment of the requirements for the degree of

Doctor of Philosophy

at the

MASSACHUSETTS INSTITUTE OF TECHNOLOGY

January 1995

Author .....
Department of Nuclear Engineering
January 20, 1995

Certified by .....
Sidney Yip
Professor of Nuclear Engineering
Thesis Supervisor

Certified by .....
Janez Megusar
Research Associate of Materials Processing Center
Thesis Reader

Accepted by .....
Allan F. Henry
Chairman, Departmental Committee on Graduate Students

Elastic Instabilities and Structural Responses of β-SiC Under Stress

by

Meijie Tang

Submitted to the Department of Nuclear Engineering
on January 20, 1995, in partial fulfillment of the
requirements for the degree of
Doctor of Philosophy

Abstract

The primary goal of this dissertation is to study the deformation response of a binary covalent lattice (cubic SiC with zincblende structure) to hydrostatic tension and compression using an atomistic approach of self-consistent elastic stability analysis combined with molecular dynamics simulations. Using a classical many-body potential function, the present study not only has demonstrated the practical feasibility of modeling mechanical behavior of crystals under stress, but also it has highlighted the role of chemical ordering and the relative importance of atomic size and mixed bond chemical preference effects in the process of pressure-induced amorphization.

The present work is based on the empirical bond-order potential function developed by J. Tersoff, originally developed for Si and later adapted for SiC. However, whenever the lattice undergoes significant volumetric deformation, unphysical effects arise which is caused by abrupt change in the number of interacting neighbors due to the use of a fixed potential range cutoff. A simple modification is introduced allowing the cutoff to vary with the density of the system, and the resulting modified potential is found to give a generally satisfactory description of bulk and surface properties of β-SiC, including the temperature variation of the elastic constants.

The modified Tersoff potential is used to study the response of a homogeneous crystalline lattice to hydrostatic deformation by applying newly developed elastic stability criteria in conjunction with direct observations of structural instability and evolution through molecular dynamics simulations. The conditions for instability at finite stress differ from the conventional criteria in that the former involve elastic stiffness coefficients that depend not only on the elastic constants but also on the applied stress.

In the case of tensile loading, the failure mode is predicted to be the vanishing of the bulk modulus, denoting a spinodal instability. This prediction is confirmed by simulation which gives a value of the critical stress, the ideal strength of the solid, in agreement with the stability analysis. Furthermore, simulation reveals that upon lattice decohesion, a brittle crack has been nucleated on the lowest surface energy plane – the {111} shuffle plane. Even though the simulation data is limited ,

evidence indicative of shear-tension coupling effects in brittle fracture is found, and rapid atomic relaxation process on the cracked planes is observed.

In the case of compressive loading, the failure mode of covalent solids is less obvious. With the bulk modulus increasing with loading, one can only expect that instability should occur when either the tetragonal shear modulus G' or the pure shear modulus G vanishes. For β-SiC, the elastic stability analysis shows that the shear instability vanishes under compression. The critical stress actually observed in simulation is again in close agreement with that predicted from the elastic stiffness coefficients. And the analysis shows that the instability is caused by large internal strain fluctuations which lead to the vanishing of the shear instability G. The unstable structural response, revealed by simulation is a homogeneous disordering process accompanied by volume expansion and decreasing of internal energy. The transition is found to be reversible in a manner analogous to the 'memory glass' effect known experimentally.

The fact that binary SiC would amorphize under pressure is in contrast to the behavior of elemental Si which undergoes structural transition (diamond cubic to β-tin) under compression. This difference points to the underlying role of chemical ordering in structural stability of covalent solids. To elucidate the relative importance of the two effects contributing to the chemical ordering, namely, the atomic size disparity and chemical preference of mixed bonds, it is shown that the modified Tersoff potential can be manipulated to suppress one effect or the other. Specifically, size difference appears through the many-body bond-order parameter, while the chemical preference is expressed through the heat of formation. In this manner, the atomic size and chemical preference effects are studied explicitly. The vanishing of shear instability in pressurized SiC is shown to be a consequence of the appreciable size difference between the Si and C atoms. Further simulation confirms that if the size effect were suppressed, then β-SiC would in fact transform from zincblende to rocksalt structure under compression. These findings are significant for future simulation studies in that they demonstrate new insights can be gained through well-defined manipulations of the interatomic interactions.

Thesis Supervisor: Sidney Yip
Title: Professor of Nuclear Engineering

Acknowledgments

I would like to take this opportunity to express my sincere gratitude to those individuals who have made this dissertation possible. About four years ago, I came to MIT for an interview. Prof. Sidney Yip introduced atomistic simulations to me for the first time and interested me in doing work in this field. Since that he has been a constant source of guidance, support and inspiration. I am grateful for his wisdom, patience, and encouragement throughout my graduate studies. I am also grateful for my thesis reader Dr. Janez Megusar, who has been encouraging through the years we work in the same project. I am also indebted to Prof. James Rice and Prof. Marry Boyce for serving in my thesis committee. Prof. Rice has truly interested and educated me in the science of continuum mechanics and fracture mechanics. Prof. Boyce has greatly inspired me as a woman scientist. In addition, I would like to thank Prof. Sow-Hsin Chen for inspiration and support during my graduate course studies.

I would also like to acknowledge the financial support I have received from the Sir Run Run Shaw Fellowship from MIT, the Teaching Assistantships from the Nuclear Engineering Department of MIT, and the AFOSR Grant 91-0285. In addition, part of the computations in this work have been performed at NSF San Diego Supercomputer Center.

I am thankful for many of my friends and colleagues. Thanks to J. H. Wang, R. Pflueger and N. Sonwalkar for friendship and help, thanks to V. Bulatov for stimulating discussions, thanks to J. F. Justo and J. Li for sincere help, thanks to C. S. Yoon and A. Isik for sharing the time working in the same project, thanks also to L. Porter, M. Nastar and P. Gallo for help during the time of my thesis writing and preparation for the thesis defense.

I am deeply indebted to my family for their love, encouragement and support since the first day I was born into this world. I want to dedicate this thesis to them–my grandparents, my parents and my sisters. Finally, I would like to thank my dearest husband, Hongjie. Without his love, encouragement and help, this thesis would not be possible.

Contents

List of Tables

List of Figures

Chapter 1

Introduction

1.1 Background and Motivation

Silicon carbide (SiC) is a material of great technological importance[1][2][3][4][5]. Various polytypes exist for this material[6]. The polytypism originates from different stacking sequences of silicon-carbon double layers in the cubic (C), hexagonal (H), or rhombohedral (R) structure. The most common polytype is 3C SiC, or β-SiC, which has a zincblende structure and is formed by $...ABCABC...$ stacking of the silicon-carbon double layers. β-SiC is a semiconductor material with unique mechanical, thermal and electronic properties. Due to its strongly directional and highly localized covalent bonding, β-SiC has great hardness and has been used as a traditional abrasive or refractory material. β-SiC has a high melting temperature, low thermal expansion coefficient and high thermal conductivity. It is a wide band gap semiconductor with high electron mobility and electron drift velocity[1]. Because of these excellent properties, β-SiC has been recognized as a particularly promising prototype for high-temperature, high-power and high-frequency operation devices. Recently, the interest in SiC is further extended to the field of advanced composite materials. It has been used as a reinforcing fiber for resin- and metal-matrix composites. And more importantly, SiC or carbon reinforced SiC matrix composite materials have attracted significant attention due to their potential ability in achieving novel materials with enhanced mechanical properties.

SiC fiber-reinforced matrix composite materials are designed to enhance the material toughness, i.e., the capacity to withstand local over-stress without catastrophic failure[7]. Although both the matrix and the reinforcing fibers have high strength, low creep rates and excellent thermal stability at high temperatures, β-SiC is a brittle material that undergoes brittle fracture by nature[8]. Accordingly, the fiber or the matrix by themselves provide minimal resistance to crack propagation and tend to catastrophic failure. However, once they form a composite material, the bonding at the interface between the matrix and fiber can control the fracture mode of the material. It is now widely recognized that the overall functionality of the fiber-matrix composite is governed to a great extent by the interface properties[7][9]. If the interface is too strong, a crack that propagates in the matrix can pass through fibers, and the composite material will fail in a brittle manner. On the other hand, a relatively weak interface will allow fiber debonding, sliding through the matrix and bridging away the crack. These effects will ultimately lead to multiple cracking of the matrix and fiber pull-out. External load will be transfered from the matrix to fibers and the material will fail progressively instead of catastrophically[7]. Thus, with relatively weak bonding at the interface, a much tougher composite material can be obtained. The matrix failure strain can be significantly increased and the ultimate failure stress of a composite material can be much higher than that of the monolithic matrix. However, it should be noticed that if the interface is too weak, no load will be transfered from the matrix to fibers, and thus the fibers loose their function. Therefore, tailoring interfaces between the matrix and fibers to achieve the optimum combination of strength and toughness is critical in designing composite materials. To understand the structure and mechanical properties of the interface over a wide range of temperature and stress and to relate the interfacial mechanical properties to the fracture characteristics of the composite material become crucial for designing composite materials.

Understanding the mechanical behavior of SiC fiber-matrix composites requires investigations of the mechanical behavior of both the pure monolithic matrix material and the interface. It is undoubtedly necessary that one must first understand

the fundamental mechanical properties of the matrix or fiber monolithic materials. Thus, fundamental concepts such as the intrinsic ideal strength and intrinsic fracture toughness of SiC crystals must be investigated before hand under different external conditions. A number of fundamental questions need to be answered for β-SiC crystals, such as what are the maximum loadings a monolithic matrix can hold? Under what conditions cracks begin to nucleate inside the SiC matrix? And under what conditions, existing cracks will propagate? Understanding these fundamental questions will provide a foundation for studies of mechanical properties and behavior of SiC composite materials.

Previously, there has been no study of the ideal strength or mechanical stability of single crystal β-SiC. In general, the ideal strength of defect-free crystalline materials has been under extensive study but remains a challenge. Perfect crystals can hold elastic strains that are well beyond what can properly be treated as infinitesimal. Their response to various loadings is not well known and complex[10]. Since the concept of ideal strength can be considered as an instability phenomenon, effort has been devoted to studying the instability of perfect crystals. These studies involve deriving the so called stability criteria, which are a set of conditions expressed in terms of materials properties, such as elastic constants or stiffness coefficients[11]. The first systematic analysis of lattice instability is attributed to Max Born who has shown that, by expanding the internal energy of a crystal in a power series of strain and by requiring convexity of the energy, one can obtain stability criteria in the form of a set of conditions imposed on the elastic constants of the crystal[12]. While Born's criteria are well known in the literature[13], it has not been satisfactorily resolved whether these criteria are capable of accurately predicting the actual onset of an instability. On the theoretical side, the difficulty lies in the different ways that the stability analyses have been formulated and in properly evaluating the elastic constants that appear in the criteria. On the experimental side, competing effects frequently render the triggering instability unclear. Thus, the validity of Born's criteria under finite load appears to go generally unquestioned. In a series of theoretical and computational studies, Hill[10] and Hill and Milstein[14] have investigated the different domains of

stability which result from different choices of stain measure. Hill[10] pointed out an inconsistency in the original Born's derivation. Other than this work, there appears to be no explicit discussion of whether Born's analysis is valid at finite strain.

Recently, Wang et al.[15][16] have re-examined the Born's criteria in several simulation studies of stability and structural change of a homogeneous lattice (fcc metal) under finite stress and temperature. They have derived generalized elastic stability criteria as finite-strain extension of the well-known Born's criteria, which have been shown to be valid only at zero load. In the newly derived stability criteria, *elastic stiffness coefficients* appear as the finite-strain generalizations of the elastic constants. Furthermore, it has been found that for each specific instability criterion, there is a corresponding mode of deformation which can be determined by solving an eigenvalue-eigenvector problem[17]. This suggests that different instability mechanisms will be signaled by different modes of deformation which could be experimentally detectable and observable in atomistic modeling. Recently, Rice has raised valid questions concerning the general derivation of the stability criteria based on the stiffness coefficients[18]. Nevertheless, for hydrostatic loading, Rice has independently shown that the stability criteria derived by Wang et al. are correct.

The new criteria derived by Wang et al. have been applied in a series of follow-up simulation studies using explicit atomistic force models. Predictions of critical strain (or stress) and deformation mode from instability analysis have been tested independently by molecular dynamics simulations. In simulations, the onset of structural instability has been clearly observed and the atomic structural configurations resulted from the instability have been determined. Remarkably, the simulation results agree well with the prediction of the instability analysis. In terms of the phenomena that could occur after an instability of a crystal is reached, the elastic stability analysis can be applied to study a number of long-standing problems of structural changes, such as melting[19], polymorphism[20] and pressure-induced amorphization[21]. For all cases, the criterion that is first violated is regarded as the instability mechanism that causes the onset of the structural change. Significant new understanding of these problems has been gained by using the new stability criteria. Some of the detailed

studies will be reviewed below.

Wang et al.[15] have studied $fcc\ Au$ single crystals under hydrostatic tension, uniaxial tension and isobaric heating by using the embedded-atom-method potential[22]. They have found that under hydrostatic tension, the spinodal instability (bulk modulus) goes to zero and the crystal lattice loses cohesion in the form of cavitation. Under uniaxial tension, they have found that the tetragonal shear (corresponding to $C_{11} - C_{12}$) goes to zero and the lattice undergoes a phase transition from fcc to bcc. In the case of isobaric heating at zero pressure, the Born's criteria based on elastic constants are equivalent to the new criteria based on stiffness coefficients. It has been found that the tetragonal shear instability sets the upper limit of superheating or metastability of the crystal lattice. Quite interestingly, it is found that instabilities occur in succession during the isobaric melting process. In all three situations, the new stability criteria predict the onset of instability very well and have been verified by simulation studies.

As a first attempt to elucidate the critical deformation behavior of lattice models of a binary intermetallic systems, Cleri et al.[23] have performed a study on Ni_3Al under hydrostatic and uniaxial tensile loadings by using an interatomic potential derived by a second moment approximation to the tight-binding model of d-band transition metals. Two lattice structures are investigated, a highly symmetric and naturally occurring L_{12} structure and a less symmetric , intrinsically less ductile hypothetical DO_{22} structure are studied. Failure modes observed are spinodal instability under hydrostatic tension and tetragonal shear instability under uniaxial tension. While simulation results confirm the new stability analysis very well, there appears to be little correlation between instability behavior and the relative ductility of a given lattice structure (with the exception of behavior of the final state).

It is well known that covalent materials differ from metals by the nature of highly directional and angular dependent bonding. The open structures in covalent materials give rise to various possibilities of structural changes at the instability. Mizushima et al.[24] have studied the structural instability and transformation of diamond cubic Si lattice under compression by using the Tersoff potential for Si[25]. It is found that the

tetragonal shear stability is violated under compression. As a result of this instability, the Si lattice undergoes a phase transition from diamond cubic to β-tin structure. Both β-SiC and Si are tetragonally bonded covalent materials with open structure. Additional complexity arises in SiC because of its binary nature, that is the chemical ordering effect. The two major factors contributing to the chemical ordering effect are the atomic size difference of Si and C atoms and the chemical preference of mixed bonds between Si and C. Tersoff has found that the effect of chemical preference of mixed bonds is much the same in crystalline and amorphous materials. However, the atomic size difference is far less effective in inducing ordering in quenched amorphous SiC than in crystal β-SiC[26]. The existence of the chemical ordering effects can play an important role in the unstable structural responses of β-SiC, and could determine the difference of instability mechanism and the actual structural responses of β-SiC and Si. Therefore, understanding the elastic instability and unstable structural response of β-SiC in the presence of chemical ordering effects remains a challenge and can lead to a rather general understanding of covalent materials including both binary compound (β-SiC) and single element crystal (Si).

1.2 Problem Statement and Scope of Thesis

The problem addressed in this thesis is an atomistic study of deformation and unstable structural responses of a bulk binary covalent crystal (SiC with zincblende structure) under hydrostatic tension and compression through an integrated approach of molecular dynamics (MD) simulations using a modified classical, many-body empirical potential function and self-consistent elastic stability analysis based on the concept of elastic stiffness coefficients. The phenomena being studied are tension-induced crack nucleation and brittle fracture and pressure-induced lattice disordering. An emphasis of the investigation is the clarification of the role of chemical ordering in the amorphization process of β-SiC, specifically, a probe of the relative importance of the atomic size disparity and mixed bonds chemical preference. The elastic stability analysis predicts the instability mechanism and the critical stress at which the insta-

bility will occur. However, it does not predict what will happen to the structure of the crystal when it reaches the instability. MD simulations on the other hand is able to provide detailed atomic configurations and allow one to examine the structure of the system at any time instant, such as before, during and after the instability driven unstable structural responses. Combing the elastic stability analysis and the MD simulations, one can predict the instability mechanism, predict the critical stress, verify the predictions from elastic stability analysis by direct MD simulations and direct observe the structural changes at the instabilities. Therefore, a comprehensive understanding of the elastic instabilities and the unstable structural responses of crystals can be obtained.

The most critical limitation of atomistic simulations is the accuracy of interatomic potential functions. It is challenging to develop an accurate empirical interatomic potential function for covalent materials due to the difficulties in describing the highly directional bonds and angular dependent forces in these materials. It is even more difficult to develop a potential function for SiC due to the additional binary nature of this material. While a number of interatomic potential functions have been developed for SiC, their accuracy and transferrability have not been critically examined. In this thesis, we have studied and compared available potential functions for SiC by calculating basic physical properties of β-SiC, such as cohesive energy, lattice constant, bulk modulus and elastic constants at low temperature ($0K$). It is found that the potential function developed by Tersoff[27] describes the equilibrium properties of β-SiC very well compared to experimental data and first principle calculations.

When further examined in conditions under stress and at finite temperatures, it is found that the Tersoff potential only works well within a limited region near the stress-free equilibrium condition. This certainly limits the study of the elastic instability of β-SiC under finite stress loading. The Tersoff potential is then modified by introducing a variable cutoff to replace the original fixed cutoff. The modified Tersoff potential has improved the original Tersoff potential significantly. The modified Tersoff potential is then applied to study fundamental properties of the bulk and surfaces of β-SiC. Extensive comparisons with experimental data, tight-binding and

first principle calculations are made. The comparisons show that the modified Tersoff potential is capable of describing realistic thermal and elastic properties of β-SiC; this in turn ensures that we can extend our study to the elastic stability and structural response of β-SiC under stress using the modified Tersoff potential.

For a crystal lattice under stress, no doubt that the lattice will ultimately fail as the deformation becomes large enough and reach a critical point. The fundamental questions one can ask are what will cause the crystal lattice to become unstable; what maximum loading the crystal can hold; and what happens to the structure once the lattice becomes unstable. The first question concerns the underlying physics of the instability. Consider the internal energy U of a crystal, stability of the crystal requires that the internal energy be a minimum, i.e., $\delta^2 U > 0$. When the inflection point of the internal energy is reached, i.e., $\delta^2 U = 0$, the crystal becomes unstable. Therefore, $\delta^2 U = 0$ defines the instability point of the crystal. If the internal energy is expanded in terms of strains of the system, it can be shown[13] that the convexity condition of the internal energy is equivalent to the condition that the matrix containing the second derivatives of the internal energy with respect to strains are positive definite. Thus, the instability condition of $\delta^2 U = 0$ can be described in terms of the standard solution of an eigenvalue problem of a matrix consisting of second derivatives of the internal energy. Following this idea, one can reach the well known Born's instability criteria expressed by a set of conditions in terms of elastic constants[13]. However, these instability criteria are found to be valid only at zero loading[15][16]. Using the principle of virtual work, one can derive the more general instability criteria replacing elastic constants with elastic stiffness coefficients in the Born's criteria[16]. Though the general derivation of the new stability criteria have been recently questioned by Rice[18], the stability criteria under hydrostatic loading have been independently worked out by Rice and are the same as that derived by Wang et al.[15][16]. In this thesis, we focus on hydrostatic loading situations including tension and compression.

Given the instability criteria of a crystal, one can examine how the instability criteria vary with external loading and which instability criterion will first go to zero at a critical stress. The criterion that first goes to zero determines the instability

mechanism of the crystal. For a cubic crystal, there are three instability criteria, i.e., the spinodal instability (vanishing of the bulk modulus), the shear instability (corresponding to C_{44}) and the tetragonal shear instability (corresponding to $C_{11} - C_{12}$). The major outcome of the elastic stability analysis are the predictions of the instability mechanism and the critical stress at which the stability is first violated. Also, by solving the eigenvalue problem corresponding to $\delta^2 U = 0$, one can obtain the accompanying eigenvectors of strains. For each instability criterion, a unique eigenmode exists corresponding to the eigenvectors. The eigenmode describes how the strains vary when a particular instability occurs. In other words, the elastic stability analysis can predict the mode of deformation which describes the condition that must be satisfied by the strain variation during the structural change triggered by the instability.

Although the elastic stability analysis can provide insight into the instability mechanism and the eigenmodes of deformation, it can not describe the final state of the structural change. Therefore, molecular dynamics simulations become necessary for such studies. From MD simulations, we can observe the actual response of the crystal along the entire deformation path. In particular, we can gain detailed knowledge of structure and properties of the crystal when the instability occurs. By studying the properties of structure factor, internal energy and system volume in simulation, we can identify changes that might have occurred in the crystal. From the change in the simulation cell shape, i.e., bifurcation or shear deformation, we can verify the mode of deformation that is predicted by the elastic stability analysis. By examining the atomic configuration and the radial distribution functions, we can determine the final structure of the system after structural changes.

Combining the elastic stability criteria and MD simulations, we have investigated the elastic instability and structural response of β-SiC under hydrostatic tension and compression using the modified Tersoff potential. The work presented in this thesis constitutes the first systematic study of the mechanical stability and structural responses of β-SiC under stress. Under tension, it is found that the spinodal stability is violated (vanishing of the bulk modulus) at a critical tensile stress and the crystal

experiences a decohesion failure manifested by crack nucleation and brittle fracture along the shuffle {111} plane, which has the lowest surface energy. Under compression, it is found that the shear stability is violated at a critical compressive stress, which triggers a solid-state amorphization in β-SiC.

The fact that β-SiC undergoes pressure-induced amorphization under compression stands in contrast to the behavior of elemental crystalline Si which undergoes a polymorphic phase transformation from diamond cubic to β-tin under compression. In the case of Si, the instability mechanism is the tetragonal shear. We believe that the differences between SiC and Si stem from the additional chemical ordering effect that exists in β-SiC. By modifying the Tersoff potential for SiC in a way that allows us to separately probe the effects of atomic size difference and chemical preference, we identify that the atomic size effect is primarily responsible for the critical internal strain relaxations which lead to the order-disorder transition of the β-SiC lattice. By suppressing the atomic size disparity, we show that the instability mechanism changes from shear to tetragonal shear for SiC; and the structural transition changes from the crystalline-amorphous transformation to a polymorphic phase transition.

Eventually this work will help to study SiC fiber reinforced composite materials in which interfacial mechanical properties play a critical role. We present in this thesis a preliminary study of a crystalline-amorphous SiC interface. We develop a methodology to construct such an interface and demonstrate the feasibility of studying the correlation between structure, interfacial bonding and mechanical properties using atomistic simulations. This work will require significant future studies.

The thesis is organized as follows. We will start with a brief review of MD simulation techniques in Chapter 2, including a discussion of the methodologies to calculate stress, strain and elastic constants. We will also discuss interatomic potential functions in Chapter 2. Results of testing existing potential functions for SiC and modifications of the Tersoff potential will be given. In Chapter 3, we will present results of calculations of fundamental physical properties of both the bulk and surfaces of β-SiC using the modified Tersoff potential, where extensive comparisons with first principle, tight-binding calculations and experimental data will be made. Both

Chapter 2 and Chapter 3 are intended to prepare for our study of the mechanical stability and structural response of β-SiC under stress. In Chapter 4, we will derive the finite strain elastic stability criteria based on elastic stiffness coefficients using the principle of virtual work method. In Chapter 5 and Chapter 6, we will present studies of mechanical stability and structural response of β-SiC under hydrostatic tension and compression respectively. In Chapter 6, following the observation of pressure-induced amorphization of β-SiC under compression, we will focus on studying the roles played by chemical ordering effects in the amorphization process of β-SiC. Two simplified models for SiC will be proposed and the effects of atomic size difference and chemical preference will be investigated explicitly. In Chapter 7, we will show our preliminary results of a crystalline/amorphous SiC interface. The main purpose of this chapter is to present a methodology for interface construction and demonstrate the feasibility of atomistic simulations to study the interplay between atomic structure, interfacial bonding and mechanical properties. This work is limited and suggestions for future work will be made. Finally, in the concluding chapter, we summarize our major results, their significance and implications, and discuss some directions for future work.

Chapter 2

Atomistic Simulation Technique and Interatomic Potential Functions in Modeling SiC

With the rapid growth of computing power and the development of advanced interatomic potential functions, atomistic simulation has become a unique research area combining the wisdom of physicists, chemists, materials scientists and engineers. It has been widely applied in investigating microscopic structures and properties of complex materials, in bridging gaps between theories and experiments, and in understanding the fundamental physical processes and mechanisms occurring at the atomic scale. Molecular dynamics (MD) simulation allows us to study complex phenomena of materials under precisely controlled condition. It offers a unique way to study both static and dynamic properties simultaneously. Nevertheless, we should point out that MD simulations also have limitations. Other than the obvious constraint imposed by the availability of computational resources, a critical limitation of MD is the availability and accuracy of interatomic potential functions being used to model materials.

In this chapter, a brief summary of modern molecular dynamics simulation technique will be first given in Sec.2.1. Since studying mechanical behavior and properties of materials under stress is one of the major goals of this thesis, in Sec. 2.2, I will dis-

cuss methods to calculate mechanical properties of a system, including stress, strain, elastic constants and stiffness coefficients. Special features of internal strain relaxation of C_{44} in non-bravais lattice systems will be addressed. Note that the strain, stress, elastic constants and stiffness coefficients will be re-discussed again in Chapter 4 in the context of elasticity theory. The discussions in this chapter focus on how to calculate these quantities in MD simulations, whereas the discussions in Chapter 4 will focus on their physical definitions and applications in deriving the new stability criteria using finite elasticity theory. Lastly, in Sec. 2.3, I will discuss some general aspects that are involved in developing advanced potential functions. In particular, I will focus on potential functions for β-SiC. I will address key issues of angle-dependent forces of covalent materials and the binary feature of SiC,i.e., how to treat interactions between different types of atoms in SiC. Also, I will present results of testing and modifying available potential functions for SiC.

2.1 Molecular Dynamics Simulation Methodology

The basic techniques of molecular dynamics simulations are now standardized and well documented [27] [28]. In brief, MD simulation is a method for generating the trajectories of N atoms in a system under conditions of finite temperature and external stress by direct numerical integration of the Newton's equation of motion. A typical numerical procedure used to solve the Newton's equation is via the fifth order predictor-corrector algorithm [29]. MD simulations require specific interatomic potential functions. It can accommodate any initial atomic configurations. Its basic output is the time-dependent positions and momenta of atoms, from which a variety of properties can be calculated. Structural, thermodynamical, mechanical, vibrational and transport properties are most frequently studied by MD simulations[27][28].

In the language of statistical mechanics, the objective of a MD simulation is to compute the phase-space trajectory. The phase-space is a $6N$-dimensional hyperspace consisting of positions and momenta of all N atoms of a system. By sampling sufficient phase-space surface, MD simulation can derive reliable macroscopic physical

properties of a system from statistical mechanics. MD simulation can study different ensembles by sampling on different surfaces of the phase-space. Each ensemble has its own conserved thermodynamic quantity such as energy, temperature and pressure. The most commonly used ensembles are microcanonical ensemble (NVE), canonical ensemble (NVT), isoenthalpic-isotension ensemble (HτN) and isothermal-isobaric ensemble (NPT). In the microcanonical ensemble (NVE), the total energy of the system is conserved. By rescaling the velocities of atoms at every time step to keep the temperature of the system constant, one obtains the canonical ensemble (NVT). The (HτN) and (NPT) ensembles can be generated by a generalized MD simulation method that is first proposed by Parrinello and Rahman[30] and later modified by Ray and Rahman[31]. In the generalized MD simulation, the shape and size of the simulation cell are no longer constant. They vary in responding to externally applied stresses. Take $\vec{a}$, $\vec{b}$ and $\vec{c}$ as the three vectors forming the simulation cell, one can construct a matrix $h = \{\vec{a}, \vec{b}, \vec{c}\}$. In the modified formulation of the Parrinello-Rahman method, in addition to the equations of motion for the N atoms in the simulation cell, the equation of motion for the variable matrix h is also considered. For a system subjected to anisotropic stress, this equation of motion is[31]

$$W\ddot{h} = \sigma V h^{T^{-1}} - h\Gamma, \quad \Gamma = V_0 h_0{}^{-1} \tau h_0{}^{T^{-1}} \tag{2.1}$$

where W is the mass of the cell; σ is the internal microscopic stress tensor; τ is the thermodynamic tension tensor and is related to the externally applied stress tensor s by

$$\tau = V h_0 h^{-1} s h^{T^{-1}} h_0{}^T / V_0 \tag{2.2}$$

where V_0 and h_0 are the volume and cell matrix corresponding to the zero stress state respectively. For a system subjected to an external hydrostatic pressure P, the equation of motion becomes

$$W\ddot{h} = (\sigma - P) V h^{T^{-1}} \tag{2.3}$$

Eq.(2.1) and (2.3) will allow h to adjust to the applied loading. At equilibrium, the internal stress of the system will be equal to the external loading. As is shown by Ray and Rahman [31], in the generalized MD simulations, the enthalpy H is conserved. Thus, one can generate the (HτN) or (HPN) ensemble. Then by rescaling velocities at each time step, one can generate the isothermal-isostress (NτT) ensemble, or the isothermal-isobaric (NPT) ensemble. In this thesis, the (NPT) ensemble is used to study structural response of systems under hydrostatic tension or compression; and the (NVE) ensemble is used for calculations of mechanical properties.

Due to the constraints of computer speed and memory, MD simulations are limited to certain size and time duration. The typical size of a MD simulation consists of $10^2 - 10^4$ atoms; and the longest time duration is about 100-1000 pica-seconds (ps). However, with the development of massive parallel computers, simulations involving as many as 10^6 atoms have now become reality [32] [33].

In order to use limited number of atoms to study bulk materials containing at least 10^{23} atoms, proper boundary conditions must be applied so that the small system being simulated can represent a macroscopic system. In this thesis, periodic boundary conditions along three Cartesian directions (x, y and z) are applied to the simulation cell to study bulk systems. The periodic conditions can yield satisfactory results in most cases. For free surfaces and interfaces, the periodic boundary condition is only applied to the two directions parallel to the surfaces and is removed along the direction normal to the surfaces. By so doing, one can study semi-infinite system with finite thickness.

Finally, using an appropriate time step and sufficient number of time steps are necessary to observe real physical phenomena and obtain reliable physical properties. In this thesis, for the Tersoff potential, the time step is taken as $1.45 \times 10^{-4} ps$. Typical runs for MD simulations in studying the response of a system under stress last about $7 - 10ps$. The runs for properties calculations (e.g., elastic constants) last about $10 - 80ps$.

2.2 Calculation of Mechanical Properties

One of the fundamental mechanical and thermodynamic properties of a general system is its elastic constants. Given an interatomic potential function, calculating elastic constants is the most important step to understand its mechanical behavior. In fact, bulk modulus usually is used to fit parameters in potential functions. Since bulk modulus only provides a description of the volumetric response to hydrostatic pressure applied to the material, elastic constants are fourth rank tensor describing the variation of stress with strain. A newly formulated elastic stability criteria[15][16] have shown that the elastic constants alone are not enough, it is the combination of the elastic constants and the applied stress, i.e., the elastic stiffness coefficients, that ultimately determine the mechanical strength of a system. It is therefore important to accurately and efficiently calculate the elastic constants and stiffness coefficients, especially under conditions of finite strain at finite temperature, where usually little experimental data exist. Generally, two methods are available to compute elastic constants in simulations. One is the stress-strain method; and the other is the recently formulated fluctuation formula[34]. The stress-strain method is valid only for calculations at $0K$. At finite temperatures, it has been found by Sprik et al.[35] and by Rahman[34] that this method is not satisfactory because of its slow convergence. Both the stress-strain method and the fluctuation formula involve calculations of stress and strain. In recent years, stress and elastic constants have been calculated for simple metals using Lennard-Jones[36][17] and EAM potentials[17][37] and for Si by Stillinger-Weber potential[34]. In all these cases, fluctuation formulae have been applied and they have led to good results. However, no study has been done for the Tersoff potential because of the complex many-body nature of this potential. It is a nontrivial task to derive the fluctuation formulae for the Tersoff potential because the derivation requires second derivatives of a many-body angular function. In this section, the focus is on how to use the general formulae to derive stress and elastic constants for many-body empirical potentials, in particular, the Tersoff potential.

2.2.1 Stress and Strain

For the purpose of finite strain study, we use the definition of Lagrangian strain

$$\epsilon = \frac{1}{2}({h_0}^{T^{-1}} h^T h h_0^{-1} - I) \tag{2.4}$$

where h and h_0 are as described in Sec. 2.1, and I is an identity matrix. In simulations, we use Eq.(2.4) to impose a strain on the system. Since this imposed strain is only a function of the simulation cell matrix, it should be taken as a global or macroscopic strain of the system. For a uniform Bravais lattice, local atomic strain is equal to this global strain everywhere. However, for non-Bravais lattices, such as diamond cubic and zincblende structures, more than one atom exist in each primitive cell. Under an imposed macroscopic shear strain, internal strain relaxation will occur between the atoms inside each primitive cell[38] [39]. This internal strain relaxation will contribute significantly to the elastic constants calculations as will be discussed more throughout this thesis.

Stress is defined as the derivative of the free energy with respect to the strain

$$V\tau_{\alpha\beta} = -\frac{\partial F}{\partial \epsilon_{\alpha\beta}} \tag{2.5}$$

where V is the volume and F is the free energy of the system. This is a straightforward generalization of the familiar thermodynamic relation $dF = -PdV$. More discussions of the precise definitions of the τ and ϵ will be given in Chapter 4. Under the condition of infinitesimal strain, the microscopic stress tensor $\sigma_{\alpha\beta}$ can be derived from Eq.(2.5) to be[40]

$$V\sigma_{\alpha\beta} = \sum_i p_{i\alpha} p_{i\beta}/m_i - \frac{1}{2}\sum_i (r_{i\alpha}\frac{\partial U}{\partial r_{i\beta}} + r_{i\beta}\frac{\partial U}{\partial r_{i\alpha}}) \tag{2.6}$$

where U is the total potential energy of the system; $p_{i\alpha}$ and $p_{i\beta}$ are the momentum component of atom i. (Note that the microscopic stress tensor calculated this way is the Cauchy stress tensor in the language of continuum elasticity, i.e., the true force per unit area at current state, as described in Chapter 2.) Readers are referred to the

work of Lutsko [40] for detailed derivation. Since Eq.(2.6) holds for any potential that is expressed as a function of atomic distances, we use it as a starting point to derive the stress for many-body empirical potentials. When applied to two-body potentials, Eq.(2.6) is reduced to the conventional Virial expression for atomic stresses. Therefore, Eq.(2.6) can be considered as a generalized Virial expression for many-body potentials. When Eq.(2.6) is applied to a system with periodic boundary conditions, it must be reduced to the expressions involving only differences in atomic coordinates. When expressed in differences of atomic coordinates, Eq.(2.6) will incorporate the periodic boundary conditions and external forces they imply [40]. Since

$$\frac{\partial U}{\partial r_{i\alpha}} = \sum_{j(j\neq i)} \frac{\partial U}{\partial r_{ij}} \cdot \frac{\partial r_{ij}}{\partial r_{i\alpha}} = \sum_{j(j\neq i)} \frac{\partial U}{\partial r_{ij}} \cdot \frac{r_{ij\alpha}}{r_{ij}} \tag{2.7}$$

where r_{ij} is the distance between atom i and j, and $r_{ij\alpha} = r_{i\alpha} - r_{j\alpha}$. we have

$$\begin{aligned} \sum_i (r_{i\alpha} \cdot \frac{\partial U}{\partial r_{i\beta}} + r_{i\beta} \cdot \frac{\partial U}{\partial r_{i\alpha}}) &= \sum_i \sum_{j(j\neq i)} \frac{\partial U}{\partial r_{ij}} \cdot (\frac{r_{i\alpha} r_{ij\beta}}{r_{ij}} + \frac{r_{i\beta} r_{ij\alpha}}{r_{ij}}) \\ &= \sum_i \sum_{j(j\neq i)} \frac{\partial U}{\partial r_{ij}} \cdot \frac{r_{i\alpha} r_{i\beta} - r_{i\alpha} r_{j\beta} + r_{i\alpha} r_{i\beta} - r_{i\beta} r_{j\alpha}}{r_{ij}} \end{aligned} \tag{2.8}$$

Since i and j are dummy indices, we find

$$\sum_i \sum_{j(j\neq i)} \frac{\partial U}{\partial r_{ij}} \cdot \frac{r_{i\alpha} r_{i\beta}}{r_{ij}} = \sum_i \sum_{j(j\neq i)} \frac{\partial U}{\partial r_{ij}} \cdot \frac{r_{j\alpha} r_{j\beta}}{r_{ij}} \tag{2.9}$$

Replacing the above equation into the right hand side of Eq.(2.8), we obtain

$$\sum_i (r_{i\alpha} \cdot \frac{\partial U}{\partial r_{i\beta}} + r_{i\beta} \cdot \frac{\partial U}{\partial r_{i\alpha}}) = \sum_i \sum_{j(j\neq i)} \frac{\partial U}{\partial r_{ij}} \cdot \frac{r_{ij\alpha} r_{ij\beta}}{r_{ij}} \tag{2.10}$$

Hence, the microscopic stress tensor for many-body potential functions with periodic boundary conditions is

$$V\sigma_{\alpha\beta} = \sum_i p_{i\alpha} p_{i\beta}/m_i - \frac{1}{2} \sum_i \sum_{j(j\neq i)} \frac{\partial U}{\partial r_{ij}} \cdot \frac{r_{ij\alpha} r_{ij\beta}}{r_{ij}} \tag{2.11}$$

Note that the same expression of microscopic atomic stress was obtained by Ray [34] using an independent approach. Eq.(2.11) can be used to derive the microscopic stress tensor for any distance based potentials, including the three-body Stillinger Weber[41] and Pearson potentials[42] and the many-body Tersoff potential[26]. The detailed derivation and formulation for Tersoff potential based on Eq.(2.11) are given in Appendix A. Pressure of the system can then be calculated using the relationship $P = \frac{1}{3}(\sigma_{xx} + \sigma_{yy} + \sigma_{zz})$.

2.2.2 Elastic Constants and Stiffness Coefficients

As mentioned earlier, elastic constants are among the most basic mechanical properties of materials. Conventional elastic stability criteria are expressed in terms of elastic constants[13]. Recently, new criteria were proposed based on elastic stiffness coefficients[15]. The stiffness coefficients are related to elastic constants by[11][16]

$$B_{ijkl} = C_{ijkl} + \frac{1}{2}[\sigma_{il}\delta_{jk} + \sigma_{jl}\delta_{ik} + \sigma_{ik}\delta_{jl} + \sigma_{jk}\delta_{il} - 2\sigma_{ij}\delta_{kl}] \tag{2.12}$$

where i, j, k, l represent x, y, or z, B_{ijkl} is the stiffness coefficient, C_{ijkl} is the elastic constant, and δ_{ij} is the Kronecker delta function. Hence, once the elastic constants are calculated, the stiffness coefficients can be obtained using Eq.(2.12).

We have employed two methods to calculate elastic constants, i.e., the direct stress-strain method and the fluctuation formulae. For cubic crystals, at infinitesimal strain, using the Voigt notation

$$\begin{aligned} xx \rightarrow 1 \quad yy \rightarrow 2 \quad zz \rightarrow 3 \\ yz \rightarrow 4 \quad xz \rightarrow 5 \quad xy \rightarrow 6 \\ zy \rightarrow 4 \quad zx \rightarrow 5 \quad yx \rightarrow 6 \end{aligned} \tag{2.13}$$

the stress-strain relation can be written as

$$\sigma_{11} = C_{11}\epsilon_{11} + C_{12}\epsilon_{22} + C_{12}\epsilon_{33} \tag{2.14}$$

$$\sigma_{22} = C_{12}\epsilon_{11} + C_{11}\epsilon_{22} + C_{12}\epsilon_{33}$$

$$\sigma_{33} = C_{12}\epsilon_{11} + C_{12}\epsilon_{22} + C_{33}\epsilon_{33}$$

$$\sigma_{12} = C_{44}\epsilon_{12};\ \ \sigma_{13} = C_{44}\epsilon_{13};\ \ \sigma_{23} = C_{44}\epsilon_{23}$$

where ϵ_{ij} is a small strain defined by Eq.(2.4). Eq.(2.14) is the relation to be used in the direct stress-strain method. The procedure of this method involves imposing small strains to the system; calculating stresses corresponding to these strains; and then obtaining the coefficients from stress-strain curves using Eq.(2.14). At $0K$, these calculations are trivial except for calculation of C_{44}. As mentioned earlier, imposing strain ϵ_{ij} is through the h matrix and ϵ_{ij} is a homogeneous strain. For a crystal (e.g. SiC) with two atoms in each primitive cell, internal strain relaxation will occur between the two sets of sublattices (Si sublattice and C sublattice). By symmetry, this internal strain relaxation affects C_{44} and does not affect C_{11} and C_{12}[38] [39]. Therefore, proper calculation of C_{44} using the stress-strain relation requires treatment of the internal strain relaxation. Several methods can be used to meet this requirement. We found that the simplest method is to perform static relaxation. First, we impose ϵ_{23} to the system, and calculate stress σ_{23} under strain ϵ_{23} without further relaxation of atomic positions. Coefficient thus obtained is C_{44}^0. As we check the forces on each atom, we find non-zero forces along the body-diagonal directions. This suggests that the internal strain relaxation will take place along the body-diagonal direction, leading atoms to zero force positions. We then relax and move atoms along the body-diagonal direction to decrease their forces. Once the zero force positions are reached, we calculate the stress σ_{23} again. σ_{23} thus obtained has taken into account of the internal strain relaxation and can be used to calculate the correct C_{44}. By repeating the static relaxation procedure for each imposed strain, we are able to correctly calculate the stress-strain curves for C_{44}. Figure 2-7 shows the results of a calculation of elastic constants for β-SiC at equilibrium condition at $0K$. Results of both C_{44}^0 and C_{44} are shown. The unrelaxed C_{44}^0 obtained from the dashed line is $3.11 Mbar$, and the relaxed C_{44} is $2.55 Mbar$. We find that internal strain relaxation decreases C_{44} significantly.

The stress-strain method described above is straightforward and efficient in calculating elastic constants at zero temperature. However, when applied to finite temperatures, the stress-strain method is not efficient and requires extremely long runs in simulation to obtain satisfactory results[35][34]. To improve the efficiency of elastic constants calculations in molecular dynamics simulations, Ray and Rahman[31] [34] have developed fluctuation formula, which we will use in this thesis to calculate elastic constants of β-SiC at finite temperatures. For a microcanonical ensemble (EhN), the fluctuation formula gives[34]

$$\begin{aligned} V_0 h_{0ip}^{-1} h_{0jq}^{-1} h_{0kr}^{-1} h_{0ns}^{-1} C_{pqrs} &= -4\delta(M_{ij}M_{kn})/k_BT \\ &\quad +2Nk_BT(G_{in}^{-1}G_{jk}^{-1} + G_{ik}^{-1}G_{jn}^{-1}) \\ &\quad + \sum_{a<b,c<d} < k(a,b,c,d)s_{abi}s_{abj}s_{cdk}s_{cdn} > \end{aligned} \tag{2.15}$$

where i, j, k, n, p, q, r,and s represent x, y, or z; s_{abi} is the scaled coordinate difference between particle a and b with respect to h, i.e., $x_{abi} = h_{ij}s_{abi}$; h_0 is the h matrix at zero stress; G is the metric tensor $G = h^T h$; M_{ij} is related to the microscopic stress tensor by $M_{ij} = -Vh^{-1}\sigma h^{T^{-1}}/2$; and $k(a,b,c,d)$ is related to the potential energy by $k(a,b,c,d) = (\partial^2 U/\partial r_{ab}\partial r_{cd} - (\partial U/\partial r_{ab})\delta_{ac}\delta_{bd}/r_{ab})/r_{ab}r_{cd}$. Fluctuation of any two quantities A and B is defined as $\delta(AB) =< AB > - < A >< B >$, where the bracket <> represents the ensemble average. The canonical ensemble (ThN) fluctuation formula for elastic constants has the same form as Eq.(2.15) except that the averages are identified as canonical ensemble averages and the elastic constants are identified as the isothermal elastic constants[43]. In this thesis, we use the canonical ensemble (ThN) to calculate the elastic constants. Furthermore, if we use a cubic simulation cell for a system with cubic symmetry, the h matrix is diagonalized, i.e., $h_{ij} = \delta_{ij}l$, where l is the simulation cell length of each side. It is easy to show that for the cubic simulation cell, the fluctuation formula for elastic constants becomes

$$C_{ijkn} = \frac{l_0}{l} \cdot [-\frac{V}{k_BT} \cdot \delta(\sigma_{ij}\sigma_{kn}) + \frac{2Nk_BT}{V} \cdot (\delta_{in}\delta_{jk} + \delta_{ik}\delta_{jn})$$

$$+ < \frac{1}{V} \sum_{a<b} \sum_{c<d} [\frac{\partial^2 U}{\partial r_{ab} \partial r_{cd}} - \frac{\partial U}{\partial r_{ab}} \cdot \frac{\delta_{ac}\delta_{bd}}{r_{ab}}] \frac{r_{abi} r_{abj} r_{cdk} r_{cdn}}{r_{ab} r_{cd}} >] \quad (2.16)$$

Three terms are involved in this equation. The first term is called the stress fluctuation term, the second is called the kinetic term which is a trivial term, and the third is the Born term. The explicit stress terms in the equation arise from the action of the derivative of the Hamiltonian over strain, the Born term arises from the action of the second derivatives of the internal energy. Details of the derivation of Eq.(2.15) are referred to a review paper by Ray [34]. As pointed out by Ray[34], the stress fluctuation term is important for calculating C_{44} because it takes into account the effects of internal strain relaxation. In the Voigt notation, the three elastic constants for cubic crystals, C_{11}, C_{12} and C_{44} are derived

$$\begin{aligned} C_{11} &= \frac{l_0}{l} \cdot [-\frac{V}{k_B T} \cdot \delta(\sigma_{xx}\sigma_{xx}) + \frac{4Nk_BT}{V} + < \frac{1}{V} C_{11}^B >] \quad (2.17) \\ C_{12} &= \frac{l_0}{l} \cdot [-\frac{V}{k_B T} \cdot \delta(\sigma_{xx}\sigma_{yy}) + < \frac{1}{V} C_{12}^B >] \\ C_{44} &= \frac{l_0}{l} \cdot [-\frac{V}{k_B T} \cdot \delta(\sigma_{yz}\sigma_{yz}) + \frac{2Nk_BT}{V} + < \frac{1}{V} C_{44}^B >] \end{aligned}$$

where the Born terms C_{11}^B, C_{12}^B and C_{44}^B are

$$\begin{aligned} C_{11}^B &= \frac{1}{V} \sum_{a<b} \sum_{c<d} [\frac{\partial^2 U}{\partial r_{ab} \partial r_{cd}} - \frac{\partial U}{\partial r_{ab}} \cdot \frac{\delta_{ac}\delta_{bd}}{r_{ab}}] \frac{x_{ab} x_{ab} x_{cd} x_{cd}}{r_{ab} r_{cd}} \quad (2.18) \\ C_{12}^B &= \frac{1}{V} \sum_{a<b} \sum_{c<d} [\frac{\partial^2 U}{\partial r_{ab} \partial r_{cd}} - \frac{\partial U}{\partial r_{ab}} \cdot \frac{\delta_{ac}\delta_{bd}}{r_{ab}}] \frac{x_{ab} x_{ab} y_{cd} y_{cd}}{r_{ab} r_{cd}} \\ C_{44}^B &= \frac{1}{V} \sum_{a<b} \sum_{c<d} [\frac{\partial^2 U}{\partial r_{ab} \partial r_{cd}} - \frac{\partial U}{\partial r_{ab}} \cdot \frac{\delta_{ac}\delta_{bd}}{r_{ab}}] \frac{y_{ab} z_{ab} y_{cd} z_{cd}}{r_{ab} r_{cd}} \end{aligned}$$

Eq.(2.17) applies for both two-body and many-body potentials. Detailed derivation of the elastic constants for the Tersoff potential is given in Appendix A. To our knowledge, this is the first time that the fluctuation formula for the Tersoff potential has been derived.

As a first test, we use both stress-strain method and the fluctuation formula to calculate elastic constants of β-SiC at $0K$. For the fluctuation formulae, only the

Born terms are used at $0K$. Table 2.1 shows the results from Born term calculation and from direct stress-strain curves. It also shows the results calculated by Tersoff[26]. The results from stress-strain curves agree well with Tersoff's calculation. C_{11} and C_{12} from the Born term calculations are exactly the same as that from the stress-strain curves. This consistency confirms that our derivations of the stress expression and the Born term are correct. However, the Born term calculation of C_{44} only produces the unrelaxed elastic constant C_{44}^0. This means that the internal strain relaxation is not considered. As pointed out by Ray[34], it is the fluctuation term calculated in MD simulations that accounts for the internal strain relaxation. In Chapter 3, we will show clearly that the effect of internal strain relaxation is represented by the stress fluctuation term of C_{44}.

2.3 Potential Functions for SiC

2.3.1 Introduction

A real-space description of the total potential energy of a condensed matter system as a function of atomic positions is useful in materials physics for several reasons. First, they provide the simplest understanding of the origin of structural features in crystalline solids, defects in crystals and disordered systems. Secondly, in addition to such improved interpretability, interatomic potentials provide computational speed essential for computer simulations of complex materials science problems, such as fracture dynamics and dislocation motion. In the last twenty years, tremendous efforts have been made in order to develop better interatomic potentials for real materials. Traditionally, the interactions between atoms are described by pairwise interactions in the so called pair potentials. Lennard-Jones type potentials are typical examples that are useful in studying inert gases and close-packed fcc metals. But for semiconductors, pair potentials fail to describe the directional covalent bonds. Including at least three-body interactions is needed in order to describe the angular forces in semiconductors. In the last decade, many researchers have devoted efforts to develop

potential functions for Si. A recent review of potential functions for Si can be found in a paper by Balamane et al.[44]. Review concluded that the potentials only work well in the regions where properties are fitted and a lack of transferrability is common for these potentials. This is one of the main reasons that stimulate the development of tight-binding molecular dynamics simulations. Tight-binding MD simulations are aimed to have better accuracy and transferrability and yet still allow less expensive simulations than first principle calculations. Nevertheless, the studies of complex physical phenomena such as melting, structural transition, fracture and dislocations still largely rely on atomistic simulations using empirical potential functions. At least, empirical potentials are used as the first approach to these problems. If necessary, tight-binding method or first principle calculations can be used as higher level follow up to study a well focused problem which is usually first analyzed during simulations using empirical potentials[45].

In this thesis, we will study the structural and mechanical properties of β-SiC using currently available empirical potential functions. Crystalline SiC is a binary covalent material. It has several polytypisms, among which the zincblende β-SiC ($3C$ polytype) is the most frequently studied phase in experiments and calculations. It is stable up to $2500°C$. β-SiC has the same local geometric bonding as in single element diamond cubic Si or dimaond C. The bonding characteristic of β-SiC is mainly covalent with about 12% ionicity[6]. Compared to Si or C, complication arises in SiC since two different types of atoms (Si and C) are involved. Currently, three empirical potential functions exist for SiC. One is developed by Pearson et al.[42], another is developed by Tersoff [26], and the third is developed by Baskes[46]. Also, tight-binding approximations [47][48][49] have been formulated and applied to study structural properties of β-SiC. In our present work, we have studied the Pearson and the Tersoff potentials. $0K$, static calculations are performed for cohesive energy, lattice constant, bulk modulus and elastic constants. The results from our calculation, tight-binding approximation[49] and experimental data are presented in Table 2.1. The comparison shows that the Tersoff potential yields much better results than the Pearson potential. Therefore, we will only briefly summarize the Pearson potential

below and will focus on the Tersoff potential in the rest of the thesis.

2.3.2 Pearson Potential

In the Pearson potential, the total potential energy of the system is written as

$$\begin{aligned} U = \sum_i U_i = \tfrac{1}{2!}\sum_{i\neq j} V^{(2)}(r_{ij}) + \tfrac{1}{3!}\sum_{i\neq j\neq k} V^{(3)}(r_{ij}, r_{ik}, r_{jk}) \\ V^{(2)}(r_{ij}) = \tfrac{\epsilon}{m-n}\left[n\left(\tfrac{R_0}{r_{ij}}\right)^m - m\left(\tfrac{R_0}{r_{ij}}\right)^n\right] \\ V^{(3)}(r_{ij}, r_{ik}, r_{jk}) = Z\left[\tfrac{1+3\cos\theta_{ij}\cos\theta_{ik}\cos\theta_{jk}}{(r_{ij}r_{ik}r_{jk})^3}\right] \end{aligned} \tag{2.19}$$

where $m = 12$, $n = 6$; ϵ, R_0, and Z are three parameters fitted from bond lengths and cohesive energies of bulk diamond Si, molecular Si_2 and other Si and C clusters. No properties of bulk diamond C has been incorporated during the fitting, and no cutoff value was given in the original paper [42]. We have determined the cutoff by reproducing the cohesive energies and lattice parameters of bulk Si and β-SiC as given in the paper. We find that the cutoff is three times the nearest neighbor distance in β-SiC. Under this cutoff, the potential involves as many as 7th shell interactions. Recently, Balamane et al.[44] also found the same long range cutoff for Si. With such a long cutoff, in β-SiC, each atom interacts with as many as 86 atoms at equilibrium conditions at $0K$. Therefore, the Pearson potential is very expensive for MD simulations. In Table 2.1, we find that the elastic constants calculated by the Pearson potential are almost three times larger than experimental values. In Figure 2-2, we show the comparison between cohesive energy curves obtained from the Pearson potential, the modified Tersoff potential (to be discussed in the coming section) and ab initio calculation [50]. One can clearly see the discrepancy between the Pearson potential and the other two methods. Thus, our results indicate that the Pearson potential does not properly describe the bulk properties of β-SiC. Since it is also extremely inefficient in simulations because of its long cutoff, we will not pursue further studies using this potential. And we turn to use the Tersoff potential described below.

2.3.3 Tersoff Potential

Formulation and Parameterization

Tersoff has developed empirical potential functions for covalently bonded solids such as silicon [51] [52] [24], carbon[53], germanium [54] and SiC[26][55]. In this potential, the electronic structural effects (e.g., sp^3 bonding) which give rise to tetrahedral coordination are described by a many-body bond ordering expression [56]. In the Tersoff potential for β-SiC, the total potential energy of the system is written as:

$$U = \sum_i U_i = \frac{1}{2}\sum_{i \neq j} V_{ij} \tag{2.20}$$

$$V_{ij} = f_c(r_{ij}) f_R(r_{ij}) + f_c(r_{ij}) b_{ij} f_A(r_{ij}) \tag{2.21}$$

$$f_R(r_{ij}) = A_{ij} \exp(-\lambda_{ij} r_{ij}) \tag{2.22}$$

$$f_A(r_{ij}) = -B_{ij} \exp(-\mu_{ij} r_{ij}) \tag{2.23}$$

$$b_{ij} = \chi_{ij}(1 + z_{ij}^{n_i})^{-1/2n_i} \tag{2.24}$$

$$z_{ij} = \beta_i \zeta_{ij} = \sum_{k(\neq i,j)} f_c(r_{ik}) \beta_i g(\theta_{ijk}) \tag{2.25}$$

$$g(\theta_{ijk}) = 1 + c_i^2/d_i^2 - c_i^2/[d_i^2 + (h_i - \cos\theta_{ijk})^2] \tag{2.26}$$

$$f_c(r_{ij}) = \begin{cases} 1 & r_{ij} < R_{ij} \\ \frac{1}{2} + \frac{1}{2}\cos\left[\frac{\pi(r_{ij} - R_{ij})}{S_{ij} - R_{ij}}\right] & R_{ij} < r_{ij} < S_{ij} \\ 0 & r_{ij} > S_{ij} \end{cases} \tag{2.27}$$

$$\lambda_{ij} = (\lambda_i + \lambda_j)/2, \quad \mu_{ij} = (\mu_i + \mu_j)/2$$

$$A_{ij} = \sqrt{A_i A_j}, \quad B_{ij} = \sqrt{B_i B_j}$$

$$R_{ij} = \sqrt{R_i R_j}, \quad S_{ij} = \sqrt{S_i S_j} \tag{2.28}$$

where i, j and k are indices of atoms in the system. f_A, f_R, f_c and b_{ij} are functions of distances or angles between atoms, others are fitted parameters. The function f_R represents a repulsive pair potential, which includes the orthogonalization energy when atomic wave functions overlap, and f_A represents an attractive pair potential associated with bonding, f_c is a cutoff function, and b_{ij} represents a measure of the bond order (i.e., binding strength). Parameters with single subscript are for Si or C, and

they are fitted from bulk properties of diamond cubic Si and diamond C respectively [52] [24] [53]. Parameters for SiC were obtained by arithmetic or geometric average depending on whether or not the parameters appear in the exponent. An additional parameter χ_{ij} was introduced for β-SiC. It was obtained by fitting the heat of formation of SiC[26]. The potential parameters for Si, C and SiC are listed in Table 2.2. It is worth mentioning that in the Tersoff potential model for β-SiC, the only property that is directly fitted is the heat of formation. In this potential, if i and j are the same type of atoms, the potential function automatically reduces to that for Si or C. This means that, in SiC, atoms of the same type, e.g., Si-Si or C-C interact as if they were in a single element diamond cubic Si or diamond C lattice. At $0K$ equilibrium condition, the cutoff only allows first nearest neighbor interactions between Si and C atoms. The results from the Tersoff potential shown in Table 2.1 are calculated with interactions between Si and C atoms only. At this stage, no interactions between Si-Si and C-C are considered yet.

Bond-order Parameter

A novel feature of the Tersoff potential is the bond-order parameter b_{ij}. Bond-order, meaning binding strength, describes the strength of attractive interactions between atoms. The larger the bond-order, the stronger the binding and the lower is the interaction energy. The essence of the Tersoff potential is that binding between two atoms relies on the local arrangement of surrounding atoms, and competition from surrounding atoms can change the binding strength. In order to understand the bond-order parameter and its function, we can consider atom i as a *central atom* and calculate its cohesive energy. Atom i will interact with a few *neighbor atoms* (4 in β-SiC). When we consider its interaction with a particular neighbor atom j, the other neighbor atoms (labeled as k's) are considered as *environmental atoms.* A schematic view is shown in Figure 2-1 to illustrate this picture. We term the binding between i and j the *primary bond,* and bindings between i and k's the *secondary bonds.* The most important feature in this atomic interaction picture is that the more environmental atoms and the closer they are to the central atom, the weaker

the primary bond is. Moreover, for sp^3 bonded structures, the angle between the primary bond and a secondary bond θ_{ijk} changes the bond-order parameter in such a way that the interaction favors a tetragonal binding geometry. Therefore, three factors determine the binding strength of a primary bond. They are (1)number of environmental (k) atoms, (2)distances between atom i and k (r_{ik}), and (3) angles (θ_{ijk}) between bond ij and ik's. In the Tersoff potential, influences of these three factors on the bond order parameter b_{ij} (binding strength of bond ij) are expressed through the so called effective coordination number (ζ_{ij}),

$$\zeta_{ij} = \sum_k f_c(r_{ik}) g(\theta_{ijk}) \tag{2.29}$$

Here the sum is over the coordination number; the cut-off function f_c depends on distance r_{ik}, and the angular dependence is treated by function $g(\theta_{ijk})$. As shown in Figure 2-3(a), once the effective coordination number is determined, the bond-order parameter can be calculated from the monotonically decreasing function of ζ_{ij} [56].

Since there is no rigorous justification for the effective coordination number and the angular function to have the forms proposed by Tersoff, it is useful to examine their behavior and understand how the bond-order concept operates. The angular functions $g(\theta)$ for central atom C and Si are plotted in Figure 2-3(b). The functions reach their minima at $\theta_c = 124.79°$ and $\theta_{si} = 126.74°$ respectively. These angles are not equal to the tetrahedral angle of 107.9° that appears in a covalent structure. In order to see how b_{ij} and the potential energy vary with angle, we rewrite the effective (many-body) energy V_{ij} as

$$\begin{aligned} V_{ij} &= V_{ij}^{(2)} + V_{ij}^{(m)} \\ V_{ij}^{(2)} &= f_c(r_{ij})[f_R(r_{ij}) + f_A(r_{ij})] \\ V_{ij}^{(m)} &= -f_c(r_{ij})[1 - b_{ij}] f_A(r_{ij}) \end{aligned} \tag{2.30}$$

where $V_{ij}^{(2)}$ is the simple distance dependent two-body term, and $V_{ij}^{(m)}$ is the many-body attractive energy that depends on the local atomic arrangement. For simplicity,

we take a triplet of atoms i, j and k, fix distances r_{ij} and r_{ik} at the equilibrium distance of β-SiC and vary θ_{ijk} to see the behavior of b_{ij} and $V_{ij}^{(m)}$. The results are shown in Figure 2-3(c) and (d). As one can see that when the angular function g reaches its minimum, b_{ij} reaches its maximum, and the many-body energy reaches its minimum. Also, the many-body energy is always positive and it favors high angle three-atom clusters rather than low angle ones. It is clear that θ_c and θ_{s_i} are the angles that determine the lowest energy configurations of three-atom clusters. In covalent materials, the local atomic configurations are tetrahedrons, where the angle between any two bonds is 107.9°. The fact that the tetrahedral angle is not directly fitted by the angular functions in the Tersoff potential stands in contrast to the three-body Stillinger-Weber potential for Si[41], where the tetrahedral angle appears explicitly in the three-body energy of the potential. As we will show throughout this thesis, although the angular functions have not been directly fitted by the tetrahedral angle, the Tersoff's potential is capable of stabilizing the tetrahedral structure of β-SiC very well.

Further more, we can study the dependence of b_{ij} on the real coordination number, i.e. the true number of interacting atoms instead of the effective coordination number ζ_{ij}. We have studied situations when atoms are fully coordinated inside bulk β-SiC and when atoms are exposed at low index surfaces. Fig. 2-4 shows how V_{ij} and atomic potential energy of U_i vary as a function of real coordination numbers in β-SiC. These results show that the cohesive energy of an atom increases as it looses bonds at the surface, and the binding energy of primary bond decreases as the coordination number decreases. Thus, the idea of the bond order parameter is indeed realized through the formulation of the Tersoff potential.

Nearest Neighbor Interaction and Cutoff

The Tersoff potential is a short-ranged potential. Under the condition of normal pressure and zero temperature, it involves only first neighbor Si-C interactions. One drawback caused by this cutoff is that the Tersoff potential can not distinguish the two common polytypisms of SiC (e.g., β-SiC and α-SiC) energetically. These two

structures have the same local bonding but differ in their long range stacking sequences. Another drawback, which is more relevant to our study of β-SiC, is that the interactions between Si-Si and C-C atoms in SiC are not included during the development of the potential because the distances between them are beyond the cutoff. For a fixed cutoff, interactions between Si-Si and C-C can occur under high stress or finite temperature condition. The question is whether the Tersoff potential can handle these situations properly. In the following, we will show that there are problems related to this way of specifying the cutoff.

We first calculate cohesive energy, pressure and bulk modulus as a function of deformation at $0K$. The results are shown in Fig.2-5(a) to (c). The cohesive energy curve in Figure 2-5(a) shows two obvious unphysical kinks. The left kink appears at a compression state where $(r/r_0)_c = 0.984$, and the right kink appears at a tension state where $(r/r_0)_t = 1.18$. We find that the left kink corresponds to the state when neighboring Si atoms begin to interact. The distance between Si-Si in β-SiC is $3.05\mathring{A}$, and the upper bound cutoff between Si-Si is $S = 3.00\mathring{A}$. Under compression, the distance between Si-Si becomes equal to S at $r/r_0 = 3.00/3.05 = 0.984$, which is exactly where the left kink appears. For similar reason, under tension, the distance $(r/r_0)_t$ where the Si-C bond length is equal to R, the cutoff distance in the function f_c, occurs at the right kind position. These two kinks do not have the same significance for β-SiC . Since elastic stability analysis in Chapter 5 will show that the largest tension strain β-SiC can hold is $r/r_0 = 1.158$, the right kink actually will not occur at any tension point below this critical strain. This means that the right kink will not be encountered in modeling β-SiC, such as modeling brittle fracture under tension (see Chapter 5). However, this artifact will occur in disordered systems such as liquid and amorphous SiC because in these disordered structures, no lattice constrain on atomic positions and atoms have possibility sitting at any distances. The left kink, on the other hand, occurs at a small strain which can be easily reached by moderate compression. The reason is that the distance between Si-Si in β-SiC ($3.05\mathring{A}$) is within only 1.6% of the upper bound cutoff for Si-Si interaction ($S = 3.00\mathring{A}$). Even at the equilibrium condition at room temperature, second neighbor Si-Si interaction already

occur from time to time due to thermal fluctuations. Thus, the artifact associated with the left kink can show up at finite temperatures. The strange behavior of elastic constants at finite temperatures shown in Figure 2-5(d) gives such an example. It is not surprising since any artifact in potential energy will be carried over into results for the forces, pressure and elastic constants, etc. In Figure 2-5(b) and Figure 2-5(c), we show the results of pressure and elastic constants under deformation at $0K$. Artificial behavior can be clearly seen in these data.

In order to show what happens when second neighbor interaction between Si-Si sets in, we plot ζ_{ij}, b_{ij} and V_{ij} as a function of r/r_0 in Fig.2-6. We find that, at $r/r_0 = 0.984$, the effective coordination number ζ_{si-c} jumps abruptly due to sudden inclusion of the Si-Si interaction. This gives an abrupt decrease in the order parameter b_{si-c} and causes an abrupt increase in the effective pair energy of V_{si-c}. Consequently, potential energy abruptly increases as shown in Fig.2-5(a). This indicates that the artifact related to the left kink is due to the abrupt change of bond order parameter when the coordination number of Si changes from 4 to 16. Physically one expects smooth changes of the bond-order parameter and other physical properties when second neighbor interactions set in. The reason is that as long as no structural change occurs, the dominant bonding in β-SiC should still be determined by the first neighbor interactions. Therefore, whether or not the Si-Si interactions are included should not affect the calculated results of physical properties significantly.

Modification of Tersoff Potential

So far, we have seen that the physical properties calculated using the Tersoff potential are in good agreement with experimental data at equilibrium condition at $0K$ (cf. Table 2.1). We have also shown that the Tersoff potential has problem due to the short-range nature of its cutoff. In simulations, cutoff is introduced so that calculations can be efficient. A good choice of the cutoff can capture the dominant physics of the interactions. For sp^3 bonded structures, electrons are highly localized in the hybridized bonds between first nearest neighbors. From this point of view, it is more reasonable to use short-range cutoff for covalent materials than for metals. Therefore,

we would like to keep the short range nature of the cutoff in the Tersoff potential while eliminating the problem discussed in last paragraph. We have used a simple method to modify the Tersoff potential. The main idea is that we replace the original fixed cutoff by a variable cutoff which scales with $(volume)^{1/3}$. By so doing, we ensure the cutoff to always lie between the first and second shells, even when systems undergoes large deformations or large thermal fluctuations at high temperature. Thus, direct interatomic interaction is limited to the first shell as long as the system remains in the zincblende structure.

With this modification, one is free to choose the cutoff distances as long as they lie between the first shell and the second shell. We choose them to be about in the middle. However, to choose the cutoff values for Si-Si and C-C, we have to use information that involves second neighbor interactions. We have used the melting temperature as our choice of properties to fit the cutoffs. Table 2.5 shows the results of melting temperatures with different cutoff sets. The reference melting temperature is about $4500K$ from a Car-Parrinello study [57]. As can be seen, the melting temperature from the cutoff Set 3 in Table 2.5 is $5000K$, sufficiently close to the Car-Parrinello result for our purposes. Thus, we choose cutoff Set 3 for all subsequent calculations in this thesis. In Table 2.3, we have given the new set of cutoff values at zero pressure at $0K$. These and the scaling rule of cutoffs varying with $(volume)^{1/3}$ constitute what we will call henceforth the modified Tersoff potential.

A first test of this modified Tersoff potential is to calculate the cohesive energy and pressure again under deformation. The results are shown in Figure 2-8 for cohesive energy and in Figure 2-9 for pressure. Also shown in the figures are results obtained from ab initio calculation [50], the universal binding curve [58] and the original Tersoff potential. The comparison shows that the modified Tersoff potential is a significant improvement over the original model. In Chapter 3, we will present several other properties calculated using the modified Tersoff potential. Comparison with experimental data and first principle calculations will be made whenever applicable.

Table 2.1: Comparison of β-SiC properties by the Tersoff potential (TP), Pearson potential (PP), tight-binding method (TBA) and from experiment (Exp't).

	TP	PP	TBA	Exp't
Lattice Parameter ($\AA$)	4.32	4.19	4.36	4.36
Cohesive Energy (ev)	−6.18	−7.71		−6.34
Bulk Modulus ($Mbar$)	2.25	9.90	2.29	2.25
C_{11} ($Mbar$)	4.36	10.95	3.72	3.90
C_{12} ($Mbar$)	1.20	9.37	1.57	1.42
C_{44} ($Mbar$)	2.55	6.06	2.56(unrelaxed)	2.56

Table 2.2: Parameters for C, Si and SiC in the Tersoff potential.

	C	Si	SiC
A (ev)	1.3936×10^3	1.8308×10^3	1.5973×10^3
B (ev)	3.467×10^2	4.7118×10^2	4.04176×10^2
λ ($\AA^{-1}$)	3.4879	2.4799	2.9839
μ ($\AA^{-1}$)	2.2119	1.7322	1.97205
β	1.5724^{-7}	1.1000×10^{-6}	
n	7.2751×10^{-1}	7.8734×10^{-1}	
c	3.8049×10^4	1.0039×10^5	
d	4.384	1.6217×10^1	
h	-5.7058×10^{-1}	-5.9825×10^{-1}	
R	1.8	2.7	2.21
S	2.1	3.0	2.51

Table 2.3: Cutoff values at equilibrium condition at $0K$.

	$R_{c-c}(\AA)$	$S_{c-c}(\AA)$	$R_{si-si}(\AA)$	$S_{si-si}(\AA)$	$R_{c-si}(\AA)$	$S_{c-si}(\AA)$
Modified	1.93	2.13	2.60	2.80	2.36	2.56
Original	2.70	3.00	1.80	2.10	2.20	2.51

Table 2.4: Comparison of elastic constants obtained by the fluctuation formulae and direct stress-strain relation

	Born Term (Mbar)	Stress-Strain (Mbar)	Tersoff's results (Mbar)
C_{11}	4.358	4.36	4.2
C_{12}	1.198	1.20	1.2
C_{44}	3.111	2.55	2.6

Table 2.5: Melting temperatures of β-SiC determined from different cutoff values of the modified Tersoff potential. Reference value from a Car-Parrinello calculation is also given.

Cut-offs ($\AA$)	Set 1	Set 2	Set 3	Car-Parrinello
$R_{cut}(C-C)$	2.85 ± 0.15	2.35 ± 0.15	2.03 ± 0.1	
$R_{cut}(Si-Si)$	2.85 ± 0.15	2.35 ± 0.15	2.70 ± 0.1	
$R_{cut}(Si-C)$	2.95 ± 0.15	2.35 ± 0.15	2.46 ± 0.1	
$T_m(K)$	2000	6000	5000	4500

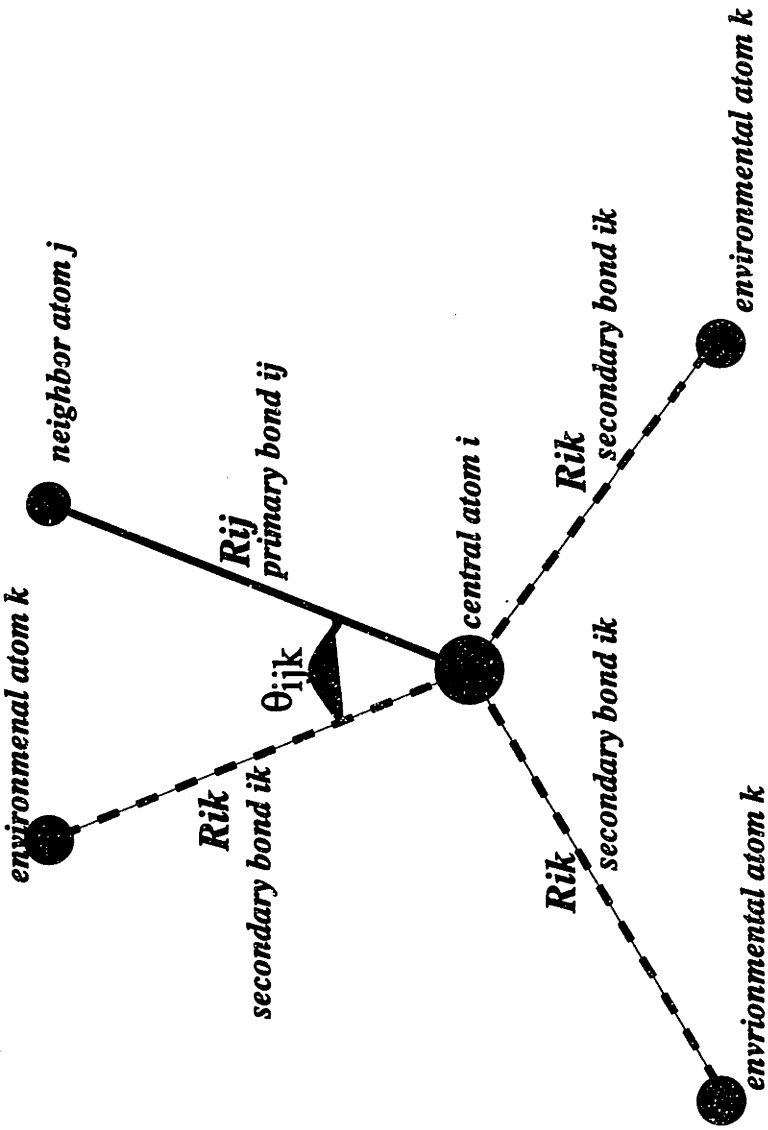

Figure 2-1: Schematic representation of interactive local atomic arrangement.

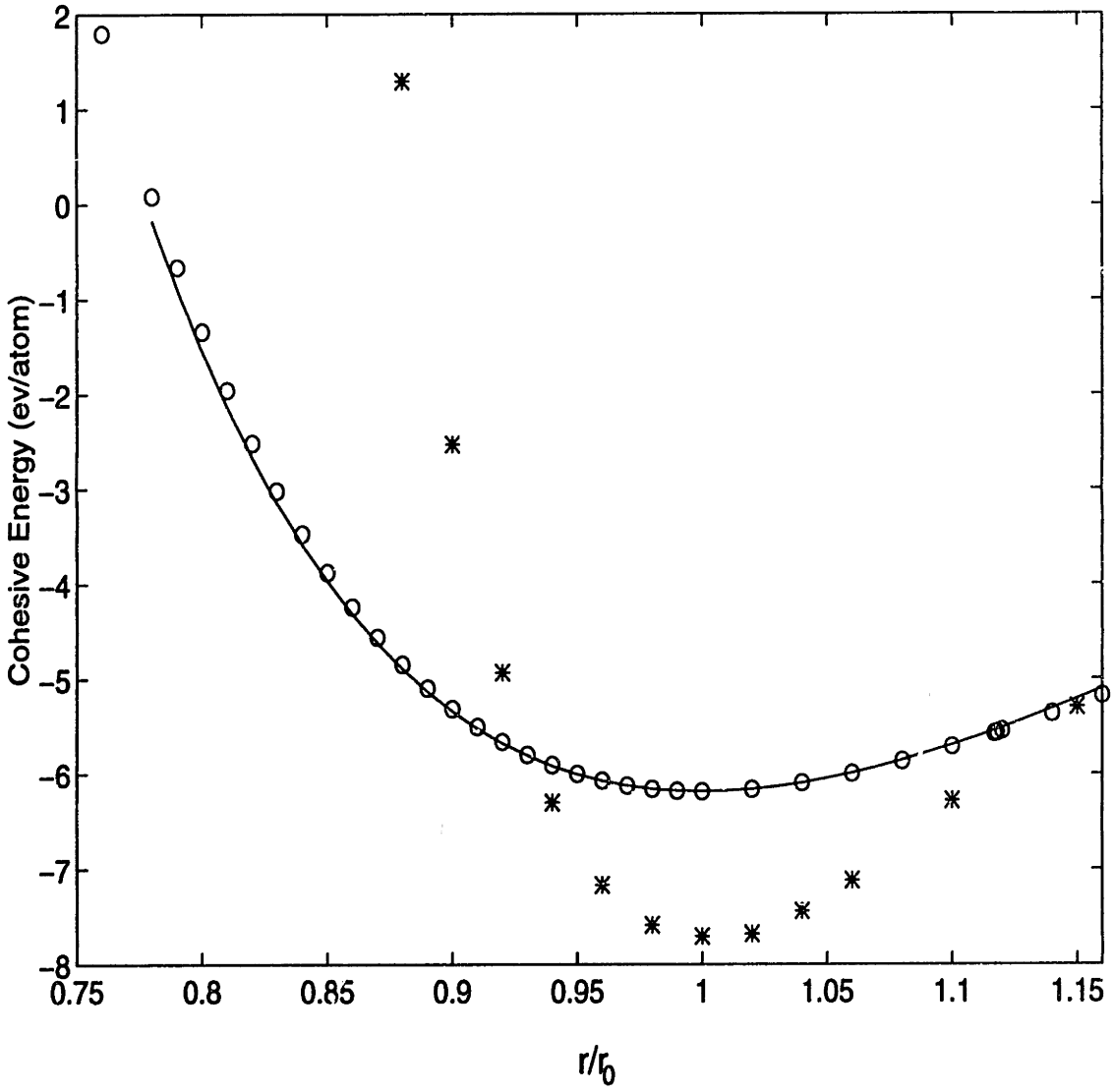

Figure 2-2: Comparison of cohesive energy curves obtained from the Pearson potential (stars), ab initio calculation (solid line) and the modified Tersoff potential (circles). r_0 is the zero pressure lattice parameter and r is the deformed lattice parameter.

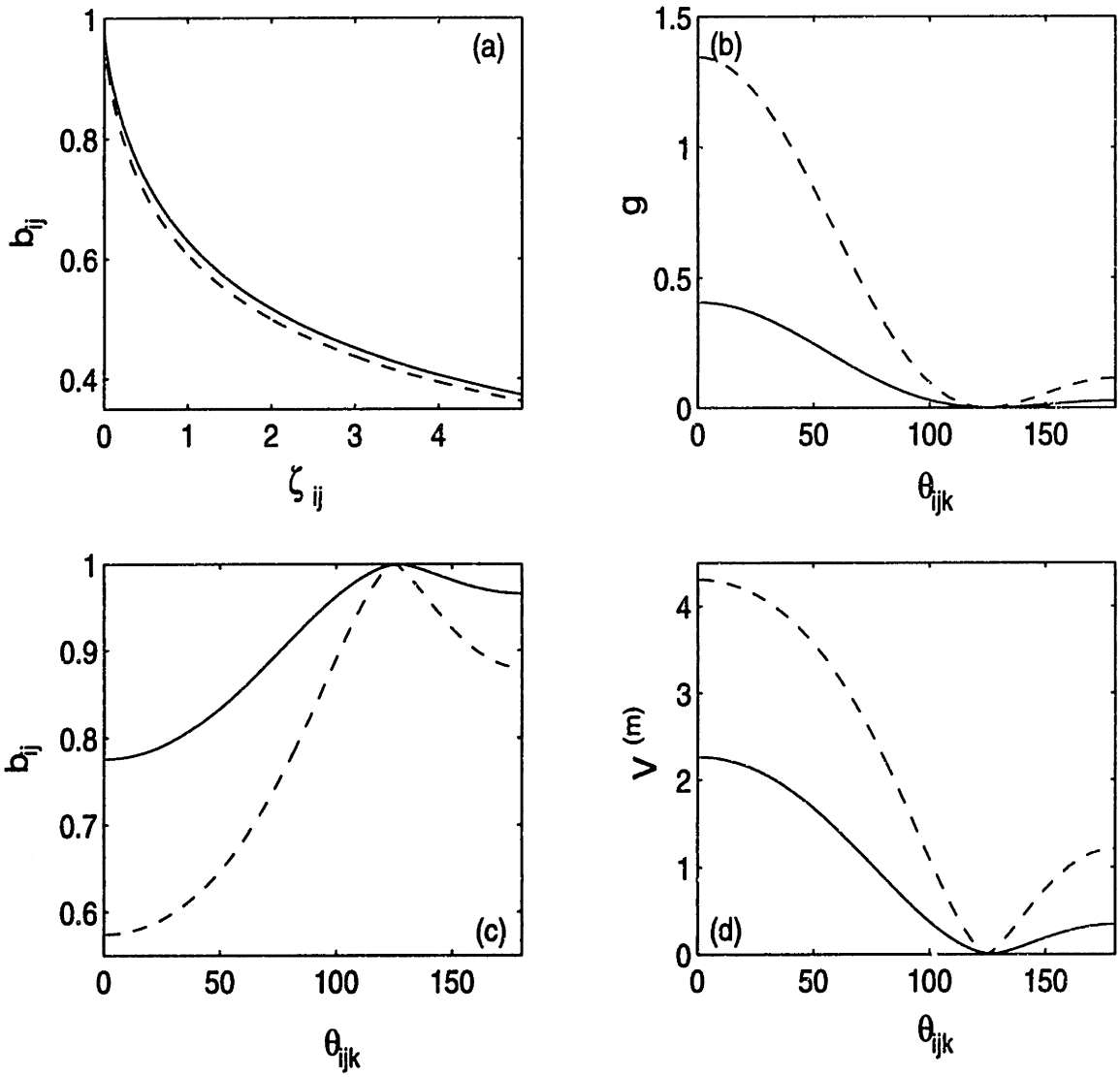

Figure 2-3: Important functions in the Tersoff potential. (a) bond-order b_{ij} vs. the effective coordination number ζ_{ij}; (b) angular function $g(\theta)$; (c) bond order b_{ij} vs. θ; (d) many-body energy $V_{ij}^{(m)}$ vs. θ. Solid lines are for Si as central atom, and dashed lines are for C as central atom.

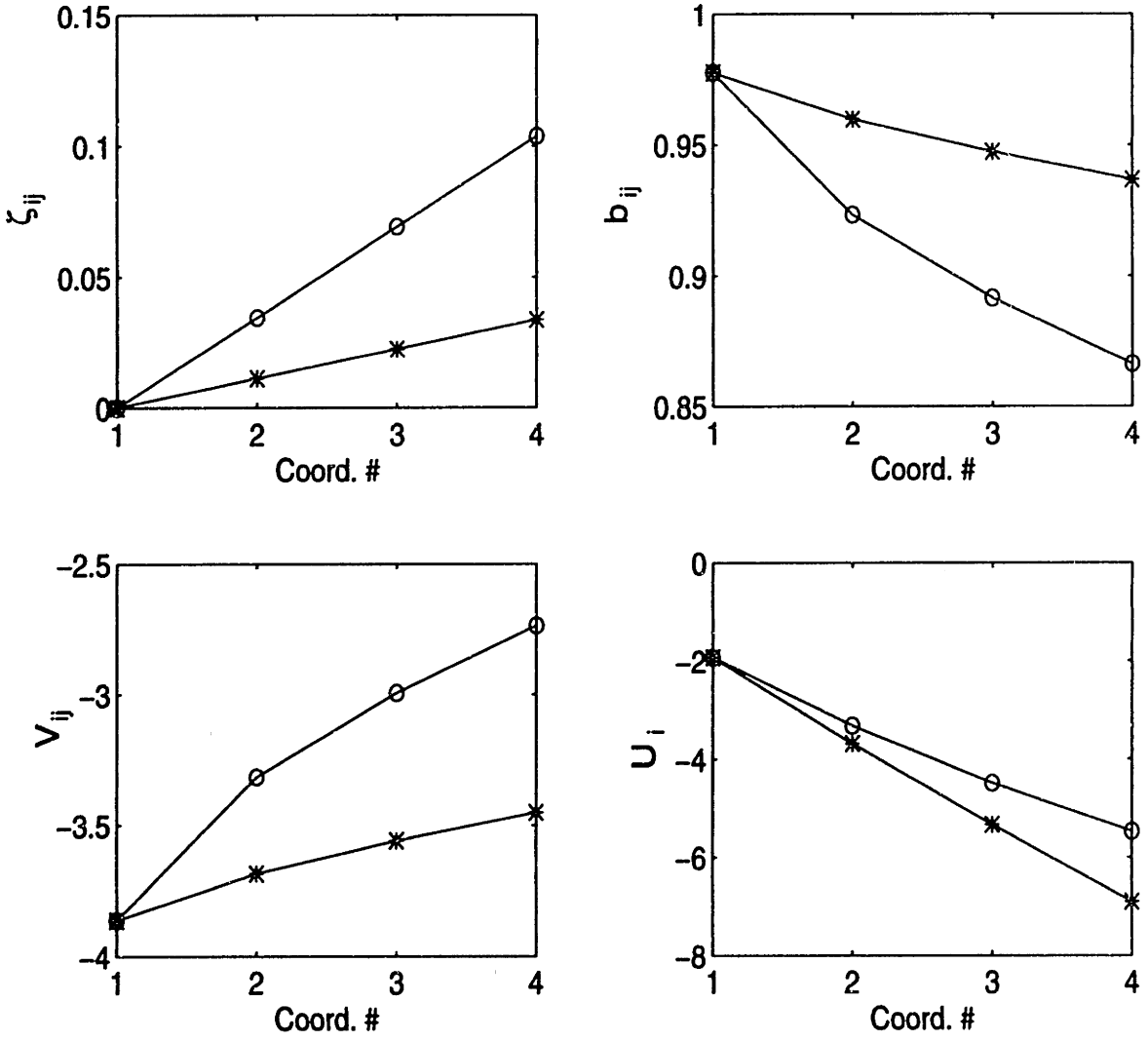

Figure 2-4: Variations of effective coordination number ζ_{ij}, bond order parameter b_{ij}, effective energy V_{ij} and cohesive energy per atom U_i with coordination number. Different coordination numbers correspond to atoms inside the bulk, exposed at (111) glide surface, (100) surface and (111) shuffle surface of β-SiC. Circles are data when a C atom is the central atom; stars are data when a Si atom is the central atom.

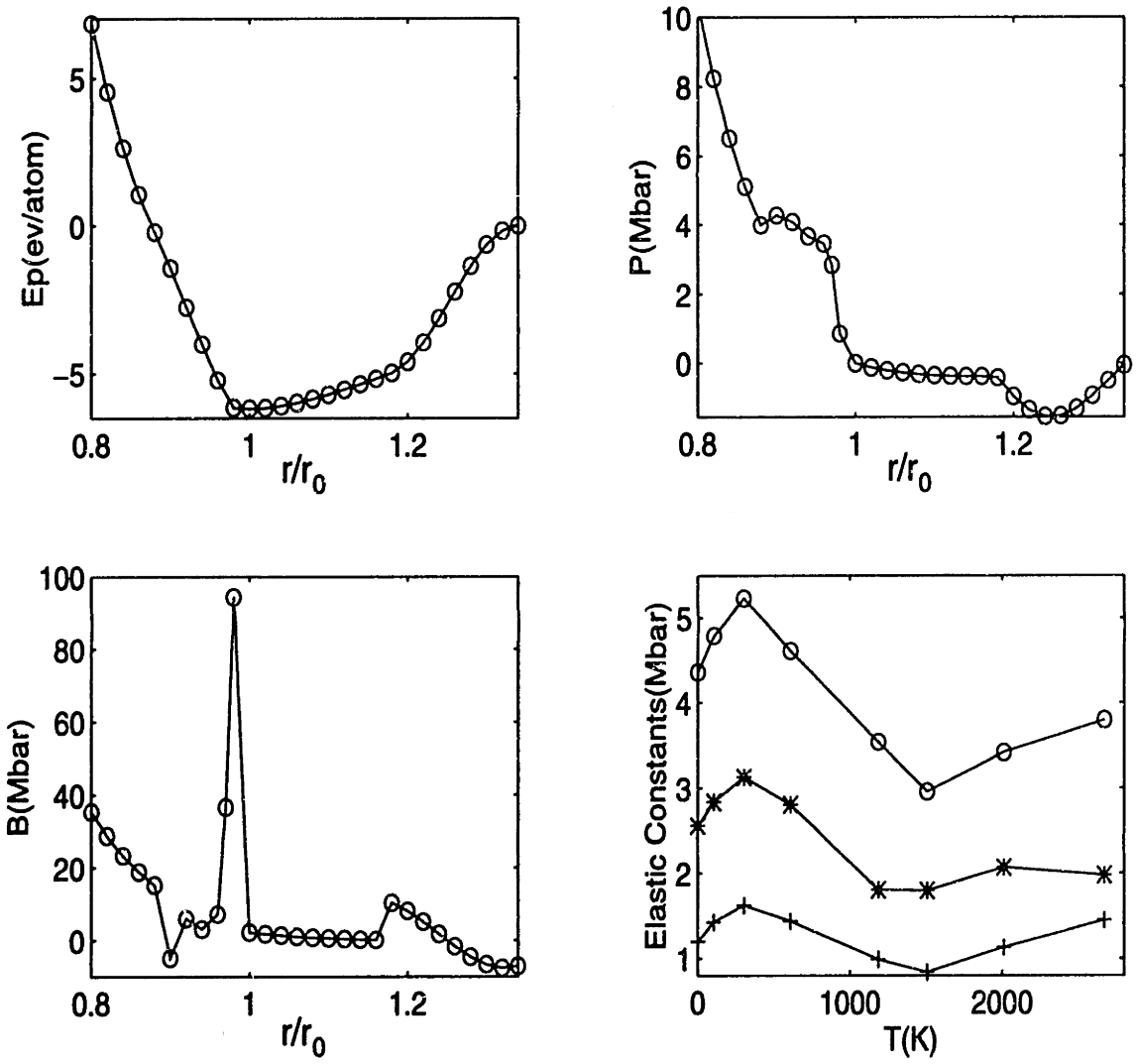

Figure 2-5: $0K$ calculation of (a) cohesive energy; (b) pressure; (c) bulk modulus under deformation. r is the current lattice constant and r_0 is the zero pressure lattice constant. (d) show the elastic constants at finite temperatures. All data are calculated using the original Tersoff potential.

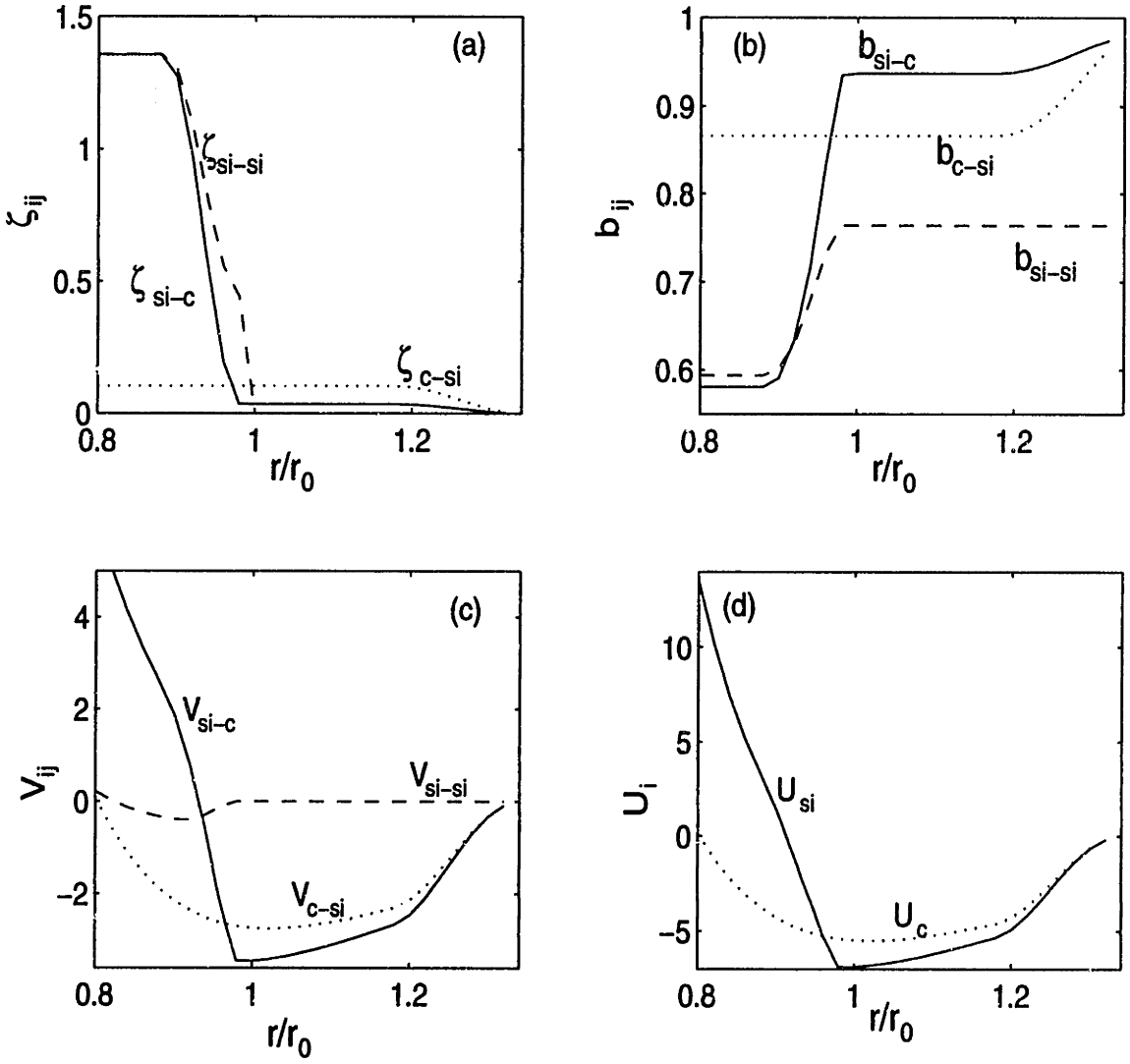

Figure 2-6: Variations of the effective coordination number ζ_{ij}, bond order parameter b_{ij}, effective energy V_{ij} and cohesive energy per atom U_i at various deformation states of β-SiC at $0K$.

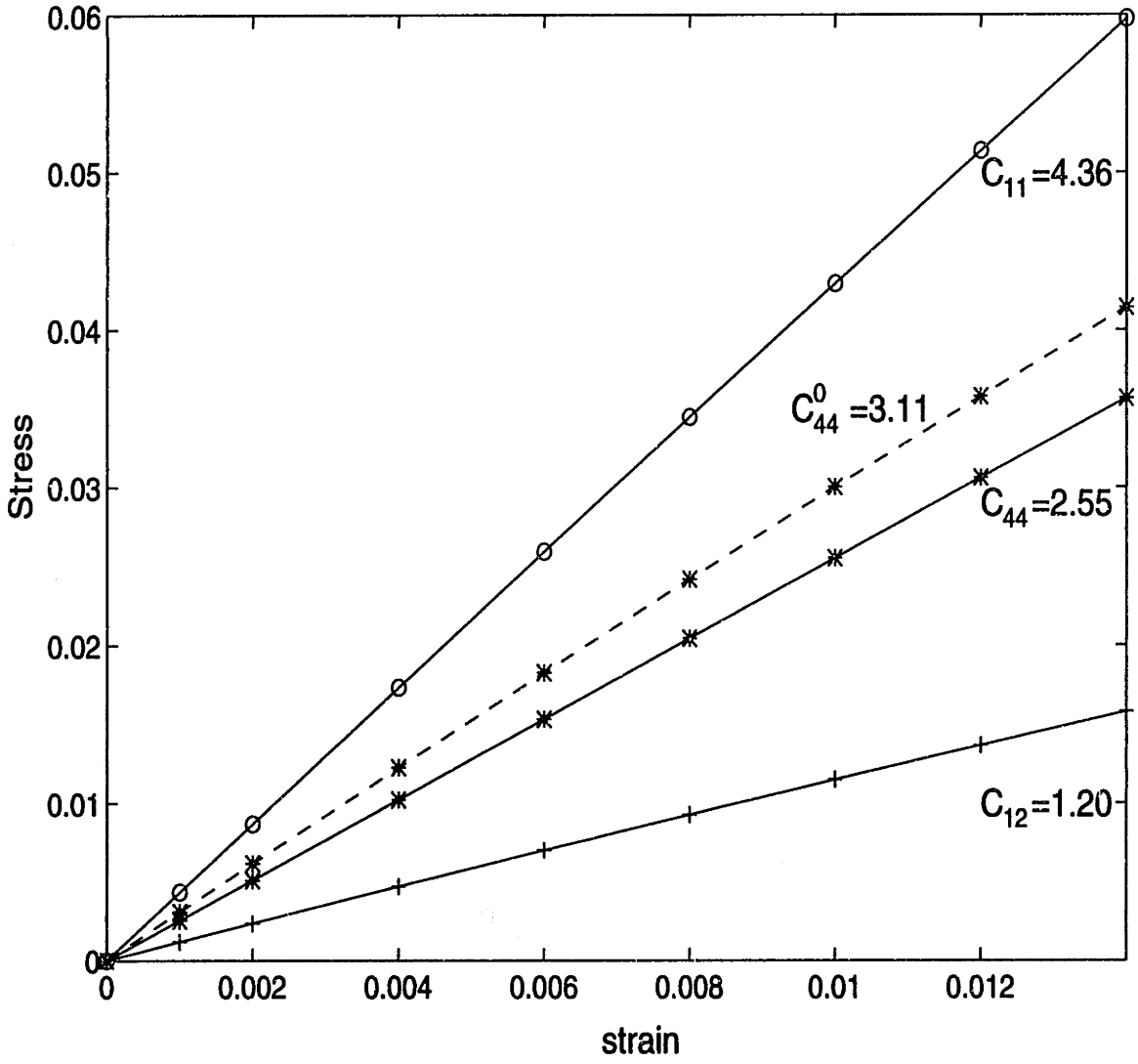

Figure 2-7: Stress-strain curves for elastic constants calculations. Circles are data for C_{11}; crosses are for C_{12}; stars are for C_{44} and C^0_{44}. C^0_{44} is calculated without internal strain relaxation.

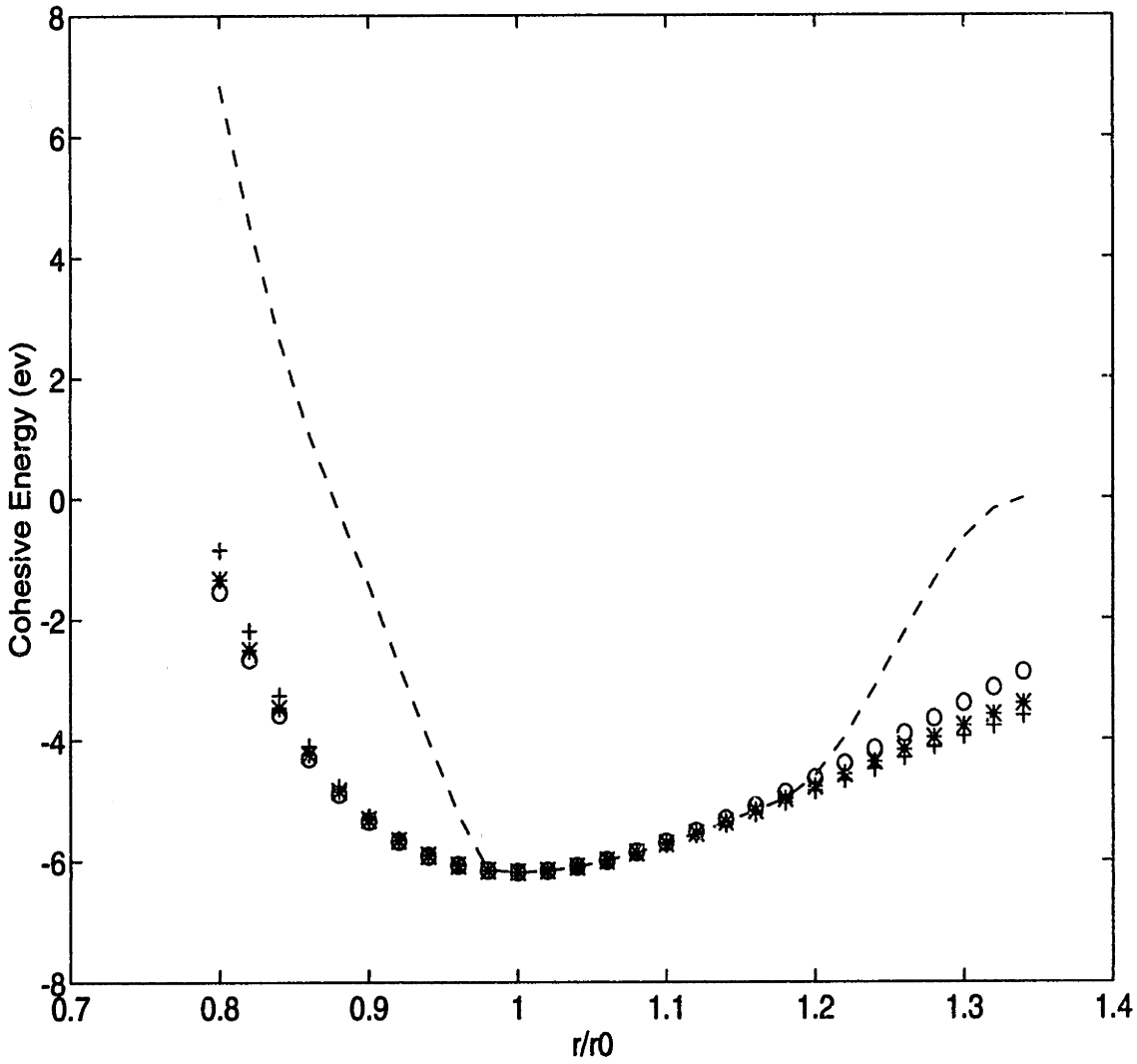

Figure 2-8: Comparison of cohesive Energy (eV/atom) of β-SiC under deformation at $0K$. Cross: from universal binding curves; circle: from ab initio calculation; dashed line: from the original Tersoff potential; star: from the modified Tersoff potential.

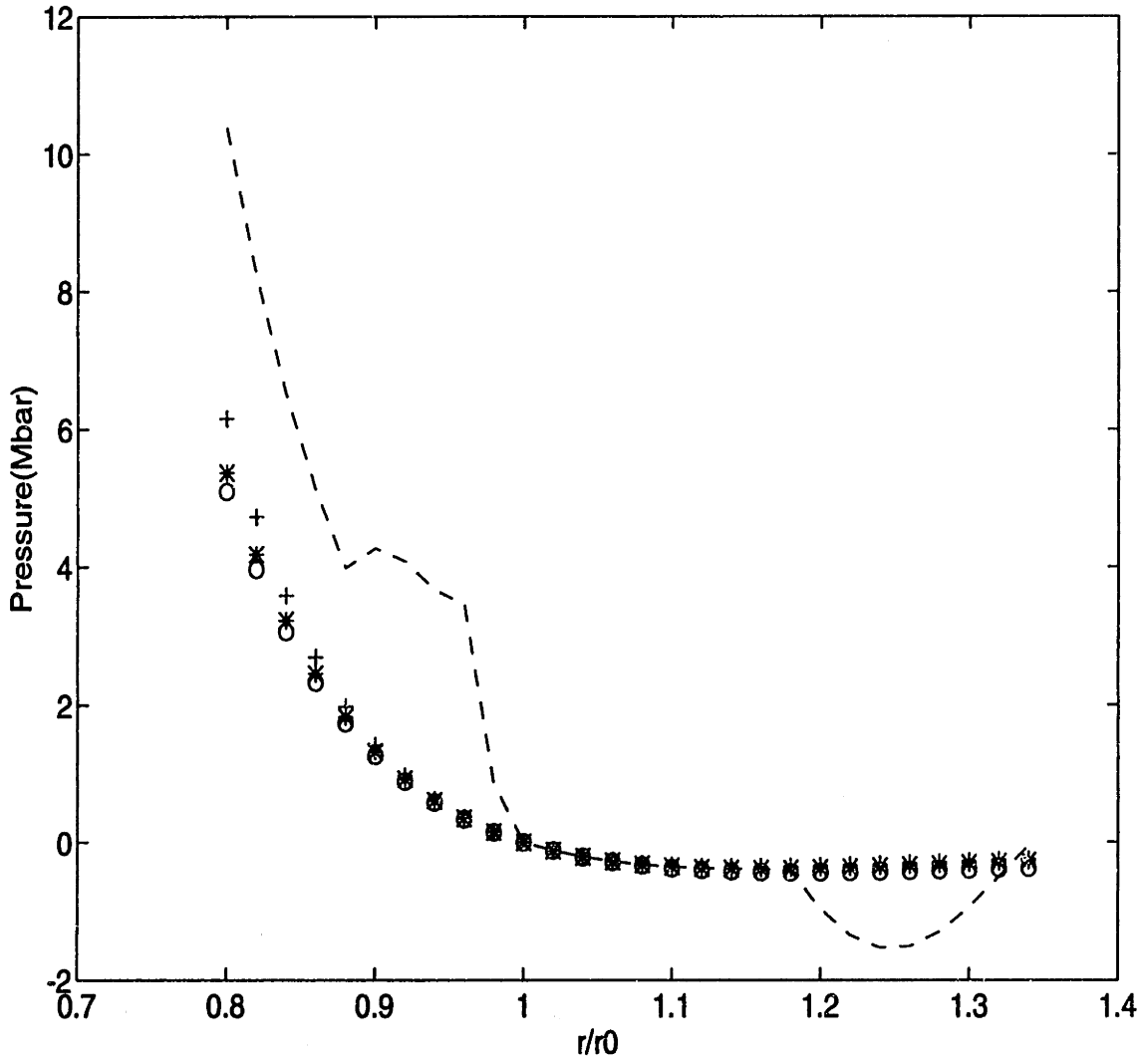

Figure 2-9: Pressure (Mbar) of β-SiC under deformation at $0K$. Cross: universal binding curve; circle: ab initio calculation; dashed line: the original Tersoff potential; star: the modified Tersoff potential.

Chapter 3

Bulk and Surface Properties of β-SiC

3.1 Structural, Mechanical and Thermal Properties of Bulk β-SiC

In this section, we present results of our studies of a number of important physical properties of β-SiC, such as cohesive energy (phase stability), equation of state, thermal expansion coefficient, elastic constants and phonon dispersion curve. All of the calculations are done using the modified Tersoff potential. The goals of this study are twofold. The first goal is to validate the modified Tersoff potential by comparing the calculated properties at equilibrium with available experimental data, tight-binding and first principle calculations. The second goal is to prepare for our later studies of the structural response of β-SiC under applied stress at finite temperature. It is therefore crucial to first ensure that the modified Tersoff potential can properly describe the behavior of the lattice constant, equation of state and elastic constants of β-SiC under stress and at finite temperatures. Moreover, the melting and quenching of β-SiC will prepare the amorphous SiC structure needed for the crystalline/amorphous interface study described in Chapter 7. For these purposes, we will make as many comparisons as possible with experimental data, first principle and tight-binding calculations.

All of the bulk calculations are carried out with a system consisting of 216 atoms and with periodic boundary conditions. The 216 atoms is composed by 3 unit cells along each direction. For studies of bulk single crystals with no defects, a few hundred atoms is typical to predict good properties[27]. As will be confirmed through this thesis, the results obtained can be compared to experimental data with sufficient accuracy and no inconsistency is found with this system size. The fifth order predictor-corrector method is used for finite step difference integrations. The time step is $1.45 \times 10^{-4} ps$. Typically, every 50–100 steps correspond to one vibrational period of the crystal.

3.1.1 Prediction of High Pressure Phase of β-SiC Based on Energetics

One of the important challenges of materials modeling is the ability to correctly predict phase stability of the ground state and to investigate the stable phases under high stress. This challenge holds for both electronic structure calculations and calculations using empirical potentials. In this section, we study the energetics of several relevant structures of crystalline SiC under static compression. Besides the zincblende structure of β-SiC, we also consider the β-tin and rocksalt type structures of SiC because they are believed to be relevant structures of crystalline SiC under high pressure according to previous first principle calculations [59] [60]. Among these three structures, zincblende and rocksalt SiC are both formed by two sets of fcc lattices of Si and C by shifting relative to each other along a body-diagonal direction of a unit cell[61]. The shifting distances are $1/4$ and $1/2$ of the body-diagonal length for zincblende and rocksalt structures respectively. The β-tin SiC structure is formed by compressing the zincblende SiC along [001] direction[61]. Figure 3-1 shows the potential energy curves of the rocksalt and β-tin structures compared with β-SiC under deformation. For the β-tin structure, we have calculated the potential energy with different c/a ratios ranging from 0.52 to 1.4. A minimum energy is found at a volume ratio v/v_0 for each c/a ratio. The lowest minimum energy is found to be $-4.623ev$ with the

c/a ratio being 0.62. At $0K$, the free energy is given by $F = E + PV$, where E is the potential energy and P is the pressure corresponding to volume V. Based on thermodynamic arguments, phase transition will occur if the free energies of the two structures become equal, and the transition pressure P_t can be determined from the common tangent of the cohesive energy curves ($E(V)$) of the two structures. For β-tin, we find that its free energy is always higher than that of β-SiC in the entire region that we have studied. This means that no transition from zincblende to β-tin structure is expected under compression. On the other hand, for the rocksalt structure, we do find a transition at $P_t = 6.49Mbar$. Table 3.1 summarizes the transition parameters that have been obtained by several independent studies, including the present calculation and two of the first principle calculations. In the latter, different final states have been predicted. Aourag et al.[59] have predicted that the phase transition should be from zincblende to β-tin SiC, while Chang et al.[60] have predicted the transition from zincblende to rocksalt SiC with a transition pressure of $0.66Mbar$. Our study predicts a transition from zincblende to rocksalt with a transition pressure of $6.49Mbar$.

Conventional electronic structure and total energy calculations can correctly predict both the ground state and low energy state of a system under stress under most circumstances[62]. In the case for β-SiC, the discrepancy between the results of Aourag et al. and Chang et al. is not understood. Moreover, even if the first principle total energy calculations could predict a correct stable phase, they are still limited in that they can provide energetics results but cannot actually observe the phase transition or provide information about the driving force of the transition. Although the Car-Parrinello method[63], based on first principle calculations, is now capable of performing MD simulation, simulating structural phase transitions is still practically restricted to calculations using empirical potentials. Also, energetics only studies a structural transition from the thermodynamics point of view, i.e., it is based on free energy calculations. Thus, the studies of energetics presented in this section are far from complete in probing high pressure phase transition of β-SiC. This is one of the reasons that we will devote considerable efforts in this thesis to study the structural

response of β-SiC under stress.

3.1.2 Phonon Dispersion Curves

The study in this section is to calculate the phonon dispersion curves of β-SiC using the modified Tersoff potential. We are interested in the vibrational properties of β-SiC at zero pressure as well as under high pressure. Analytical expressions for force constants have been worked out which involve the second derivatives of the potential function and symmetry arguments to simplify the force constants calculations. Using the calculated force constants, we follow the method of Smith[64] to obtain the phonon dispersion curves as shown in Figure 3-2 together with some experimental data [65]. We find that the acoustic modes qualitatively agree with experimental results, but with actual values overestimated. The optical modes, however, show obvious discrepancy. At the high symmetry Γ point, experimental results show a split transverse and longitudinal optical modes; while our calculations show that they are degenerate. The splitting of the optical modes is caused by the electric field induced by charge effect in SiC[66]. Since the charge effect is not taken into account by the Tersoff potential, the inability to describe the splitting is a drawback of the Tersoff potential.

In order to relate the the phonon behavior to the elastic stability (to be discussed in Chapter4 in detail), we have studied the behavior of the phonon dispersion curves under compression. It is known that the frequencies of all normal modes must be real in order for a lattice to be stable against small deformations. Once the frequencies of normal modes become imaginary, the lattice becomes unstable[13]. We have calculated the phonon dispersion curves under various pressures at $0K$. It is found that the optical modes and the longitudinal acoustic mode become harder under compression, while the transverse acoustic modes become softer. As the system is compressed to $r/r_0 = 0.76$, the transverse acoustic mode starts to approach zero along the $[\iota\iota 0]$ direction from the zone boundary where the wave vectors k are close to the Γ point. This result is shown in Figure 3-3(a). As the system is compressed further, we find that the transverse acoustic modes go to zero over a larger k region. Finally, as

$r/r_0 = 0.734$ is reached, the whole branch of the transverse acoustic modes become zero, as shown in Figure 3-3(b). As we will show later in Chapter 4, $r/r_0 = 0.734$ is exactly the point where instability is predicted to occur under compression by the elastic stability criteria. This suggests that the elastic instability is due to the softening of the transverse acoustic modes. This softening behavior of transverse acoustic modes in SiC under compression has been observed in experiment[67].

3.1.3 Equation of State

The equation of state of β-SiC has been studied at room temperature under both tension and compression. For clarity, we will leave the discussion of the equation of state in the tension region to Chapter 5. In this section, we focus on the equation of state under compression and compare the result with experimental data. The result of the pressure-volume (P-V) curve under compression calculated at room temperature is shown in Figure 3-4. The symbols are data from the modified Tersoff potential and experimental measurements [68] [69]. It is found that the results obtained from the modified Tersoff potential agree well with experimental data in the entire region being studied. The lines in the figure are fitted from the data using either the Birch-Murnaghan equation of state[70]

$$P = \tfrac{3}{2}k_0[(r_0/r)^7 - (r_0/r)^5][1 - \tfrac{3}{4}(4 - k_0')\{(r_0/r)^2 - 1\}] \tag{3.1}$$

or the simpler Murnaghan equation of state [11]

$$P = k_0/k_0'[(r_0/r)^{3k_0'} - 1.0] \tag{3.2}$$

In both cases, r is the current lattice parameter, $r_0 = 4.326\mathring{A}$ is the lattice constant at zero pressure, k_0 is the isothermal compressibility at zero pressure, and $k_0' = (\partial k/\partial P)_0$ is the first coefficient in the pressure expansion of the compressibility. Note k_0 and k_0' are parameters that can be obtained from the fitting. Generally, the Murnaghan equation of state is valid only in the low pressure region, and the Birch-Murnaghan

equation of state provides a better description for both low and high pressure regions. We have fitted our simulation data to the Birch-Murnaghan equation of state and obtain a very good agreement. This means that the modified Tersoff potential is able to describe realistically the behavior of volumetric deformation of β-SiC under compression. In Table 3.2, k_0 and k_0' obtained from the fitting of simulation data are compared with those obtained from fitting of the two sets of experimental data. As we can see, k_0 is in good agreement with the two experimental data, while k_0' is in good agreement with the value used by Strossner [69] and is slightly larger than that obtained by Yoshida [68].

To summarize, the equation of state calculated from the modified Tersoff potential agrees very well with experimental results. This suggests that the homogeneous response of β-SiC to hydrostatic compression can be well predicted by the modified Tersoff potential.

3.1.4 Thermal Expansion

So far, we have focused on studying β-SiC at low temperatures, i.e., at $0K$ and $300K$. We now present the result of lattice constant of β-SiC as a function of temperature at zero pressure. Parrinello-Rahman MD simulation is performed at each temperature to determine the zero pressure lattice constant. The results are summarized in Figure 3-5. Experimental data[71] are also shown for comparison. We find that the difference between our simulation data and experimental data is less than 1%. Data from both simulation and experiment are fitted to polynomial functions of T. The fit from experimental data yields [71]

$$a(nm) = 0.43577 + 1.3887 \times 10^{-6}T + 7.8494 \times 10^{-10}T^2 - 2.4434 \times 10^{-13}T^3 \quad (3.3)$$

And the fit from simulation data is

$$a(nm) = 0.43253 + 2.4719 \times 10^{-6}T + 1.5980 \times 10^{-10}T^2 + 1.0706 \times 10^{-14}T^3 \quad (3.4)$$

By definition, the linear thermal expansion coefficient is $\alpha = 1/a(\partial a/\partial T)$. From Eq.(3.3) and Eq.(3.4), we find that the thermal expansion coefficients determined by simulation is $\alpha = 2.5 \times 10^{-6}/^{\circ}K$; and that determined by experiment is $\alpha = 1.4 \times 10^{-6}/^{\circ}K$. Therefore, the modified Tersoff potential produces sufficiently good results of the lattice constant as a function of temperature.

3.1.5 Thermal Softening of Elastic Constants

The behavior of elastic constants as a function of temperature will be described in this section. The study in this section is important since it concerns the essence of mechanical deformation of a crystal, which is the elastic constants behavior under stress and at finite temperatures. While bulk modulus and equation of state describe the volumetric response of a crystal lattice to hydrostatic loadings, the general response of the crystal lattice to arbitrary loadings is described by the elastic constants. It is possible that two different systems can have the same bulk modulus and equation of state but very different behavior of elastic constants, and thus the ultimate response of the two systems to stress can be drastically different. A detailed example will be given in Chapter 6 to demonstrate this point. Since no experimental data of elastic constants under stress is available, we here focus on the elastic constants behavior at finite temperatures.

Using the fluctuation formulae derived for the modified Tersoff potential in Chapter 2, we have performed MD simulations to calculate elastic constants at finite temperatures. Typically, we use $50,000$ (about $7ps$) steps to calculate the Born terms, and $150,000 - 200,000$ (about $22ps$ to $30ps$) steps to calculate the stress-fluctuation terms. The calculated results of elastic constants and experimental data[72] are shown in Figure 3-6. The experimental data at $300K$ [73] are shown as crosses. (Note that the experimental data of single crystal β-SiC at $300K$ has been controversial as discussed by Lambrecht et al.[73]. We have found that values given by Lambrecht et al. are most reasonable.) There is no experimental data on the temperature dependence of elastic constants of single crystal β-SiC at higher temperatures. In literature, only an estimation was made by combining room temperature data of single crystals and

the temperature dependence of the elastic moduli of polycrystals[72]. As shown in the figure, significant improvement of the elastic constants at elevated temperatures is achieved by the modified Tersoff potential compared to the original Tersoff potential (data shown in Figure 2-5(d)). For the temperature range being studied, all elastic constants show the expected thermal softening behavior[74] and they can be well fitted to linear functions of temperature. This is the universal behavior of thermal softening of elastic constants, which has also been observed in simulation of metals [17]. The slopes of the elastic constants vs. temperature curves are summarized in Table 3.3. All data obtained from our simulation are of the same order of magnitude as experimental results.

In Figure 3-7, we show contributions to the total elastic constants from individual terms, i.e., the Born and the stress fluctuation term. Clearly, the stress fluctuation term in C_{44} is a much more dominant factor than in C_{11} and C_{12}. This proves that the internal strain relaxation has indeed been properly treated by the stress fluctuation term through MD simulations. Thus, we have learned in this section that the modified Tersoff potential predicts the correct behavior of elastic constants of β-SiC at finite temperatures, which suggests that the modified Tersoff potential is able to describe the general mechanical response of β-SiC correctly.

3.1.6 Mechanical Melting and Amorphous SiC

Melting of a crystal is a fundamental process during which the solid changes to a liquid at a critical temperature T_m. This process can be classified into categories according to the underlying mechanisms [75]. The first is called thermodynamic melting, and the second is called mechanical melting. Thermodynamic melting is evidenced by the heterogeneous nucleation and growth of the liquid phase at extended lattice defects, such as point defect and free surfaces. Mechanical melting is now known as governed by the elastic stability criteria [15]. In MD simulations, melting of a pure single crystal with periodic boundary conditions is a mechanical melting process.

We have studied the mechanical melting of β-SiC using MD simulations. We vary the system temperature incrementally by rescaling the velocities of atoms. At each

temperature, we allow the system to fully relax until it reaches an equilibrium state. When the temperature reaches a critical value, we find that the system melts into a liquid. The melting temperature of β-SiC is fitted to be around $5000°K$ using the modified Tersoff potential (see Chapter 2). After obtaining a fully melted equilibrium liquid at $8000°K$, we quench down the system to room temperature and obtain an amorphous SiC. The simulations of melting and quenching are both done at approximately zero pressure. The data of energy and volume as a function of temperature during the melting-quenching process is shown in Figure 3-8. As we can see in this figure, during the melting transition, both energy and volume jump, which indicates that the mechanical melting is a first order phase transition.

In order to examine the structure of the amorphous SiC obtained by the melting and quenching process in our simulation, we take the amorphous SiC structure obtained by Finocchi et al.[57] for comparison. Finocchi et al. have performed state-of-the-art Car-Parrinello MD simulations to obtain an amorphous structure of SiC by quenching. We plot the radial distribution functions (g(r)) of Si-Si, Si-C and C-C in Figure 3-9. The radial distribution function $g(r)$ is defined as [27]

$$\rho g(r) = \frac{1}{N} < \sum_{i}^{N} \sum_{j \neq i}^{N} \delta[r - r_{ij}] > \tag{3.5}$$

where $\rho = N/V$ is the number density, r_{ij} is the distance between atoms; and the angular brackets represent a time average. It measures how atoms organize themselves around one another. Specifically, it is proportional to the probability of finding two atoms separated by distance $r \pm \Delta r$. Figure 3-9(a) are the results of our simulation and (b) are the results of Finocchi et al. In Table 3.4, we also summarize dominant peak (the first peak) positions and coordination numbers of atoms obtained by both simulations.

As we can see from Table 3.4, the first peak positions obtained by two simulations are in good agreement. These positions are similar to the equilibrium distances that are determined by the interactions between Si-Si, C-Si and C-C. Under the condition of zero pressure and zero temperature, the equilibrium distances are $2.35\mathring{A}$, $1.87\mathring{A}$

and 1.54$\AA$ between Si-Si, C-Si and C-C respectively. The coordination number of C-Si (meaning the number of neighboring Si(or C) atoms of each C(or Si)) from the two simulations is exactly the same. However, the coordination number of C-C from our simulation is much smaller. No coordination number has been given by Finocchi et al.

Comparing the overall shapes of g(r)'s in Figure 3-9, we find that a significant gap exists in the g(r) of Si-Si between the first peak and the second peak in (a). Also, we observe an additional small but sharp peak in each of the three g(r)'s in (a). Each of the three small peaks are located after the first peak and before other peaks in the respective g(r)'s. The positions of these peaks are found to be at 2.93$\AA$, 2.24$\AA$ and 2.69$\AA$ for Si-Si, C-Si and C-C respectively. We find that these positions are exactly equal to the upper bound cutoff distances (see Chapter 2 for details about cutoff) between Si-Si, C-Si and C-C. Hence, these three peaks are not determined by the intrinsic interactions between atoms, but are introduced by the cutoff and should be considered as artifacts. Among the three artificial peaks, the peak in the g(r) of Si-Si is the most pronounced. This is the reason that a gap exists in the g(r) of Si-Si. That is, instead of moving closer to each other, some Si atoms are stopped and accumulated at the artificial peak position. Similarly, some C atoms are also stopped at the artificial peak position instead of moving closer to each other. This is the cause of the lower coordination number of C-C. Note that although an artificial peak also exists in the g(r) of C-Si, we still obtain the correct coordination number of C-Si comparing to Finocchi's result. The explanation is that the first peak in the g(r) of C-Si already exists in the crystal lattice before melting; whereas the first peaks in the g(r) of C-C and Si-Si in amorphous SiC are not present in the crystal lattice. As the crystal lattice collapses during melting, atoms can move far away from their crystalline sites. This large motion allows Si and C atoms to move close enough to interact with the same type of atoms and stabilize at the equilibrium distance determined by the interactions. Thus, the first peaks in the g(r) of Si-Si and C-C are formed due to the same type of atoms moving close to each other crossing the artificial peak positions from far away. However, the artificial peaks have stopped

certain atoms (roughly about 30% as estimated from the coordination number of C-C) from coming closer and contributing to the first peaks. On the other hand, for C-Si, since atoms are at the first peak already before melting, the artificial peak in the g(r) of C-Si will not affect the first peak significantly.

Besides comparing our results with that of Finocchi, we have also compared the calculated mass density of amorphous SiC with the experimental data. The calculated density of the amorphous structure we have obtained is $2.88 g/cm^3$; while the experimental result is $2.55 g/cm^3$ [76], a difference of 13%.

In summary, for the structure of amorphous SiC, we have obtained reasonable first peak positions in g(r)'s and correct coordination number of C-Si. The mass density of amorphous SiC calculated by us is in close agreement with experimental data. The amorphous structure obtained in this section will be used to construct a crystalline/amorphous interface in Chapter 7.

3.2 Surface Energies of β-SiC

Part of our efforts to investigate the transferrability of the Tersoff potential is to study the surfaces of β-SiC. We have calculated surface energies and studied structural surface relaxation at low temperatures for (100), (110) and (111) surfaces. Surface reconstruction study is done for (100) surface only owing to its simplicity and the availability of experimental and tight-binding results for comparison. For (100) and (111) surfaces, both the C-terminated and Si-terminated surfaces are investigated in the surface relaxation studies.

To set up the initial geometry for surface studies, the minimum repeatable stacking layers of a unit cell along each index direction is used as a *layer unit.* Along (100) and (110) directions, layers are uniformly spaced; along (111) direction, layers are alternatively spaced at two distances. Given that the bond length between Si-C is l, the interlayer spacing along the (100) direction is $l/\sqrt{3}$; the interlayer spacing along the (110) direction is $(\sqrt{2}/\sqrt{3})l$. Along (111), the longer interlayer spacing is l and the shorter spacing is $l/3$. The plane that cuts through the shorter spacing is called

a *glide plane*; and the plane that cuts through the longer spacing is called a *shuffle plane*. The number of layers in each *layer unit* is 4, 2 and 6 for the (100), (110) and (111) surfaces respectively. A schematic view of the structure of each *layer unit* is shown in Figure 3-10. We use 2, 2 and 3 *layer units* for the studies of (100), (111) and (110) surface respectively. Within each layer, approximately 10-20 atoms are used. Periodic boundary conditions are applied only along the two directions (y and z) that are parallel to the surfaces. Along the direction (x) perpendicular to the surface, atoms in the bottom *layer unit* is fixed to represent a bulk material attached to a free surface generated at the top. These structures are thick enough since all the surface relaxation and reconstruction only involve atoms at the top two layers, as will be confirmed by the results. MD simulations at $T = 10°K$ are performed to study surface relaxation and reconstruction.

The definition of surface energy is [77]

$$\gamma_e = \frac{(E_s - E_b)}{A} \tag{3.6}$$

where E_s and E_b denote potential energy per atom in the bulk and at the surface respectively; A is the exposed surface area *per* atom. For the (110) surface, since both Si and C atoms appear at the surface layer, γ_e takes the average value of the surface energy of the two types of atoms. Physically, surface energy is the energy increase due to dangling bonds. *Unrelaxed surface energy* is the surface energy calculated from an ideally truncated surface without any relaxation of atomic positions. Calculating the unrelaxed surface energy differs significantly for pair potentials and the Tersoff potential. For a pair potential, the surface energy is completely determined by the dangling bonds. The remaining bonds will not be affected by the dangling bonds if no relaxation occurs. But, for the Tersoff potential, as atoms lose bonds at the surface, the remaining bonds are automatically re-strengthened. This is because that the strength of each bond is determined by the local atomic arrangement in the many-body function. Thus, the bond-order parameter b_{ij} changes because of the change of local coordination number. Details of the bond-order parameter has been discussed

tical layer displacement and energy gain are consistent with that of tight-binding calculations both qualitatively and quantitatively.

Relaxation of the (110) surface is more complicated than that of (100) and (111) surfaces because it involves atomic displacements in the lateral directions. Atoms at the surface are initially chained together. During atomic relaxation, C and Si atoms can move in and out of the bulk in different ways. Hence, atomic buckling of the chain structure on the (110) surface is observed during surface relaxation. In Table 3.8, the results of relaxation and buckling of the (110) surface are summarized and are compared with the tight-binding calculation[79] and ab initio calculation [80]. The calculated energy gain from the Tersoff potential is in close agreement with that from the ab initio calculation. However, the Tersoff potential predicts inward relaxation of C atoms from the top layer to the bulk, and slight outward relaxation of Si atoms away from the bulk. This is not consistent with predictions made by tight-binding and ab initio calculations. Both these calculations predicted inward relaxation of C and Si atoms towards the bulk with the displacement of Si atoms being larger than that for C atoms. This discrepancy can again be attributed to the fact that the Tersoff potential has not taken into account electron transfer between Si and C atoms and the resulting charge effect[80] [79].

3.3.2 {100} Surface Reconstruction

The change in symmetry of the surface layer structure relative to the layer structure embedded in the bulk is called surface reconstruction. Surface reconstruction of β-SiC (100) surfaces has been studied by STM [81] and LEED [82] measurements. Several reconstruction patterns have been observed, such as 2×1 and 2×2 . We have studied the (100) surface reconstruction by MD simulations. In the simulation, we first intentionally move the atoms towards the expected reconstruction sites in order to overcome the energy barrier for reconstruction and make the simulation more efficient at low temperature. Then we allow atoms to relax to their equilibrium positions. If no reconstruction is favored, we find atoms move back to their initial equilibrium positions. Using this method, we have observed 2×1 and 2×2 dimers on both C-(100)

and Si-(100) surfaces for the Tersoff potential. For the Pearson potential, no 2×1 dimers are observed on the Si-(100) surface. In Table 3.9, we summarize the results from the Tersoff potential, the Pearson potential and the tight-binding calculation[79]. From the bond lengths and energy gain, we find that the 2×1 reconstruction is favored over the 2×2 reconstruction. Also, for the 2×1 reconstruction, we find the bond length of C-dimer ($1.48\mathring{A}$) is smaller than the bond length ($1.54\mathring{A}$) in bulk diamond C, and the bond length of Si-dimer ($2.46\mathring{A}$) is larger than the bond length ($2.35\mathring{A}$) in bulk diamond cubic Si. These results suggest that reconstruction on the C-(100) surface is energetically favored than that on the Si-(100) surface.

3.4 Conclusions and Discussions

From the results of bulk and surface properties of β-SiC presented in this chapter, we conclude that, in general, the modified Tersoff potential yields reasonable thermal and mechanical properties of β-SiC under deformation and at finite temperatures. In particular, the calculated equation of state and the elastic constants of β-SiC are in excellent agreement with experimental data. These give us confidence in using the modified Tersoff potential to study the structural response of β-SiC under stress in Chapter 5 and Chapter 6.

In this chapter, we have also identified some major pitfalls of the Tersoff potential. First, the Tersoff potential does not explicitly consider the charge effect. As a result, it cannot correctly describe the (110) surface relaxation and the splitting of the optical phonon modes. Secondly, the second nearest neighbor interactions between Si-Si and C-C have not been systematically studied in the original Tersoff potential. Although the modified Tersoff potential is an improvement in describing β-SiC, the cutoff introduces artifacts in the structure of amorphous SiC. This problem will be relevant to our study of structural transitions of β-SiC under compression and will be noted in Chapter 6.

Table 3.1: Comparisons of high-pressure phases of β-SiC and transition parameters predicted to different studies. The volume is normalized by the zero pressure volume (v_0) of zincblende SiC.

Pressure (Mbar)	v/v_0 (zincblende)	Structure	Reference
6.49	0.48	rocksalt	Present study
0.66 ± 0.05	0.81	rocksalt	Chang and Cohen
		β-tin	Aourag et al.

Table 3.2: Comparison of bulk modulus k_0 and its pressure derivative k_0'.

$k_0(GPa)$	k_0'	Reference
219 ± 1	4.11 ± 0.05	Present study
260 ± 9	2.9 ± 0.3	Yoshida
230 ± 4	4.0 (fixed)	Strossner

Table 3.3: Comparison of slopes of elastic constants variations with respect to temperature

	$dC_{11}/dT(GPa/C)$	$dC_{12}/dT(GPa/C)$	$dC_{44}/dT(GPa/C)$
Present work	-0.036	-0.0046	-0.038
Li and Bradt	-0.025	-0.011	-0.007

Table 3.4: Comparison of peak positions and coordination numbers of amorphous SiC obtained by the Tersoff potential and the Car-Parinello method.

	Tersoff Potential			Car-Parrinello		
	si-si	c-si	c-c	si-si	c-si	c-c
first peak position ($\AA$)	2.47	1.83	1.49	2.32	1.89	1.50
coordination #	2.6	2.1	1.22	/	2.1	1.8

Table 3.5: Comparison of bond-order parameter b_{ij} of C and Si atoms at various local bonding geometries including inside bulk β-SiC, at (111)-shuffle, (110) (same as (100)) and (111)-glide planes of β-SiC.

	bulk	(111) shuffle (or (110))	(100)	(111) glide
Coord.#	4	3	2	1
C	0.8663	0.8917	0.9234	0.9776
Si	0.9368	0.9475	0.9599	0.9776

Table 3.6: Unrelaxed surface energies at β-SiC obtained from the modified Tersoff potential

Planes	Energy (erg/cm^2)
shuffle (111)	2525
(110)	3093
(100)	4618
glide (111)	8219

Table 3.7: Summary of energy decrease and vertical layer displacements due to surface relaxation of β-SiC. dE is the energy decrease per surface atom; dH_n is the averaged atomic displacement from bulk positions in the nth-layer; dD_{mn} is the change in percentage of interlayer spacing between nth and mth layers compared to their bulk spacing. Negative (or positive) sign represents inward (or outward) movement to (or away from) the bulk.

	TP	PP	TB	Ab initio
C-(100) Relaxation				
dE $(ev/atom)$	0.49	0.25	0.34	
dH_1 $(\AA)$	−0.17	−0.15	−0.17	
dD_{12} (%)	−23.0	−14.0	−22.0	
dH_2 $(\AA)$	0.04	−0.01	0.07	
Si-(100) Relaxation				
dE (ev)	0.09	0.18	0.02	
dH_1 $(\AA)$	−0.04	−0.07	−0.04	
dD_{12} (%)	−6.2	−8.4	−4.6	
dH_2 $(\AA)$	0.03	−0.02	0.01	
C-(111) Relaxation				
dE (ev)	0.83	0.62	0.43	
dH_1 $(\AA)$	−0.27	−0.30	−0.21	
dD_{12} (%)	−51.2	−61.2	−52.4	
dH_2 $(\AA)$	0.05	0.08	0.12	
Si-(111) Relaxation				
dE (ev)	0.11	0.31	0.03	
dH_1 $(\AA)$	−0.04	−0.06	−0.05	
dD_{12} (%)	−11.8	−20.5	−11.1	
dH_2 $(\AA)$	0.03	0.06	0.02	
(110) Relaxation				
dE (ev)	0.29	0.41		0.21
dH_1 $(\AA)$	−0.17	−0.15	−0.17	
dD_{12} (%)	−23.0	−14.0	−22.0	
dH_2 $(\AA)$	0.04	−0.01	0.07	

Table 3.8: Relaxation and buckling of the (110) surface of β-SiC. C(1) (or Si(1)) stands for C (or Si) atoms on the top layer; C(2) (or Si(2)) stands for C (or Si) atoms on the second layer from the surface. dX is the vertical displacement of the top layer atoms, dY and dZ are the lateral displacements of the top layer atoms.

	TP		PP		TB		Ab initio	
dE ($ev/atom$)	0.29		0.41				0.21	
	C	Si	C	Si	C	Si	C	Si
dX ($\AA$)	−0.22	0.03	−0.27	−0.01	−0.12	−0.21	−0.05	−0.17
dY ($\AA$)	−0.00	0.00	0.00	0.00			0.00	0.00
dZ ($\AA$)	−0.18	0.01	0.21	0.02			0.02	−0.14
Bond Length ($\AA$) Between:								
C(1)-Si(1)	1.788		1.730		1.76			
C(1)-Si(2)	1.814		1.748		1.89			
Si(1)-C(2)	1.873		1.797		1.84			
Bond Angle: (degree)								
Si(1)-C(1)-Si(1)	117.3		117.6		122			
Si(1)-C(1)-Si(2)	116.9		118.2		106			
C(1)-Si(1)-C(2)	100.2		99.4		112			

Table 3.9: Surface reconstruction of the (100) surfaces of β-SiC.

	Energy Gain ($ev/atom$)		Bond Length ($\AA$)		Top Layer Lateral Displacement ($\AA$)	
	2 × 1	2 × 2	2 × 1	2 × 2	2 × 1	2 × 2
C-(100)						
TP(SiC)	2.42	2.29	1.48	1.49	±0.79	±0.78
PP(SiC)	2.97	2.90	1.49	1.49	±0.74	±0.73
TB(SiC)	2.31		1.74		±0.67	
Si-(100)						
TP(SiC)	0.67	0.63	2.46	2.54	±0.30	±0.26
PP(SiC)	No Dimer	0.41	No Dimer	2.49	No Dimer	±0.24
TB(SiC)	1.03		2.16		±0.45	

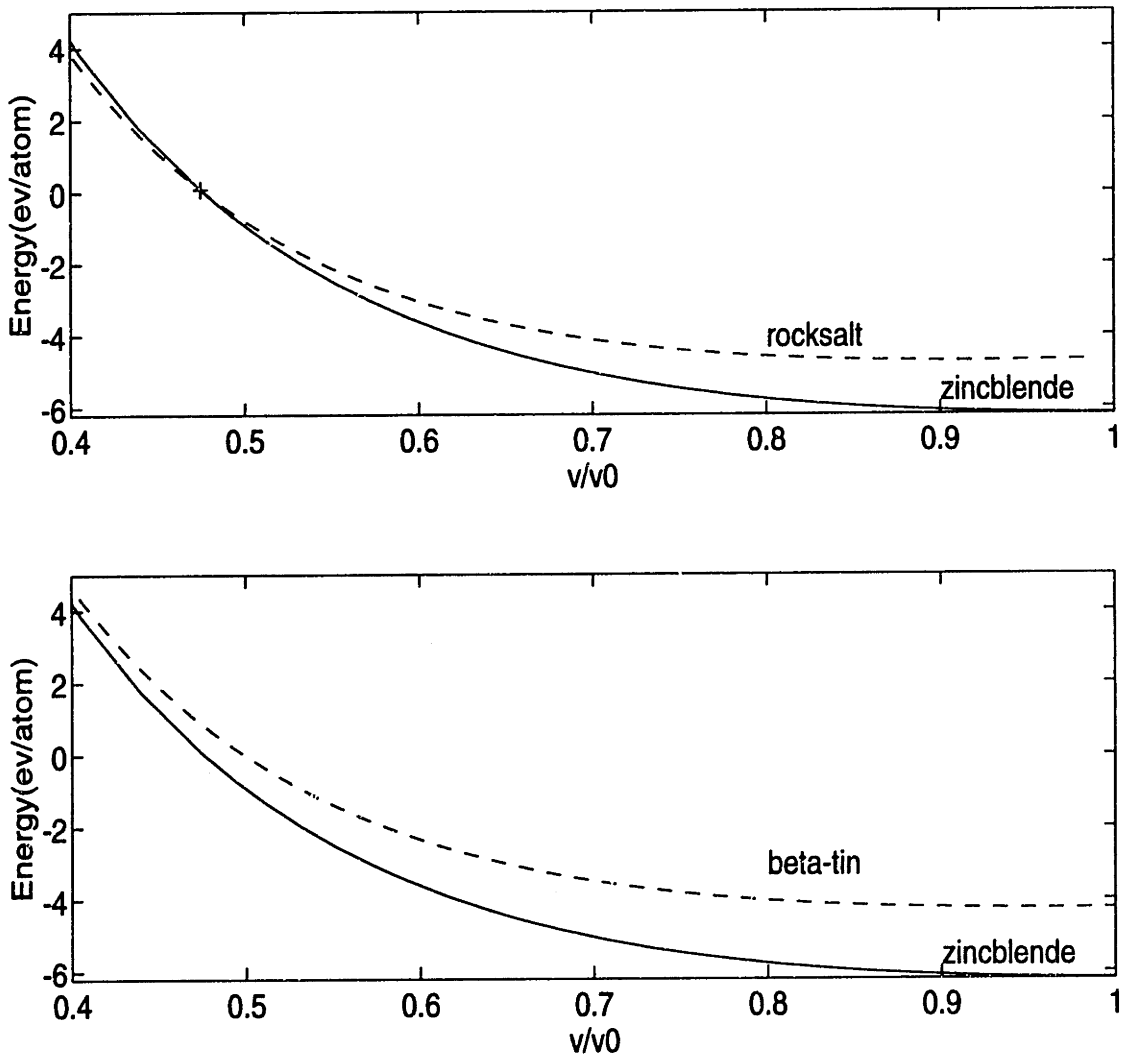

Figure 3-1: Energy per atom versus volume normalized by the volume of β-SiC under zero pressure and at $0K$. The c/a ratio for the β-tin curve is 0.62.

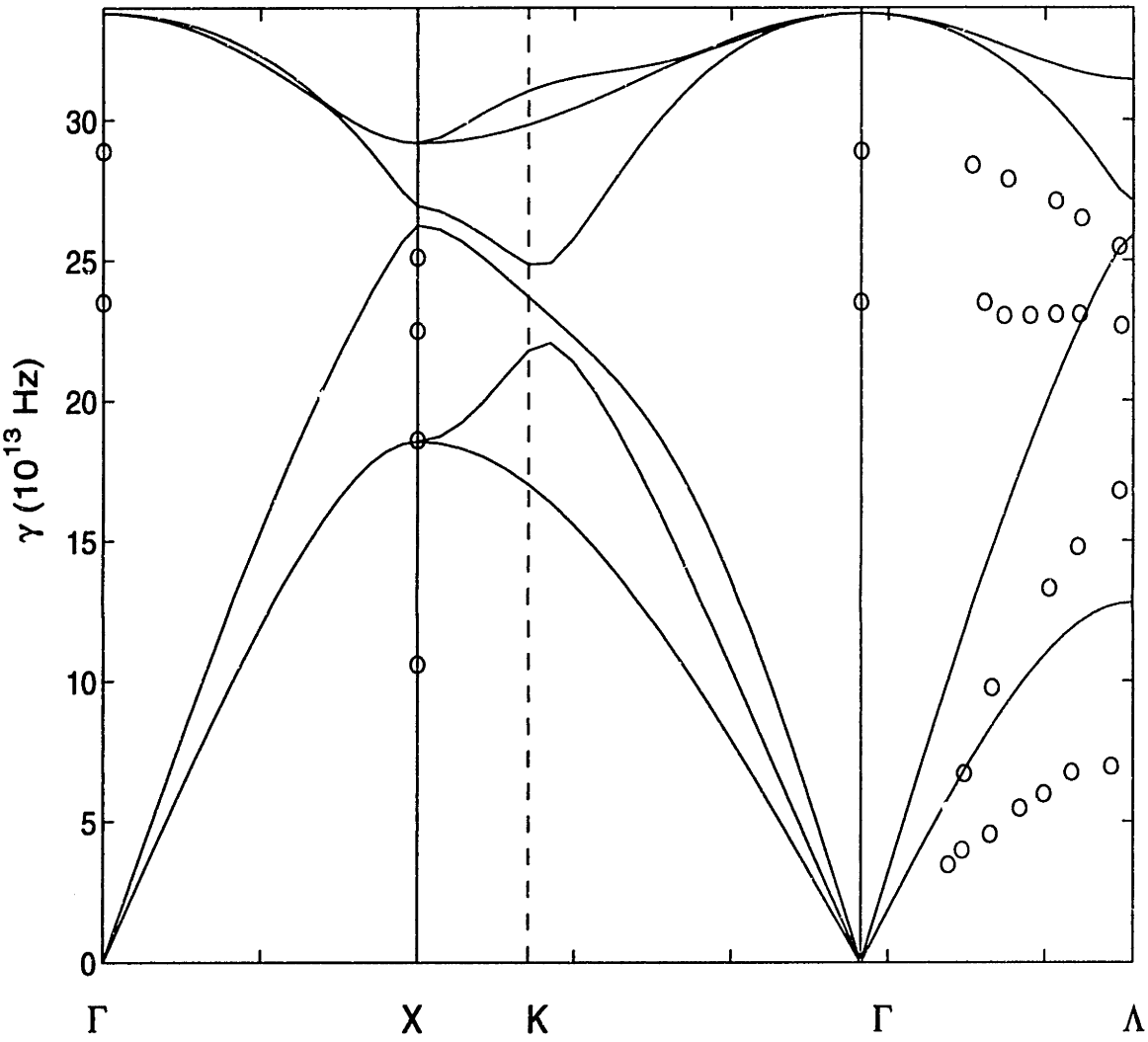

Figure 3-2: Phonon dispersion curves of β-SiC. Circles are experimental data.

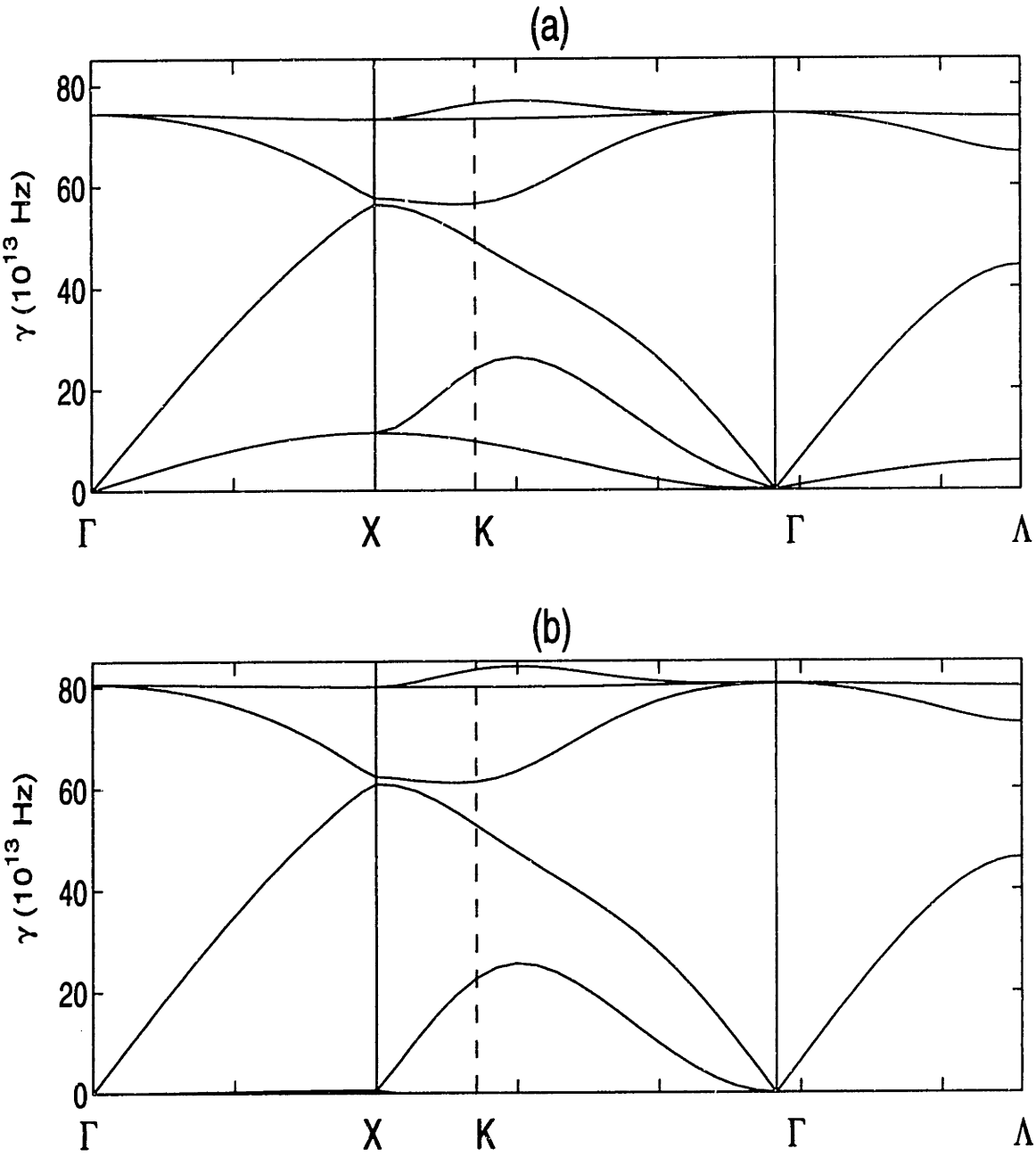

Figure 3-3: Phonon dispersion curves of β-SiC under compression at (a) $r/r_0 = 0.76$ and (b) $r/r_0 = 0.734$, where r_0 is the zero pressure lattice constant and r is the deformed lattice constant.

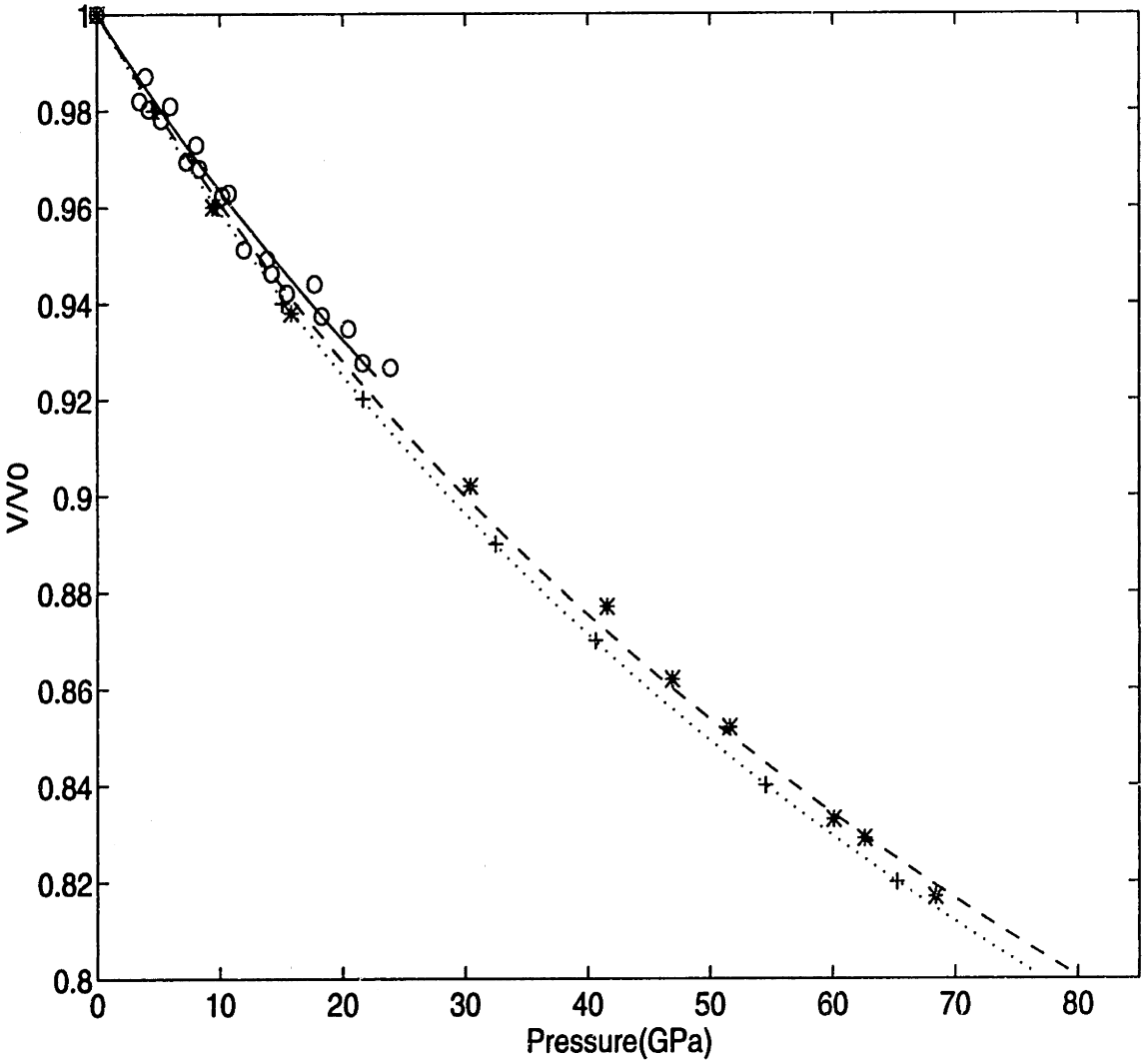

Figure 3-4: Pressure-volume curve for β-SiC under compression. Circles: experimental data of Yoshida; solid line: fitted from circles by the Murnaghan equation with $B_0 = 260 \pm 9(GPa), B_0' = 2.9 \pm 0.3$; star: experimental data of Bassett; dashed line: fitted from stars by the Birch-Murnaghan equation with $B_0 = 230.2 \pm 4.(GPa), B_0' = 4$; cross: Data from the modified Tersoff potential; dotted line: fitted from crosses by the Birch-Murnaghan equation with $B_0 = 218.5 \pm 1.0(GPa), B_0' = 4.11 \pm 0.05$.

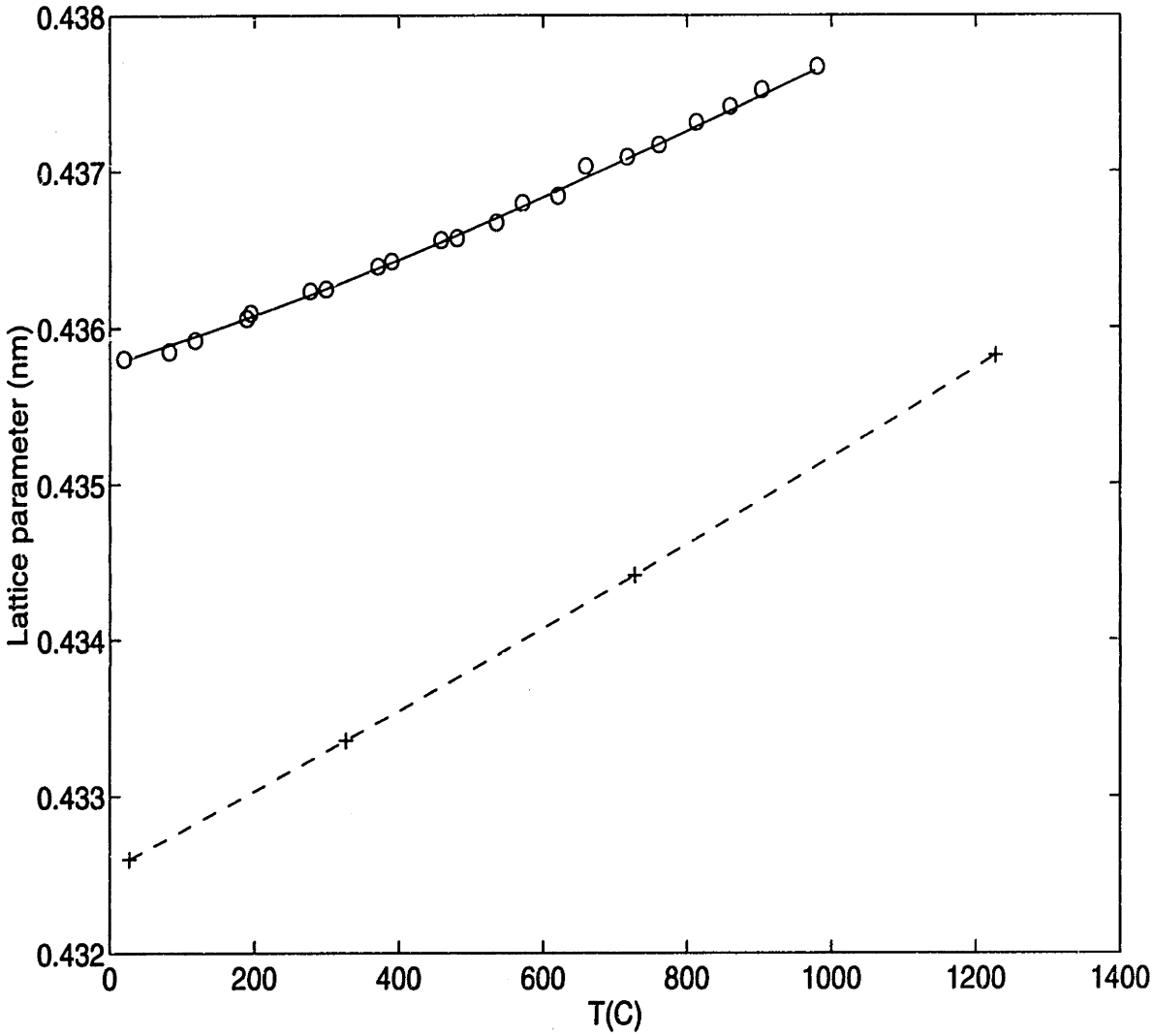

Figure 3-5: β-SiC lattice constant versus temperature. Circles: experimental data; solid line: fitted from circles; cross: simulation data; dashed line: fitted from crosses.

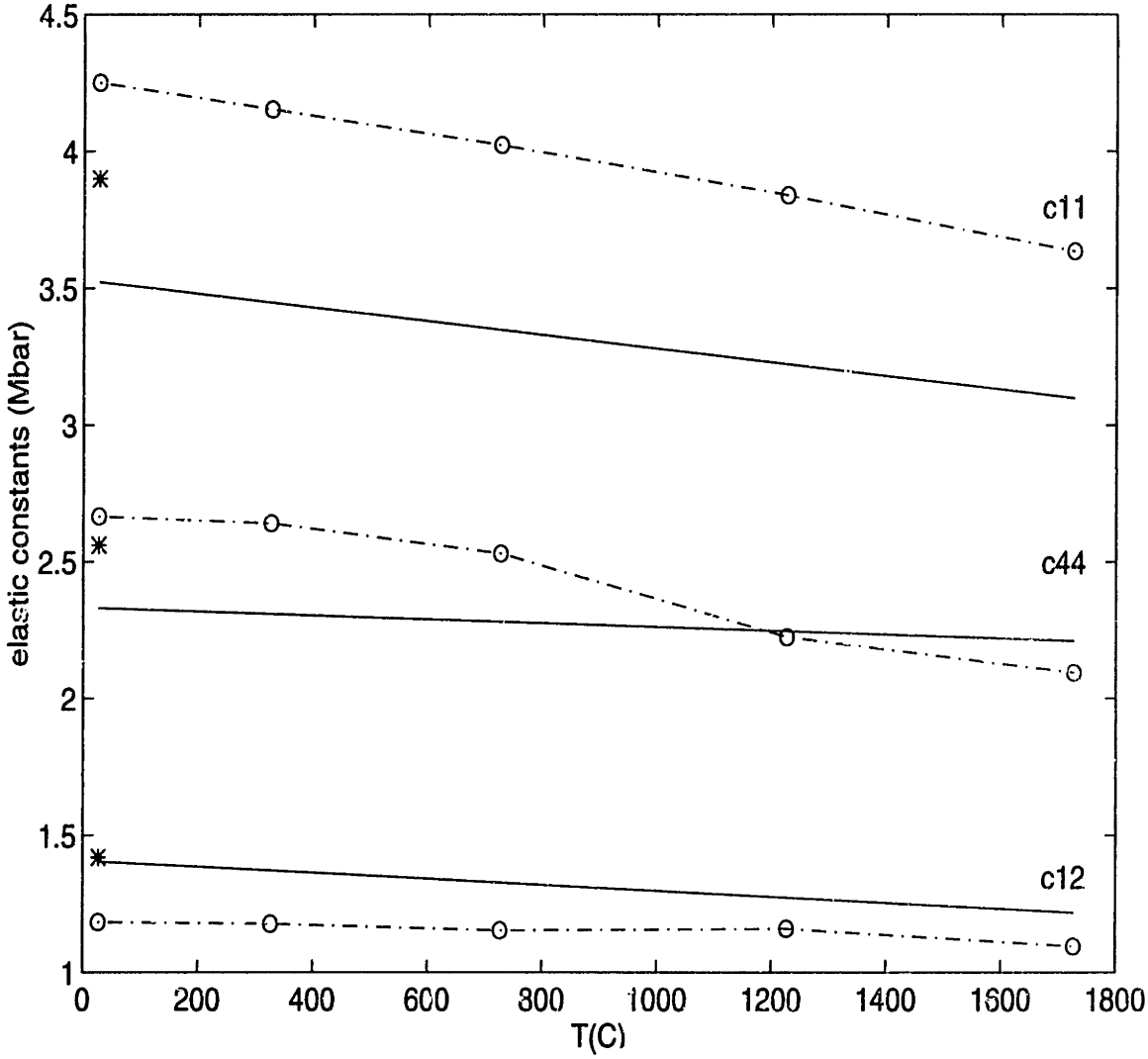

Figure 3-6: Temperature variation of elastic constants of β-SiC. Circles: data from the modified Tersoff potential; dashed line: fitted from the circles; solid line: results of Li and Bradt. Stars are experimental data of β-SiC at $300K$.

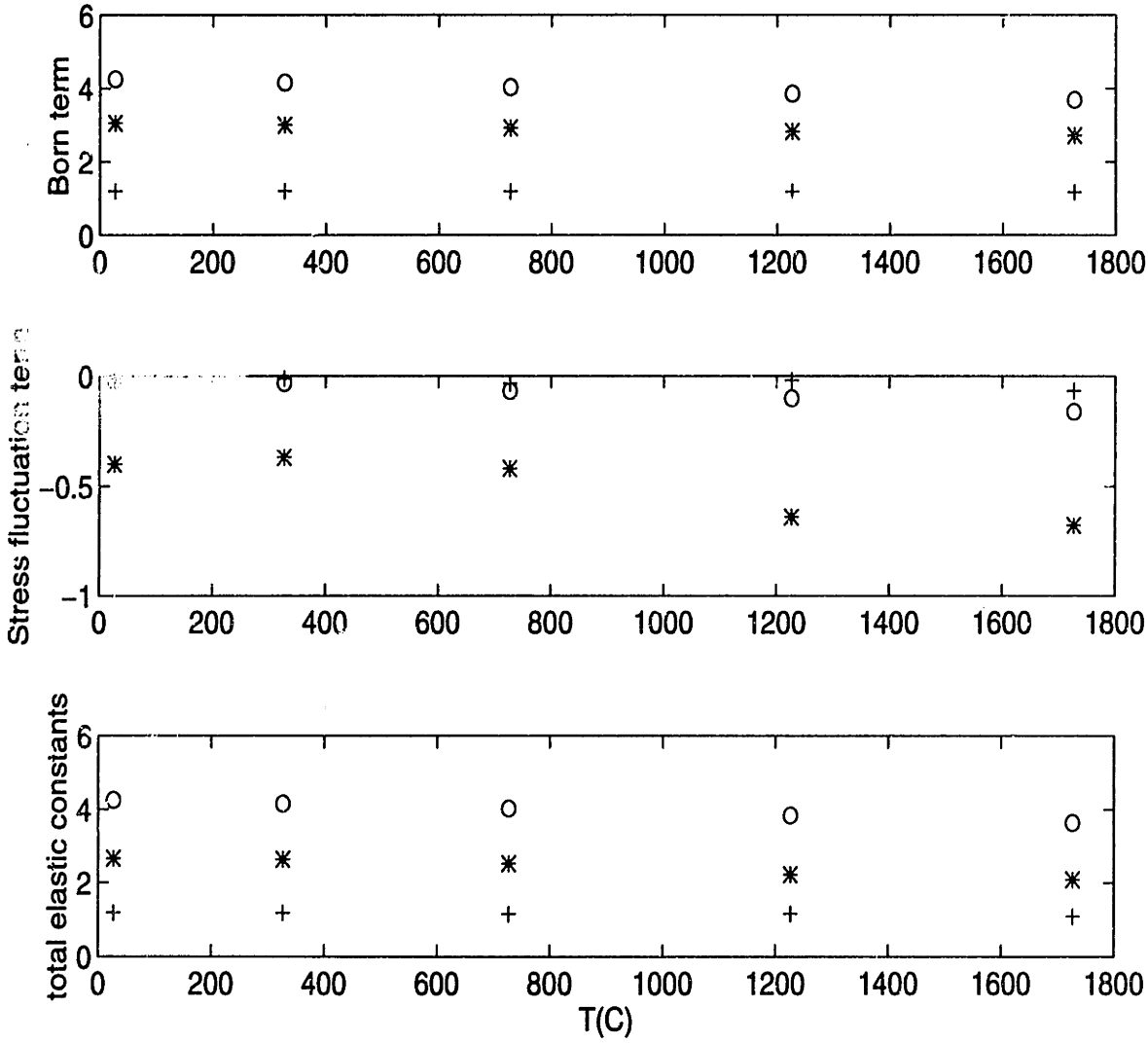

Figure 3-7: The Born term, stress fluctuation term and total elastic constants of β-SiC as a function of temperature. Circles: data for C_{11}; crosses: data for C_{12}; stars: data for C_{44}. Notice the larger values of stress fluctuation term of C_{44} compared to that of C_{11} and C_{12}.

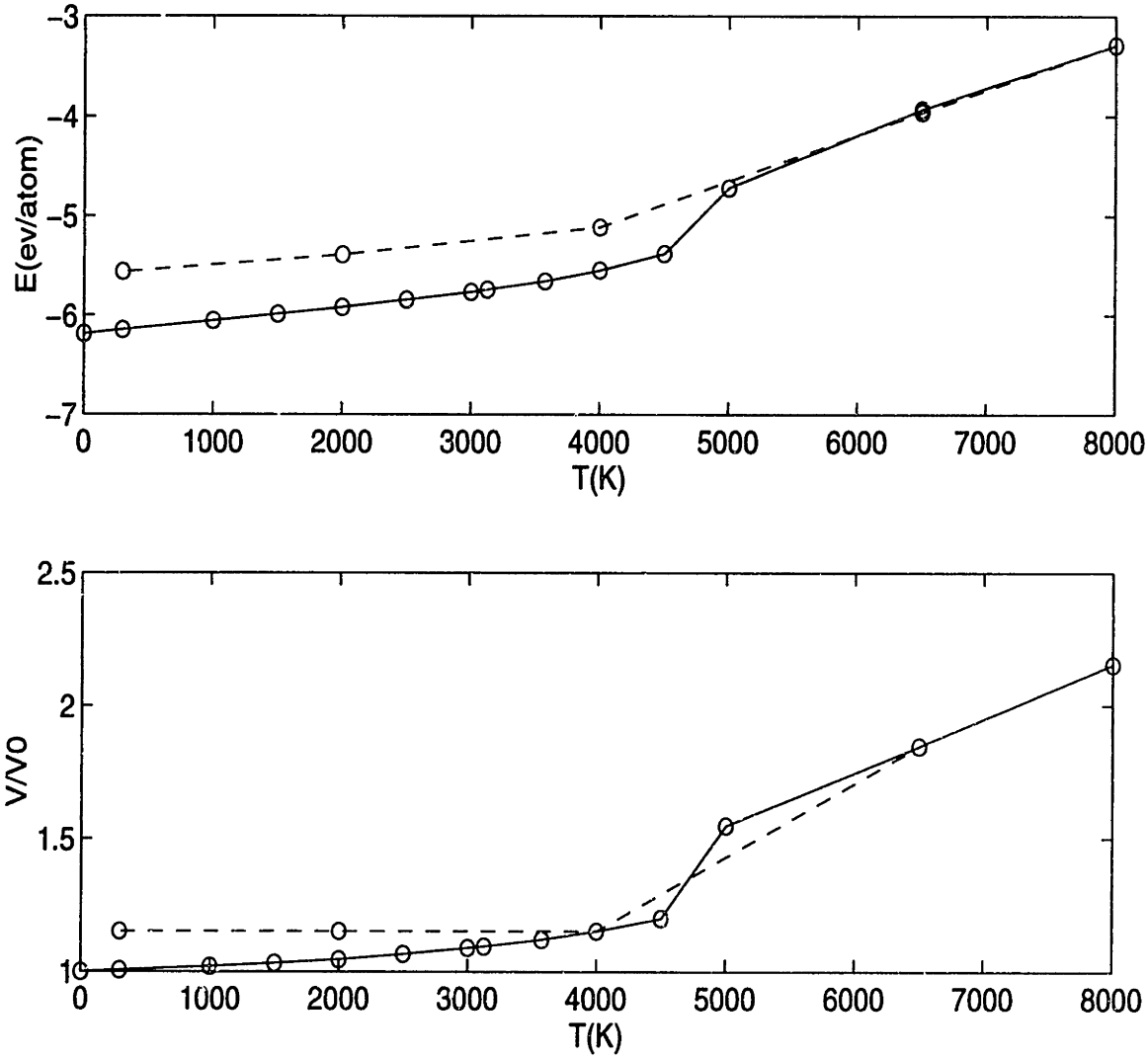

Figure 3-8: Energy and volume of β-SiC as a function of temperature during the melting-quenching process. Data are obtained at zero pressure.

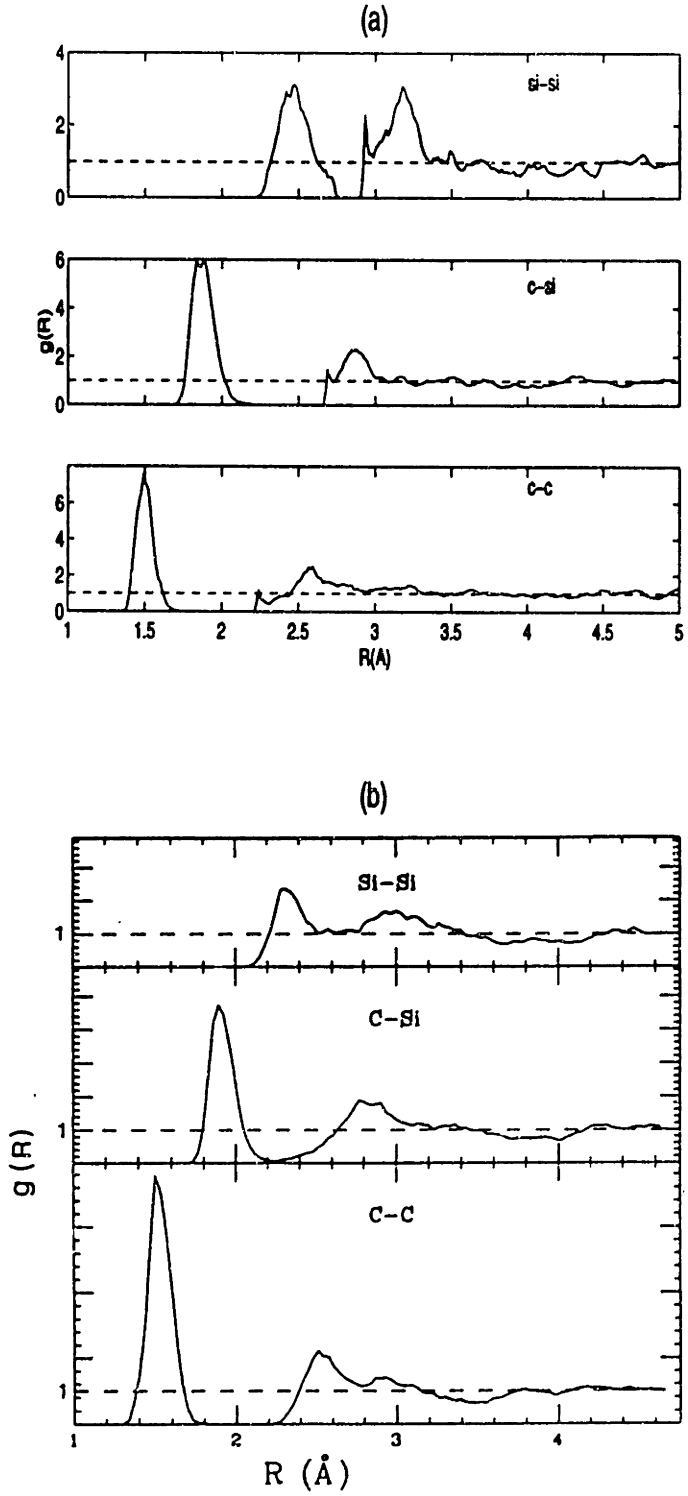

Figure 3-9: Radial distribution functions of amorphous SiC obtained from (a) the present work and (b) the work by Finocchi et al.

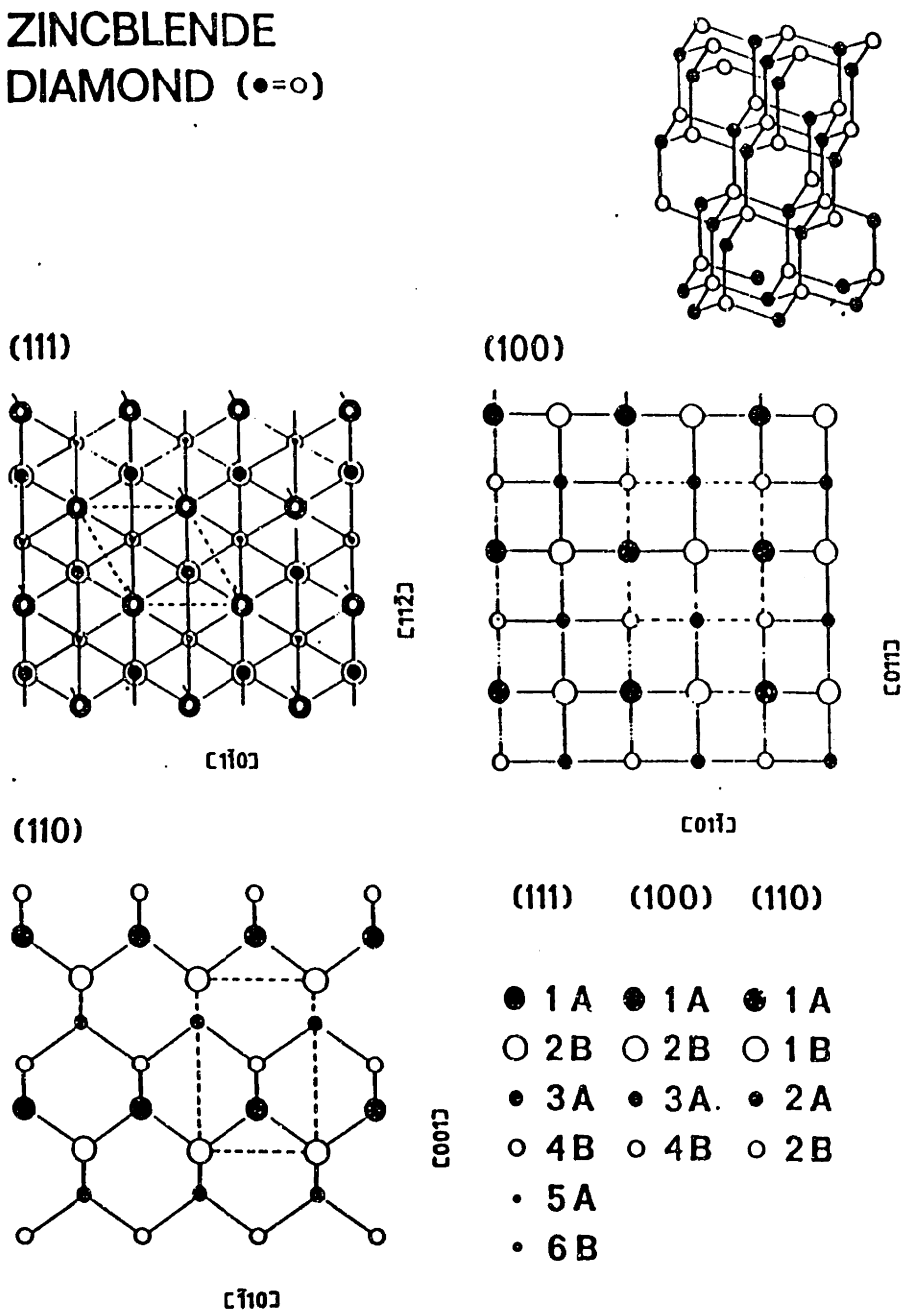

Figure 3-10: Schematic view of layer structures in β-SiC.

Chapter 4

Continuum Analysis of Elastic Stability of Homogeneous Crystals Under Hydrostatic Loading

4.1 Introduction

In the past, studies of structural transformation of a strained lattice due to lattice instabilities were based on stability criteria expressed in terms of elastic constants[13]. For important long-standing physical phenomena such as melting, polymorphism and pressure-induced amorphization, the criterion being violated was regarded as the mechanism causing the onset of the structural transformation. The first systematic analysis of lattice stability was attributed to M. Born who showed that by expanding the internal energy of a crystal into a power series in strain and demanding convexity of the energy, one could obtain stability criteria in terms of elastic constants [12]. While Born's results are well known in the literature [13], their validity under conditions of finite load have not been generally questioned except in a series of studies made by Hill [10] and Hill and Milstein [14] who showed that different domains of stability can result from different choices of strain measure. A recent study by Wang et al.[15][16] showed that the conventional criteria due to Born are

valid only at zero load. They derived a new formulation of stability criteria based on elastic stiffness coefficients that appear as the finite-strain generalization of elastic constants. In this formulation, the stress terms appear explicitly in the stability criteria[16]. The validity of the new formulation was demonstrated by a number of molecular dynamics simulations [15] [84] [24] [23] [16]. Recently, Rice has given valid questions of the general derivations of the new stability criteria[18]. He has independently shown that the new stability criteria for hydrostatic loading developed by Wang et al.[16] are correct.

The theoretical description of mechanical behavior of a crystal has been largely based on elasticity theory. For problems related to instability of homogeneous crystals (meaning single crystals without any kind of defects), deformation with finite strain is involved. Therefore, finite strain elasticity is needed to study the instability problems. In this chapter, we will first review some basic concepts of continuum elasticity theory in Sec. 4.2 and Sec. 4.3. Our emphasis is to provide clear thermodynamic definitions of stress, strain, elastic constants and stiffness coefficients in the context of finite strain elasticity. These concepts will be related back to what we have discussed in Chapter 2. By so doing, we will ensure that the mechanical properties we calculated in Chapter 2 are consistent with the classical continuum elasticity theory. In Sec. 4.4, we derive the new formulation of elastic stability criteria for hydrostatic loading following the work of Rice[18]. In Sec. 4.5, we derive the specific elastic stability criteria and their deformation modes for a cubic lattice. Lastly, in Sec. 4.6, we will summarize a number of studies where the new stability criteria have been applied and new insight into structural transformations of crystals have been obtained.

4.2 Finite Strain and Stress

For thermodynamic calculations, a crystal is considered as a homogeneous, anisotropic elastic medium. Consider a homogeneously deformed elastic object, having an arbitrary initial configuration $\mathbf{x}$ corresponding to an arbitrary applied stress Σ and finite strain $\boldsymbol{\eta}$. The combined first and second laws of thermodynamics states that

$dU = TdS - dW$ as a crystal deforms from $\mathbf{x}$ to $\mathbf{X}$, where U and S are internal energy and entropy per unit volume (at $\mathbf{x}$) respectively; dW is the work per unit volume. For arbitrary stress loading, $dW = \tau_{ij} d\eta_{ij}$, which is in strict analogy to $dW = -PdV$ for the pressure-volume case. Since $F = U - TS$, where F is the Helmholtz free energy per unit volume, the differential of F is

$$dF = -SdT - \tau_{ij} d\eta_{ij} \quad (i, j = x, y, z) \tag{4.1}$$

It is important to point out that, for finite strain deformation, the definitions of τ_{ij} and η_{ij} in this equation are not unique. It is required, however, that τ_{ij} and η_{ij} must refer to the **same reference state** and $\tau_{ij} d\eta_{ij}$ must give the work increment dW per unit volume. Under the condition of constant temperature T or constant entropy S, the work W becomes a state function of the system. And a fundamental relation must hold between the stress and strain

$$\tau_{ij} = (\frac{\partial W}{\partial \eta_{ij}})_T \tag{4.2}$$

where W is a strain energy function. Different finite-strain definitions satisfying this requirement have been proposed[85], and they fall into two classes: (1) definition in terms of the initial configuration (denoted as $\mathbf{x}$); and (2) definition in terms of the deformed configuration (denoted as $\mathbf{X}$). When coordinates are involved, the first class employs material coordinates in the undeformed configuration $\mathbf{x}$, and the second class uses spatial coordinates in the deformed configuration $\mathbf{X}$. The formulation in terms of the undeformed configuration is called the **Lagrangian formulation**; and the formulation in terms of the deformed configuration is called the **Eulerian formulation**. A generally adopted strain measure is the Lagrangian (or Green's) finite strain tensor. This strain tensor is measured with respect to the undeformed configuration[85]

$$\boldsymbol{\eta} = \frac{1}{2}(\mathbf{J}^T\mathbf{J} - \mathbf{I}) \tag{4.3}$$

where $\mathbf{J}$ is the deformation gradient (or Jacobian) matrix, i.e., $J = d\mathbf{X}/d\mathbf{x}$; and $\mathbf{I}$ is the identity matrix. Note that $\mathbf{J}$ is related to the simulation cell matrix h described in Chapter 2, and $d\mathbf{X}$ and $d\mathbf{x}$ are written as $h \cdot ds$ and $h_0 \cdot ds$ respectively, where s is in the reduced coordinate with respect to h. If we use h_0 for the simulation cell of the undeformed configuration (zero stress state) and h for the simulation cell of the deformed configuration, we have

$$\mathbf{J} = \frac{d\mathbf{X}}{d\mathbf{x}} = \frac{h \cdot ds}{h_0 \cdot ds} = hh_0^{-1} \tag{4.4}$$

And the Lagrangian strain becomes

$$\boldsymbol{\eta} = \frac{1}{2}[(hh_0^{-1})^T(hh_0^{-1}) - I] = \frac{1}{2}(h_0^{T^{-1}}h^T h h_0^{-1} - I) \tag{4.5}$$

This is the exact definition we used in Chapter 2 (see Eq.(2.4)). The Lagrangian strain can also be written as[86]

$$\eta_{ij} = \frac{1}{2}(u_{i,j} + u_{j,i} + u_{k,i}u_{k,j}) = \epsilon_{ij} + \frac{1}{2}u_{k,i}u_{k,j} \tag{4.6}$$

where $u_i = X_i - x_i$ is the displacement, $u_{i,j} = \frac{\partial u_i}{\partial x_j}$ and ϵ_{ij} is the small strain defined by

$$\epsilon_{ij} = \frac{1}{2}(u_{i,j} + u_{j,i}) \tag{4.7}$$

The finiteness of strain makes it necessary to distinguish between stresses referred to the initial and final configurations of the elastic body, as well as between the true stress and the stresses that are associated by work dW with various finite strain tensors[86]. We discuss the three important stress definitions and their relationship following the work of Bazant and Cedolin[86]. Corresponding to different finite strain definitions, three important stresses are defined, i.e., the **Cauchy (true) stress** σ, the **nominal stress** (or the **first Piola-Kirchhoff stress**) n and the **second Piola-Kirchhoff stress** τ. The Cauchy stress is identical to the microscopic stress

concept we used in Chapter 2 and the second Piola-Kirchhoff stress is identical to the thermodynamic tension concept we used in Chapter 2. The Cauchy stress σ_{ij} is referred to the current deformed state. σ_{ij} represents the force in the x_i-direction on a small unit cube that is cut out from the body in its final configuration (i.e., after the incremental deformation). Stress n_{ij} is referred to the initial configuration $\mathbf{x}$. n_{ij} represents the forces acting in the final configuration in X_i-direction on a deformed material element that was a unit cube in the initial configuration. The second Piola-Kirchhoff stress tensor $\boldsymbol{\tau}$ is the stress conjugate to the Lagrangian strain for the strain energy. In terms of the Cauchy stress tensor $\boldsymbol{\sigma}$, the expression for $\boldsymbol{\tau}$ is [85]

$$\boldsymbol{\tau} = V\mathbf{J}^{-1}\boldsymbol{\sigma}(\mathbf{J}^{-1})^T/V^0 \tag{4.8}$$

where V^0 and V refer to the volume at the reference state and the deformed state respectively. The physical meaning of $\boldsymbol{\tau}$ is that, instead of the actual force $\mathbf{dP}$ on per unit area dS in the spatial coordinate, $\boldsymbol{\tau}$ gives a force $\mathbf{d\tilde{P}}$ on per unit area dS_0 in the material coordinate, and the force $\mathbf{d\tilde{P}}$ is related to the force $\mathbf{dP}$ in the same way that a material vector $d\mathbf{x}$ at $\mathbf{x}$ is related by the deformation to the corresponding spatial vector $d\mathbf{X}$ at $\mathbf{X}$. That is,

$$\mathbf{d\tilde{P}} = \mathbf{J}^{-1} \cdot \mathbf{dP}, \quad just\ as \quad d\mathbf{x} = \mathbf{J}^{-1} \cdot d\mathbf{X} \tag{4.9}$$

Since $\mathbf{J} = hh_0^{-1}$, we obtain

$$\boldsymbol{\tau} = Vh_0h^{-1}\boldsymbol{\sigma}h^Th_0^T/V^0 \tag{4.10}$$

Thus, it becomes clear that the second Piola-Kirchhoff stress tensor is indeed the same as the thermodynamic tension described in Chapter 2 (see Eq.(2.2)). Based on our choice of the Lagrangian strain $\boldsymbol{\eta}$, the stress that satisfies Eq.(4.2) is the second Piola-Kirchhoff stress $\boldsymbol{\tau}$, i.e.,

$$dW = \boldsymbol{\tau}d\boldsymbol{\eta} = Tr(\boldsymbol{\tau}d\boldsymbol{\eta}) \tag{4.11}$$

4.3 Elastic Constants and Elastic Stiffness Coefficients

The relation between the three stresses described in the last section is[86]

$$Tr(n \cdot \dot{J}) = Tr(\tau \cdot \dot{[\frac{1}{2}J^T \cdot J]}) = det(J)\ Tr(\sigma \cdot \dot{J} \cdot J^{-1}) \tag{4.12}$$

Then one obtain

$$n = \tau \cdot J^T = det(J)\ J^{-1} \cdot \sigma \tag{4.13}$$

or

$$n_{ij} = \tau_{ik} J_{jk} = det(J)\ J^{-1}_{ik} \sigma_{kj} \tag{4.14}$$

For convenience, J is chosen with respect to the initial configuration. For small deformation from the initial pre-stressed configuration, $J_{ij} = \delta_{ij} + u_{i,j}$.

Consider a pre-stressed state under stress σ^0_{ij}, $J^0_{ij} = \delta_{ij}$. For a deformation with small displacement u_i from the pre-stressed state, $J_{ij} = \delta_{ij} + u_{i,j}$. The relations between the stress increments for the small displacement u_i is

$$\begin{aligned} n_{ij} - \sigma^0_{ij} &= \tau_{ij} - \sigma^0_{ij} + \sigma^0_{ik} u_{j,k} \\ &= \sigma_{ij} - \sigma^0_{ij} + u_{k,k}\sigma^0_{ij} - u_{i,k}\sigma^0_{kj} \end{aligned} \tag{4.15}$$

The definition of the elastic constants C_{ijkl} is

$$\tau_{ij} - \sigma^0_{ij} = C_{ijkl} \epsilon_{kl} \tag{4.16}$$

where ϵ_{kl} is defined in Eq.(4.7). Correspondingly, a rotation tensor ω_{kl} is defined as

$$\omega_{kl} = \frac{1}{2}(u_{k,l} - u_{l,k}) \tag{4.17}$$

It is clear from Eq.(4.16) that only when the initial state is a stress-free state, one can write the familiar relation

$$\sigma_{ij} = C_{ijkl}\epsilon_{kl} \tag{4.18}$$

The inverse of Eq.(4.18) expresses strain in terms of stress

$$\epsilon_{kl} = [C_{ijkl}]^{-1}\sigma_{ij} \tag{4.19}$$

where $\mathbf{S} = \mathbf{C}^{-1}$ is the compliance tensor.

The number of independent elastic constants or compliances depends on the symmetry of the system. Within the principal coordinate system [87], using the Voigt notation

$$\begin{aligned} xx &\to 1 \quad yy \to 2 \quad zz \to 3 \\ yz &\to 4 \quad xz \to 5 \quad xy \to 6 \\ zy &\to 4 \quad zx \to 5 \quad yx \to 6 \end{aligned} \tag{4.20}$$

the elastic constant tensor of a cubic crystal is characterized by three independent elastic constants C_{11}, C_{12} and C_{44}, is

$$C = \begin{pmatrix} C_{11} & C_{12} & C_{12} & 0 & 0 & 0 \\ C_{12} & C_{11} & C_{12} & 0 & 0 & 0 \\ C_{12} & C_{12} & C_{11} & 0 & 0 & 0 \\ 0 & 0 & 0 & C_{44} & 0 & 0 \\ 0 & 0 & 0 & 0 & C_{44} & 0 \\ 0 & 0 & 0 & 0 & 0 & C_{44} \end{pmatrix}$$

and the compliance tensor is

$$S = \begin{pmatrix} S_{11} & S_{12} & S_{12} & 0 & 0 & 0 \\ S_{12} & S_{11} & S_{12} & 0 & 0 & 0 \\ S_{12} & S_{12} & S_{11} & 0 & 0 & 0 \\ 0 & 0 & 0 & S_{44} & 0 & 0 \\ 0 & 0 & 0 & 0 & S_{44} & 0 \\ 0 & 0 & 0 & 0 & 0 & S_{44} \end{pmatrix}$$

Elastic moduli can be obtained from the inverse of the diagonal elements of the compliance tensor [88] [89]. For a cubic crystal, the Young's moduli are

$$Y = Y_x = Y_y = Y_z = S_{11}^{-1} = \frac{(C_{11} - C_{12})^2(C_{11} + 2C_{12})}{C_{11} + C_{12}} \tag{4.21}$$

The bulk modulus is

$$B = [S_{11} + S_{22} + S_{33} + 2(S_{12} + S_{13} + S_{23})]^{-1} = \frac{C_{11} + 2C_{12}}{3} \tag{4.22}$$

The shear moduli are

$$G_{yz} = G_{xz} = G_{xy} = C_{44} \tag{4.23}$$

Eq.(4.21) - Eq.(4.23) are the basic relations between the elastic constants and elastic moduli.

Using Eq.(4.15), Eq.(4.16) and the relation

$$u_{k,l} = \frac{1}{2}(\epsilon_{kl} + \omega_{kl}) \;\; u_{l,k} = \frac{1}{2}(\epsilon_{kl} - \omega_{kl}) \tag{4.24}$$

we obtain

$$n_{ij} - \sigma_{ij}^0 = C_{ijkl}\epsilon_{kl} - \sigma_{ij}^0\epsilon_{kk} + \sigma_{ik}^0(\epsilon_{kj} - \omega_{kj}) + \sigma_{kj}^0(\epsilon_{ik} + \omega_{ik}) \tag{4.25}$$

Rearrange the above equation, one obtain

$$\sigma_{ij} - \sigma^0_{ij} + \sigma^0_{ik}\omega_{kj} - \omega_{ik}\sigma^0_{kj} = C_{ijkl}\epsilon_{kl} - \sigma^0_{ij}\epsilon_{kk} + \sigma^0_{ik}\epsilon_{kj} + \epsilon_{ik}\sigma^0_{kj} \tag{4.26}$$

The elastic stiffness coefficient B_{ijkl} is defined by

$$\sigma_{ij} - \sigma^0_{ij} + \sigma^0_{ik}\omega_{kj} - \omega_{ik}\sigma^0_{kj} = B_{ijkl}\epsilon_{kl} \tag{4.27}$$

Under the condition of no rigid body rotation, $\omega_{ij} = 0$ and B_{ijkl} can be written as

$$B_{ijkl} = (\partial\sigma_{ij}/\partial\epsilon_{kl})_\omega \tag{4.28}$$

This is the familiar definition used by Wallace[11]. The general relation between the stiffness coefficients **B** and the elastic constants **C** is[11]

$$B_{ijkl}(\mathbf{x}) = C_{ijkl}(\mathbf{x}) + \Sigma_{ijkl}(\mathbf{x}) \tag{4.29}$$

$$\Sigma_{ijkl}(\mathbf{x}) = \frac{1}{2}[\sigma_{il}(\mathbf{x})\delta_{jk} + \sigma_{jl}(\mathbf{x})\delta_{ik} + \sigma_{ik}(\mathbf{x})\delta_{jl} + \sigma_{jk}(\mathbf{x})\delta_{il} - 2\sigma_{ij}(\mathbf{x})\delta_{kl}] \tag{4.30}$$

Eq.(4.30) shows that the stiffness coefficient tensor depends explicitly on the state of applied loading. The explicit stress-dependent terms can be shown to arise from the requirement of rotational invariance of the strain energy[16][90]. Consequently, except for isotropic or zero stress, it has different symmetry from the elastic constant tensor. In view of Eq.(4.30), the symmetry

$$B_{ijkl} = B_{jikl} = B_{ijlk} \tag{4.31}$$

still holds, but not the Voigt symmetry[11][15][16], i.e.,

$$B_{ijkl} \neq B_{klij} \tag{4.32}$$

4.4 Lattice Stability at Finite Strain under Hydrostatic Loading

We now follow the work of Rice[18] to derive the stability criteria for a crystal under finite hydrostatic loading, i.e., $\tau_{ij} = -P\delta_{ij}$. As discussed by Bazant and Cedolin[86], in stability problems, the energy and work variations must be calculated on the basis of finite strain tensor components that are accurate up to terms of second-order small in displacement gradients $u_{i,j}$. Consider a crystal with a deformation of volume change δV under constant pressure P, the variation of internal energy is δU and the work done is δW. In order for the crystal to be stable against this small deformation, one must have

$$\delta U > -P\delta V \tag{4.33}$$

The variation of internal energy that is correct to all orders is

$$\delta U = \int_{V^0} (\phi - \phi^0) dV^0 \tag{4.34}$$

where V^0 is the volume of the initial configuration, ϕ is the strain energy after the deformation per unit volume in the initial configuration, and ϕ^0 is the strain energy before the deformation per unit volume in the initial configuration. Since $d\phi = \tau_{ij} d\eta_{ij}$, one can write

$$\phi - \phi^0 = \sigma^0_{ij}\eta_{ij} + \frac{1}{2}\eta_{ij}C_{ijkl}\eta_{kl} + \cdots \tag{4.35}$$

Since

$$\eta_{ij} = \epsilon_{ij} + \frac{1}{2}u_{k,i}u_{k,j} \tag{4.36}$$

to be correct to the second order of $u_{i,j}$, one obtain

$$\phi - \phi^0 = \sigma_{ij}^0 \eta_{ij} + \frac{1}{2}\epsilon_{ij} C_{ijkl} \epsilon_{kl} = -P\eta_{ii} + \frac{1}{2}\epsilon_{ij} C_{ijkl} \epsilon_{kl} \tag{4.37}$$

The variation of volume is

$$\delta V = \int_{V^0} (det[J] - 1) dV^0 \tag{4.38}$$

Since

$$det[J] = det \begin{bmatrix} 1 + u_{1,1} & u_{1,2} & u_{1,3} \\ u_{2,1} & 1 + u_{2,2} & u_{2,3} \\ u_{3,1} & u_{3,2} & 1 + u_{3,3} \end{bmatrix}$$

one derive $det(J)$ to the second order

$$\begin{aligned} det[J] - 1 &= 1 + u_{1,1} + u_{2,2} + u_{3,3} + u_{1,1}u_{2,2} + u_{2,2}u_{3,3} + u_{1,1}u_{3,3} \\ &\quad -u_{1,2}u_{2,1} - u_{1,3}u_{3,1} - u_{2,3}u_{3,2} \\ &= u_{i,i} + \frac{1}{2}(u_{i,i})^2 - \frac{1}{2}u_{i,j}u_{j,i} \\ &= \epsilon_{ii} + \frac{1}{2}(\epsilon_{ii})^2 - \frac{1}{2}\epsilon_{ij}\epsilon_{ij} + \frac{1}{2}\omega_{ij}\omega_{ij} \end{aligned} \tag{4.39}$$

Thus, we have

$$\delta U + P\delta V = \int_{V^0} \{-P\eta_{ii} + \frac{\epsilon_{ij} C_{ijkl} \epsilon_{kl}}{2} + P[\epsilon_{ii} + \frac{(\epsilon_{ii})^2}{2} - \frac{\epsilon_{ij}\epsilon_{ij}}{2} + \frac{\omega_{ij}\omega_{ij}}{2}]\} dV^0 \tag{4.40}$$

Since

$$\begin{aligned} \eta_{ii} &= \epsilon_{ii} + \frac{1}{2}u_{k,i}u_{k,i} \\ &= \epsilon_{ii} + \frac{1}{2}[(\epsilon_{ki} + \omega_{ki})(\epsilon_{ki} + \omega_{ki}) \\ &= \epsilon_{ii} + \frac{1}{2}\epsilon_{ki}\epsilon_{ki} + \frac{1}{2}\omega_{ki}\omega_{ki} \end{aligned} \tag{4.41}$$

We obtain

$$\delta U + P\delta V = \int_{V^0} [\frac{1}{2}\epsilon_{ij} C_{ijkl} \epsilon_{kl} + \frac{1}{2} P(\epsilon_{ii})^2 - P\epsilon_{ij}\epsilon_{ij}] dV^0 \tag{4.42}$$

Use Eq.(4.29) and Eq.(4.30), for hydrostatic loading $\sigma_{ij} = -P\delta_{ij}$, we obtain

$$C_{ijkl} = B_{ijkl} + \frac{P}{2}[\delta_{il}\delta_{jk} + \delta_{jl}\delta_{ik} + \delta_{ik}\delta_{jl} + \delta_{jk}\delta_{il} - 2\delta_{ij}\delta_{kl}] \tag{4.43}$$

Put above equation into Eq.(4.42), we obtain

$$\begin{aligned} \frac{1}{2}\epsilon_{ij} C_{ijkl} \epsilon_{kl} &= \frac{1}{2}\epsilon_{ij} B_{ijkl} \epsilon_{kl} \\ &\quad + \frac{1}{2}\epsilon_{ij}[\frac{P}{2}(\delta_{il}\delta_{jk} + \delta_{jl}\delta_{ik} + \delta_{ik}\delta_{jl} + \delta_{jk}\delta_{il} - 2\delta_{ij}\delta_{kl})]\epsilon_{kl} \\ &= \frac{1}{2}\epsilon_{ij} B_{ijkl} \epsilon_{kl} + P\epsilon_{ij}\epsilon_{ij} - \frac{P}{2}(\epsilon_{ii})^2 \end{aligned} \tag{4.44}$$

Therefore, we obtain

$$\delta U + P\delta V = \int_{V^0} \frac{1}{2}\epsilon_{ij} B_{ijkl} \epsilon_{kl} \tag{4.45}$$

The instability occurs at

$$\delta U + P\delta V = 0 \tag{4.46}$$

Since the strain ϵ_{ij} is arbitrary and $B_{ijkl}\epsilon_{kl}$ are independent linear coefficients of strain, the instability condition for hydrostatic loading becomes

$$B_{ijkl}\epsilon_{kl} = 0 \tag{4.47}$$

This is an eigenvalue problem where the non-zero eigenvalues of $\mathbf{B}$ give the instability criteria and the corresponding eigenvectors ϵ describe the modes of deformation [17].

4.5 Stability Criteria and Deformation Modes for a Cubic Lattice

We now discuss explicitly a cubic lattice under hydrostatic stress

$$\sigma_{ij} = -P\delta_{ij} \tag{4.48}$$

where P is negative for tension and positive for compression, and we follow the convention that inward pressure is positive while inward stress is negative. Using Eq.(4.30), we obtain

$$\Sigma_{ijkl} = \frac{P}{2}[\delta_{il}\delta_{jk} + \delta_{jl}\delta_{ik} + \delta_{ik}\delta_{jl} + \delta_{jk}\delta_{il} - 2\delta_{ij}\delta_{kl}] \tag{4.49}$$

It is clear that $\Sigma_{ijkl} = \Sigma_{klij}$. Therefore, both Σ_{ijkl} and B_{ijkl} have the Voigt symmetry in this case. Using Eq.(4.29) and (4.30), we obtain the stiffness coefficients $\mathbf{B}$ in the Voigt notation

$$\begin{aligned} B_{11} &= B_{22} = B_{33} = C_{11} - P \\ B_{12} &= B_{21} = B_{13} = C_{12} + P \\ B_{44} &= B_{55} = B_{66} = C_{44} - P \end{aligned} \tag{4.50}$$

We now can solve the eigenvalue problem in Eq.(4.47) to obtain the stability criteria for a cubic crystal under hydrostatic stress loading. In order for Eq.(4.47) to have nontrivial solutions, the necessary and sufficient condition is that the determinant of

the coefficient matrix is identically zero, i.e., $det(\mathbf{B}) = 0$:

$$\begin{vmatrix} B_{11} & B_{12} & B_{12} & 0 & 0 & 0 \\ B_{12} & B_{11} & B_{12} & 0 & 0 & 0 \\ B_{12} & B_{12} & B_{11} & 0 & 0 & 0 \\ 0 & 0 & 0 & B_{44} & 0 & 0 \\ 0 & 0 & 0 & 0 & B_{44} & 0 \\ 0 & 0 & 0 & 0 & 0 & B_{44} \end{vmatrix} = 0$$

The solutions are

$$\begin{aligned} B_{11} + 2B_{12} &= 0 \\ B_{11} - B_{12} &= 0 \\ B_{44} &= 0 \end{aligned} \tag{4.51}$$

These three equations are the stability criteria at finite strain for cubic crystals under hydrostatic stress. They are in exact analogy with that derived by Born[13]. The important difference is that the elastic constants $\mathbf{C}$ in Born's criteria have been replaced by the stiffness coefficients $\mathbf{B}$. Using Eq.(4.50), we can also express the new instability criteria in terms of $\mathbf{C}$

$$\begin{aligned} C_{11} + 2C_{12} + P &= 0 \\ C_{11} - C_{12} - 2P &= 0 \\ C_{44} - P &= 0 \end{aligned} \tag{4.52}$$

The physical significance of the above criteria is that, the response of the crystal lattice will not only depend on elastic constants C, but also depend on the applied stress P.

In the Voigt notation, Eq.(4.47) gives six homogeneous equations for a cubic crys-

tal under hydrostatic stress

$$\begin{aligned} B_{11}\epsilon_{xx} + B_{12}(\epsilon_{yy} + \epsilon_{zz}) &= 0 \\ B_{12}(\epsilon_{xx} + \epsilon_{zz}) + B_{11}\epsilon_{yy} &= 0 \\ B_{12}(\epsilon_{xx} + \epsilon_{yy}) + B_{11}\epsilon_{zz} &= 0 \\ B_{44}\epsilon_{yz} &= 0 \\ B_{44}\epsilon_{xz} &= 0 \\ B_{44}\epsilon_{xy} &= 0 \end{aligned} \tag{4.53}$$

Using the eigenvalues obtained in Eq.(4.51), we can solve the above equations to obtain the corresponding eigenvectors ϵ_{ij}. The eigenvectors will specify the eigenmodes for each instability criterion.

- For the first instability criterion, the eigenvalues satisfy $B_{11} + 2B_{12} = 0$, $B_{11} - B_{12} \neq 0$ and $B_{44} \neq 0$. Combining $B_{44} \neq 0$ and the last three equations of Eq.(4.53), we obtain

$$\epsilon_{yz} = \epsilon_{xz} = \epsilon_{xy} = 0 \tag{4.54}$$

Subtracting the second equation from the first equation in Eq.(4.53), we obtain

$$(B_{11} - B_{12})(\epsilon_{xx} - \epsilon_{yy}) = 0 \tag{4.55}$$

Since $B_{11} - B_{12} \neq 0$, one must have

$$\epsilon_{xx} - \epsilon_{yy} = 0 \tag{4.56}$$

Substituting Eq.(4.56) into the third equation in Eq.(4.53) and using $B_{11} = -2B_{12}$, we obtain

$$\epsilon_{zz} = \epsilon_{xx} \tag{4.57}$$

Hence, the eigenvectors of the first instability is

$$\epsilon = (1, 1, 1, 0, 0, 0)\epsilon \tag{4.58}$$

with no constraint on ϵ.

- For the second instability criterion, the eigenvalues satisfy $B_{11} + 2B_{12} \neq 0$, $B_{11} - B_{12} = 0$ and $B_{44} \neq 0$. Since $B_{44} \neq 0$, the shear strains must be zero, i.e.,

$$\epsilon_{yz} = \epsilon_{xz} = \epsilon_{xy} = 0 \tag{4.59}$$

Since $B_{11} = B_{12}$, the first three equations in Eq.(4.53) are identical and they all become

$$\epsilon_{xx} + \epsilon_{yy} + \epsilon_{zz} = 0 \tag{4.60}$$

which means that ϵ_{xx}, ϵ_{yy} and ϵ_{zz} can be arbitrary values as long as their sum is zero. Physically this requires volume conservation along the deformation path. Thus, the eigenvectors of the second instability is

$$\epsilon = (\epsilon_{xx}, \epsilon_{yy}, \epsilon_{zz}, 0, 0, 0) \tag{4.61}$$

with the constraint of volume conservation.

- For the third instability criterion, the eigenvalues satisfy $B_{11} + 2B_{12} \neq 0$, $B_{11} - B_{12} \neq 0$ and $B_{44} = 0$. Since $B_{11} \neq B_{12}$, we have

$$\epsilon_{xx} = \epsilon_{yy} = \epsilon_{zz} \tag{4.62}$$

Summing up the first three equations in Eq.(4.53), we obtain

$$(B_{11} + 2B_{12})(\epsilon_{xx} + \epsilon_{yy} + \epsilon_{zz}) = 0 \tag{4.63}$$

Since $B_{11} + 2B_{12} \neq 0$, we obtain

$$\epsilon_{xx} + \epsilon_{yy} + \epsilon_{xy} = 0 \tag{4.64}$$

with no restriction on the values of ϵ_{yz}, ϵ_{xz} or ϵ_{xy}.

In summary, for a cubic crystal under finite hydrostatic stress, the three instability criteria and corresponding eigenmodes of deformation are

$$\begin{aligned} C_{11} + 2C_{12} + P = 0, &\qquad (1,1,1,0,0,0)\epsilon \\ C_{11} - C_{12} - 2P = 0, &\qquad (\epsilon_{xx}, \epsilon_{yy}, \epsilon_{zz}, 0, 0, 0)\epsilon \\ &\qquad \epsilon_{xx} + \epsilon_{yy} + \epsilon_{zz} = 0 \\ C_{44} - P = 0, &\qquad (0,0,0,\epsilon_{yz},0,0) \end{aligned} \tag{4.65}$$

These results have clear interpretations. The first criterion clearly has to do with volumetric deformation, as indicated by its eigenmode. Also, with $C_{11} + 2C_{12} = 3B_T$, where B_T is the bulk modulus, we see that for $K(P) = C_{11} + 2C_{12} + P = 0$ to be satisfied, P would have to be negative. Thus, the nature of this instability is lattice decohesion by pure dilatation since it involves the vanishing of the bulk modulus. This is referred to as the **spinodal instability**. The second instability in Eq.(4.65) involves symmetry breaking (bifurcation) with volume conservation; the vanishing modulus here may be identified as the tetragonal shear, $G' = (C_{11} - C_{12})/2$. This is referred to as the **Born instability** or **tetragonal shear instability**. The third instability is simply shear along one of the symmetry directions with volume conservation, and the modulus here is $G = C_{44}$. This is referred to as the **shear instability**.

4.6 Discussion

Based on the new criteria of Eq.(4.65), or its general form of Eq.(4.47), molecular dynamics simulations have been used to study the deformation and structural transition of homogeneous crystals [15] [16] [84] [24][23]. In these studies, the critical stress and instability mechanism at which a crystal becomes unstable have been well predicted

by the stability criteria. Since the instability criteria can not predict the structure of the system after instability occurs, direct molecular dynamics simulations are useful to reveal the unstable structural response of the system. Moreover, MD simulations can provide the critical stress independently, which can be used to verify the prediction made by the stability criteria. MD simulations can reveal details of the unstable structural deformation and eigenmodes of the instability can be identified. So far, MD studies of crystal instability include mechanical melting [15] of metals; brittle fracture of β-SiC [84] (see Chapter 5 of this thesis); phase transition of Si under compression [24] and brittle fracture of intermetallic compounds [23]. All these studies demonstrate that the instability criteria based on the stiffness coefficients can correctly predict the critical stresses and identify instability mechanisms. Thus, the new instability criteria have provided important insight into the structural transitions of materials. In Chapter 6 of this thesis, we will study pressure-induced amorphization of β-SiC using the new stability criteria.

Chapter 5

Lattice Instability and Brittle Fracture of β-SiC under Hydrostatic Tension

5.1 Introduction

How a crystal lattice responds to hydrostatic stress is a fundamental problem in elasticity [91][10] which can be analyzed in terms of interatomic forces derived from specific potential function models [92][93]. While elasticity analysis can produce stability criteria expressed in terms of elastic constants, such results seldom have been carefully tested by subjecting the predicted instability to direct verification, a process which is feasible for atomistic simulations [30]. Recently, it has been shown that to predict the critical strain at which a stressed lattice becomes structurally unstable, the applied stress must appear explicitly in the instability condition[15][16]. This result stands in contrast to the well-known stability criteria where the effects of applied stress enter only through the elastic constants [13].

The purpose of this chapter is to present a molecular dynamics analysis of the structural stability of β-SiC under hydrostatic tension. This study stems from our interest in modeling the mechanical properties of SiC using empirical interatomic

potentials which treat this solid as fully covalent. It is also motivated by the recent results on elastic instability in crystalline solids which gave new insights into the unstable structural responses of an fcc metal under tension loading [15][16]. For β-SiC, there has been no previous study of its mechanical behavior, especially under conditions of large lattice deformation.

We have shown in Chapter 3 that the potential model proposed by Tersoff [26], which accounts for the many-body interaction effects through a bond ordering formulation, is able to describe the elastic constants and certain surface properties, provided the potential cutoff is modified to exclude interactions with the second nearest neighbors. Details of the testing and modification of the Tersoff potential are directed to Chapter 2 and 3. In Figure 5-1 we show the pressure-lattice parameter relation in the dilatation region described by the modified Tersoff potential. The molecular dynamics simulation data, obtained at $300K$ using a simulation cell with 216 atoms and periodic boundary conditions, can be fitted well to the two-parameter Birch-Murnaghan equation of state of Eq.(3.1). The value of the low pressure expansion coefficient of the bulk modulus k_0' is obtained to be 4.4 from the fitting. In contrast, the simpler Murnaghan equation of state of Eq.(3.2) is seen to breakdown at high tension. To present our molecular dynamics simulations in another way, we show in Figure 5-2 two sets of independent results of the pressure vs. lattice parameter curves at $300K$. One of the curves is obtained by calculating the pressure at various fixed values of the lattice parameter in the (NVT)-ensemble; and the other is by calculating the lattice response to various hydrostatic loadings in the $(N\Sigma T)$-ensemble [34], where Σ is the applied loading. The close agreement between the results over the entire range of deformation gives us confidence in our simulation procedure of applying hydrostatic tension.

Using the modified Tersoff potential, we study here the inherent stability of the β-SiC lattice under dilatation. Applying the elastic stability criteria [15][16] derived in terms of elastic stiffness coefficient as discussed in Chapter 4, we derive, in Sec. 5.2, a quantitative prediction of the critical tension at which the zincblende β-SiC lattice becomes mechanically unstable. The direct observation of the structural instability

under dilatation and its consequences by means of molecular dynamics simulation will be described in Sec. 5.3 and Sec. 5.4, thus providing explicit data to confirm the stability analysis. In Sec. 5.4, we examine the simulation results to find that the observed spinodal instability is accompanied by local decohesion on {111} planes. From the details of the local atomic displacements, we find that surface relaxation occurs so quickly as to become essentially integral part of the crack nucleation process. Finally, in Sec. 5.5 we consider possible effects of charge transfer in treating the interatomic forces which have been neglected in this work.

5.2 Prediction of Lattice Instability by Elastic Stability Criteria

The modified Tersoff potential has been applied to calculate the elastic constants of β-SiC at equilibrium conditions and also at elevated temperatures. This was carried out using fluctuation formulas which we have derived and tested against stress-strain simulation. Details are referred to Chapter 2 and 3. Here we will determine the variation of the elastic constants with applied tension and the behavior of elastic stiffness coefficients (described in Chapter 4), the latter being the quantities needed to predict structural instability of the lattice.

Figure 5-3 shows the variation of the elastic constants as the lattice is dilated. It also shows experimental values of elastic constants[72]. The molecular dynamics results are obtained by giving the 216-atom simulation cell a certain lattice parameter and allowing the system to equilibrate in 10 to 15×10^3 time steps (each step corresponds to $1.451 \times 10^{-4} ps$), and accumulating trajectories for 100 to 150×10^3 steps for property calculations. (Because of the long runs the error bars in these results associated with statistical fluctuations are no larger than the size of the symbols.) The atomic configurations obtained at the end of a run are then used for the succeeding one. In each case the internal stress σ is calculated along with the elastic constants C_{ij}. One sees in Figure 5-3 the elastic softening behavior generally expected, each

elastic constant decreasing in a monotonic, concave manner[36][17]. The fact that C_{44} is significantly greater than C_{12} indicates the relative brittleness of the system and importance of angle-dependent forces [36].

The elastic stiffness coefficients, defined as $B \equiv \partial s/\partial \eta$, where s and η are the applied stress and Lagrangian strain tensors respectively, can be related to the elastic constant tensor C, $B = C + \Lambda$, where tensor Λ is a linear function of the applied stress [11]. For hydrostatic stress imposed on a cubic lattice, the stiffness coefficients (in Voigt notation) become simply[15][94][92]:

$$B_{11} = C_{11} - P, \quad B_{12} = C_{12} + P, \quad B_{44} = C_{44} - P \tag{5.1}$$

where P is the pressure ($P < 0$ for tension). Figure 5-4 shows how these quantities vary with tensile loading. Notice that while B and C have the same symmetry under hydrostatic stress, in general the presence of Λ means B will have a different symmetry from C[15] [11]. As we will discuss next, the significance of B is that in principle it, rather than C, determines the conditions for elastic stability.

A conventional approach to lattice stability analysis, originally developed and applied by Born and co-workers [13], holds that a cubic crystal lattice becomes mechanically unstable whenever one of the following conditions is violated

$$(C_{11} + 2C_{12})/3 > 0, \quad (C_{11} - C_{12})/2 > 0, \quad C_{44} > 0 \tag{5.2}$$

By identifying each of the left hand sides as a modulus, the isothermal bulk modulus K, the modulus against tetragonal shear G', and the modulus against rhombohedral shear G, respectively, one may express Eq. (5.2) as

$$K(P) > 0, \quad G'(P) > 0, \quad G(P) > 0 \tag{5.3}$$

which then has the form of the classical Lagrange-Dirichlet criterion for elastic stability, where P is the hydrostatic pressure[91][10]. The distinction between Eqs. (5.2) and (5.3) has been discussed by Milstein and Hill who pointed out that when $P \neq 0$,

they predict different domains of stability, and that the basis of Eq. (5.2), the requirement of convexity of the internal energy, is not coordinate invariant [92][93].

Recently the general utility of Eq. (5.2) is questioned by showing explicitly that they do not predict correctly the lattice instability induced in an fcc metallic lattice by hydrostatic tension [15][16]. It is also shown that by replacing the elastic constants in Eq. (5.2) by the stiffness coefficients in Eq. (5.1), the resulting stability criteria still have the form of Eq. (5.3), or

$$K = (C_{11} + 2C_{12})/3 + P/3 > 0 \tag{5.4}$$
$$G' = (C_{11} - C_{12})/2 - P > 0$$
$$G = C_{44} - P > 0$$

Using the results from Figure 5-3 and Figure 5-4, the variations with tensile strain of the three moduli in Eq. (5.2) and Eq. (5.4) are shown in Figure 5-5. At the last two values of strain indicated, the values of the bulk modulus calculated from the fluctuation formula are slightly negative, while the system still appears to be stable. By interpolation, based on Eq. (5.4), the spinodal instability (vanishing of K) is predicted to occur at critical strain $\eta_c = r/r_0 - 1 = 0.153$, with corresponding critical stress of $\sigma_c = 0.370 Mbar$. On the basis of Eq. (5.2) the critical strain and stress would be $\eta_c = 0.166$ and $\sigma_c = 0.367 Mbar$. Even though the critical strains and stresses predicted by Eq. (5.2) and Eq. (5.4) are very close in this case, one can see the accuracy of Eq. (5.4), rather than Eq. (5.2), from the pressure data obtained by simulation. From a different standpoint, the bulk modulus is just the pressure derivative of volume. Therefore, it should vanish when the pressures reaches its minimum. From this data, we find that the minimum value is reached between $r/r_0 = 1.150$ and $r/r_0 = 1.161$, which is consistent with the critical strain value predicted by Eq. (5.4), rather than by Eq. (5.2). The vanishing of the spinodal instability under tension for β-SiC has also be predicted by an elastic stability analysis using a tight-binding method[49], where the predicted critical stress and strain are in close agreement with our results.

Comparing Eqs. (5.2) and (5.4), we see that in formulating the stability criteria in terms of elastic stiffness coefficients, the competition between the three modes of instability now depends explicitly on the hydrostatic loading. This distinction is shown to be crucial in predicting the structural stability of close packed structures, such as an fcc metal, under pure dilatation[15][16]. One can see from Eq. (5.4) that the general effects of hydrostatic tension are to enhance the stability against shear while lowering effective lattice cohesion. In applying this analysis to Au, it is found that whereas Eq. (5.2) would predict an instability with G' vanishing, Eq. (5.4) predicts the instability to be due to vanishing of K, the correct behavior as shown by direct simulation[15][16]. This result is in contrast to what we find here for SiC where both Eqs.(5.2) and (5.4) give predictions very close to each other. The difference (cf. Figure 5-3) is seen to lie in the much larger value of C_{11} and only moderately higher value of C_{12} for SiC relative to Au, such that $C_{11} - C_{12}$ is considerably greater for SiC. Thus, the relative stability against shear over decohesion under dilatation is sufficiently robust that it is not altered by the tension loading.

5.3 Simulation of Unstable Structural Response

In order to directly observe the structural response to lattice dilatation, we apply the method of Parrinello and Rahman [30] for imposing a homogeneous stress on the system. We choose a wall mass of 5 (in units of mass of Si), maintain constant temperature by velocity rescaling, and impose a hydrostatic loading by defining $\underline{\Sigma} = < \underline{h} >^{-1} \underline{s} < \underline{h}^T >^{-1} < V >$, where $\underline{s}$ is the external stress tensor, $\underline{h}$ is the matrix defining the simulation cell, V is the cell volume, and $\underline{\Sigma}$ has only three equal diagonal elements represented by Σ. Simulation runs are carried out covering the range of Σ from 0 to 5.575, in incremental steps of 0.3 initially but decreasing to 0.025 when approaching critical value. Equilibration is determined by looking at time-averaged properties to see when the averaged values no longer change significantly over 5000 steps. Most runs consist of 1000 to 2000 steps for equilibration (adjustment to new stress level), and 10,000 steps for properties calculation; as before the final atomic configurations

of each run are used as initial configurations for the next one.

Figure 5-6 shows the overall system responses to the applied tension, expressed in terms of Σ as defined above. One sees that the instability manifests as an abrupt release in internal pressure, increase in potential energy, and increase in lattice parameter. While these indicate that undoubtedly a significant structural change has taken place, it does not appear that the lattice has lost cohesion uniformly as in a process of homogeneous disintegration. At the step where $\Sigma = 5.55$, the system is stable in that all properties do not vary significantly with time after equilibration. The time averaged values of strain and internal stress at this step are $\eta = 0.1506$ and $\sigma = 0.369 Mbar$. At the next step, $\Sigma = 5.575$ (the last data indicated in the figure), the system becomes unstable and properties show no signs of convergence at the end of the simulation period (about 10,000 time steps). Thus the observed critical loading Σ_c lies between 5.55 and 5.575. From the results of Sec. 5.2, the predicted values of the critical internal stress and the critical strain, when transformed according to the definition of Σ, is 5.566 from Eq. (5.4) and 5.593 from Eq. (5.2). So we see the accuracy of Eq. (5.4) again.

In order to see in more detail the nature of the instability we show in Figure 5-7 the time-dependent variation of the shape of the simulation cell, expressed in terms of elements of the matrix $\underline{h}$[30], and correspondingly, the elements of the internal stress tensor. Also given in Figure 5-7 is the variation of the energy per atom. In Figure 5-7(a) the persistent increase of the three diagonal elements of $\underline{h}$, each representing the edge length of the cubic simulation cell, means the system is undergoing continuous dilatation. One can discern two regimes, an initial period when the cell maintained its cubic shape and a second period (after about step 3800) when the cell has become tetragonal and volume expansion is occurring at a higher rate. In Figure 5-7(b), the diagonal elements of the stress tensor also show this change of symmetry, and in addition one sees a sharp decrease occurring at time step approximately 2700. Notice that symmetry breaking apparently takes place after the abrupt change has set in. Figure 5-7(c) and Figure 5-7(d) show the corresponding behavior of the off-diagonal elements of the cell matrix and stress tensor, respectively. From these data one can

conclude that the system has undergone a significant shear deformation and that the deformation is accompanied by the presence of appreciable level of von Mises shear stress[95]

$$\bar{\sigma} = \{\frac{1}{2}[(\sigma_{11} - \sigma_{22})^2 + (\sigma_{22} - \sigma_{33})^2 + (\sigma_{11} - \sigma_{33})^2] + 3(\sigma_{12}^2 + \sigma_{13}^2 + \sigma_{23}^2)\} \qquad (5.5)$$

Finally, in Figure 5-7(e) we see the energy increasing (becoming less negative) initially as the system becomes dilated, but at time step about 2700 a decrease is seen during the early stage of the shear deformation, then followed by subsequent increase.

Although the temporal evolution behavior shown in Figure 5-7 indicates a rather complex structural response which involves dilatation as well as shear deformation, we still do not know precisely what is the atomic configuration of the unstable lattice. For more information, it is necessary to scrutinize the molecular dynamics trajectories in greater detail, as will be discussed in the next section.

5.4 Crack Nucleation and Brittle Fracture

We now show that the unstable structural responses described in Figure 5-7 correspond to crack nucleation and brittle fracture. Figure 5-8 shows a sequence of the instantaneous atomic configurations obtained at four instants during the simulation. The simulation cell is oriented to display the stacking sequence along the body diagonal $[1\bar{1}1]$, $\cdots$ =Si-C=Si-C=Si- $\cdots$, where - and = denote alternating interplanar separation distances of $l/12$ and $l/4$ (l is the length of the body diagonal of the unit cell), respectively. The stacking of alternating $\{1\bar{1}1\}$ planes which contain only Si or C is most clearly visible in Figure 5-8(a), at the stage of simulation (about 0.3ps after the applied stress is increased from $\Sigma = 5.55$ to 5.575) when lattice instability apparently has not yet set in.

The existence of two interplanar separations means that one should distinguish two types of $\{1\bar{1}1\}$ planes between the Si and C atoms, corresponding to the well-known **glide** and **shuffle** planes in the diamond cubic lattice. With each Si or C atom

having three of its four nearest neighbors (of opposite species) across the glide plane and the fourth across the shuffle plane, it follows that in order to form a crack on the glide plane three bonds have to be broken, whereas the breaking of only one bond is required for the shuffle plane. For this reason, if cracks are nucleated on $\{1\bar{1}1\}$, the shuffle plane should be favored.

In Figure 5-8(b) the atomic configuration at $0.45ps$ into the simulation clearly indicate a crack opening from the right on the shuffle plane in the lower right part of the cell. Notice that on the two opposing surfaces of the nucleated crack, one has only Si atoms and the other only C atoms; this is as it should be if the crack has just been nucleated and atomic relaxation has not yet set in. In addition, there appears somewhat less pronounced distortion in the upper left part of the cell. In interpreting the present results on decohesion, we should keep in mind that when a Si-C bond is broken (as in the case here) the change in energy for the Si atom is different from that for the C for two reasons. The first is that a Si is bonded to three C while a C is bonded to three Si; secondly these two types of bonds have different strengths. As described in Chapter 2, in the Tersoff potential, $V_{c-s_i} \neq V_{s_i-c}$. This point will be further illustrated in Chapter 6.

In Figure 5-8(c), the configuration at $0.06ps$ later, we see both nucleated cracks begin to propagate and some details of atomic relaxation on the crack surfaces become visible. Specifically one can see the appearance of mixing of Si and C atoms on the crack surfaces (a layer is visualized by imaging a line drawn through the centers of atoms).

In Figure 5-8(d) the configuration after another $0.09ps$ shows quite clearly the consequence of the structural instability induced by the tension loading. Both cracks have propagated in a rather clean fashion through the simulation cell, with crack surfaces which appear to be well relaxed. Although the present data are obviously too limited to attempt definite conclusions, it is possible to discern interesting differences in surface relaxation between those crack surfaces which originate from C and Si layers. For example, in the lower crack, the C-surface (lower surface) relaxation appears to be more complete compared to that on the Si-surface which still shows

some separation among the Si and C atoms.

The foregoing results show that brittle fracture has occurred on the $\{1\bar{1}1\}$ shuffle plane. This is not unexpected considering that the unrelaxed surface energies, given in Table3.6, show that the shuffle $\{111\}$ plane is indeed the one with lowest energy. The only literature value of surface energy, available for $\{111\}$, is $2180 erg/cm^2$ [78].

5.5 Discussions

We have presented a molecular dynamics simulation study of mechanical stability of β-SiC under hydrostatic tension using a potential model which has provided an adequate description of the properties around the equilibrium state. Although the explicit effects of external loading on the stability criteria, which were previously shown to be critical in predicting the stability of a ductile close-packed structure [15], are found to be unimportant here, we have nonetheless confirmed that the observed onset of instability and the nature of the unstable deformation for an open structure stabilized by covalent bonding can be predicted from generalized stability criteria.

In contrast to the structural responses in an fcc lattice with metallic bonding, a decidedly ductile system[15], we find essentially brittle behavior. As a consequence of a spinodal instability which apparently then triggers considerable shear deformation as shown in Figure 5-7(c) and (d), a crack is nucleated as demonstrated in Figure 5-8. By examining the potential energy response during the period of bond rupturing and propagation (cf. Figure 5-7(e)) we can discern energy lowering processes which we associate with relaxation of the newly created crack surfaces and with internal (bulk) relaxation resulting from the reduction of normal stresses. From the rapid build up of the von Mises shear stress during this period, we surmise that shear-tension coupling effects[96] are more important in systems with strong angular forces. Finally we should keep in mind that once the system has become inhomogeneous, one needs to beware of possible artifacts associated with the periodic boundary condition and finite system size. Thus, more work along the lines of the present study is needed to confirm the physical meaningfulness of our results pertaining to the system response

after crack initiation.

A result which lies beyond the domain of stability analysis is the observation of decohesion in the form of cracking on the $\{1\bar{1}1\}$ shuffle plane. While this is self consistent with respect to the potential model, the expected cleavage plane for zinc blende structure materials such as SiC is expected to be $\{110\}$ [8]. This is in contrast with the known cleavage plane $\{111\}$ for diamond cubic materials such as Si and C. The difference lies in the charge transfer effects in zinc blende crystals when bonds are broken [97]. Charge transfer produces an electrostatic interaction which raises the surface energy of non-neutral planes, including $\{111\}$. As a result, the neutral plane $\{110\}$ becomes the lowest energy plane. However, it is not obvious that β-SiC should be treated as a typical zinc blende material given that bonding in this lattice is basically covalent in nature, with only a small ionic component (12%) [6]. We believe this issue deserves further study.

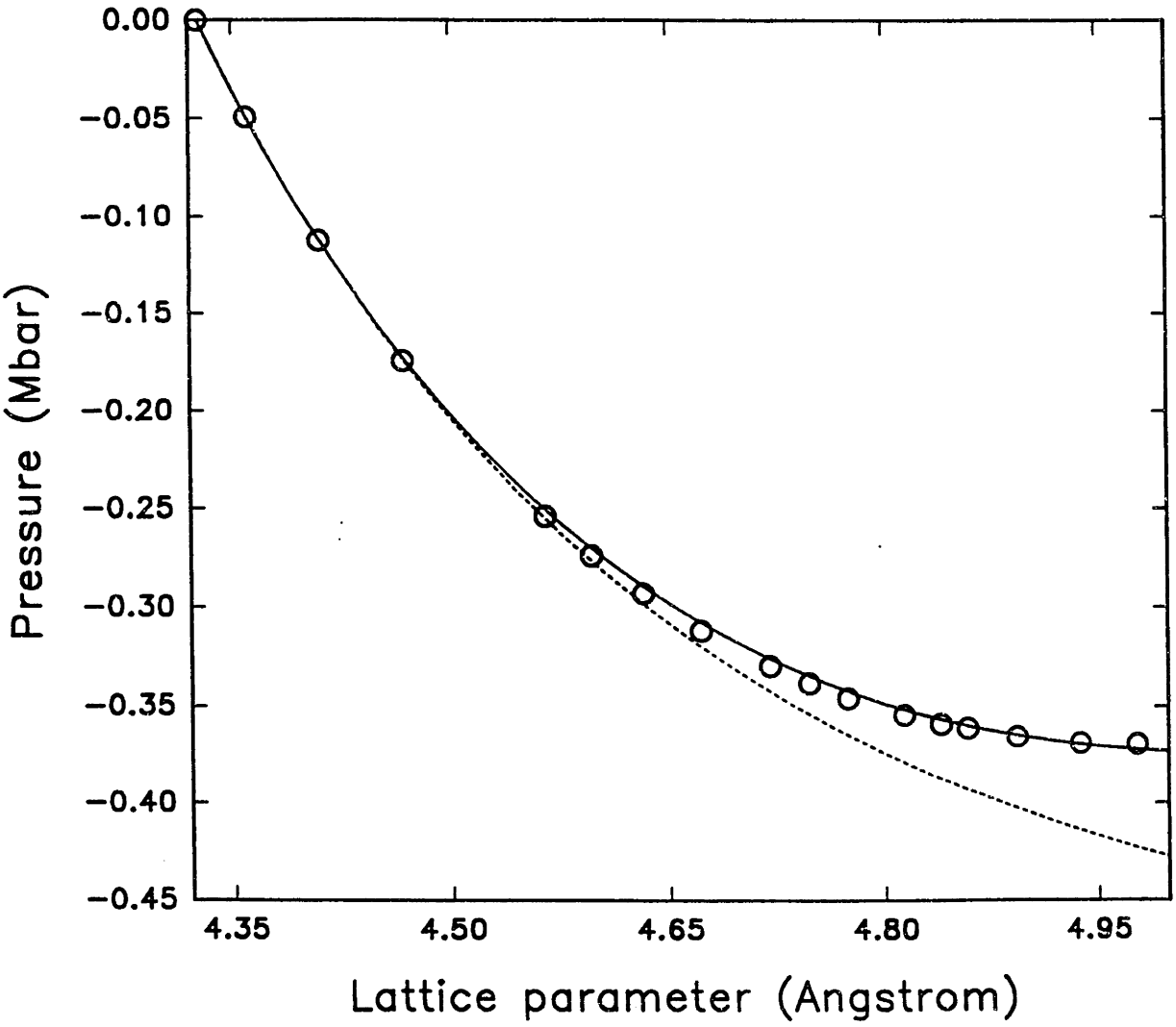

Figure 5-1: Pressure-lattice parameter relation for β-SiC at $300K$ simulated using the modified Tersoff potential (open circles); fitted equations of state are Birch-Murnaghan (solid line) and Murnaghan (dashed line).

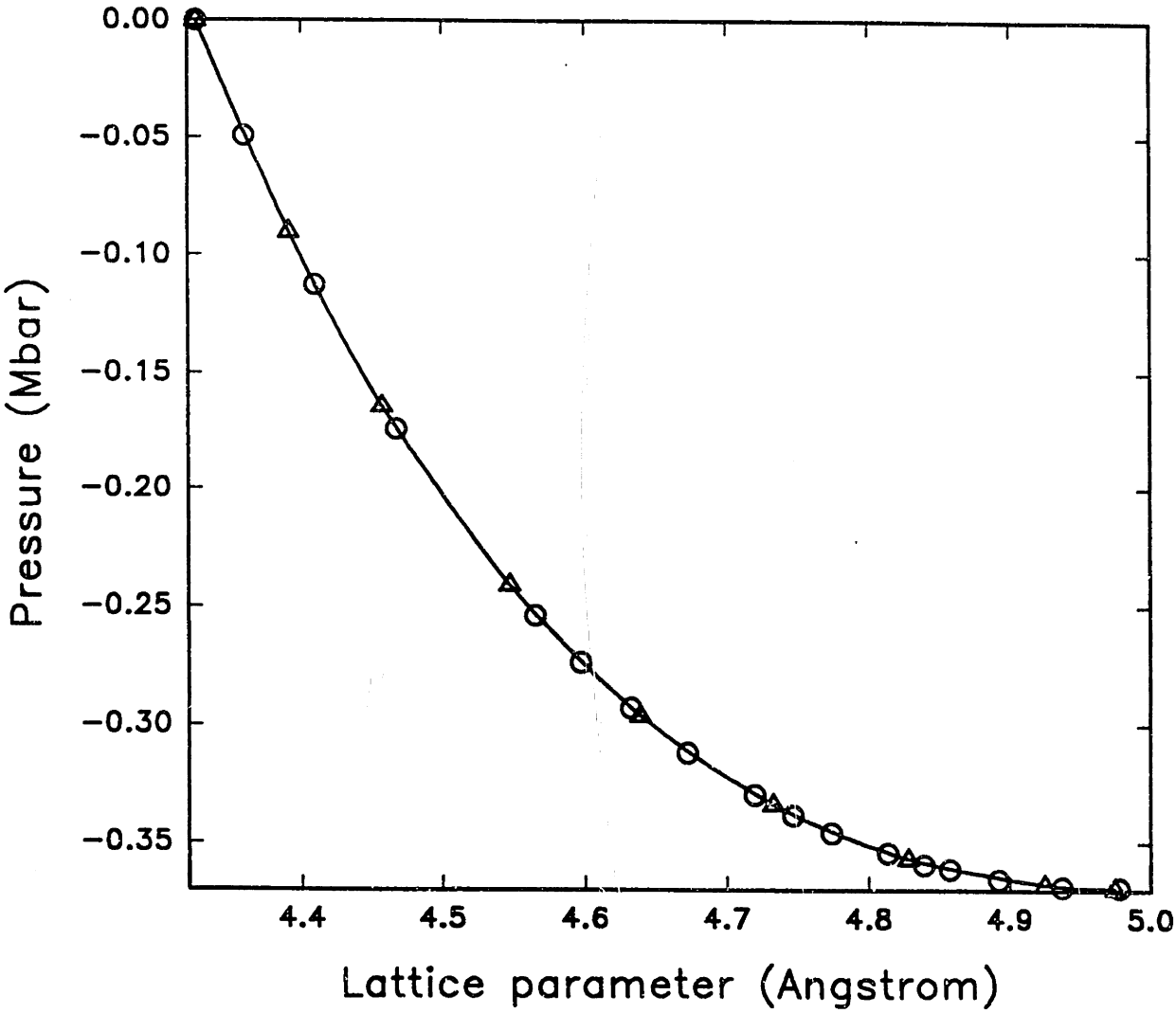

Figure 5-2: Pressure-lattice parameter relations for β-SiC at $300K$ obtained using two different simulation methods, tensile straining (open triangles) and applied hydrostatic tension (open circles).

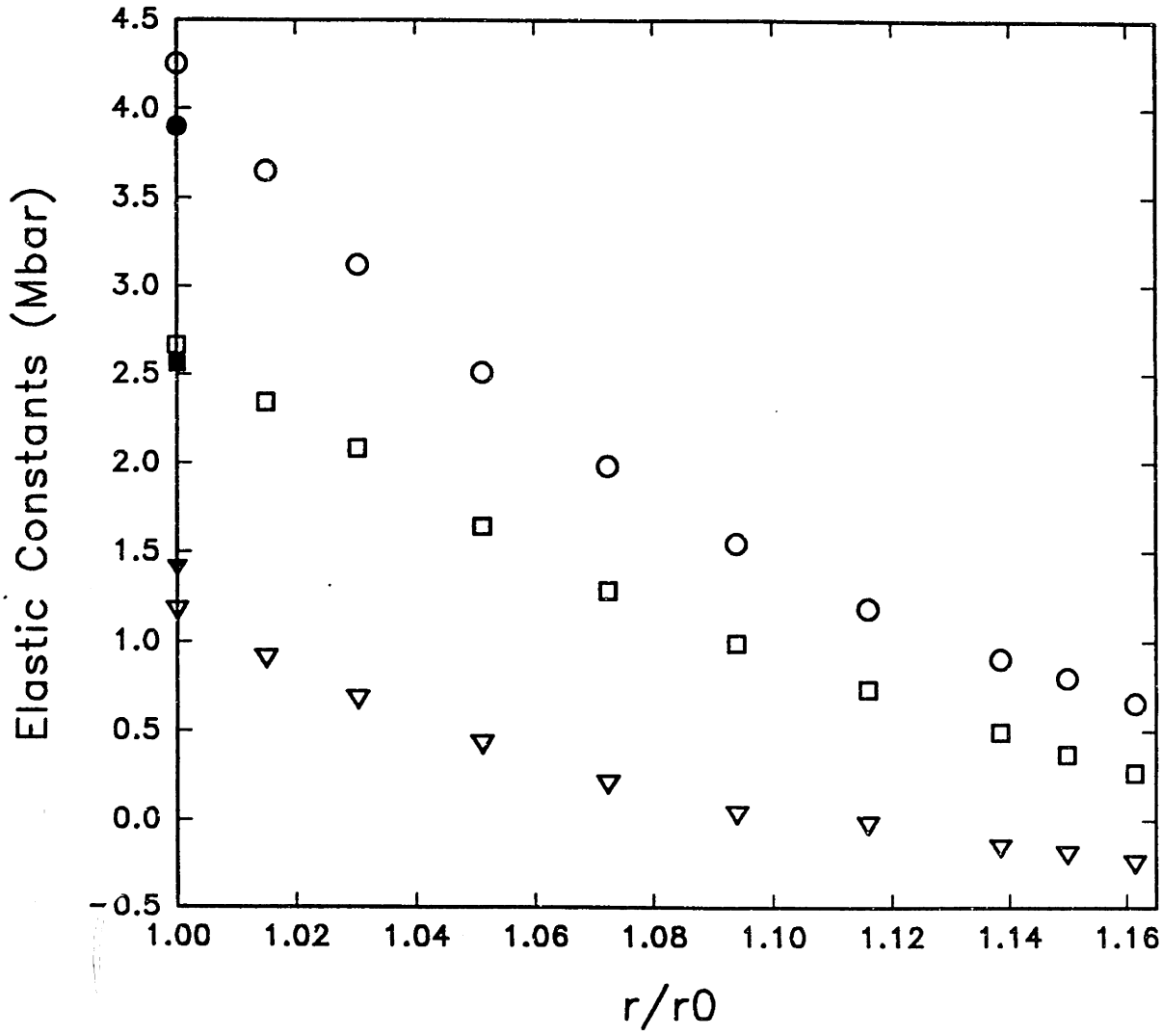

Figure 5-3: Current elastic constants of β-SiC at $300K$ at various states of dilatation (r/r_0) calculated using the modified Tersoff potential. Open circles: C_{11}, open triangles: C_{12} and open squares: C_{44}. Filled circle, triangle and square are experimental values of C_{11}, C_{12} and C_{44}.

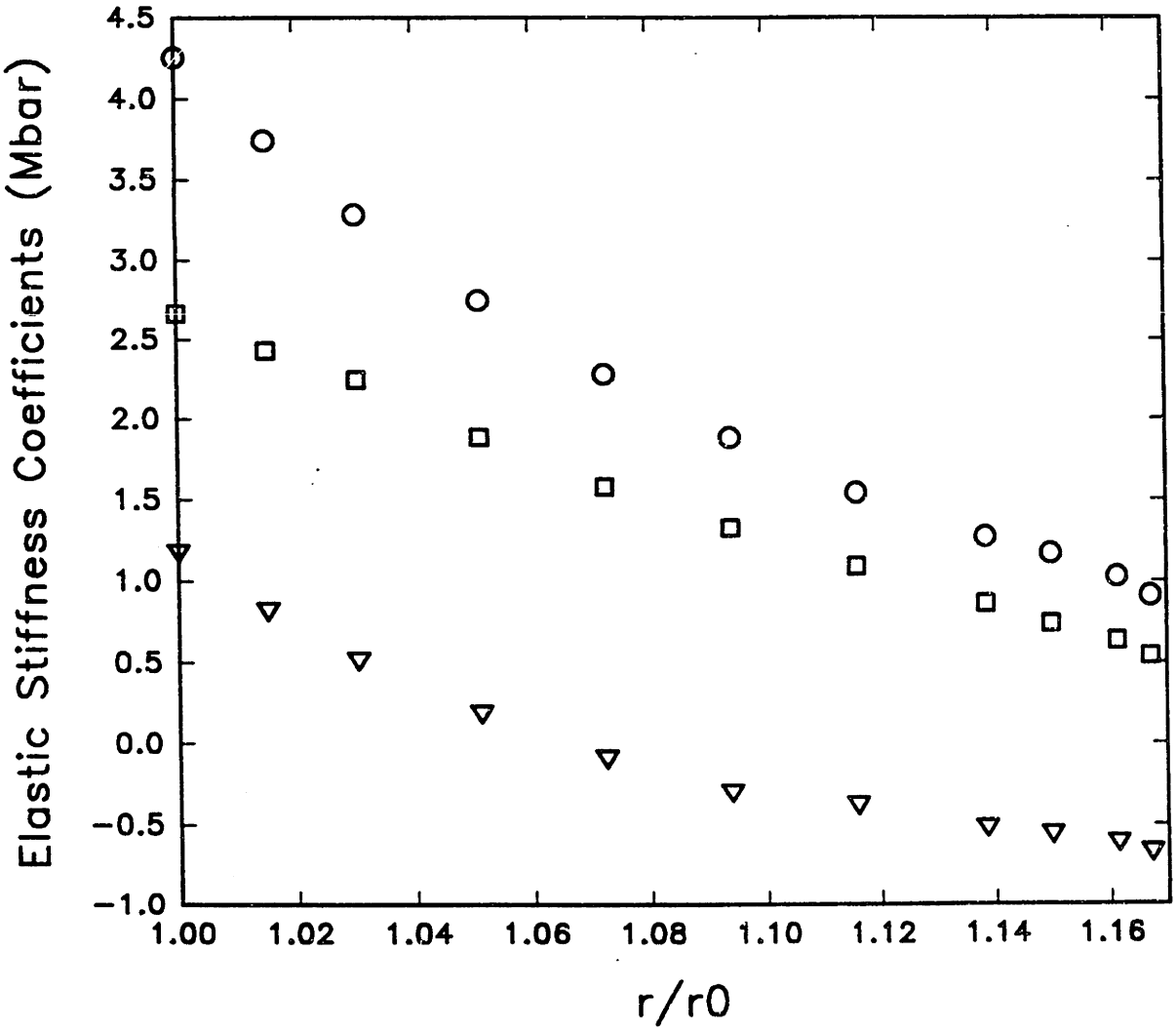

Figure 5-4: Current elastic stiffness coefficients corresponding to Figure 5-3.

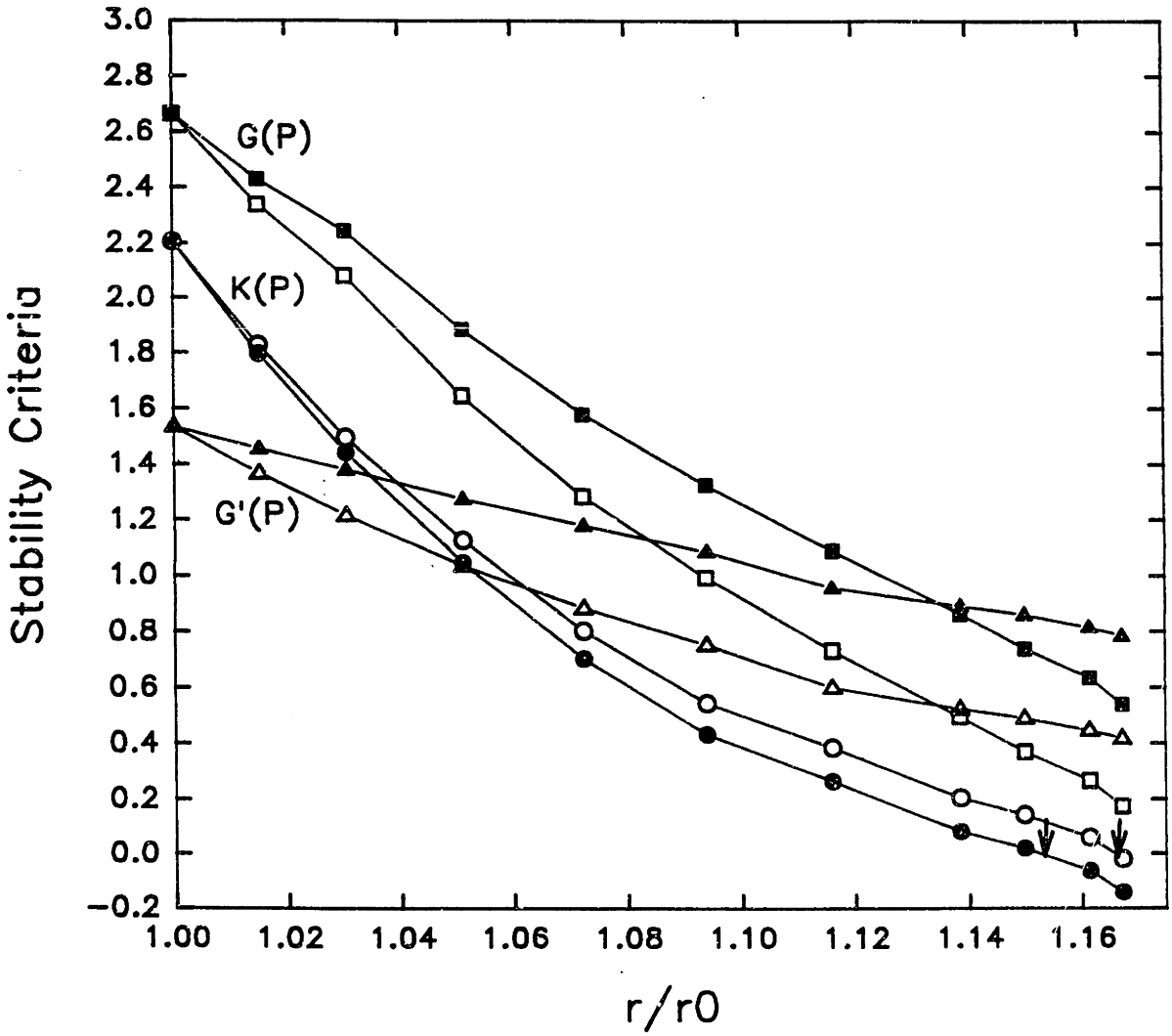

Figure 5-5: Elastic stability criteria based on stiffness coefficients of Figure 5-4 and elastic constants of Figure 5-3. Closed symbols are from stiffness coefficients and open symbols are from elastic constants. Arrows indicate where the spinodal stability is violated. Lines are drawn to connect the data points.

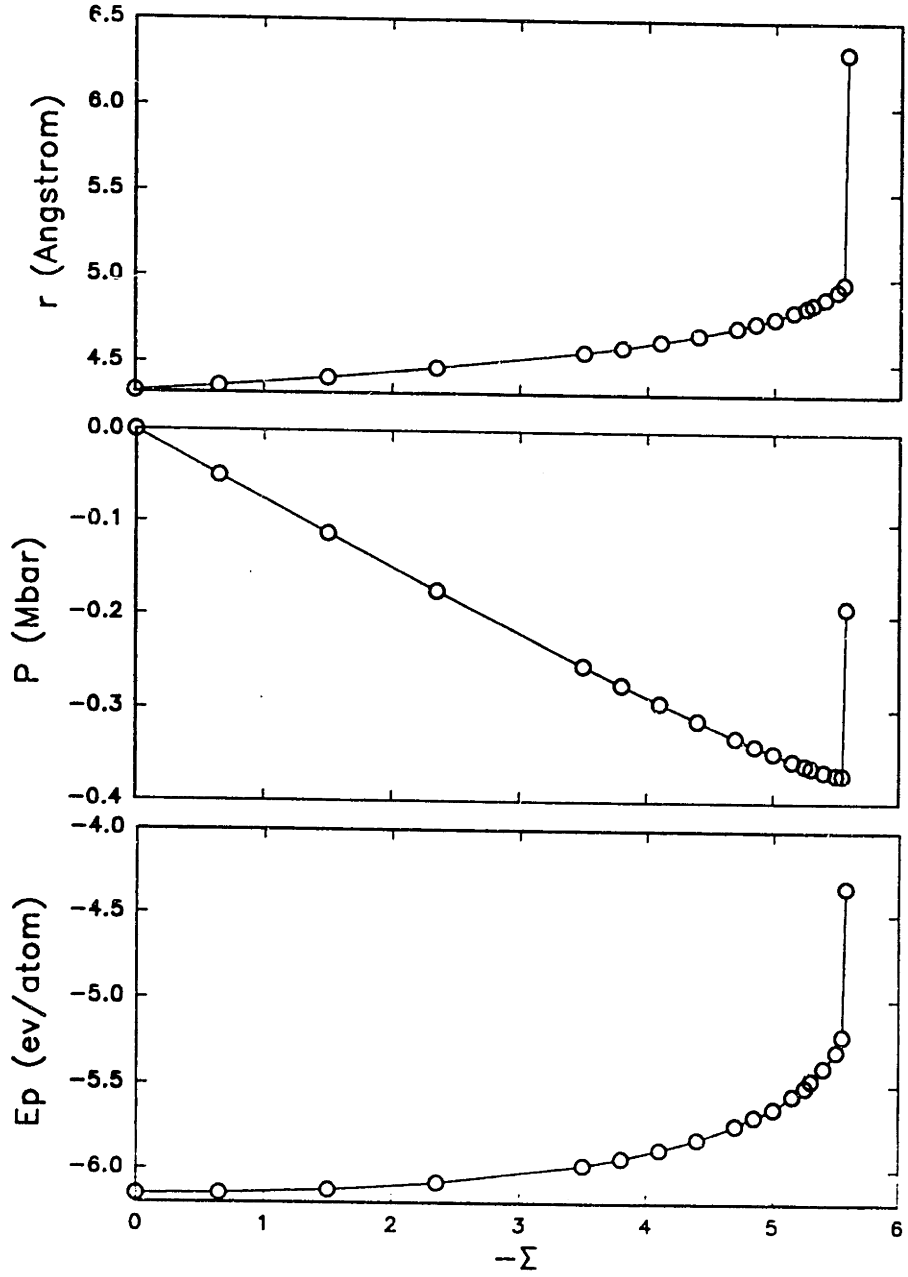

Figure 5-6: System responses of β-SiC at $300K$ to applied hydrostatic tension simulated using the modified Tersoff potential. Results for internal pressure P, potential energy Ep, and lattice parameter r are values averaged over the length of each simulation run except for the last point where the system has become unstable and continued to change in time.

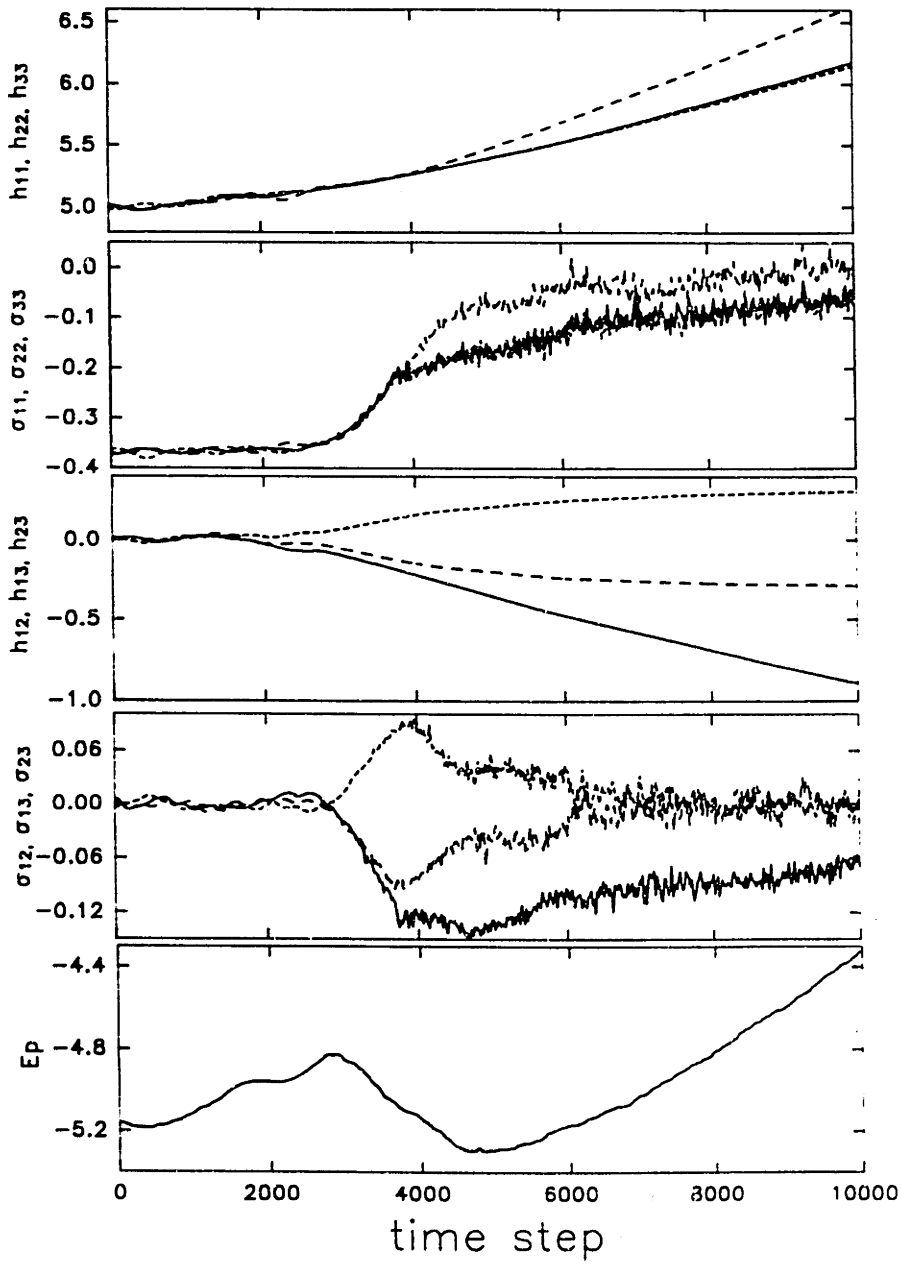

Figure 5-7: Time-dependent system responses at $\Sigma = 5.575$, from top to bottom are (a) diagonal elements of h matrix (in unit of $\mathring{A}$), (b) diagonal elements of stress tensor (in unit of *Mbar*), (c) off-diagonal elements of cell matrix (in unit of $\mathring{A}$), (d) off-diagonal elements of stress tensor (in unit of *Mbar*), (e) potential energy per atom (in unit of *ev*).

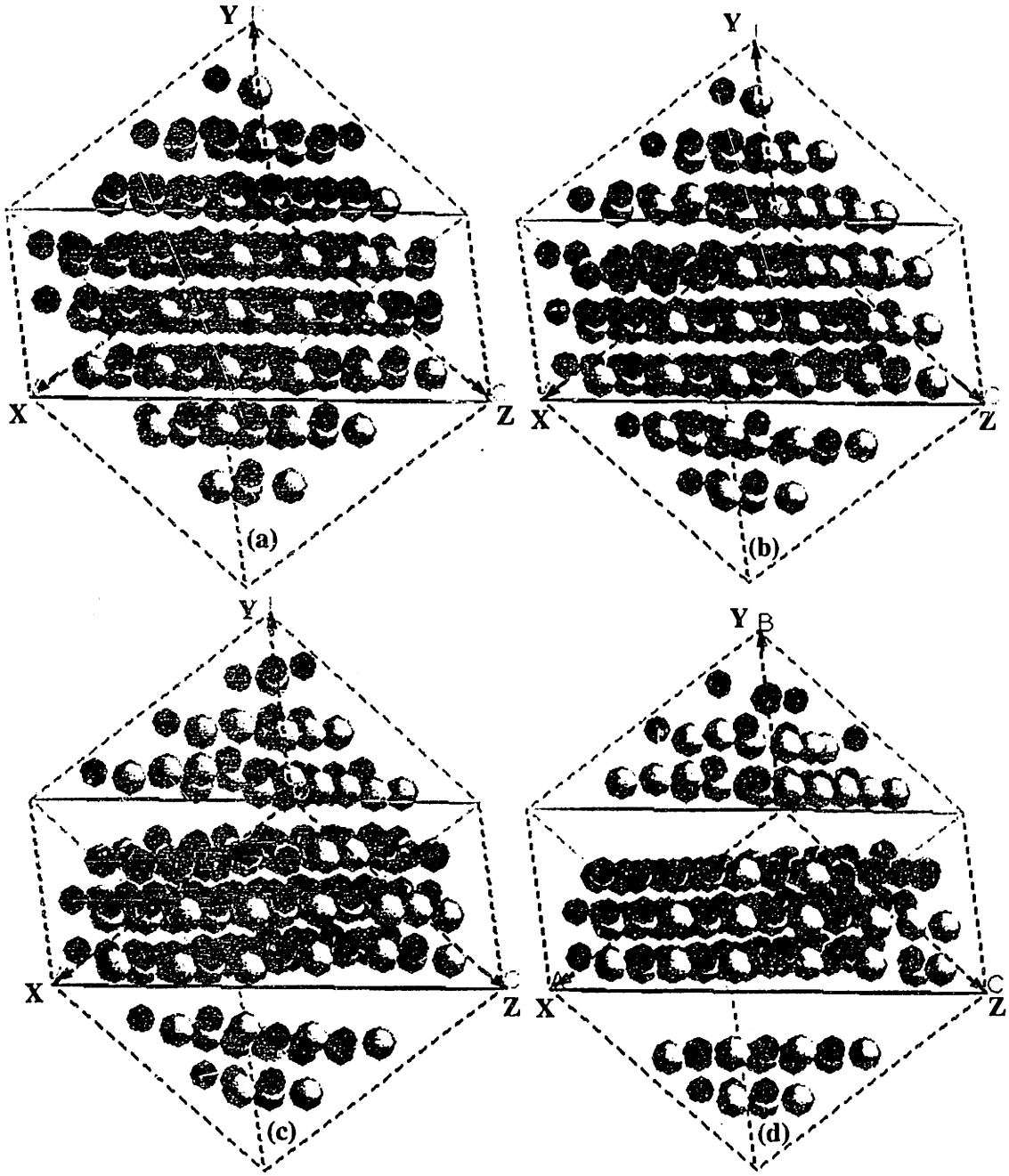

Figure 5-8: View of simulation cell showing instantaneous atomic configurations at several instants during simulation at supercritical tension. C and Si atoms are shown as dark and light spheres, respectively. X, Y and Z are along [100], [010] and [001] respectively. Two solid lines in the middle are $\{1\bar{1}1\}$ planes that are perpendicular to the plane to the paper. (a) at $0.3ps$ into the simulation (time step 2000) after applying a small step increase in tension, prior to the onset of instability; (b) at about $0.15ps$ later (time step 3000) when interplanar decohesion has occurred; (c) at about $0.06ps$ later (time step 3400) than (b) showing two well-defined crack propagations and indications of atomic relaxation on the crack surfaces; (d) at another $0.09ps$ later (time step 4000) showing two relatively clean cracks with relaxed surfaces.

Chapter 6

Solid-State Amorphization of β-SiC under Hydrostatic Compression

6.1 Introduction

Solid-state crystalline-amorphous transformation was first observed in the 70s and early 80s. Since then, solid-state amorphization has received considerable attention[98][99] due to the non-conventional method it offers to produce bulk amorphous materials and the intellectually challenging questions it raises in terms of understanding the underlying mechanisms and characteristics of the process. It has been found that a variety of irradiation-, chemically-, and mechanically-driven processes are able to transform a crystalline material into an amorphous solid. Currently, pressure-induced crystalline-amorphous phase transformation is receiving renewed attention because new experimental evidence has been observed in a number of ionic crystals[100][101][102] as well as in a binary covalent material [103]. New understanding of the driving force for such phase transformations has been obtained[104] [105]. Several studies[100][102][103] have suggested that pressure-induced amorphization is a kinetically frustrated phase transformation; while the study by Binggeli and Chelikowsky [104] has suggested

that pressure-induced amorphization is triggered by the onset of the lattice shear instability.

Since the lattice instability of a crystal can be clearly analyzed by the new formulation of the elastic stability criteria[15][16]that we derived in Chapter 4, we here present a study of the lattice instability of β-SiC and its structural response under high pressure. This study is motivated by our general interest in understanding the mechanical behavior of SiC under various stress conditions, such as tension (see Chapter 5) and compression. It is also one of the series studies of applying the new instability criteria to investigate the structural transitions of metal, covalent materials and intermetallic compounds[15][16][83][23][22], among which the study on diamond cubic Si lattice has revealed that Si undergoes a phase transition from diamond cubic to β-tin under compression[23]. While β-SiC and Si are both tetragonally bonded covalent materials, an additional effect of chemical ordering exists in β-SiC due to the fact that two types of atoms are involved in the β-SiC lattice. The chemical ordering effect can be classified by two controlling factors, i.e., the atomic size difference and the chemical preference of mixed bonds [25]. Due to the chemical ordering effect, it is possible that different behavior of β-SiC could exist under compression compared to Si. Because of these considerations, we believe that it is important to study the structural transition of β-SiC under compression by combining the elastic instability criteria with molecular dynamics simulations, and with our special focus on the roles played by the chemical ordering effect in the transition.

Using the modified Tersoff potential (see Chapter 2 and 3), we have obtained the elastic constants and the equation of state of β-SiC at room temperature. These results agree well with experimental data. We have also successfully applied this potential in studying the structural response of β-SiC under tension (Chapter 5), where we observe crack nucleation and brittle fracture when the spinodal instability criterion is violated. In this chapter, we use the modified Tersoff potential to study the instability and structural response of β-SiC under hydrostatic compression. In Sec. 6.2, we first perform a constant temperature and constant pressure (HτT) simulation of the structural response of β-SiC under hydrostatic compression, where we observe

pressure-induced amorphization of β-SiC at room temperature. The amorphous SiC thus obtained recovers its original crystal structure upon release of pressure, which is in analogy with the 'memory glass' effect discovered by Kruger and Jeanloz in their experiment[100]. We will show that the critical pressure at which amorphization occurs in simulation can be well predicted by the elastic instability criteria that will be derived in Sec. 6.3. It is found that the shear instability is the underlying mechanism of amorphization. This is similar to the result of Binggeli and Chelikowsky[104]. In Sec. 6.4, we investigate the roles of chemical ordering in amorphization of β-SiC by modifying the potential in such a way that we can probe the atomic size effect and the chemical preference effect separately. We will identify that the atomic size effect is essential for the amorphization of β-SiC. Finally, in Sec. 6.5, we summarize the significance of this work and discuss some unsolved issues.

6.2 Simulation of Hydrostatic Compression

Using the modified Tersoff potential and the generalized MD simulation technique developed by Parrinello-Rahman[30], we perform a constant temperature and constant pressure simulation of β-SiC under compression. We employ a cubic crystal of β-SiC with 216 atoms subjected to the periodic boundary conditions. We use an initial time step of $\delta t = 1.451 \times 10^{-4} ps$ and a time step of $\frac{1}{3}\delta t$ when the system is close to a critical point. Using the Parrinello-Rahman simulation technique, we impose external hydrostatic compression incrementally to the system. At each applied loading, we allow the system to respond to the loading and reach its new equilibrium state after about 20,000 time steps. For each equilibrium state, we use another 20,000 time steps for the system to relax and to calculate the properties of internal pressure (same as the applied pressure at equilibrium), potential energy, volume and structure factor $s(k)$. The structure factor is defined as

$$s(k) = |\frac{1}{N}\sum_i [\cos(\vec{r_i}\cdot\vec{k}) + i\sin(\vec{r_i}\cdot\vec{k})]|^2 \tag{6.1}$$

where $\vec{k}$ is chosen to be a constant wavevector $\frac{2\pi}{a}(1,1,1)$. The structure factor is a standard function to characterize the ordering of a system. For a perfect β-SiC crystal, $s(k)$ is normalized to be 0.5 for $\vec{k} = \frac{2\pi}{a}(1,1,1)$. For a β-SiC crystal under thermal fluctuations, $s(k)$ is smaller but very close to 0.5. Figure 6-1 shows the overall system responses to the applied compression as a function of the internal pressure P. As can be seen in Figure 6-1, all properties exhibit an abrupt change at the end of each curve. The last points in each curve correspond to a state which is obviously different from other states along the curve. We call this state B, and the state right before state B is called state A. State A is the last stable state of β-SiC under compression. As shown in Figure 6-1(a), the structure factor $s(k)$ suddenly drops to zero at state B. Correspondingly, we see an internal energy decrease in Figure 6-1(b) and a volume increase in Figure 6-1(c). All these suggest a change in the β-SiC structure at state B. The pressure at state B is $P_c = 707GPa$. In order to show more detailed change of properties of the system from state A to B, we plot the time-dependent system responses in Figure 6-2, where the mean square displacement (MSD) in the bottom plot is defined as

$$MSD(t) = \frac{1}{N}\sum_i [\vec{r_i}(t) - \vec{r_i}(0)]^2 \tag{6.2}$$

The MSD describes the mobility of atoms in the system and their averaged derivation from original equilibrium positions. For a solid, either crystalline or amorphous, MSD is a very small constant; while for a liquid the MSD increases almost linearly with time. In Figure 6-2, we can clearly see that, during the transition from A to B, the structure factor drops; the potential energy decreases; the volume increases; the diagonal elements of cell matrix h increases; the off-diagonal elements grow to non-zero values; and the mean square displacements for both Si and C atoms jump from one constant to another. Combining these data, we conclude that a structural transition of β-SiC to another solid structure has taken place. During the transition, the appearance of non-zero components of the off-diagonal elements of h indicates shear deformation. It is of particular interest to compare the detailed data of the cell

volume and the cell matrix off-diagonal elements in order to identify whether shear deformation precedes over volume expansion or vice versa. We carefully examine the volume and the off-diagonal elements of h_{12}, h_{13} and h_{23} in Figure 6-2(c) and (e), and we plot the corresponding data in the time step range of 12000 to 15000 in Figure 6-3. As we can clearly see in Figure 6-3, the off-diagonal elements begin to grow to non-zero values at step 12200, while the volume expansion occurs at step 12560. This suggests that the shear deformation occurs before the volume expansion. This information will be used in Sec. 6.3 to verify the instability eigenmodes.

In order to examine the final structure at state B, we plot the atomic configuration projections along x, y and z directions in Figure 6-4, and the radial distribution functions between $Si - Si$, $C - Si$ (same as $Si - C$) and $C - C$ in Figure 6-5. The atomic configurations show a completely disordered structure at state B. The radial distribution functions show that $g(r)$ goes to 1 as r approaches large distances, which means that the system has lost its long range order completely. The lack of long range order is a characteristics of an amorphous structure. Thus, these results strongly suggest that structural transition shown in Figure 6-2 represents a crystalline-amorphous phase transformation. In other words, pressure-induced amorphization of β-SiC under compression has been observed in our simulation.

To understand the amorphous structure in more detail, we have calculated the coordination numbers of atoms by integrating the area under the first peak of the radial distribution function of Si-C. We find that each Si (or C) atom is still four-fold coordinated by C (or Si) atoms. However, the local tetrahedral geometry is distorted. In Figure 6-6, we plot the distributions of number of atoms at distance r_{ij}, the tetrahedral angle θ_{ijk} and the potential energy E_p before and after amorphization respectively. Before the amorphization, the system is in its crystalline structure and all properties are sharply peaked around their equilibrium values. The distances between nearest atoms are peaked at $1.45\mathring{A}$; the tetrahedral angles are peaked at the perfect tetrahedral angle of 109.47°; the potential energy of Si atoms is $-1.55(eV)$ and the potential energy of C atoms is $1.6(eV)$. The broadening of the distributions in all of the distributions is due to thermal fluctuations. In contrast, in the amorphous

SiC, although every Si (or C) atom is still 4-fold coordinated with C (or Si) atoms, the nearest neighbor distances, the tetrahedral angles and the cohesive energies of atoms have much broader distributions, especially for the tetrahedral angle and the potential energies. The nearly flat distribution of the tetrahedral angles over several tens of degrees suggests a randomly distorted structure.

To further study the pressure-induced amorphous SiC at state B, we let the system relax for another $30,000$ steps under P_c. We find that the system is very stable with all of the properties fluctuating around their equilibrium values. We then release the applied pressure to zero and let the system respond. Figure 6-7 shows the time-dependent responses of the system after the pressure release, where we also plot the data of equilibrium properties of β-SiC under zero pressure at room temperature by circles at time step 30000. We find that the structure factor $s(k)$ increases from 0 to 0.2. This suggests that the SiC structure has partially recovered its original β-SiC crystalline structure. We also observe that the volume increases and the potential energy decreases. At the end of the figure, the volume and the potential energy of the system are close to the values of β-SiC. Furthermore, by examining the atomic configuration shown in Figure 6-8 and the radial distribution functions in Figure 6-9 after the release of pressure, we find that the amorphous SiC has indeed partially recovered its original β-SiC crystal structure. The degree of the recovery can be increased by thermal annealing. Figure 6-10 shows the $g(r)$'s of the system after annealing at $1000K$. The peak positions and the overall shape agree well with the $g(r)$ of crystalline β-SiC at the same temperature. These results indicate that the pressure-induced amorphous SiC has a 'memory' effect. Unlike the amorphous SiC formed by conventional melting and quenching method, pressure-induced amorphous SiC 'remembers' its original crystal structure before amorphization. Experimentally, similar 'memory' effect has been observed in $AlPO_4$ by Kruger and Jeanloz[100]. An explanation of this 'memory glass' effect will be given in the next section.

6.3 Shear Instability Driven Amorphization

So far, we have shown that β-SiC undergoes pressure-induced amorphization under compression. In order to elucidate the driving force of the amorphization, we have carried out the elastic stability analysis using the new criteria derived in Chapter 4. First, we perform the stability analysis at $0K$ and identify that the instability mechanism of β-SiC under compression is the shear instability. Secondly, we calculate the shear instability criterion at $300K$ to estimate the critical pressure and compare the result with that obtained from direct simulation described in the last section.

In Chapter 3 we have shown that the elastic constants of β-SiC do not change significantly in the temperature range between $0K$ and $300K$. Therefore, we believe that the instability mechanism of a crystal will not change in this narrow temperature range, although the critical pressure (or critical strain) at which the instability will occur will vary with temperature; and the higher the temperature is, the lower the transition pressure will be. Thus, we first perform a stability analysis of β-SiC at $0K$ to investigate which instability criterion is violated under compression. We calculate the elastic constants C_{11} and C_{12} at $0K$ using their Born terms in the fluctuation formulae (see Chapter 2). Then, using the relation between the stiffness coefficients and elastic constants

$$B_{11} = C_{11} - P \quad B_{12} = C_{12} + P \tag{6.3}$$

we obtain B_{11} and B_{12}. Since the Born term of C_{44} does not take into account the contribution of the internal strain relaxation, we use the method of direct stress-strain calculation plus static relaxation (described in Chapter 2) to obtain B_{44}. In the Voigt notation, the stress-strain relation for B_{44} is

$$B_{44} = \frac{1}{2}\frac{\partial \sigma_{23}}{\partial \epsilon_{23}} \tag{6.4}$$

where σ_{23} is the microscopic stress under the imposed strain ϵ_{23} after internal strain relaxation; ϵ_{23} is a small strain calculated by using each compression state as the

reference state. If the reference state is the zero pressure state, Eq.(6.4) yields C_{44}. If r_0 is the zero pressure lattice constant, and r is the current lattice constant at a compression state, we can calculate B_{11}, B_{12} and B_{44} for each r/r_0 using Eq.(6.3) and Eq.(6.4). The results are shown in Figure 6-11. We find that both B_{11} and B_{12} increase under compression, while B_{44} increases first, then bends over and decreases. Recall the three instability criteria for a cubic crystal derived in Chapter 4

$$K(P) = (B_{11} + 2B_{12})/3 \tag{6.5}$$

$$G'(P) = (B_{11} - B_{12})/2 \tag{6.6}$$

$$G(P) = B_{44} \tag{6.7}$$

we have calculated the three criteria for β-SiC under compression at $0K$ and the results are shown in Figure 6-12(a). It delineates that under compression, the spinodal instability criterion $K(P)$ and the tetragonal shear instability G' increase, whereas the shear instability $G(P)$ increases first, then decreases to zero at $r/r_0 = 0.734$. This corresponds to a critical pressure of $P_c = 1156GPa$. Therefore, $G(P)$ is the only instability criterion that has been violated under compression and hence the instability mechanism of β-SiC under compression is the shear instability.

In order to determine the critical pressure at $300K$ when the shear instability is violated, we first calculate the elastic constant C_{44} of β-SiC at $300K$ using the fluctuation formulae given in Chapter 2. Then, we use

$$B_{44} = C_{44} - P \tag{6.8}$$

to obtain B_{44} which is the shear instability criterion $G(P)$. To calculate the contributions of individual terms to the shear instability, we write

$$G(P) = C_{44} - P = C_{44}^B + C_{44}^S + C_{44}^K - P \tag{6.9}$$

where C_{44}^B is the Born term; C_{44}^S is the stress fluctuation term and C_{44}^K is the kinetic term. The kinetic term is usually negligible since it is smaller than other terms by

orders of magnitude. The results of the Born term, the fluctuation term and the shear instability criterion $G(P)$ of β-SiC under compression at $300K$ are plotted in Figure 6-13. We find that the Born term increases linearly as pressure increases because the interaction between atoms become stiffer. The fluctuation term, on the other hand, first decrease slowly with pressure to a certain point, and then decreases much faster. The significant decrease of this term brings the total $G(P)$ to zero under compression. Since the stress fluctuation term takes into account the contribution to the elastic constant due to the internal strain relaxation, if a shear strain is imposed to the system, the higher the applied pressure, the larger is the internal strain relaxation. With the continuous increase of pressure, the internal strain relaxation reaches a point beyond which it causes the system to be unstable. Thus, the internal strain relaxation is responsible for the vanishing of the shear instability under compression. The critical pressure where $G(P)$ goes to zero is determined to be $P_c = 714GPa$ from Figure 6-13(c), which is in close agreement with the value of $P_c = 707GPa$ obtained from the direct simulation described in Sec. 6.2. This is convincing evidence that the pressure-induced amorphization of β-SiC observed in simulation is triggered by the vanishing of the shear instability.

We can further confirm that the pressure-induced amorphization is triggered by the shear instability by studying the mode of deformation corresponding to the shear instability. As discussed in Chapter 2, the expected eigenmodes corresponding to the shear instability should be shear deformation with volume conservation. We show in Figure 6-3 that this is indeed the case, i.e., shear deformation precedes volume expansion at the beginning of the structural transition. It is important to point out that for unstable structural transitions triggered by the elastic instability, instabilities could occur successively[15] during the transition. In other words, once a structural transition has taken place, other new instabilities may set in. Strictly speaking, the new criteria should be calculated based on the new structure after the initial structural transition. It is thus difficult to clearly identify all eigenmodes during the whole transition process due to the fact that different eigenmodes related to different criteria may follow each other closely. Nonetheless, the eigenmodes of the instability

that is violated first can always be clearly identified at the very beginning of the structural transition.

The shear instability driven amorphization process that we have observed can be considered as a kinetically frustrated phase transformation. Recall that in Chapter 3, we have predicted a transition of β-SiC from zincblende to rocksalt structure at a critical pressure of $P_t = 649GPa$ based on thermodynamic stability, i.e., free energy calculations. However, our simulations presented above have demonstrated that β-SiC undergoes an order to disorder transition under compression instead of the transition to rocksalt structure. The critical pressure for amorphization is $P_c = 707GPa$, which is higher than P_t. This indicates that the process of the pressure-induced amorphization in β-SiC observed at $300K$ is a frustrated phase transformation. Because of the relatively low thermal fluctuation and the fact that no defects of any kind exist in the simulation system, the phase transformation to rocksalt structure at the lower pressure ($P_t = 649GPa$) is impeded thermodynamically. The system is forced to go beyond this thermodynamic instability point until eventually reaches its elastic shear instability that results in amorphization.

The above scenario can help to explain the 'memory glass' effect described in Sec. 6.2 in a simple manner. The originally crystalline β-SiC is compressed beyond its thermodynamic stability limit at P_t. At a higher pressure P_c, β-SiC finally becomes unstable and transforms to the amorphous structure through the deformation triggered by the shear instability. Because of small thermal fluctuation at room temperature, atoms cannot move too far away from their positions in the original crystal structure. In particular, diffusive motion is precluded. This is evidenced by the fact that the coordination number of atoms remains 4-folded between Si-C as described in Sec. 6.2. Therefore, atoms simply randomly displace themselves around their original crystallographic sites. From the mean square displacements in Figure 6-2(f), we find that during the amorphization process, atoms move by about $20 - 30\%$ of an interatomic distance on average. So when the pressure is released, it is natural for the atoms to slip back to the lowest free energy state, i.e., the original β-SiC crystalline structure. This process results in the so called 'memory glass' effect. Therefore,

we believe that the key factor in 'memory glass' effect is diffusive motion of atoms. That is, if no significant long-range diffusive motion occurs, the coordination number of atoms will remain unchanged, and this conservation in coordination number can be considered as a signal for the 'memory glass' effect. If the coordination number changes after the transition, it will usually be impossible for the system to exhibit the 'memory' effect. This interpretation is supported by a study of pressure-induced amorphization of α-quartz[104], where the coordination number changes from 4 to 6, and no 'memory' effect of the crystalline structure has been observed.

The fact that no significant diffusive motion of atoms has occurred during the sudden amorphization process of SiC is also consistent with the potential energy decrease as shown in Figure 6-2, which is in contrast to the expected potential energy increase for normal order to disorder transitions. At the highly compressed state before the transition, the potential energies for atoms to stay at their crystalline sites are very high. As soon as disordering takes place, atoms lower their energy significantly by simply shifting to nearby non-crystalline lattice positions. This is possible because the β-SiC is an open structure with considerable free space around each lattice position. However, if long-range diffusive motion is allowed, such as in melting, atoms can change coordination number (usually increase) and form new bonds with atoms that are initially far away before the transition. In the case of the binary system of SiC, two possibilities exist if the long-range diffusive motion is allowed. One is that significant new bonds will form between Si-Si or C-C besides the existing Si-C bonds to give an increase of the coordination number. The other is that new bonds between Si-Si or C-C will replace some of the previous bonds between Si-C to still conserve the total coordination number. In the latter case, however, the coordination number between Si-C will certainly change. In either case, the potential energy of the system will increase because the average binding energy between Si-Si or C-C is higher than that of Si-C by the heat of formation energy *per bond.* But in the amorphization process, the coordination number between Si-C remains unchanged and no significant bonding between Si-Si and C-C are formed. This is the reason that we have observed the decrease of the potential energy during the amorphization

process.

6.4 Chemical Ordering in Amorphization: Role of Chemical Preference and Atomic Size

Our observation that β-SiC undergoes amorphization under compression stands in clear contrast to the behavior of elemental crystal Si since the latter undergoes a polymorphic transition from diamond cubic to β-tin under compression[23]. In Figure 6-12(b), we show the instability criteria for Si. We find that under compression the spinodal instability $K(P)$ increases; while both the tetragonal shear instability $G'(P)$ and the shear instability $G(P)$ increase first, then decrease and drop to zero at certain compression states. The instability that is first violated in diamond cubic Si under compression is the tetragonal shear instability $G'(P)$. It reaches zero at $r/r_0 = 0.86$, which corresponds to a critical pressure of $P_c = 111GPa$. Thus, the instability mechanism of Si under compression is the tetragonal shear instability, as oppose to the shear instability of β-SiC. Since both Si and SiC are tetragonally bonded covalent materials, we believe that the additional effect of chemical ordering in β-SiC is responsible for the different instability mechanisms of the two materials under compression. Using the modified Tersoff potential, we are able to study the chemical ordering effect in β-SiC explicitly.

In β-SiC, chemical ordering is governed by two factors, i.e., the atomic size difference between Si and C atoms and the chemical preference of mixed bonds. The determination of the chemical preference is as follows. If the binding energy of a Si-C bond is $E(s_i - c)$, the binding energy of a Si-Si bond is $E(s_i - s_i)$ and the binding energy of a C-C bond is $E(c - c)$, then the chemical preference is defined as the energy of a Si-C bond relative to the mean of a Si-Si and a C-C bond in the diamond structures, i.e.,

$$\Delta H = E(s_i - c) - \frac{1}{2}[E(s_i - s_i) + E(c - c)] \tag{6.10}$$

By definition, the chemical preference is the same as the heat of formation energy per Si-C bond in β-SiC. Therefore, by adjusting the heat of formation of SiC, one can vary the chemical preference. It happens that in the Tersoff potential for SiC, a parameter χ is introduced purposely to adjust the heat of formation. The initial value of χ has been fitted by Tersoff using experimental data of the heat of formation energy[26]. Recall that in the Tersoff potential, the binding energy per pair of atoms is written as

$$V_{ij} = f_c(r)[A_{ij}exp(-\lambda_{ij}r) - B_{ij}\chi b_{ij}exp(-\mu_{ij}r)] \tag{6.11}$$

where χ is the extra parameter introduced for β-SiC to describe the heat of formation and chemical preference. For diamond cubic Si or diamond C, $\chi = 1$. Since

$$E(s_i - c) = \frac{1}{2}(V_{s_i-c} + V_{c-s_i}) \tag{6.12}$$

by varying χ in Eq.(6.11), we can change $E(s_i - c)$ in Eq.(6.10) and thus adjust the chemical preference ΔH. To eliminate the chemical preference in β-SiC by setting $\Delta H = 0$, we can continuously adjust the χ parameter until the condition $E(s_i - c) = \frac{1}{2}[E(s_i - s_i) + E(c - c)]$ is satisfied. Notice that as we change χ in Eq.(6.11), the equilibrium lattice constant r_0 will also be changed. Therefore, for consistency $E(s_i - c)$ to be used in Eq.(6.10) should be calculated by using the new equilibrium condition. In Table 6.1, we have listed the results of binding energies, χ values and equilibrium lattice constants corresponding to the SiC with zero heat of formation and the SiC with the original fitted value of heat of formation by Tersoff. The χ parameter has changed from its original value of 0.9776 to 0.9689 and the equilibrium lattice constant has changed from 4.32$\mathring{A}$ to 4.34$\mathring{A}$.

The second governing factor of the chemical ordering in $\beta - SiC$ is the atomic size difference. The experimental values of the covalent radii of Si and C in β-SiC are $R_c = 0.77\mathring{A}$ and $R_{s_i} = 1.17\mathring{A}$ respectively[6]. The difference is about 34%. In the Tersoff potential, no direct parameter controls the sizes of atoms explicitly. However, the atomic size effect is embedded in the bond-order parameter b_{ij}. To demonstrate

this point clearly, it is necessary to review the formulation of the Tersoff potential for β-SiC. Initially, Tersoff developed two potential functions for diamond cubic Si and diamond C respectively. By averaging the two sets of parameters and introducing the additional parameter χ, he later developed the potential function for SiC which is the one we have been using. While the parameters of A_{ij}, λ_{ij}, B_{ij} and μ_{ij} in Eq.(6.11) are averaged over those for Si and C, i.e.,

$$\begin{aligned} A_{c-s_i} &= \sqrt{A_{c-c}A_{s_i-s_i}}, \quad B_{c-s_i} = \sqrt{B_{c-c}B_{s_i-s_i}}, \\ \lambda_{c-s_i} &= \frac{\lambda_{c-c}+\lambda_{s_i-s_i}}{2}, \quad \mu_{c-s_i} = \frac{\mu_{c-c}+\mu_{s_i-s_i}}{2} \end{aligned} \tag{6.13}$$

the bond-order parameter b_{ij} is not averaged over b_{i-i} and b_{j-j}, i.e.,

$$b_{c-s_i} \neq \sqrt{b_{c-c}b_{s_i-s_i}} \tag{6.14}$$

Instead, b_{ij} remains the same functional form as that for Si or C in the diamond structures, depending if the central atom i is a Si or C atom. Recall that b_{ij} is defined as

$$\begin{aligned} b_{ij} &= (1+\beta_i^{n_i}\zeta_{ij}^{n_i})^{-1/n_i} \\ \zeta_{ij} &= \sum_{k\neq i,j} f_c(r_{ik})g(\theta_{ijk}) \\ g(\theta_{ijk}) &= 1 + c_i^2/d_i^2 - c_i^2/[d_i^2 + (h_i - \cos\theta_{ijk})^2] \end{aligned} \tag{6.15}$$

the parameters of β_i, n_i, c_i, d_i and h_i do not take the average values of i and j, but are only dependent on the type of the central atom i. Consider two geometric sets of interactive local atomic configurations similar to that shown in Figure 2-1, with all conditions (atomic positions and type of atoms) to be the same except that in one set the central atom is C and in the other set the central atom is Si. Based on the Tersoff potential, the values of b_{ij} calculated for the two atomic configurations will

be different, i.e.,

$$b_{c-j} \neq b_{s_i-j} \tag{6.16}$$

Since the only difference in the two configurations is the different atomic sizes of the central atoms, we conclude that the information of atomic sizes is embedded in the bond-order parameter b_{ij}. For the local tetrahedral configuration in a perfect β-SiC lattice, the values of the bond order parameters are $b_{c-s_i} = 0.866$ and $b_{s_i-c} = 0.937$. A direct consequence of Eq.(6.16) is that, in β-SiC,

$$V_{c-s_i} \neq V_{s_i-c} \tag{6.17}$$

Since the cohesive energies are

$$E_c = \sum_j V_{c-j}, \quad E_{s_i} = \sum_j V_{s_i-j} \tag{6.18}$$

for C and Si atoms respectively, we have

$$E_c \neq E_{s_i} \tag{6.19}$$

This means that in terms of the Tersoff potential, the cohesive energy is not equally divided between the two types of atoms. For the local tetrahedral configuration in a perfect β-SiC lattice, we obtain

$$\begin{aligned} V_{c-s_i} = -2.736(eV) \quad V_{s_i-c} = -3.451(eV) \\ E_c = -5.472(eV) \quad E_{s_i} = -6.902(eV) \end{aligned} \tag{6.20}$$

from calculations made at the equilibrium condition at $0K$. As shown by Eq.(6.20), $E_c > E_{s_i}$ based on the Tersoff potential.

The fact that the cohesive energy of a C atom is higher than that of a Si atom in β-SiC can be easily justified by simple electronic energy arguments. In the tight-binding

formulation of the cohesive energy of a covalent solid, one can write [86][97]

$$-U_{coh} = E_{pro} + V_0(r) - E_{bond}(r) \tag{6.21}$$

where $-U_{coh}$ is the cohesive energy *per atom*; E_{pro} is the promotion energy which stands for the energy increase of an atom when its two $2s$ and two $2p$ electron states form four sp^3 hybridized states; $E_{bond}(r)$ is the energy-lowering due to electron redistribution which leads to bond formation; and finally, $V_0(r)$ is the repulsive interaction between neighboring atoms due to their overlapping sp^3 states. Since both $E_{bond}(r)$ and $V_0(r)$ are functions of interatomic distances and are due to interactions between atoms, it is natural to equally divide $E_{bond}(r)$ and $V_0(r)$ between Si and C atoms. However, the promotion energy is an intrinsic property of each atom, therefore, the contribution to the cohesive energy from the promotion energy is different for different types of atoms. In other words, two atoms of the same type should have the same cohesive energy because their promotion energies are the same. But for two different types of atoms, they have different cohesive energies due to their different promotion energies. Since the promotion energies for Si and C are $E^{si}_{pro} = 3.52(eV)$ and $E^{c}_{pro} = 4.26(eV)$ respectively [97], from Eq.(6.21), we have $-U^{c}_{coh} > -U^{si}_{coh}$, which is in qualitative agreement with our result obtained from the Tersoff potential. Thus, we have shown that, in the Tersoff potential, the atomic size difference is embedded in the bond-order parameter b_{ij}, and this difference leads to the non-equal division of the cohesive energy between the two types of atoms (Si and C). The fact that the cohesive energy of C is higher than that of Si as obtained from the Tersoff potential can be properly justified by electronic energy consideration.

Atomic Size Effect on Elastic Constants

So far, we have demonstrated that both the atomic size effect and the chemical preference of mixed bonds can be properly treated by the Tersoff potential. The chemical preference can be directly controlled by the parameter χ in Eq.(6.11); while the atomic size difference is embedded in the bond-order parameter b_{ij}. In order to understand the different behavior of Si and SiC under compression, we investigate the

roles played by the atomic size and chemical preference in the process of amorphization of β-SiC. We believe that the major difference between the two materials is these two chemical ordering effects. We modify the Tersoff potential such that we can probe the atomic size and the chemical preference separately. We first keep the atomic size difference and vary the chemical preference. In order to compare the results with Si, we set the chemical preference ΔH to zero in SiC by choosing $\chi = 0.9689$ as given in Table 6.1. We call this modified Tersoff potential CP-SiC. This potential function keeps the atomic sizes the same as given by the original Tersoff potential, but suppresses the chemical preference to zero. On the other hand, we can allow the two types of atoms to have the same atomic size by setting the functional form of b_{c-j} to be the same as b_{s_i-j}. This will change the heat of formation energy if the χ parameter remains the same. In order to keep the same chemical preference, we must adjust χ as we modify the bond-order parameter so that the heat of formation remains the same as the original Tersoff potential. The new χ parameter is found to be 0.9407. By so doing, we create another modified Tersoff potential for SiC called AS-SiC, which keeps the chemical preference of the original Tersoff potential but removes the atomic size disparity. We have used these two modified potentials to study the elastic constants and the instability mechanisms of SiC under compression. The results obtained at $0K$ are summarized in Table 6.2.

From Table 6.2, we find that the properties calculated by the CP-SiC potential are very close to that of the original Tersoff potential. The instability mechanism under compression remains unchanged (shear instability). This suggests that the chemical preference does not play a dominant role in determining the instability of SiC under compression. On the other hand, using the AS-SiC potential, we obtain very different but interesting results. First, we find that the cohesive energy, lattice constant and bulk modulus remain unchanged. This is to be expected since we have left unaltered the heat of formation energy in the AS-SiC potential. Thus the cohesive energy and the lattice constant should not change. Also, since it is defined by the second derivative of the cohesive energy, the bulk modulus remains unchanged. Secondly, we find that, although the bulk modulus $B = \frac{C_{11}+2C_{12}}{3}$ remains unchanged, the elastic

constants C_{11}, C_{12} and C_{44} are affected significantly by the atomic size effect. As a result, at zero pressure, the relative magnitude of C_{44} and $(C_{11} - C_{12})$ has been reversed compared to that calculated from the original Tersoff potential. The direct consequence of this reversal is that under compression, the instability mechanism changes from shear instability $(C_{44} - P)$ to tetragonal shear instability $(\frac{C_{11}-C_{12}}{2} - P)$ once the atomic size disparity is suppressed in the Tersoff potential. This tetragonal shear instability is exactly the instability criterion violated in elemental Si under compression; and it is also the cause of the structural phase transition from diamond cubic to β-tin in Si.

Phase Transition vs. Amorphization

In order to investigate the consequence of the tetragonal shear instability in AS-SiC, we have performed molecular dynamics simulations using this modified potential function to elucidate the structural behavior of SiC under compression. Similar to the procedure in Sec. 6.2, we use the Parrinello-Rahman technique to apply pressure to the system incrementally. In Figure 6-14, we show the system responses to compression at $300K$. The state that corresponds to the last points in the figure is called state B, and the state right before B is called state A. At state B, we observe that the structure factor $s(k)$ drops to zero, the potential energy E_p decreases and the volume also decreases. The corresponding critical pressure is $P_c = 197GPa$. In Figure 6-15, we show the time-dependent variations of relevant properties from state A to B. In this figure, the evolution of the structure factor, internal energy, volume and diagonal and off-diagonal elements of the cell matrix h as a function of time can be clearly seen. In order to identify the eigenmodes of this transition, in Figure 6-16, we plot the detailed data of the volume V and the diagonal and off-diagonal elements of the cell matrix h within time steps between 0 to 10000. As labelled by circles in Figure 6-16(b), a bifurcation of diagonal elements of the cell matrix h occurs at time step 2500; while in Figure 6-16(a), the volume decreases after time step 5000; and in Figure 6-16(c), shear deformation occurs at time step 5800. Thus, during this transition, the bifurcation precedes the volume decrease and the shear deformation. In other words, at the very beginning of this transition, we see bifurcation of simula-

tion cell with volume conservation, which is exactly the expected eigenmodes derived in Chapter 2 corresponding to the tetragonal shear instability. Therefore, using the AS-SiC potential, we have observed a structural transition that is triggered by the tetragonal shear instability.

To examine the final structure at state B, we plot the radial distribution functions of the structure in Figure 6-17, and compare them with that of the β-SiC structure. We find that the structure of state B is a well ordered crystalline structure since well separated peaks appear in its $g(r)$'s. The $g(r)$'s for Si-Si and C-C from the new structure are identical to that of the β-SiC structure. However, the $g(r)$ between Si-C has changed. In the new structure, the first peak of $g(r)$ of Si-C has shifted to a larger distance compared to that in β-SiC structure. It is well known that β-SiC is formed by shifting the two sets of fcc lattices of Si and C by $1/4$ of the body-diagonal length of the unit cell along the body-diagonal direction. We find that the new structure is formed by shifting the two sets of fcc lattices of Si and C by $1/2$ of the body-diagonal. This is exactly the structure of the rocksalt SiC. Therefore, the structural transition observed by using the AS-SiC potential is a phase transformation from β-SiC to rocksalt SiC. This result is significant since it demonstrates that by suppressing the atomic sizes of the two types of atoms in β-SiC, the structural behavior of SiC under compression changes drastically from amorphization to polymorphic phase transition. This is due to the fact that the instability mechanism changes from shear to tetragonal shear upon suppression of the atomic size disparity. Thus, we have identified that the atomic size effect is the dominant factor that causes β-SiC to undergo amorphization under compression.

Finally, the reason that the phase transition leads to rocksalt SiC instead of β-tin SiC can be understood from calculations of energetics performed at $0K$ using the AS-SiC model. The relative energetics of β-SiC (zincblende), β-tin SiC and rocksalt SiC under compression at $0K$ is shown in Figure 6-18, where we clearly see that the rocksalt structure is more energetically favorable than the β-tin structure under compression.

6.5 Conclusion and Discussions

In the present work, we have observed pressure-induced solid-state amorphization of β-SiC under compression at room temperature. The amorphization is triggered by the vanishing of the shear instability. To understand the difference in the structural behavior of Si and SiC under compression, we have investigated chemical ordering, i.e., the atomic size difference and the chemical preference of mixed bonds in β-SiC. We have modified the Tersoff potential and developed two simplified models (CP-SiC and AS-SiC) to probe the chemical preference and atomic size effect separately. We have identified that the atomic size effect is essential to the amorphization of β-SiC. The results presented in this chapter is significant in several ways. First, it has been realized in experimental work of solid-state amorphization that the atomic size ratio of the two types of atoms in a binary system is an important criterion for solid-state amorphization [106]. However, experimentally, it has not yet been possible to separate the atomic size effect from other effects, such as the chemical preference effect. For the first time, combining computer simulations and elastic stability analysis, we have clearly identified that the size difference of atoms in a binary system is the dominant factor that causes solid-state amorphization. Secondly, we have found that the atomic size effect has significant influence on elastic constants and ultimately the instability mechanism of a crystal. This suggests that the atomic size difference can determine the general mechanical behavior of a system since the local strain response depends on the atomic size difference. Thirdly, in Table 6.2, we have shown an example of two systems (described by the Tersoff potential and the AS-SiC potential) with the same cohesive energy, lattice constant and even bulk modulus, but have very different elastic constants. This implies that, if a potential function can only describe the bulk modulus of a system properly, it may not be capable of predicting the mechanical behavior of a system correctly. In other words, if the fitting of an empirical potential only employs bulk modulus without considering elastic constants, the potential function may not be reliable for studies of materials mechanical properties and behavior.

Although within the frame work of the modified Tersoff potential, we have obtained interesting results and significant understanding of the pressure-induced amorphization of β-SiC under compression, there are still unsolved issues related to this topic. First, as mentioned earlier in Chapter 2, two independent first principle calculations have predicted different structural transitions for β-SiC under compression. Chang and Cohen[60] have predicted a transition from β-SiC to rocksalt structure; while Aourag et al.[59] have predicted a transition from β-SiC to β-tin structure. Therefore, it requires further work for theoretical calculations to fully resolve this issue. Secondly, an experimental study by Yoshida et al.[68] has reported observation of phase transition from β-SiC to rocksalt SiC in polycrystalline powdered samples. So far, in our simulations, we have only studied single crystals of β-SiC without any defects; while in the experimental samples, the existence of defects such as grain boundaries could play important roles in determining the observed structural transition. These defects may affect energy barrier and act as nucleation centers for the transition. In general, it is still an open question regarding what roles defects play in structural transitions, especially in the context of elastic stability analysis. This is a subject that deserves extensive future studies.

Despite the problems described above, we can relate our study of pressure-induced amorphization of β-SiC to several recent experiments. First, solid-state amorphization induced by electron irradiation has been observed in a single crystal β-SiC [107]. Secondly, pressure-induced amorphization has been observed in a BAs crystal[103], which is a similar material to SiC. Both of them are covalently bonded with slight ionicity, and both of them have zincblende structures. Interestingly, both of them have been predicted to undergo a phase transition from zincblende to rocksalt under compression by first principle calculations done by Chang and Cohen [60] and by Wentzcovitch, Cohen and Lam[108] respectively. In the experimental work of BAs, the critical pressure of amorphization is higher than the theoretically predicted transition pressure to rocksalt structure, and a kinetically frustrated phase transformation to amorphous structure has been observed. This is very similar to what we have observed in β-SiC using the modified Tersoff potential.

Finally, we need to point out that the SiC structure obtained in our simulation of pressure-induced amorphization is not free from artifacts. In Figure 6-5, we find that the first peak in the $g(r)$ of Si-Si or C-C is located very closely to the cutoff distance between Si-Si or C-C. And as we slightly vary the cut-off between Si-Si or C-C, the first peak position shifts with the cut-off. However, importantly, the first peak position in the $g(r)$ of Si-C does not change. We believe that the artifact observed here is similar to that in the quenched amorphous SiC described in Chapter 3. This suggests that some Si or C atoms have probably been prevented from getting closer to each other at the first peak positions in the $g(r)$ of Si-Si and C-C. As a result, one cannot be sure that the conservation of the coordination number between Si-C, the potential energy decrease, and the 'memory glass' effect are really intrinsic to the amorphization process. We are still in the process of eliminating this difficulty with the modified Tersoff potential. So far, we have found that it is possible to remove the artifact in the amorphous structure by modifying the cutoff function f_c in the Tersoff potential. On the other hand, we should emphasize that the elastic stability analysis and the conclusion that β-SiC will amorphize under compression are not affected by the cutoff.

Table 6.1: Cohesive energies, heat of formation, equilibrium lattice constant and parameter χ, where $\chi = 0.9776$ is from the original Tersoff potential for β-SiC.

ΔH (eV)	χ	$E(s_i - c)$(eV)	$E(s_i - s_i)$ (eV)	$E(c - c)$ (eV)	r_0 ($\mathring{A}$)
-0.08	0.9776	-3.093	-2.315	-3.711	4.32
0.00	0.9689	-3.013	-2.315	-3.711	4.34

Table 6.2: Comparison of Tersoff SiC with two simplified models. CP-SiC stands for SiC with chemical preference suppressed; AS-SiC standards for SiC with atomic size difference suppressed.

	Tersoff SiC	AS-SiC	CP-SiC
Lattice Parameter [$\mathring{A}$]	4.32	4.32	4.34
Cohesive Energy [eV]	-6.19	-6.19	-6.03
Bulk Modulus [GPa]	2.25	2.25	2.18
C_{11} [GPa]	4.36	**3.31**	4.19
C_{12} [GPa]	1.20	**1.72**	1.17
C_{44} [GPa]	2.56	**1.61**	2.42
$(C_{11} - C_{12})$ [GPa]	3.16	**1.59**	3.02
Instability Mechanism	shear	**tetragonal shear**	shear

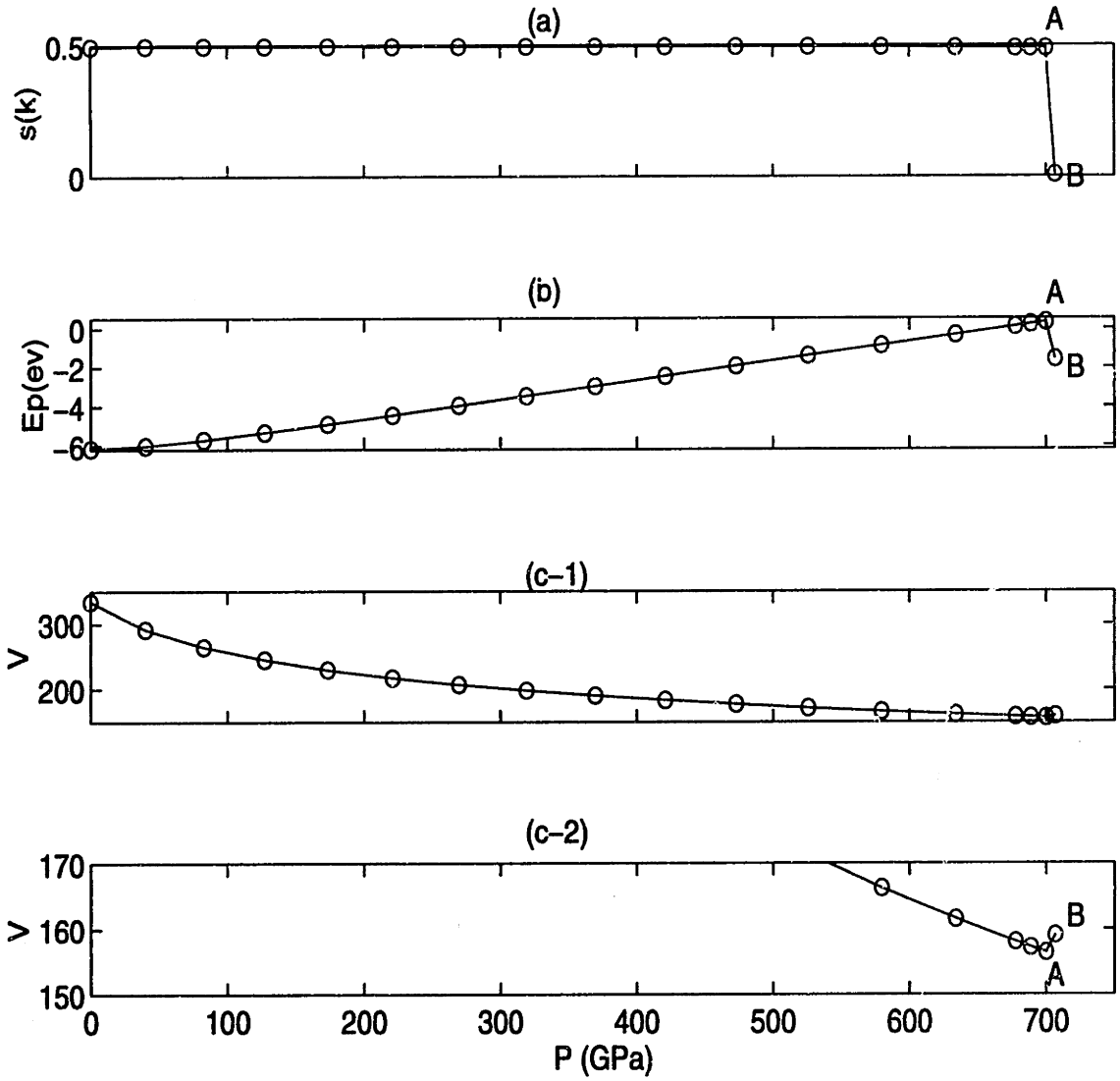

Figure 6-1: System responses to compression. P is the internal pressure at each equilibrium state. From top to bottom, (a) structure factor $s(k)$, (b) potential energy per atom $E_p(ev)$, (c-1) volume V in units of $6.538\mathring{A}^3$, and (c-2) same as (c-1) except that data are shown in a scale that allows one to see clearly the volume increase of the last point in the plot.

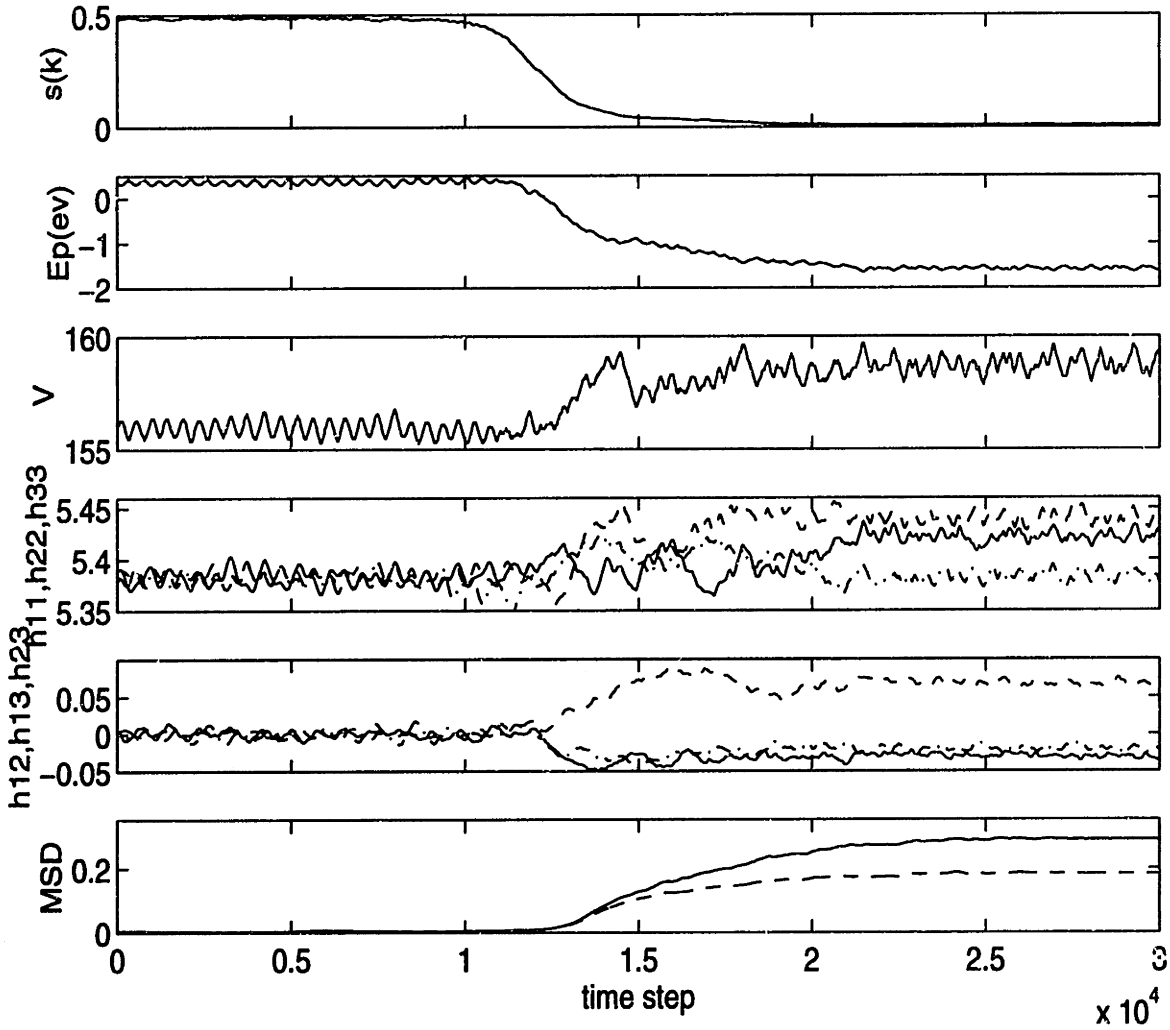

Figure 6-2: Time-dependent system responses at the critical transition pressure. From top to bottom, (a) structure factor $s(k)$; (b) internal energy per atom $E_p(ev)$; (c) volume in units of $6.538\mathring{A}^3$; (d) diagonal elements of cell matrix h; (e) off-diagonal elements of matrix h; and (f) mean square displacements of Si (dashed line) and C (solid line) atoms. All lengths are in unit of $1.87\mathring{A}$.

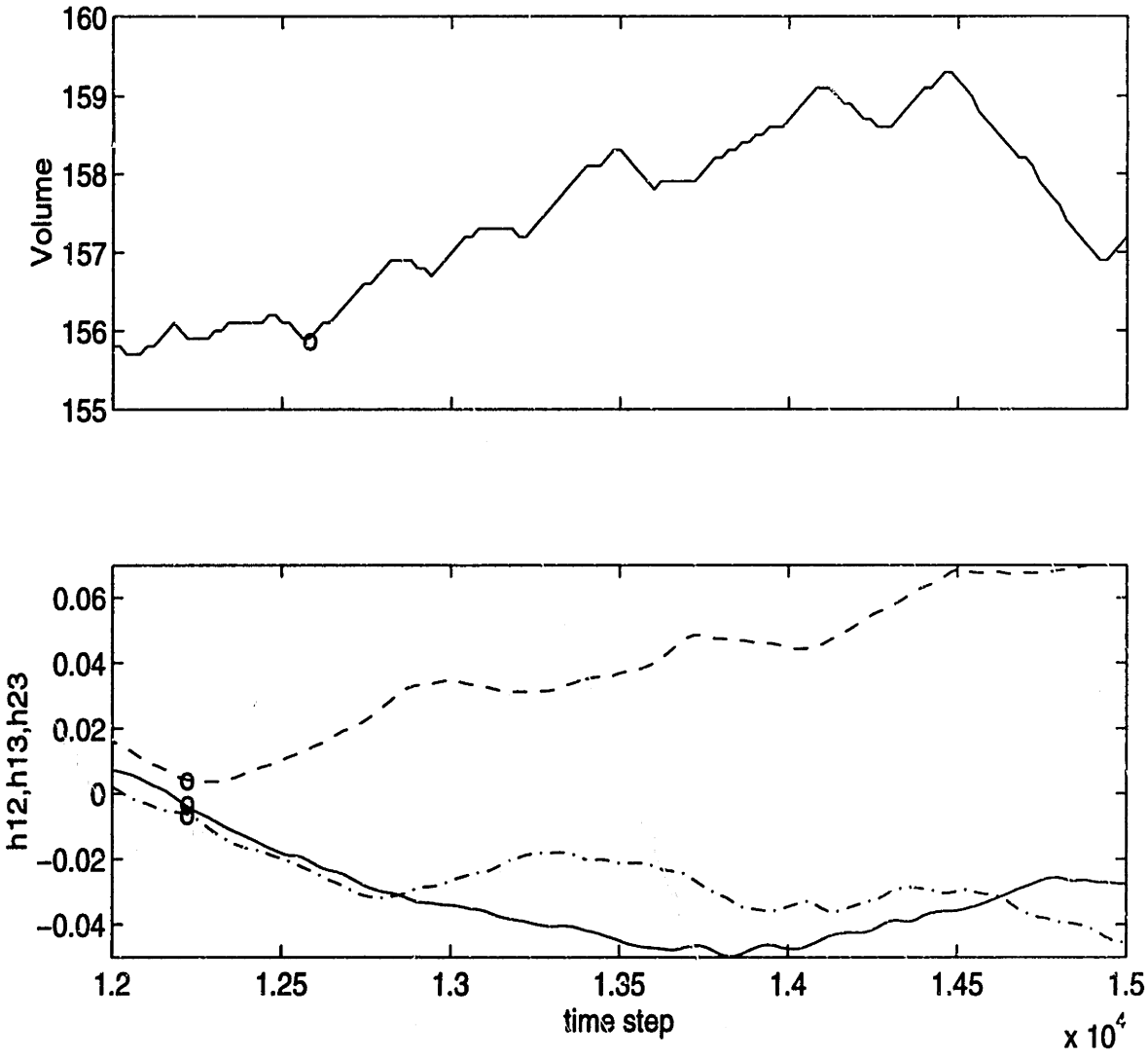

Figure 6-3: Detailed time-dependent responses of volume and off-diagonal elements of the matrix h from step 12000 to step 15000 of Figure 6-2. In top graph, circle indicates where volume expansion begins; in bottom graph, circles indicate where shear deformation of simulation cell begins. Shear deformation is identified to occur at step 12200; while volume expansion occurs at step 12560.

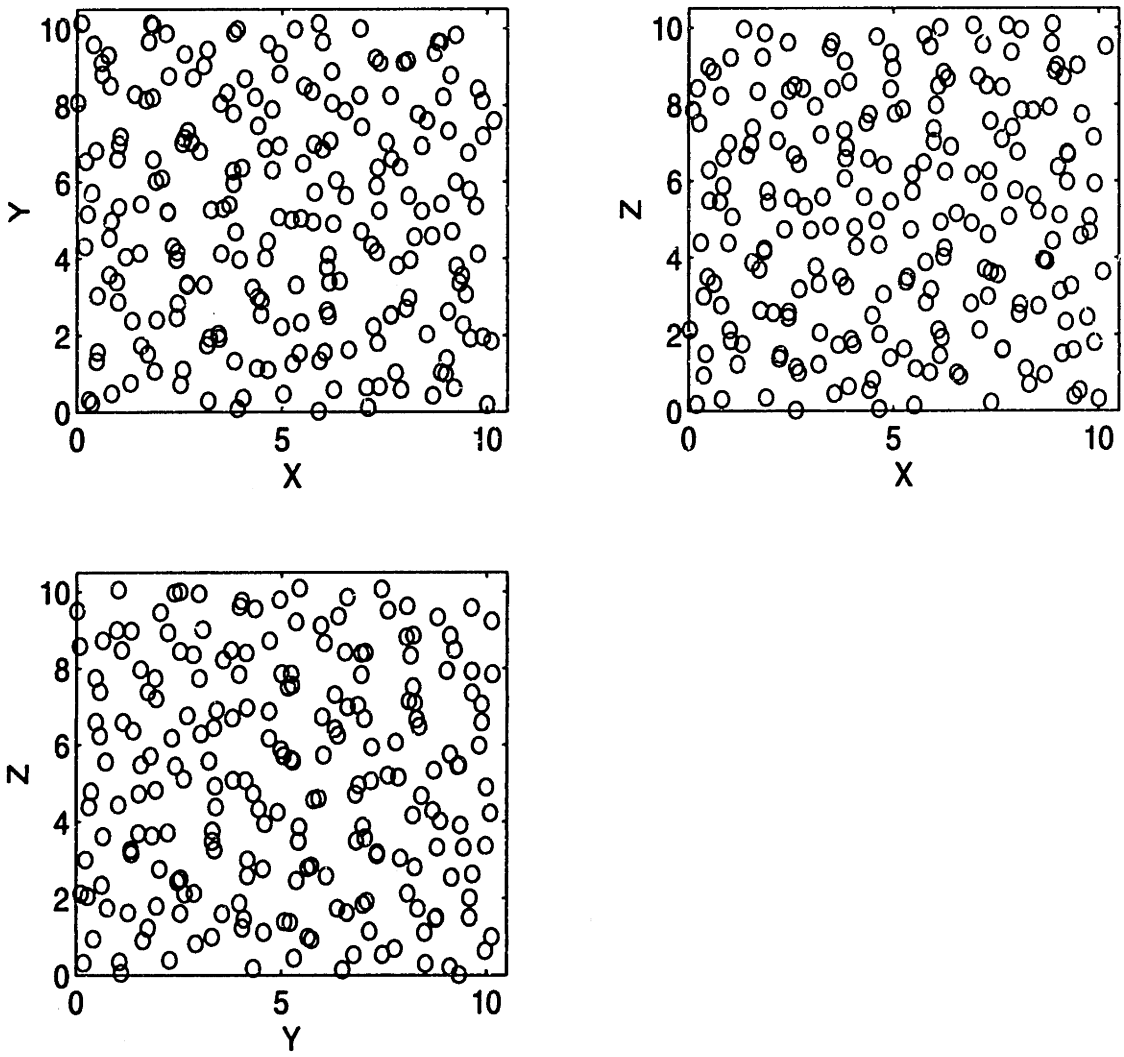

Figure 6-4: Projections of the atomic configuration of SiC after amorphization.

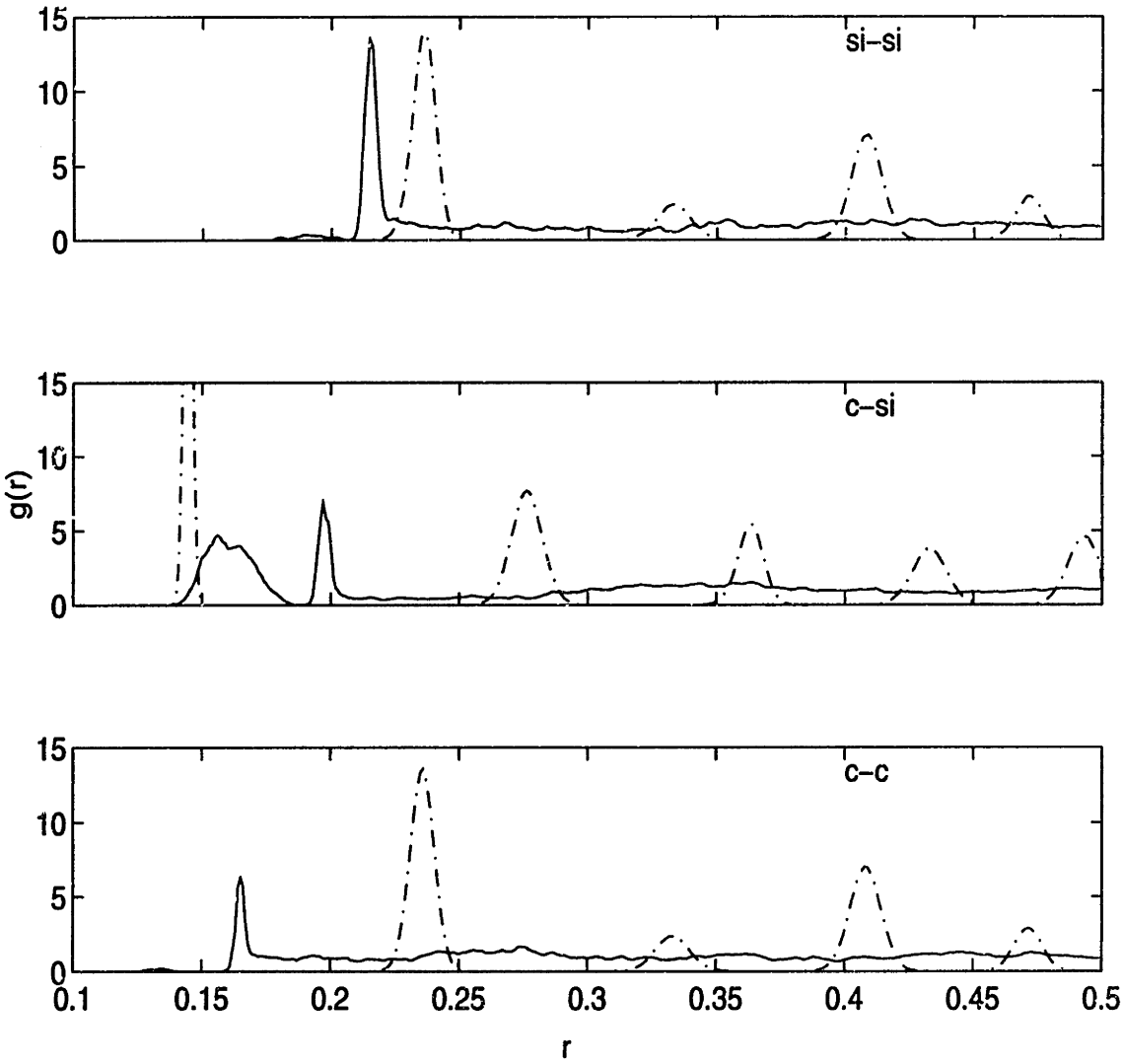

Figure 6-5: Radial distribution functions of SiC before (dashed line) and after (solid line) amorphization. r is the distance between atoms in reduced units, i.e., rescaled with respect to the simulation cell length.

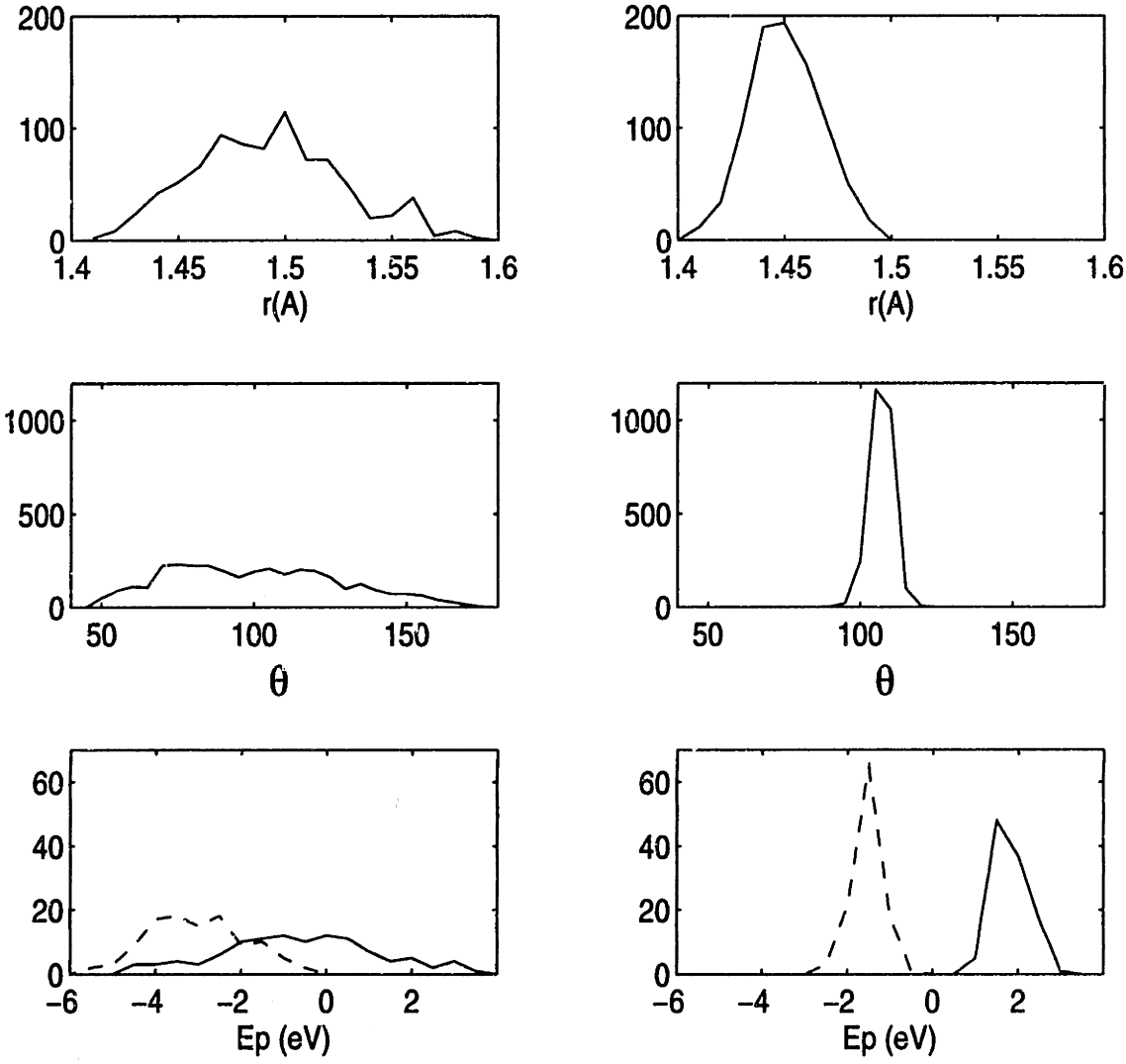

Figure 6-6: Number distribution of distance r_{ij}(Å), tetrahedral angle θ_{ijk} and potential energy $E_p(eV)$ before (right hand side) and after (left hand side) amorphization. In the two bottom figures, dashed line is for Si atoms; solid line is for C atoms.

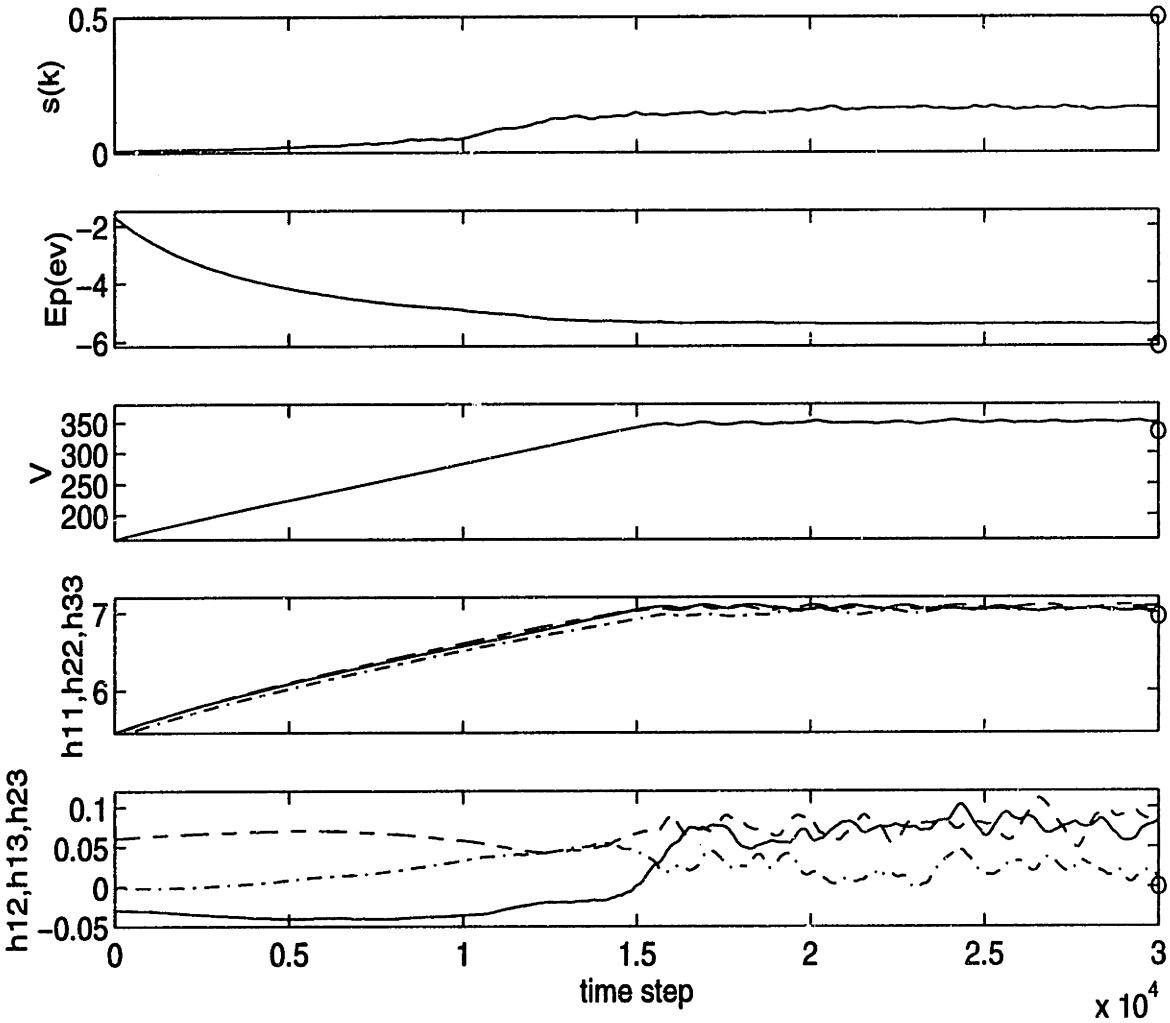

Figure 6-7: Time-dependent system responses after release of pressure. From top to bottom, (a) $s(k)$; (b) internal energy per atom $E_p(ev)$; (c) volume in units of $6.538\mathring{A}^3$; (d) diagonal elements of cell matrix h; and (e) off-diagonal elements of matrix h. Circles indicate the equilibrium properties of β-SiC under zero pressure at room temperature.

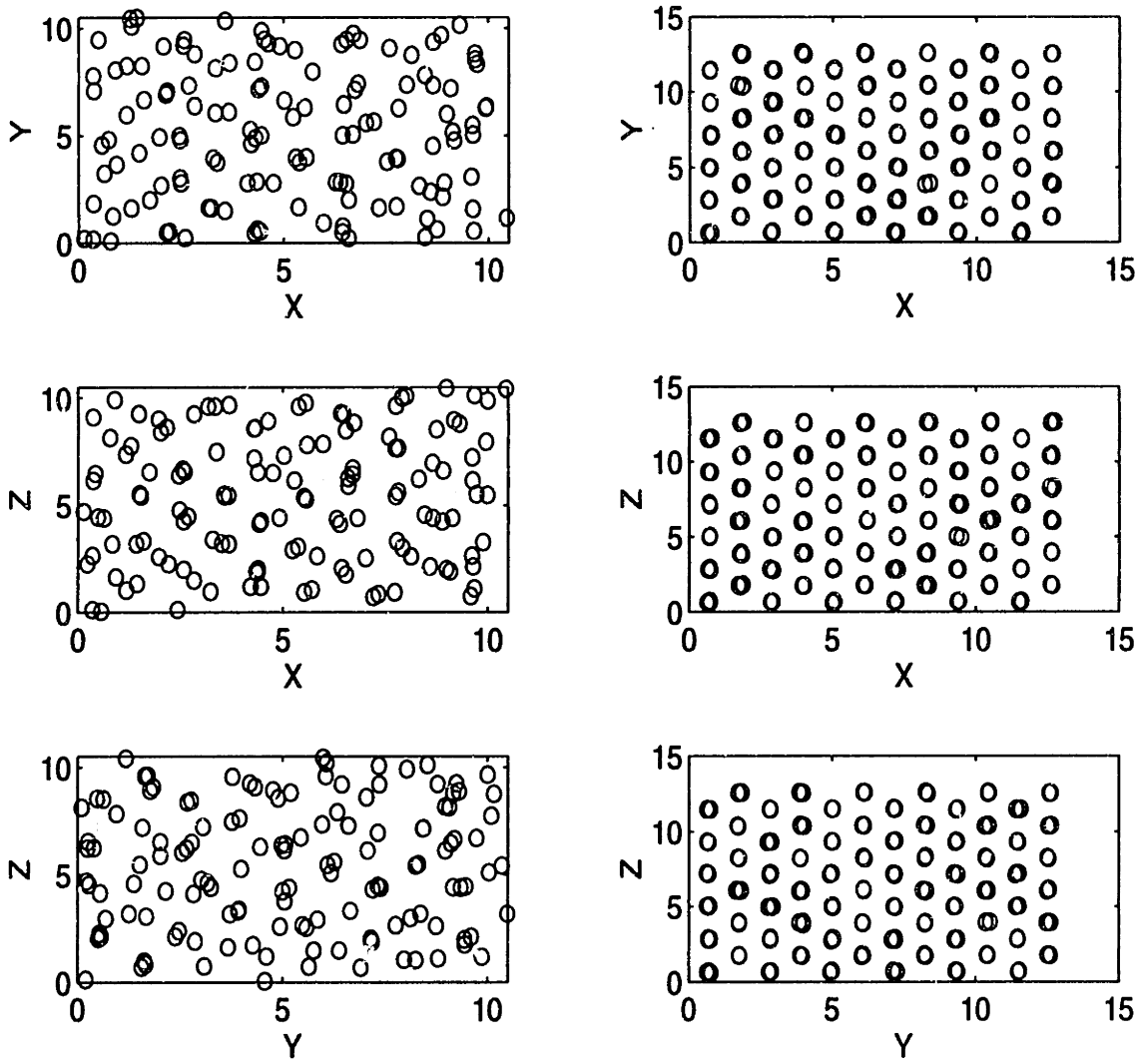

Figure 6-8: Atomic configurations of SiC after release of pressure (left panel) and of β-SiC at $300K$(right panel).

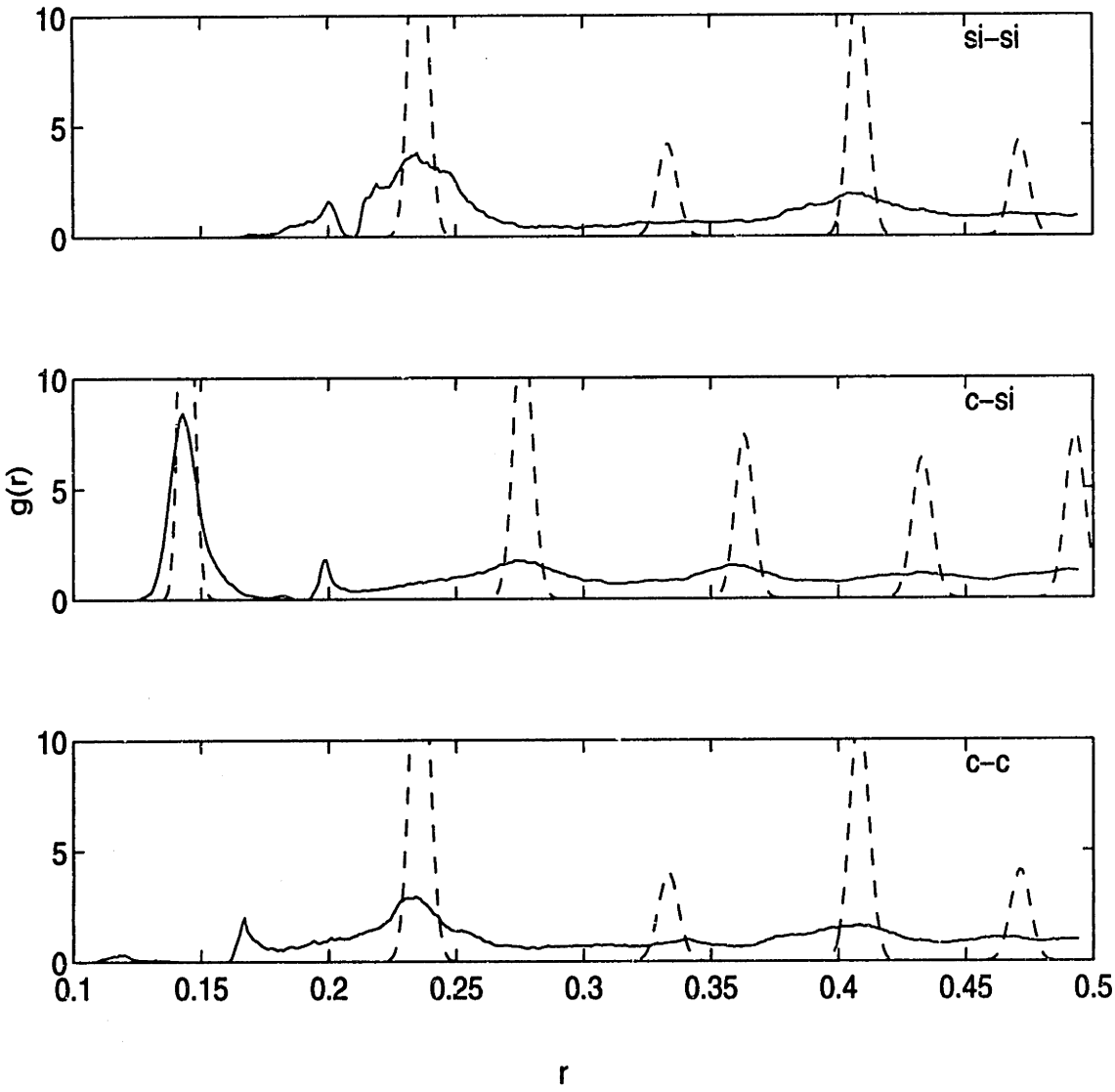

Figure 6-9: Radial distribution functions of SiC after release of pressure (solid line) compared with those for β-SiC at $300K$ (dashed line). The distance r is rescaled with respect to the simulation cell length.

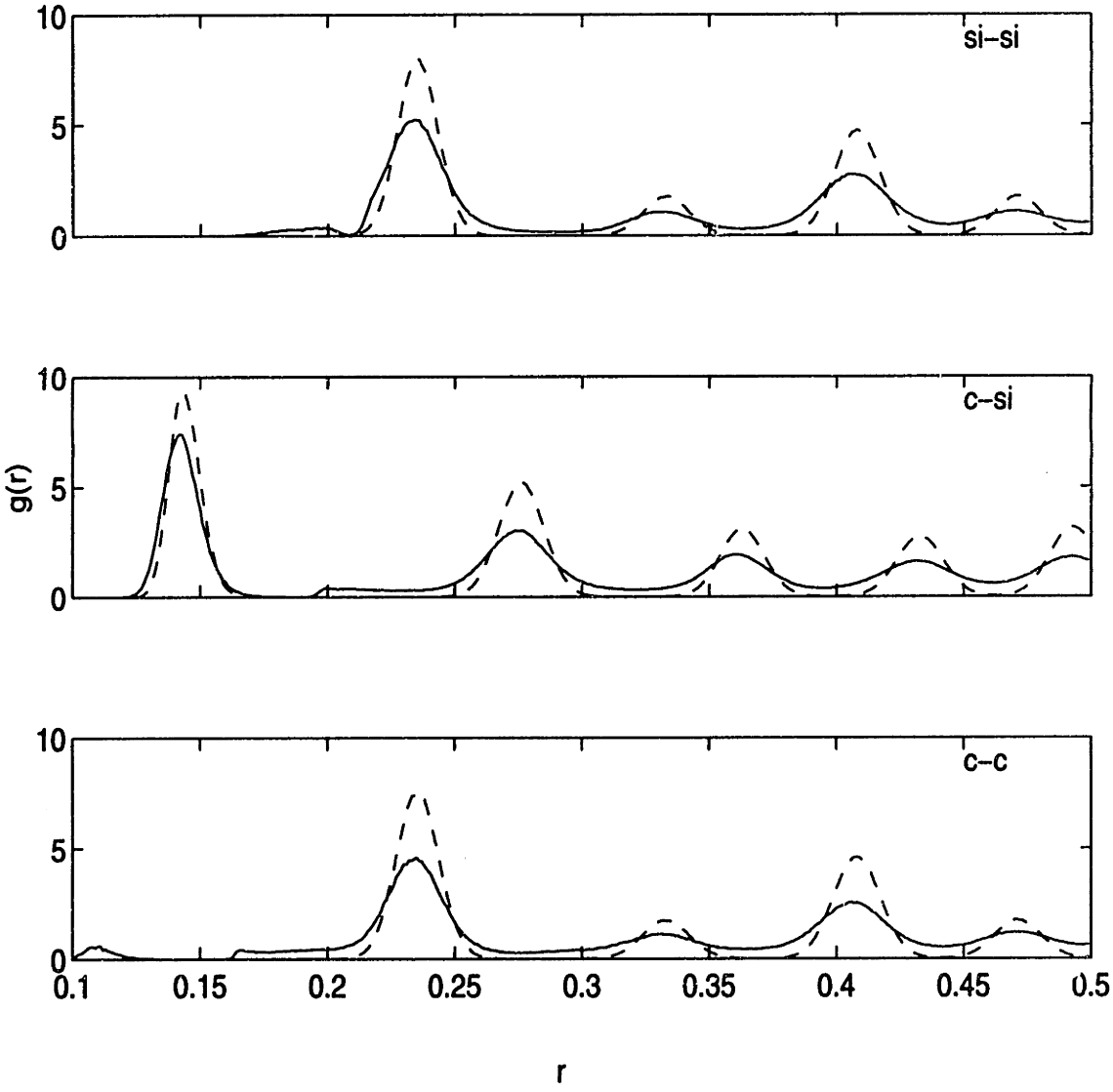

Figure 6-10: Radial distribution functions of SiC after release of pressure and annealed to $1000K$ (solid line) compared with those of β-SiC at $1000K$(dashed line). The distance r is rescaled with respect to the simulation cell length.

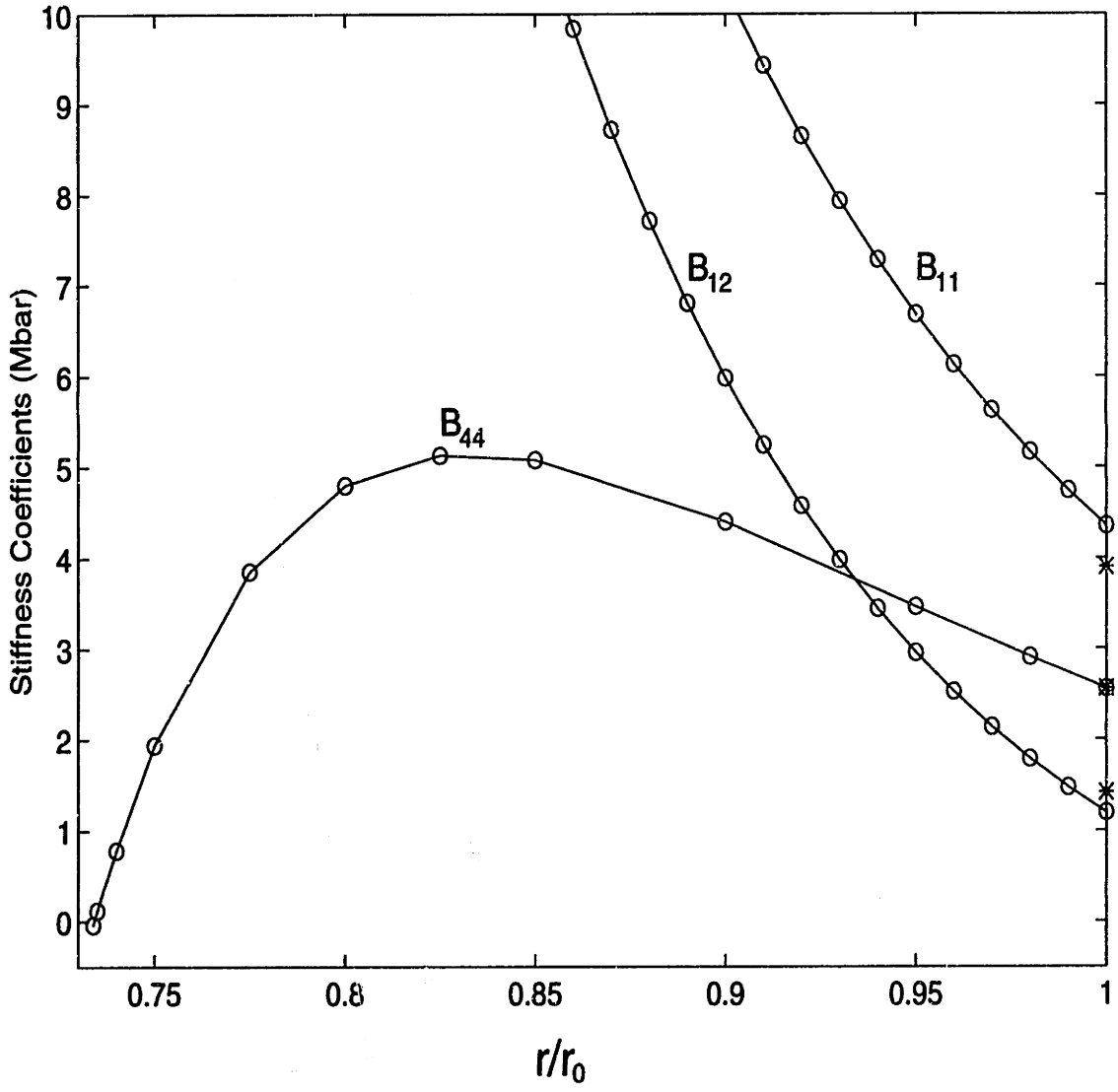

Figure 6-11: Elastic stiffness coefficients of β-SiC at $0K$ at various states of compression (r/r_0) calculated using the modified Tersoff potential.

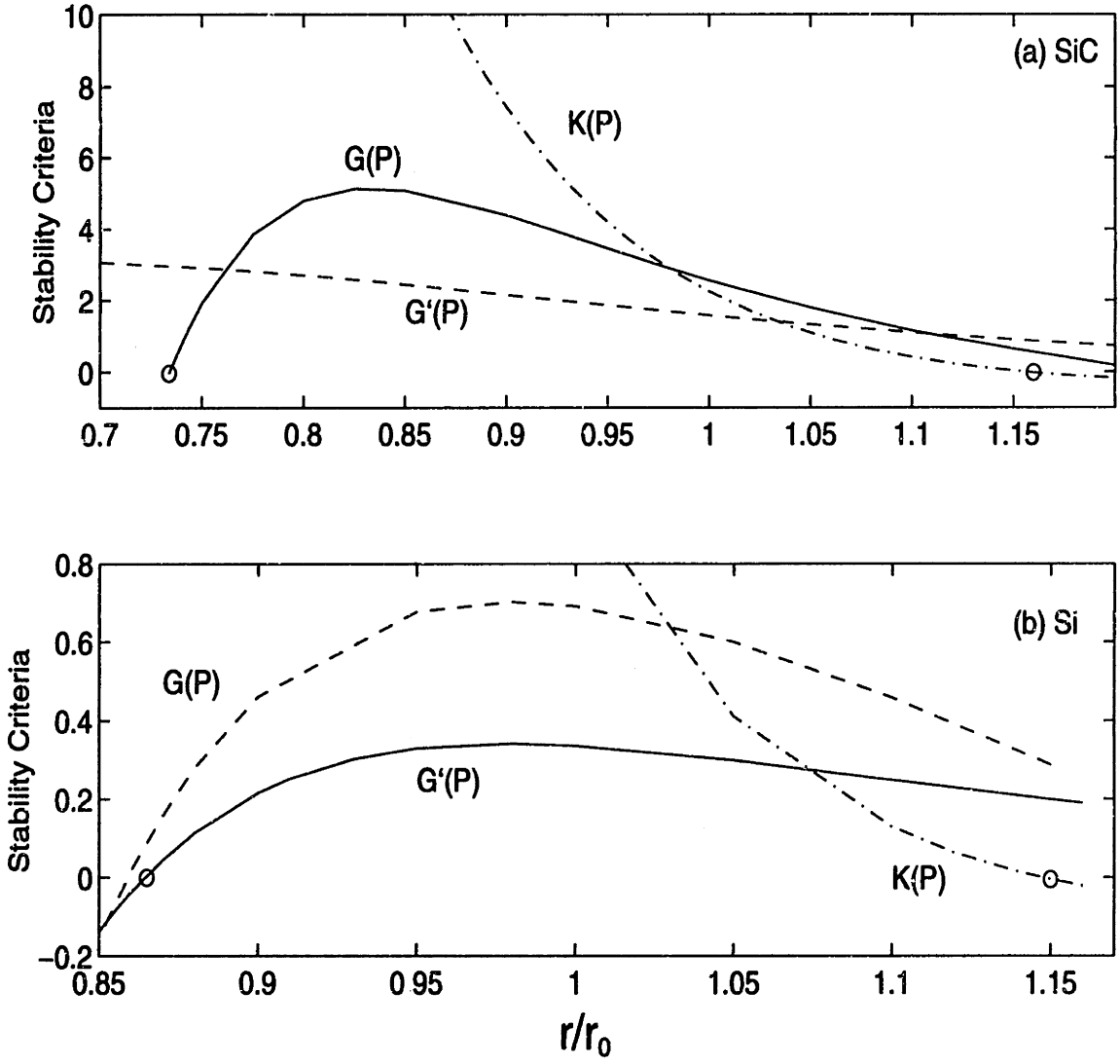

Figure 6-12: Elastic stability analysis for (a) β-SiC and (b) Si at $0K$. r and r_0 are the current and the zero pressure lattice constant respectively. $K(P)$ refers to the spinodal instability; $G(P)$ refers to the shear instability; and $G'(P)$ refers to the tetragonal shear instability. Circles label the critical states where the first stability criterion is violated.

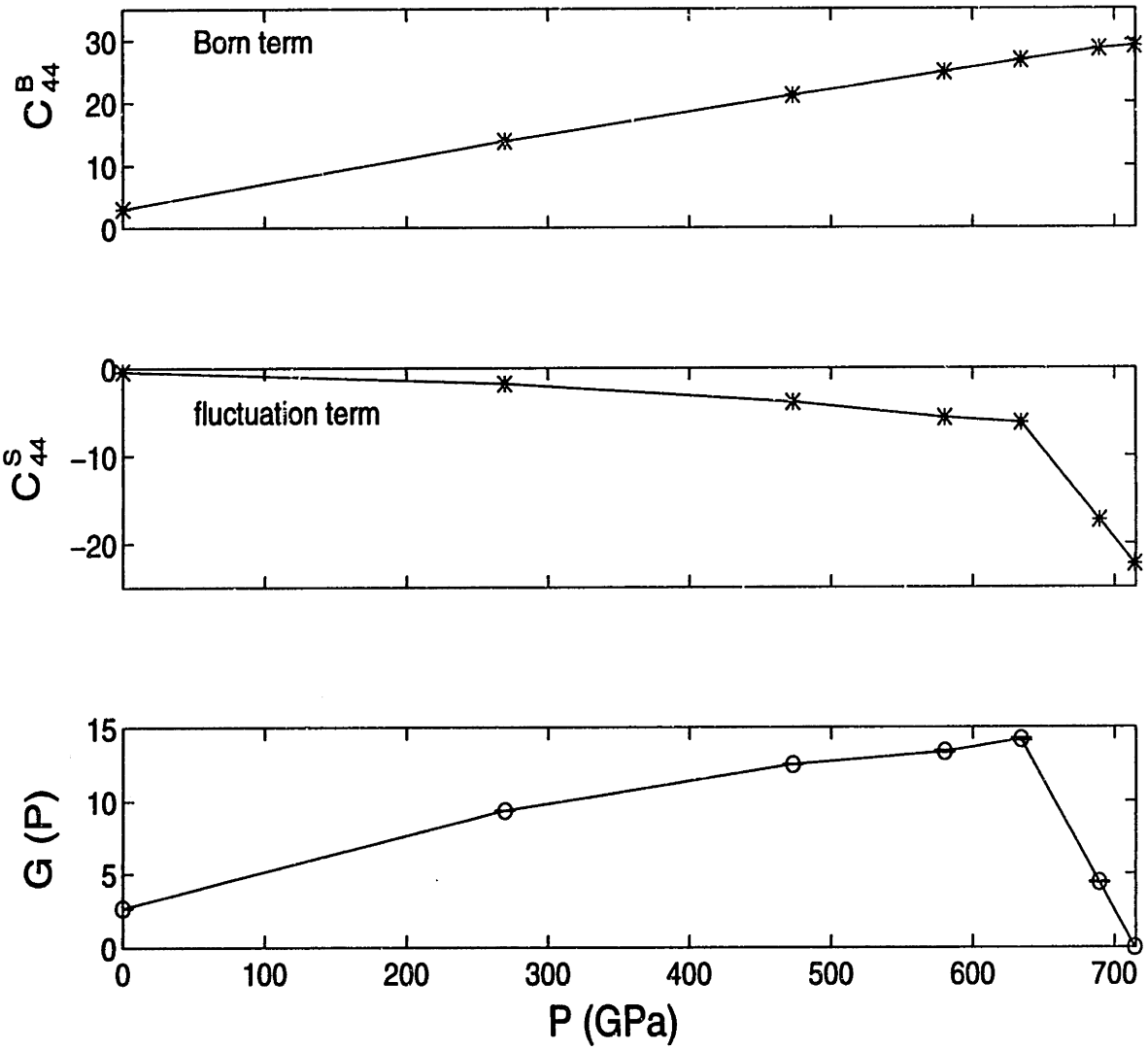

Figure 6-13: Shear instability criterion $G(P)$ of β-SiC under pressure $P(GPa)$. (a) Born term; (b) fluctuation term and (c) stiffness coefficient B_{44}, or $G(P)$.

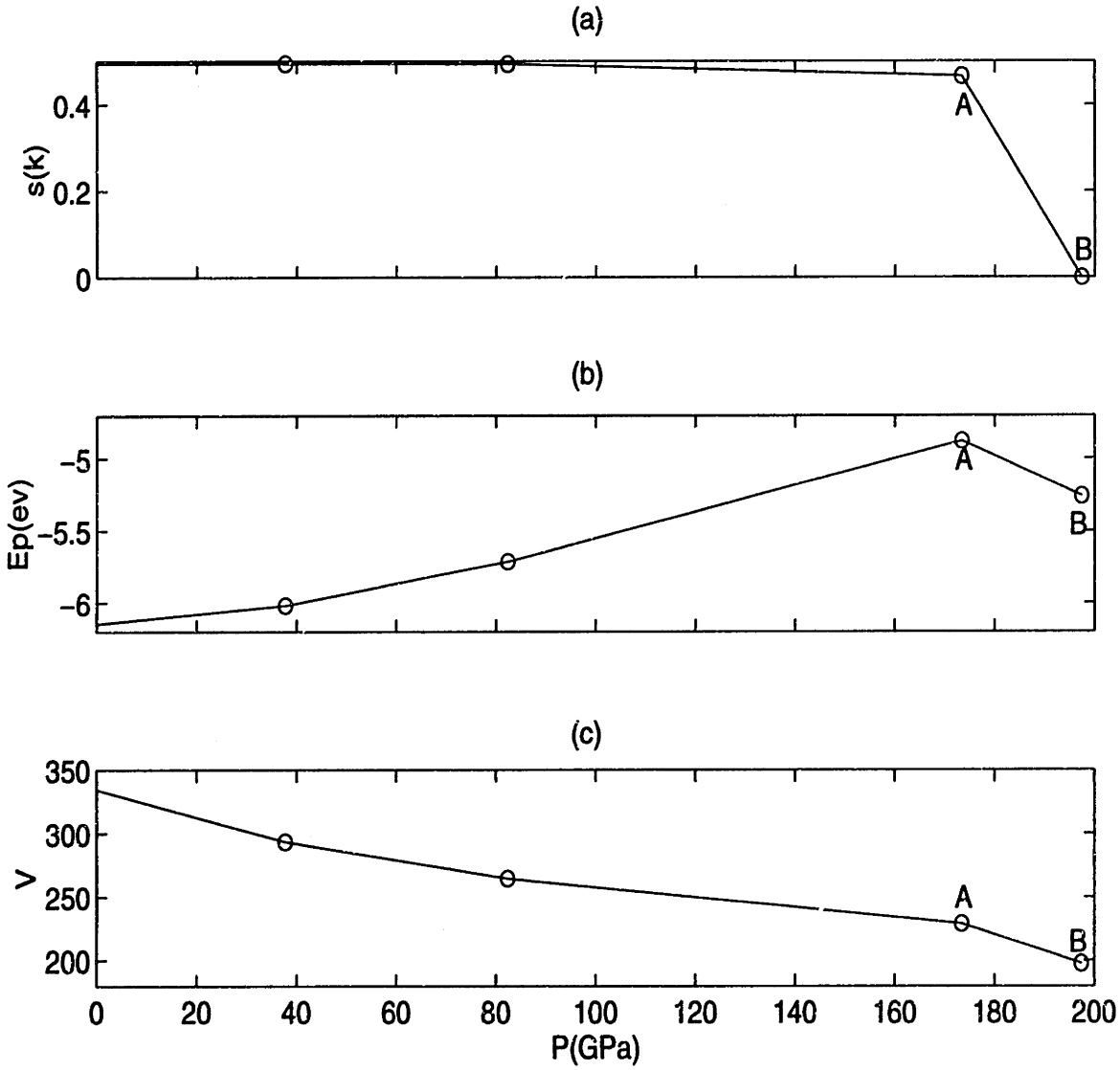

Figure 6-14: System responses to compression modeled by the AS-SiC potential. From top to bottom, (a) structure factor $s(k)$, (b) internal energy per atom $E_p(ev)$, (c) volume V in unit of $6.538\mathring{A}^3$.

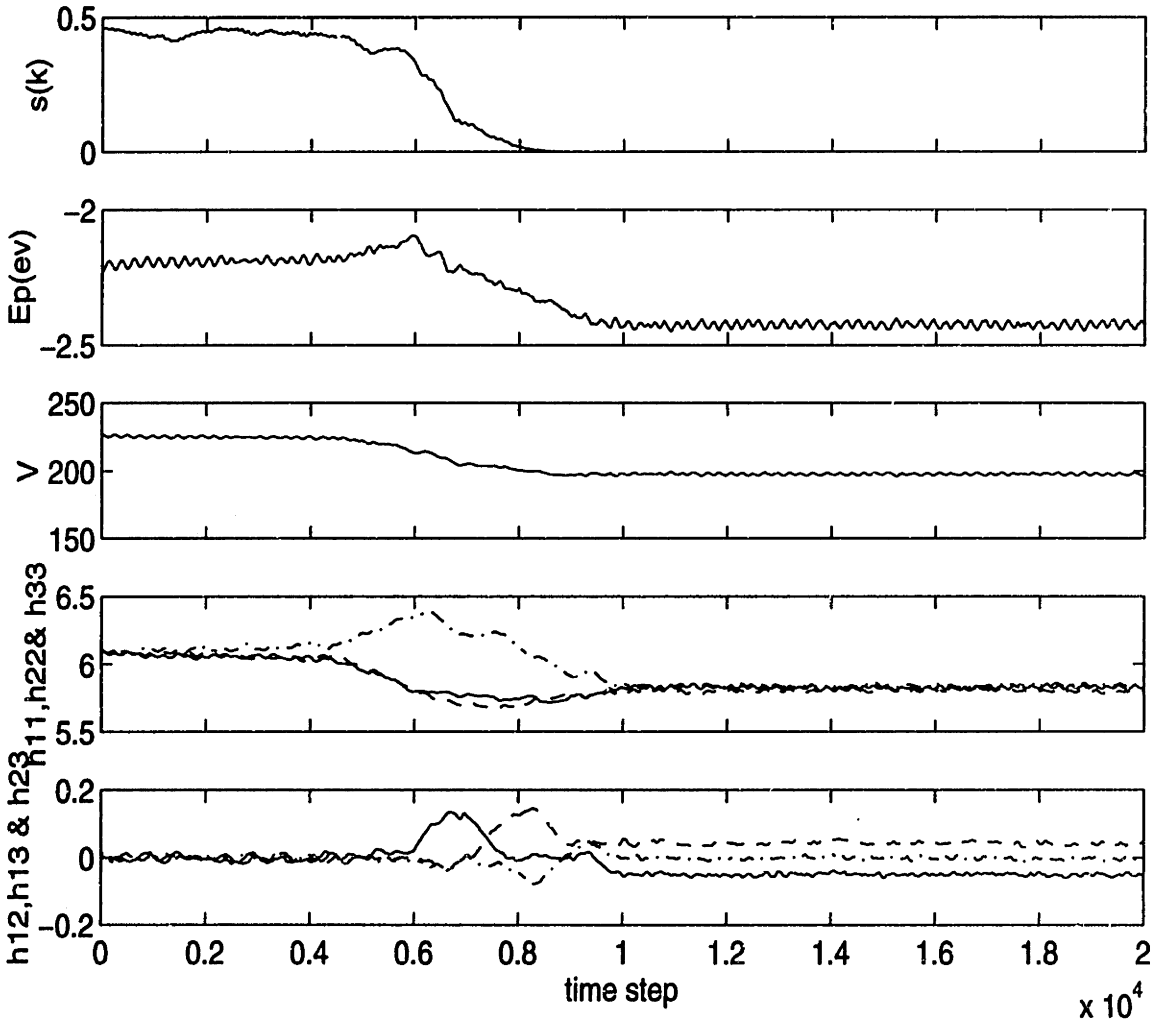

Figure 6-15: Time-dependent system response at the critical pressure modeled by the AS-SiC potential. From top to bottom, (a) structure factor $s(k)$; (b) internal energy per atom $E_p(ev)$; (c) volume in units of $6.538\mathring{A}^3$; (d) diagonal elements of cell matrix h; (d) off-diagonal elements of matrix h. Lengths are in unit of $1.87\mathring{A}$.

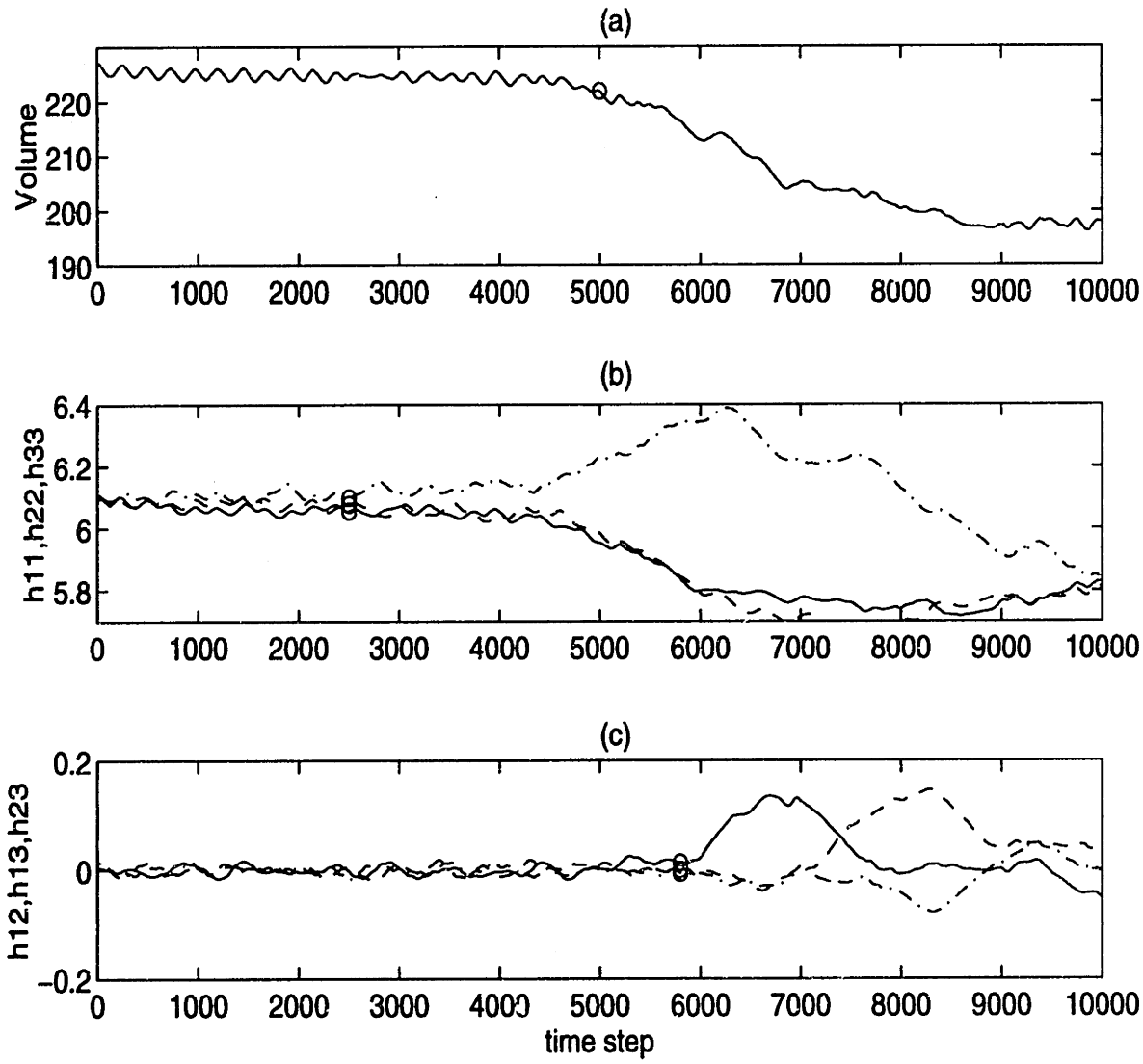

Figure 6-16: Detailed data of response of (a) the simulation cell volume V, (b) the diagonal elements h_{11}, h_{22} and h_{33}, and (c) the off-diagonal elements of h_{12}, h_{13} and h_{23} of the cell matrix h of Figure 6-15. As indicated by circles, bifurcation of the diagonal elements occurs at step 2500, while volume decreases after step 5000 and slight shear perturbation occurs after the bifurcation.

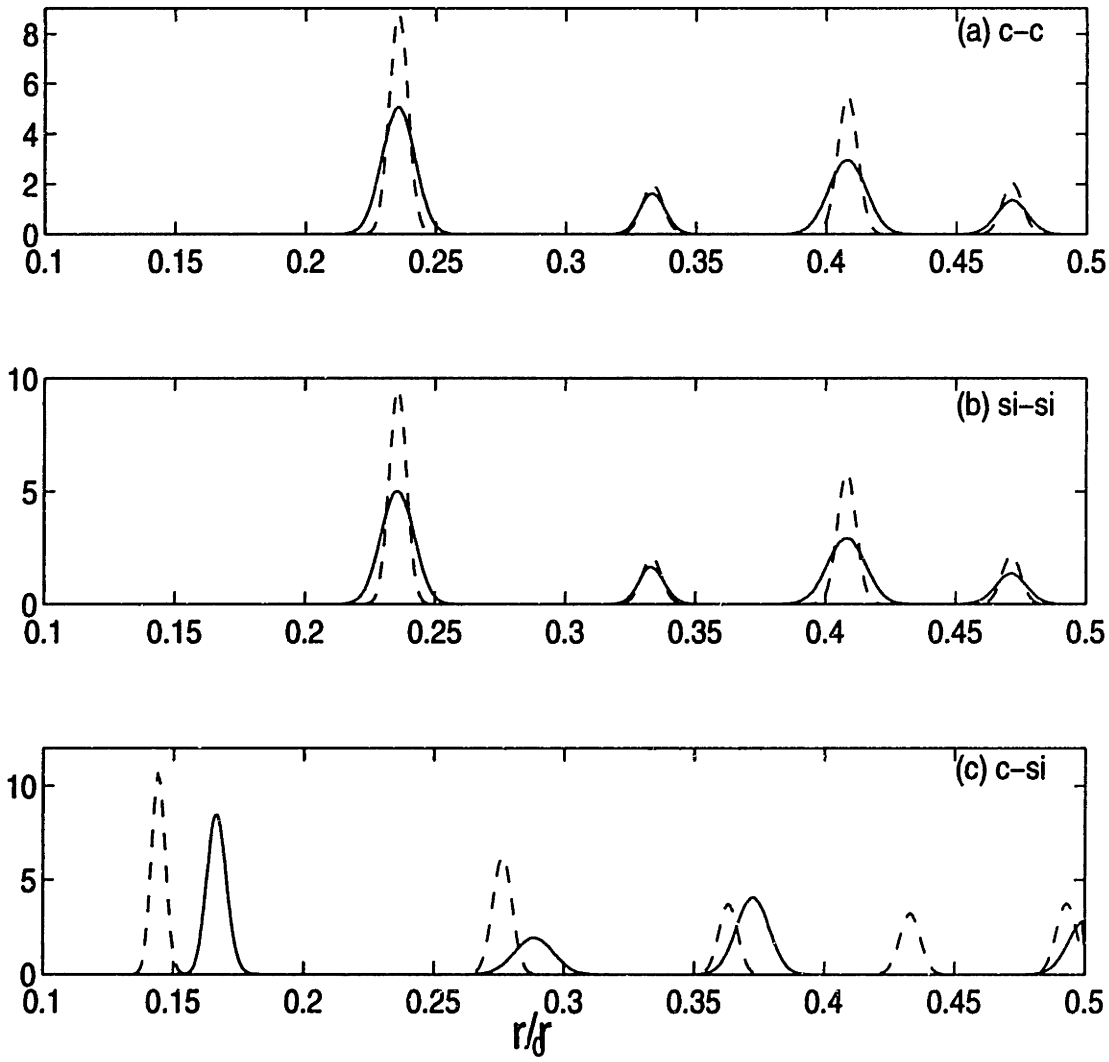

Figure 6-17: Radial distribution functions of rocksalt SiC (solid line) and zincblende SiC (dashed line), where r is in reduced units respect to the length of the simulation cell.

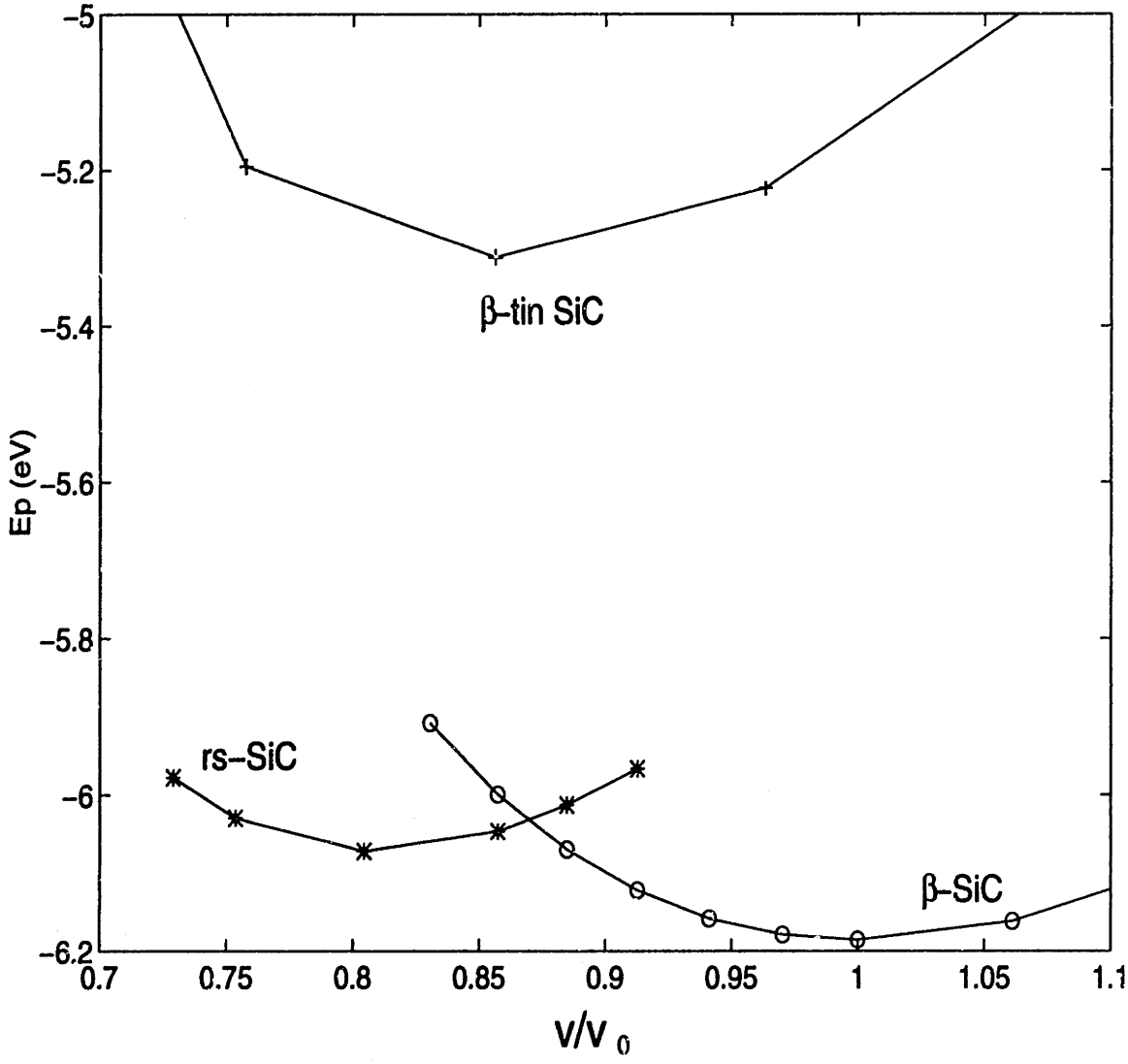

Figure 6-18: Cohesive energies of zincblende SiC (β-SiC), rocksalt SiC (rs-SiC) and β-tin under compression at $0K$.

Chapter 7

Structure and Bonding of Crystalline/Amorphous SiC Interface

7.1 Introduction

Interfaces of solid materials have been a focal point of research in several fields, including composite materials (metal, ceramic and intermetallic matrix composites), tribology and high technology semiconductor devices. Materials with interfaces have inherent inhomogeneity, i.e., the structural and mechanical properties at or near the interfaces can differ dramatically from those of the nearby bulk materials[109]. And the interfacial region is typically only a few atomic layers in extent. A fundamental understanding of interfacial bonding and adhesion requires knowledge of atomic-level structure and force. Although it has been difficult to probe internal solid interfaces experimentally, simulation methods of molecular dynamics are unique in providing such details. It can provide fundamental understanding of interfacial structure, bonding and adhesion. Progress has been made in developing methodologies to study interfaces using atomistic simulations[110][111]. So far, simulation studies have focused on crystals with grain boundaries, such as to investigate the fundamental process

of grain-boundary premelting[112], and to characterize the mechanical properties of grain boundaries through calculations of local elastic constants[113][114][115].

Crystalline/amorphous SiC interfaces may exist between fiber/fiber-coating or fiber-coating/matrix in SiC fiber-matrix composite materials. To some extent, the mechanical behavior of such interfaces controls the performance of the composite materials[7][9]. Therefore, it is important to obtain understanding of the correlation between interface structure, bonding and adhesion, and to investigate the interplay between the structure and interfacial fracture behavior. While progress has been made in studying interfaces involving grain-boundaries, little has been done on crystalline/amorphous interfaces. Stillinger et al.[116] have constructed crystalline/amorphous interfaces by packing hypothetical disks and spheres. Their focus has been on the packing procedure and little is known about the structures and properties of the interfaces.

In this chapter, we present a preliminary study on a crystalline/amorphous (c/a) SiC interface modeled by the modified Tersoff potential. This work is aimed to develop a general methodology for interface constructions and to demonstrate the feasibility of atomistic simulations in the studies of crystalline/amorphous interfaces. This work is still in its early stage and deserves future work in the future. In Sec. 7.2, we present a methodology to construct a c/a SiC interface. In Sec. 7.3, we calculate the work of adhesion of the interface. In Sec. 7.4, we summarize the results and discuss future work.

7.2 Construction of an Interface Model

7.2.1 Methodology

For modeling grain boundaries, the initial atomic coordinates of the interfacial structure can be provided by experiments or based on total energy calculations by first principle or tight-binding calculations. The study done on SiC grain boundaries by Kohyama et al. is such an example[47]. For modeling SiC c/a interfaces, no previous

data of experiment or total energy calculations exist. We will produce a SiC c/a interface by physically compressing two halves of bulk crystal SiC and amorphous SiC. The success of such a method will depend on whether stable bonding can be formed between atoms of the two halves. A recent work has used similar method to study an amorphous carbon/graphite interface[117], where the method seems practical and has provided reasonable results of c/a interfaces.

A crystal SiC and an amorphous SiC each containing 216 atoms are used to construct the interface. The x, y and z coordinates of the crystal are aligned along the crystallographic [100], [010] and [001] directions respectively. The interface will be formed parallel to yz plane. On the crystal side, 12 layers of atoms with 18 atoms per layer parallel to the interface are used. As will be shown later, the 12 layers of atoms are sufficient to represent a crystal with both surface region and bulk region, and 18 atoms per layer are sufficient to capture the characteristics of atomic bonding at the interface. The amorphous SiC is obtained by melting and rapid quenching of a crystal SiC with 216 atoms. The results of melting and quenching have been shown in Chapter 3. At zero pressure and room temperature, the simulation cell lengths of the crystal and amorphous SiC are 12.98$\AA$ and 13.50$\AA$ respectively. In order to apply periodic boundary conditions along y and z directions to avoid lateral translation of the two halves in the yz plane[118], the amorphous SiC is slightly compressed along y and z directions so that simulation lengths along these two directions are the same as that of the crystal. Since the difference between the simulation cell lengths of the two sides is small, no significant stress is caused by this adjustment. Along x direction, the periodic boundary condition is removed so that we will focus on one single interface between the two sides. Thus, before the interface is constructed, we have a crystal block with two free surfaces exposed at its (100) planes and an amorphous block with two free surfaces exposed at the ends parallel to yz planes.

A schematic view of the methodology to construct the c/a SiC interface is shown in Figure 7-1. We bring the amorphous block close towards to the crystal block by changing the separation d_{sep} between the two halves. d_{sep} is the distance between the two simulation cells containing the crystal and amorphous SiC respectively. It

is different from the actual distance between atoms at the two sides. Atoms on the first two layers of the far end of the crystal are frozen to represent a fixed bulk crystal. On the other hand, the amorphous SiC is free to move along x direction to allow deformation and volume change and to release stress accumulation during the interface formation. The two halves are fully relaxed at $300K$ before we systematically bring the amorphous block close to the crystal block by decreasing d_{sep}. As soon as we observe bonding begins to form between atoms of the two halves, we decrease d_{sep} slowly in a step of $0.187\mathring{A}$, which is one tenth of the equilibrium bond length in SiC. At each separation d_{sep}, we use 2500 steps to let the system fully relax, and use 5000 steps to calculate relevant properties. During this process, the temperatures of both sides are kept at $300K$ except for the two frozen layers on the far end of the crystal. Thermal fluctuations at $300K$ can help the system to fully relax and the temperature distribution in the system can be used to monitor if equilibrium is reached across the interface[119]. If stress accumulates in the system, a higher temperature distribution will usually develop in that high stress region than in other areas of the system.

For the benefit of interface study, we divide the whole system into equally spaced layers and calculate the structure and properties layer by layer. The crystal side is divided into 12 layers. By the same layer spacing, the amorphous side is divided into 14 layers. Therefore, the system consists of a total of 26 layers of atoms. These layers are labelled from far left of the crystal to the far right of the amorphous block. The first two layers are fixed, the last layer in the crystal side is layer 12 and the first layer in the amorphous side is layer 13.

7.2.2 Results

Figure 7-2 shows the properties of the two halves when they are separated by $5\mathring{A}$ and no interactions of atoms between the two sides. In the crystal side, since Si and C atoms have different cohesive energies in β-SiC lattice, the potential energy profile exhibit fluctuations across the alternating Si and C layers. At the two free surfaces of the crystal, atoms have dangling bonds and thus higher potential energies. For atoms inside a bulk β-SiC, each atom is 4-fold coordinated. For an atom exposed at (100)

surface, two dangling bonds exist. We find that the coordination number of layer 1 is 2, but the coordination number of layer 12 is close to 3. This difference is caused by surface reconstruction of atoms at layer 12. Figure 7-3 shows the yz plane projection of atomic configuration of atoms at layer 12 before and after surface relaxation at $300K$, where a combination of 2×1 and 2×2 reconstruction (see Chapter 3) can be seen. Because of surface reconstruction, each atom at layer 12 form one bond with an atom in the same plane and increase the coordination number from 2 to 3, and decrease the potential energy of layer 12 accordingly. The temperature distribution of the crystal shows slightly higher values at the two surfaces. This phenomena is expected and may eventually contribute to premelting at the surfaces when the melting point of the system is reached[112].

For the amorphous side, we also find that the two surface layers have higher potential energies and lower coordination numbers compared to atoms in the inside region. The coordination number of the two surfaces are 2.7 and 1.9 respectively. And the averaged coordination number of atoms inside the bulk amorphous SiC is about 4 (see Chapter 3). For the bulk region inside the amorphous SiC, the layer profile of the number of atoms, the potential energies and the coordination numbers all show large fluctuations from layer to layer. This means that the system size of 216 atoms is not large enough to represent a uniform amorphous SiC. A larger system size will allow more atoms at each layer and offer better statistics of averaged layer properties. However, using the current system size of 216 atoms, the characteristics of a bulk region with two free surfaces are still captured clearly.

Once the crystal and the amorphous SiC are fully relaxed, we bring the amorphous block close to the crystal block to form the c/a interface. At a separation $d_{sep} = 3\mathring{A}$, atoms at the surfaces of the two sides begin to interact and form bonds. As d_{sep} is further decreased, the number of atoms that interact with atoms at the other side N_{int} increases; the potential energies of both the crystal and the amorphous side decrease; and the distance between the averaged layer positions of layer 12 and layer 13, i.e., $d_{c/a}$ decreases. $d_{c/a}$ is used to describe the actual distance between the crystal and the amorphous sides, while d_{sep} is only the controlling separation between the two

simulation cells. When d_{sep} becomes smaller than $1\mathring{A}$, properties become stabilize, i.e., do not change significantly upon further decrease of d_{sep}. This means that the interactions of atoms at the crystal and the amorphous surfaces have reached their equilibrium condition and we have formed a c/a interface. Under the equilibrium condition, the time-averaged number of interacting atoms N_{int} reaches 18 which is the total number of atoms at the surface layer of the crystal side. This means that all atoms at the foremost crystal plane have formed bonds with atoms at the amorphous side. Also, the final distance $d_{c/a}$ is about $1.612\mathring{A}$ which is smaller than the equilibrium bond length of β-SiC ($1.87\mathring{A}$).

The properties calculated layer by layer of the interface system is shown in Figure 7-5. We find that the coordination number of layer 12 has increased from 2.9 to 3.8, and the coordination number of layer 13 has increased from 2.7 to 3.6. Thus, on averaged, each atom at the crystal surface has formed one bond with an atom at the amorphous side. The temperature distribution of the system is uniform and no signature of inhomogeneity across the interface. This means that the system has reached equilibrium across the interface. This equilibrium ensures a stable interface that will not vary significantly with time. The projections of the atomic configuration of the interface is shown in Figure 7-6. Since the spacing between two crystal layers is only $1.08\mathring{A}$, the interface spacing $d_{c/a}$ ($1.61\mathring{A}$) is much larger. This larger spacing is due to weaker bonding of atoms across the interface compared to the atomic bonding across a (100) surface inside the bulk β-SiC. Inside bulk β-SiC, each atom is 4 fold coordinated and 2 bonds per atom are formed across a (100) surface, while only one bond per atom is formed across the interface.

7.3 Estimation of Work of Adhesion

One of the important properties of an interface is the interfacial strength, which is a physical quantity difficult to characterize both experimentally and theoretically[120]. In order to establish a correlation between the interfacial strength and more accessible physical quantities, the work of adhesion is introduced as a measure of the strength

of the interface[121]. It is defined as the work required to reversibly separate the two sides of the interface[122],

$$W_{ad} = \gamma_{int} - \gamma_1 - \gamma_2 \tag{7.1}$$

where γ_1 and γ_2 are the energies of the relaxed surfaces of the two sides respectively, and γ_{int} represents the energy of the relaxed interface between side 1 and side 2. The work of adhesion is important to describe the mechanical properties of the interface and is related to the fracture toughness of the interface. If a crack propagates along the interface in a cleavage manner, the fracture toughness K_c or the critical energy release rate G_c scales with the work of adhesion[123]. For this reason, the work of adhesion is also termed the intrinsic toughness of the interface. Experimentally, the work of adhesion is difficult to measure because it is strongly influenced by both chemical and structural defects at interfaces[122]. Atomistic simulations are ideal to characterize the work of adhesion because detailed interface structure can be obtained and the correlation between structure and properties can be established. In the following, we present the result of the calculated work of adhesion for our c/a SiC interface model.

The potential energies of the crystal and amorphous SiC before and after the interface formation have been shown in Figure 7-2 and Figure 7-5 respectively. The energy decrease due to the interface formation can be used to estimate the work of adhesion, i.e.,

$$W_{ad} = E_p^{int} - E_p^c - E_p^a \tag{7.2}$$

However, it is difficult to define the potential energy of the interface E_p^{int} since it requires to identify the interface region unambiguously. To do this, we compare the potential energies and the coordination numbers before and after the interface formation and plot the results in Figure 7-7. As can be seen clearly, during the interface formation, the coordination number and the potential energies change significantly only for layer 12 and layer 13. The coordination numbers of layer 12 and layer 13 have changed from 2.9 to 3.8 and from 2.7 to 3.6 respectively; and their atomic po-

tential energies have changed from -4.319 to $-5.257(eV)$ and -4.032 to $-4.746(eV)$ respectively. Thus, in terms of the coordination numbers and the potential energy, the interface region only consists of these two layers. However, the number of atoms for these two layers are not the same before and after the interface formation. However, in terms of the number of atoms per layer, the interface consists of more than just two layers of 12 and 13. As can be seen in Figure 7-7(c), the number of atoms change for the first 6 layers in the amorphous side. Here, small change such as 1 or 2 are important because the total potential energy is calculated by the multiplication of the atomic potential energy times the number of atoms. Therefore, to calculate the work of adhesion accurately, we must use 7 layers for the interface potential energy, 6 layers at the amorphous side and 1 layer at the crystal side. We find that the total number of atoms for these 7 layers are the same before and after the interface formation, and the number is 105. And the total potential energy decrease for the 7 layer interface region is $38.9(eV)$. Since the area of the interface is $168.5\mathring{A}^2$, the work of adhesion is calculated to be $W_{ad} = 0.231eV\mathring{A}^2$ or $W_{ad} = 3.8J/m^2$. No direct data of the work of adhesion energy for the c/a SiC interface is available in the literature. An estimation on a universal binding curve[58] has been done on a SiC coating/Pitch-55 carbon interface (C/SiC)[123], and the work of adhesion has been estimated to be $3.28J/m^2$. This suggests that our calculation is in the correct range.

7.4 Discussion and Future Work

In this study, we have developed a methodology to construct a c/a SiC interface. The methodology is successful that a stable interface has been obtained at room temperature. The interface is found to be weaker than a (100) surface in bulk β-SiC. The work of adhesion of the interface has been calculated and the number seems reasonable. During the study, we have demonstrated that atomistic simulations are capable of providing atomic-level information about structure, bonding and their correlation, and the interface region can be identified clearly.

This study is only on its initial stage. Further work is needed to explore the

structure of the c/a SiC interface we have constructed. For example, we can study the local geometric arrangements of atoms bonded across the interface. We have found that each atom at the foremost crystal side is 3-fold bonded with atoms at the crystal side (2 with atoms at an inner layer and 1 with atom at the same layer), and has formed one bond on average with atoms at the amorphous side. It is not clear how the atom from the amorphous side is bonded across the interface. We can study the bonding lengths bonding angles between different pair of atoms to identify the geometric structure of local atomic bonding. This study will offer more detailed structural information about the interface. Also, our current study, the system size is not large enough. It will be desirable to study a large system size with over 100 atoms per layer, which will then allow us to perform more structural detailed analysis of the interface and to identify possible defects such as voids or dislocations.

The c/a interface we have constructed is on (100) plane of β-SiC. Using the same methodology, we can construct c/a interfaces on different crystallographic planes of β-SiC. Particularly, if the interface can be formed on a glide $\{111\}$ plane of β-SiC, the interface will be much stronger than the one we have studied because atoms at the glide $\{111\}$ have initially 3 dangling bonds and can form significant bonding with atoms at the amorphous side. And therefore, the work of adhesion calculated from the glide $\{111\}$ c/a interface will be larger than the (100) interface we have studied. By doing this, one is able to relate the work of adhesion to different structures of the interface and to establish structure-property correlation.

While the work of adhesion is regarded as the intrinsic toughness of the interface, for interfaces with pre-existing cracks, the fracture toughness K_c is an important quantity that controls the interfacial fracture behavior. An important future work is to study the interface crack tip response by an integrated approach combining molecular dynamics simulations and elastic dislocation nucleation theory[124][125]. Such an approach will allow us to examine the interface crack tip response under external loading, to study the competition between atomic decohesion and dislocation nucleation at the crack tip under different stress and temperature conditions, and to study the brittleness or ductility of the interface. During such studies, detailed atom-

istic analysis of stresses and displacements near the crack tip will lead to significant understanding of the shear-coupling nature of an interface crack.

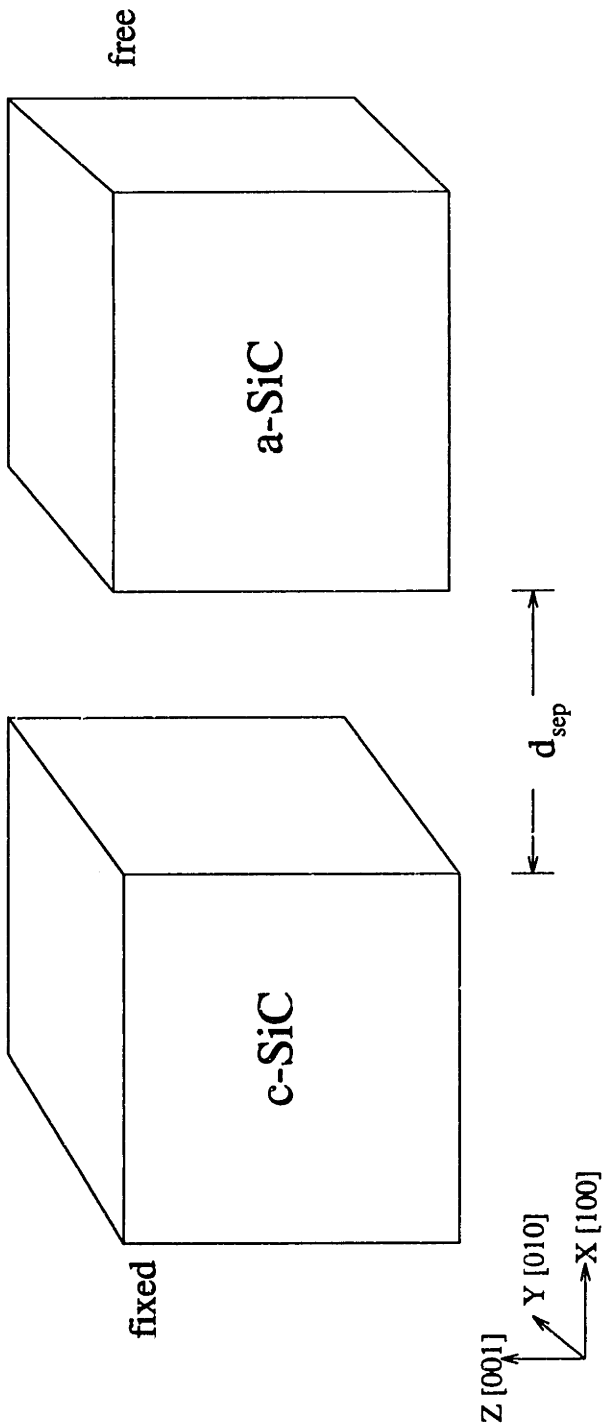

Figure 7-1: Schematic representation of the methodology to construct a c/a SiC interface.

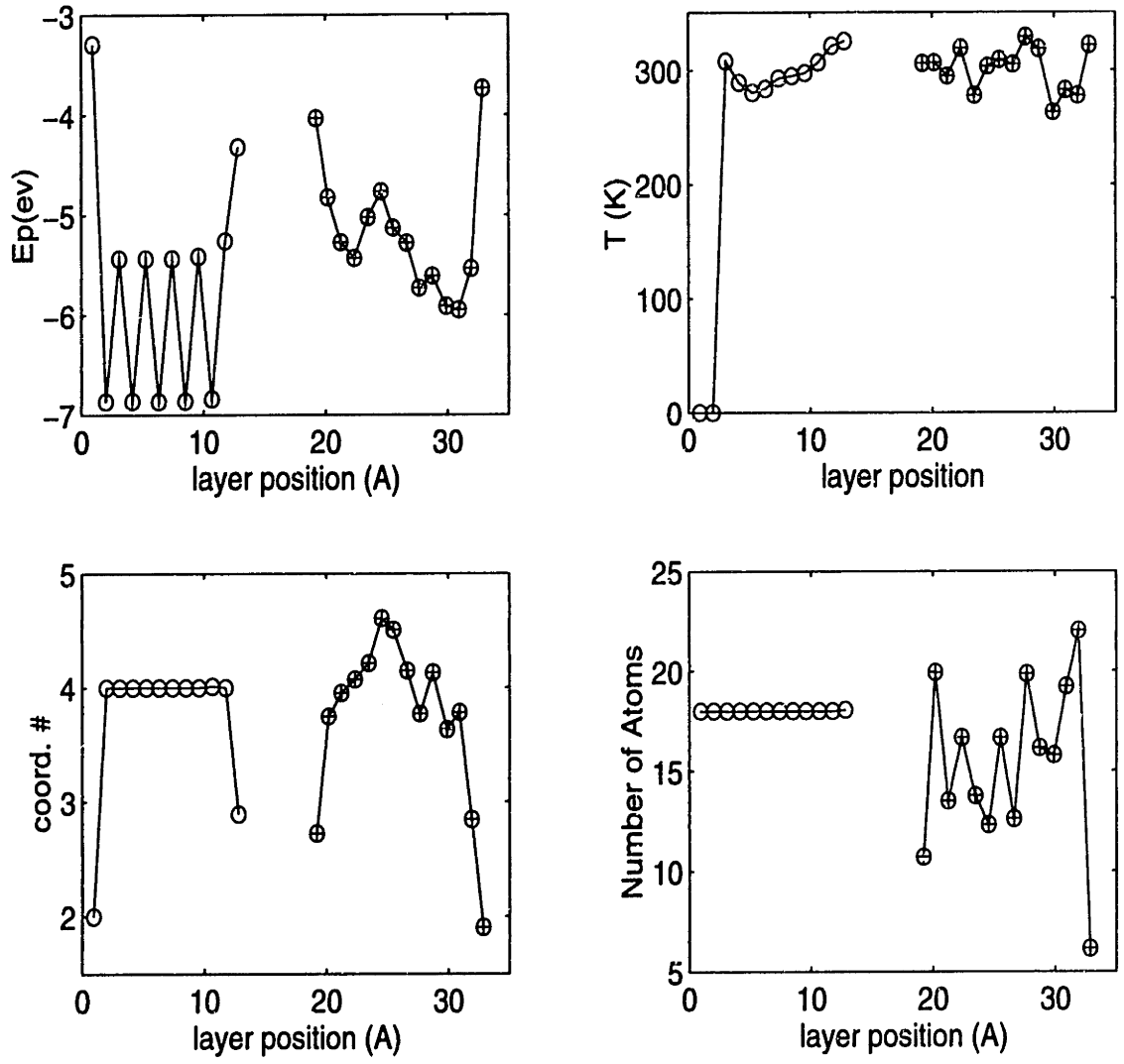

Figure 7-2: Layer profile of structure and properties of crystalline and amorphous SiC before interface formation. (a) Potential energy $E_p(eV)$; (b) temperature $T(K)$; (c) coordination number; and (d) number of atoms. Circles: crystalline side; circles with crosses inside: amorphous side.

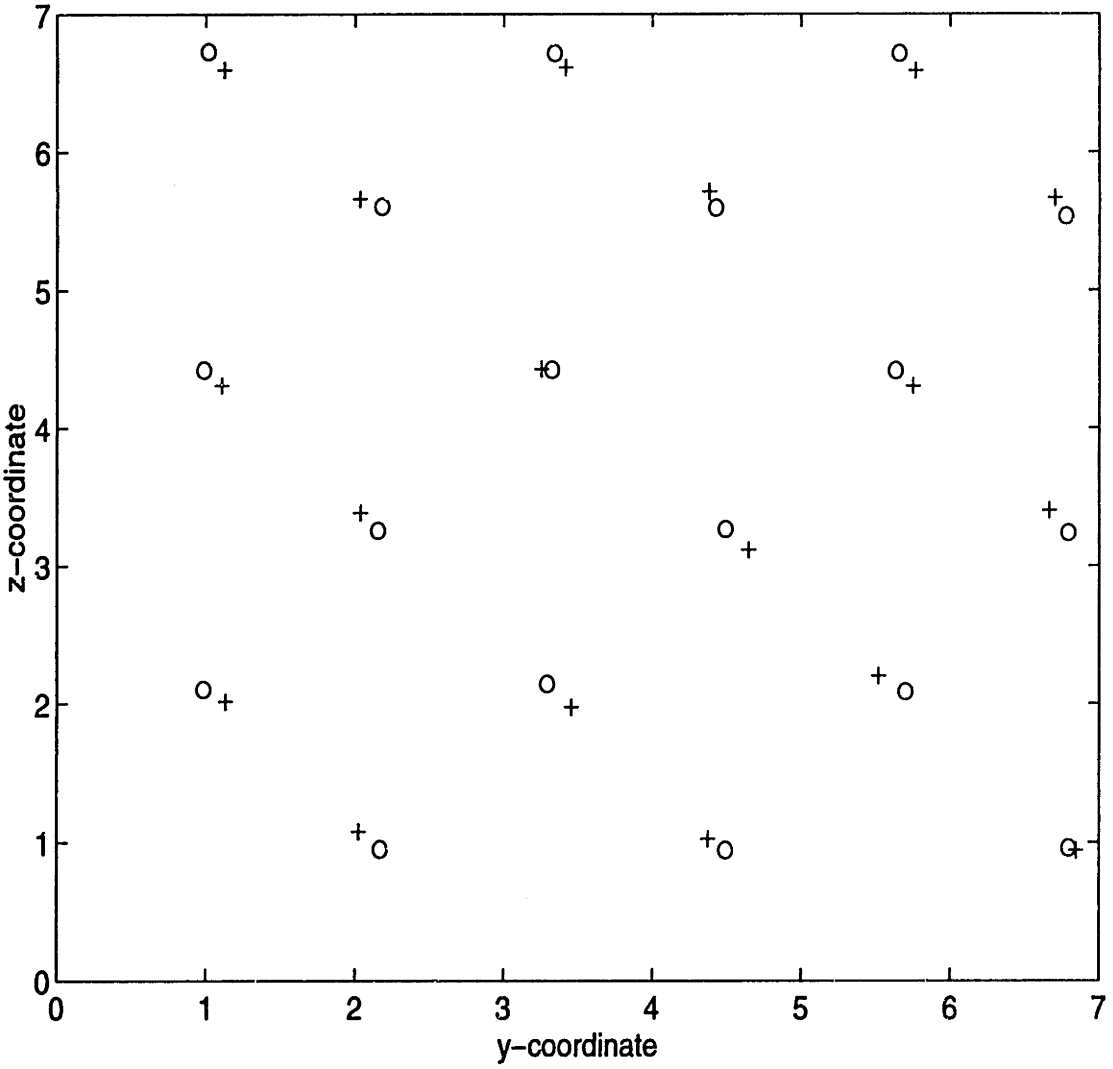

Figure 7-3: Reconstruction of the (100) β-SiC surface. Circles: before relaxation; crosses: after relaxation at $300K$.

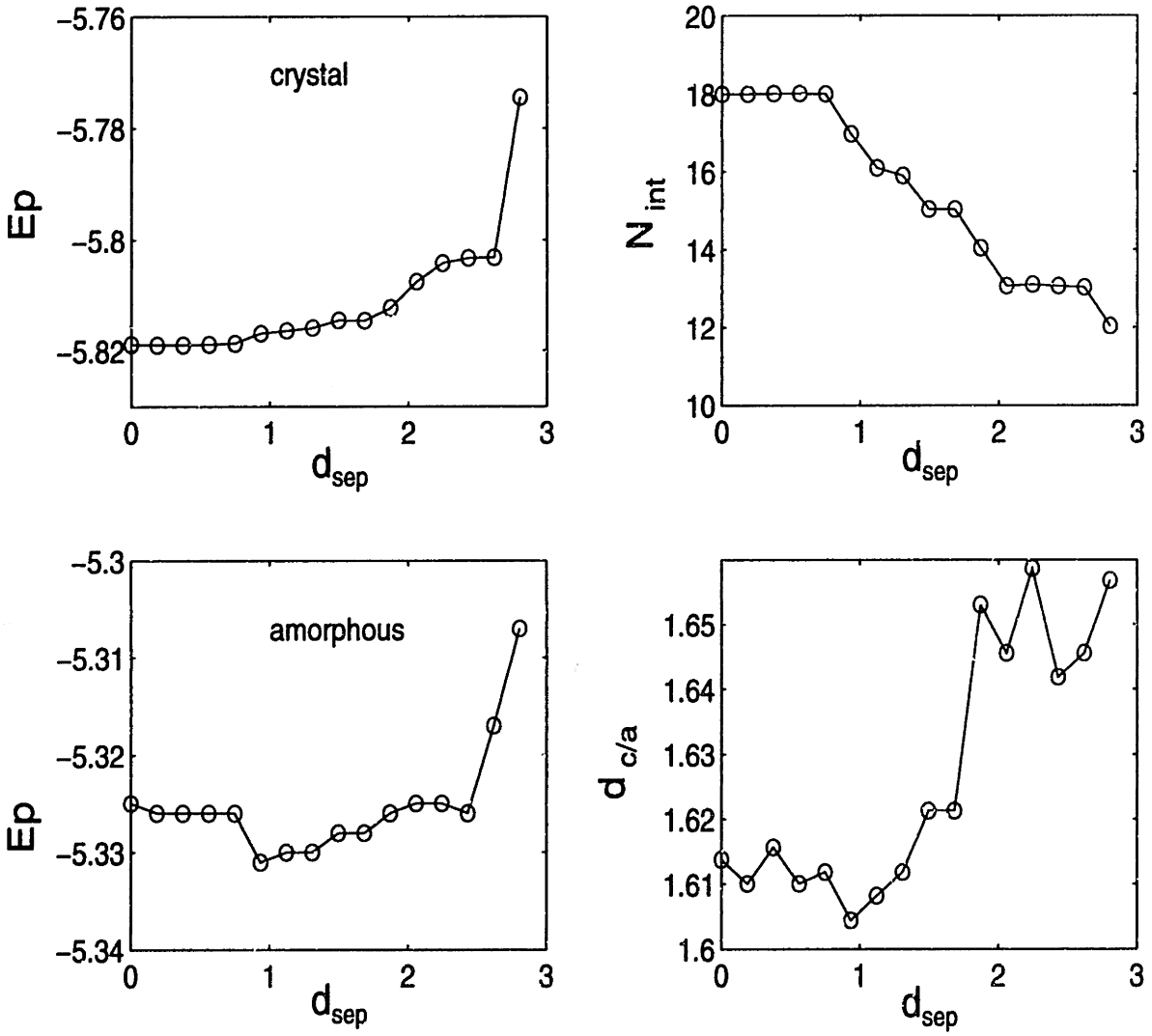

Figure 7-4: Property variation during interface formation. (a) Potential energy per atom in the crystal side; (b) potential energy per atom in the amorphous side; (c) number of atoms forming bonds across the interface; (d) distance between layer 12 and layer 13. d_{sep} is the pulling distance between the two simulation cells for crystal and amorphous SiC.

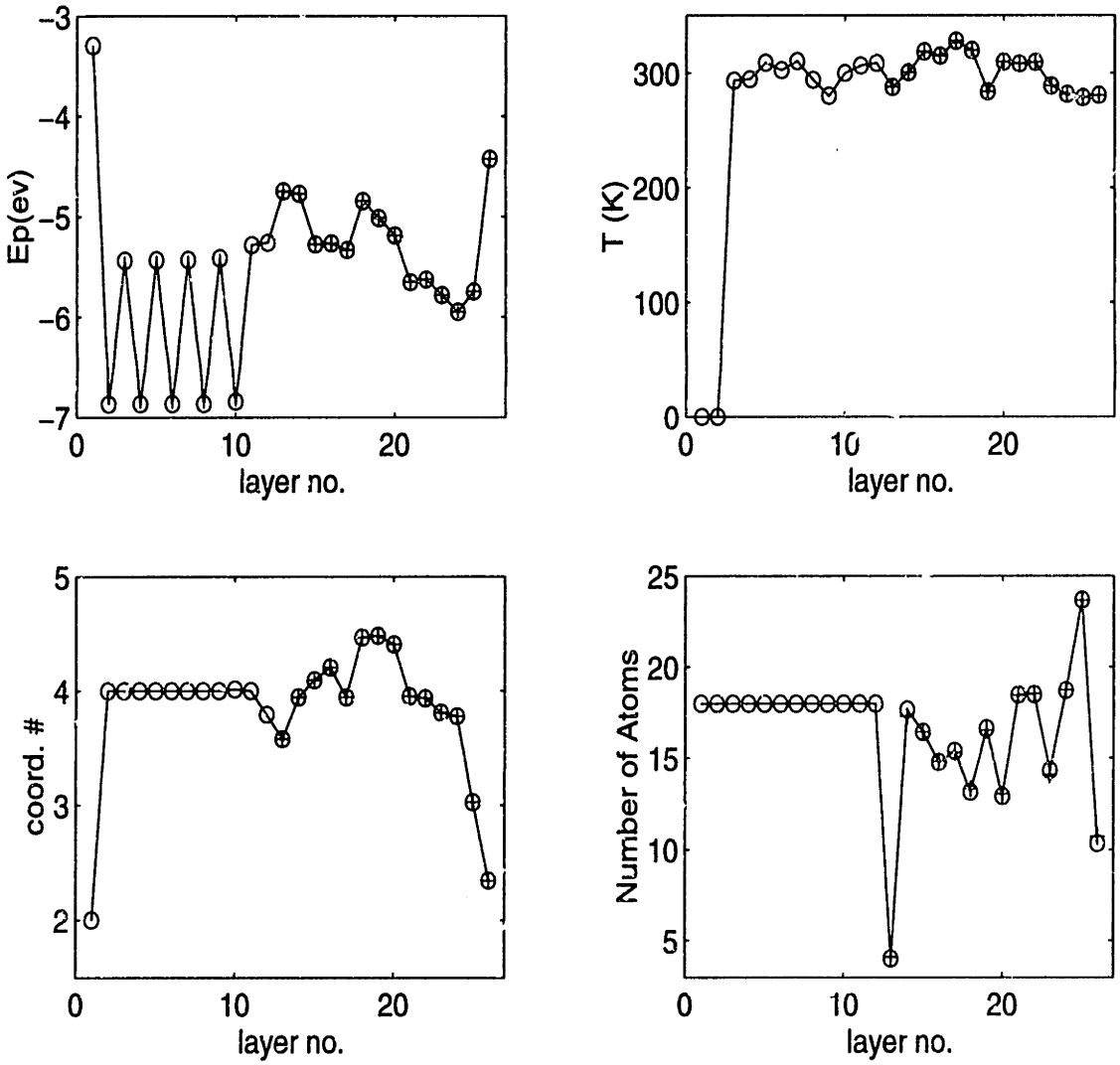

Figure 7-5: Layer profile of structure and properties across the c/a interface. (a) Potential energy $E_p(eV)$; (b) temperature $T(K)$; (c) coordination number; and (d) number of atoms per layer. Circles: crystalline side; circles with crosses inside: amorphous side.

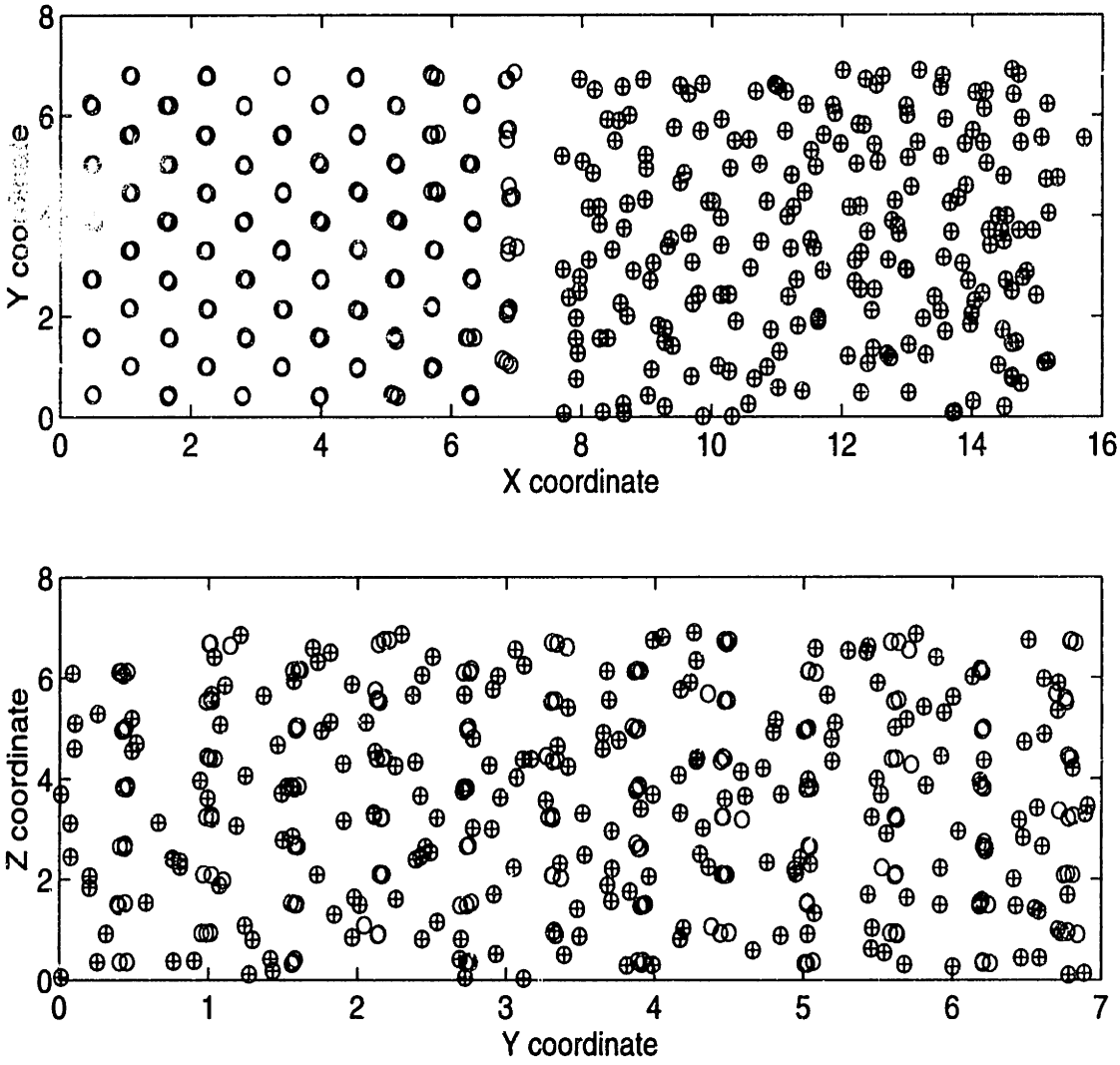

Figure 7-6: Projectins of atomic configuration of the c/a interface. Circles: atoms at the crystal side; circles with crosses inside: atoms at the amorphous side.

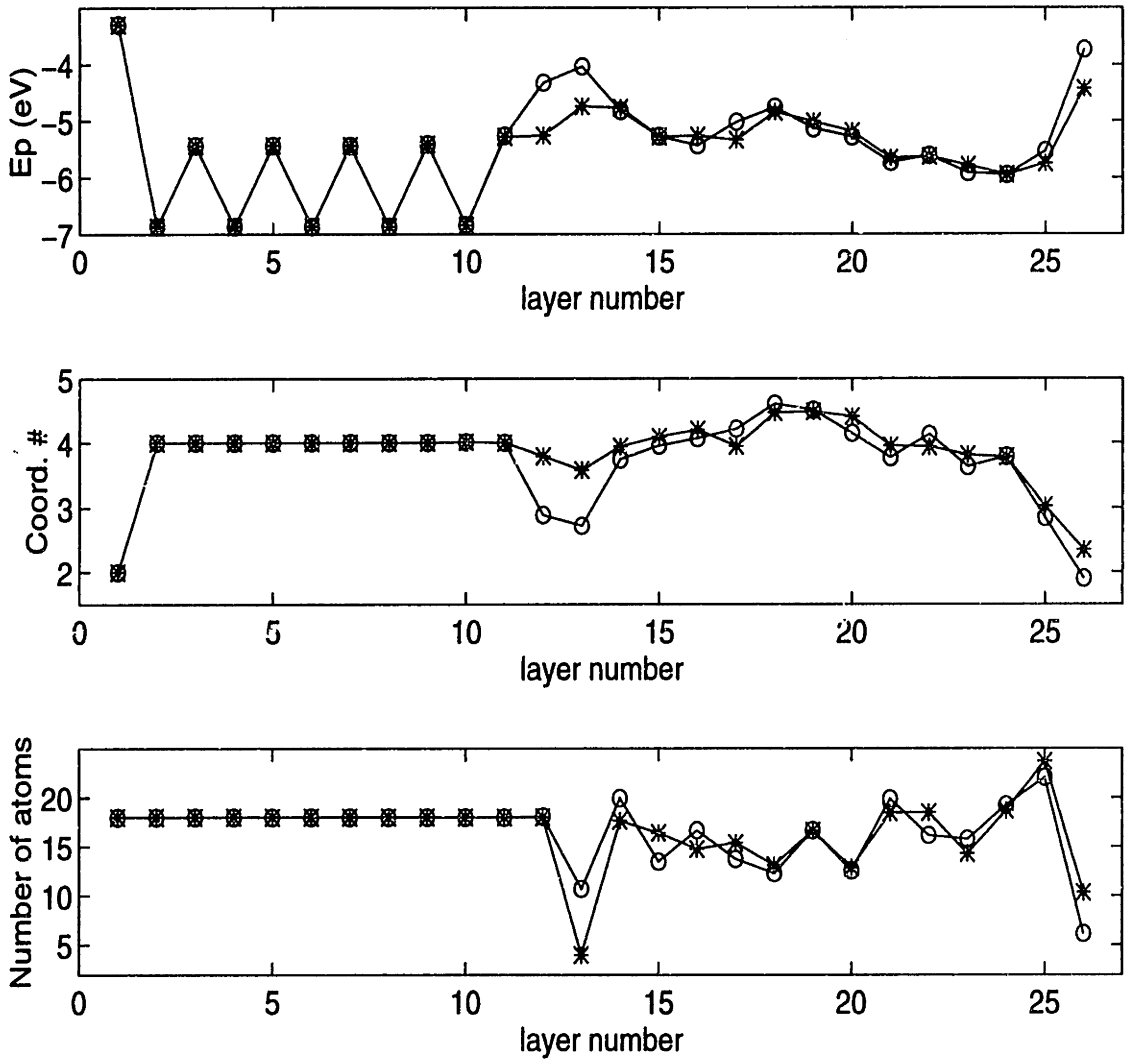

Figure 7-7: System properties before (circles) and after (stars) the interface formation. From top to bottom, (a) potential energy layer distribution; (b) coordination number layer distribution; (c) number of atoms per layer.

Chapter 8

Conclusions and Discussions

8.1 Conclusions

The elastic stability and structural response of β-SiC under external stress have been studied using an integrated approach combining molecular dynamics simulations with the newly formulated elastic stability analysis in the framework of the modified Tersoff potential. The major results and achievements from this study are summarized below followed by detailed discussions of their significance and implications.

- The many-body Tersoff potential has been modified and implemented with capability to calculate elastic constants of β-SiC under any stress and temperature condition. Molecular dynamics simulations using the Parrinello-Rahman technique have been carried out to study structural changes in β-SiC. Independent elastic stability analysis based on stiffness coefficients have been performed for β-SiC under hydrostatic tension and compression.

- Under hydrostatic tension and at room temperature, when the spinodal instability is violated, β-SiC loses its cohesion and fails by crack nucleation and brittle fracture along the shuffle $\{111\}$ plane, which is the plane with the lowest surface energy.

- Under hydrostatic compression and at room mperature, β-SiC undergoes pressure-induced amorphization which is driv he shear instability (C_{44} –

P). The critical internal strain relaxation is responsible for the vanishing of the shear instability and leading to the disordering.

- An analysis using two simplified potential models of SiC reveals that the existence of the atomic size disparity of Si and C atoms is essential for the amorphization of β-SiC. Without this disparity, polymorphic phase transformation would occur instead in β-SiC under compression.

To the field of atomistic simulation, significant contributions of this thesis include analytical derivations of the interatomic force, atomic stress and especially the elastic constants for the complicated many-body Tersoff potential. In the past, the Tersoff potential has been used to calculate only energy and at most atomic forces of the systems being studied. To our knowledge, this is the first time that the fluctuation formulae of elastic constants are properly derived for the Tersoff potential as has been shown in this thesis. The derivation has been verified self-consistently with the direct stress-strain method for elastic constants calculations. The fluctuation formulae offer a powerful method to calculate elastic constants under any stress and temperature conditions. This capability has formed a solid foundation of this thesis. The elastic stability analysis would be impossible without this capability.

The original Tersoff potential is useful in describing the mechanical properties of β-SiC at low temperature ($0K$). From this potential, the three elastic constants of β-SiC are calculated to be $C_{11} = 4.36Mbar$, $C_{12} = 1.20Mbar$ and $C_{44} = 2.55Mbar$ compared to the experimental data of $3.90Mbar$, $1.42Mbar$ and $2.56Mbar$ respectively at room temperature. The results are satisfactory considering the fact that the potential function has not been fitted to elastic constants. However, temperature dependence of the elastic constants can not be correctly described by the original Tersoff potential. As a result, the elastic constants calculated at room temperature ($C_{11} = 5.23Mbar$, $C_{12} = 1.63Mbar$ and $C_{44} = 3.13Mbar$) are inconsistent with the experimental data. Our modified Tersoff potential, on the other hand, not only keeps the same elastic constants at $0K$, but also correctly describes the temperature dependence of the elastic constants. The room temperature elastic constants of β-SiC

calculated from the modified Tersoff potential are $C_{11} = 4.25Mbar$, $C_{12} = 1.18Mbar$ and $C_{44} = 2.66Mbar$, which are in excellent agreement with that of the experimental data. Importantly, the close agreement in C_{44} demonstrates that the modified Tersoff potential can describe very well the angular dependent forces in covalent SiC.

In studies of mechanical behavior of materials that employ empirical potential functions, the correct elastic constants are of critical importance. It is the elastic constants that eventually determine the elastic instabilities and the nature of structural changes of the material. We have demonstrated clearly in this thesis that although two potential models can predict the same cohesive energy, lattice constant and even bulk modulus, they can predict very different elastic constants. As a result, the instability mechanism and the final structural change predicted by these two models are fundamentally different. This emphasizes the importance of our modification of the original Tersoff potential to obtain correct elastic constants at room temperature.

By applying the new instability criteria based on stiffness coefficients to study the stability of β-SiC, we have clearly seen the effects of external loading on the stability of the system. In general, the effects of hydrostatic tension are to enhance the stability against shear and lower the stability against effective lattice cohesion. While these effects are similar in both covalent and metallic materials, the actual structural responses of the two types of materials are quite different at the instability points where the crystals lose their cohesion. At low temperatures, Au metal loses its cohesion by cavitation[17]; on the other hand, when decohesion occurs in β-SiC, cracks nucleate on well defined crystallographic planes and the system fails by cleavage fracture. This indicates the much more brittle nature of β-SiC compared to a simple metal.

The underlying physics for the differences between covalent and metallic materials originate from different atomic binding in the two systems. In metals, atoms are closely packed with 12 nearest neighbors in simple fcc structures; while in covalent β-SiC, atoms are only 4-fold bonded with their nearest neighbors and each bond is highly directional. As a result, different surface planes of β-SiC have very different surface energies. Therefore, when decohesion occurs, the crystal tends to crack along

the lowest surface energy plane, i.e., the shuffle {111} plane of β-SiC. Also, in covalent materials, the binding strength between each pair of atoms is much stronger than that in a metal. Thus, a much larger force exerts on an atom after a covalent bond is broken in decohesion. This large directional force causes atoms to loose decohesion in a fast and clean manner and allows cracks penetrating through the material, which results in cleavage fracture. The large forces can quickly bring atoms exposed at the cracked surfaces to reach their new equilibrium positions. Thus, spontaneous surface relaxation is observed along with the process of crack propagation.

While decohesion under tension is a general behavior of covalent materials, the structural response of covalent materials under compression is more complicated. Since covalent materials have open structures, under compression, different structural behavior may occur. A study of crystalline Si shows a polymorphic phase transformation[24], while our study of β-SiC reveals a pressure-induced amorphization. Under compression, the effect of the hydrostatic pressure is to enhance the lattice bulk modulus, but the effects on the two shear instabilities are rather complicated. In the case of Si, the instability mechanism under compression is the tetragonal shear which results in a phase transformation from diamond cubic to β-tin. For β-SiC, the instability mechanism is pure shear instability under compression. Particularly, the shear instability of β-SiC is related to the internal strain relaxation that occurs between the two types of atoms (Si and C) inside a primitive cell when a macroscopic shear strain is applied. The effect of the hydrostatic compression to β-SiC is to increase the internal strain relaxation in correspondence with the same global shear strain. When the pressure is high enough, the internal strain relaxation reaches a critical state that brings down the shear stability of the system to zero and triggers the order-disorder transition in β-SiC.

Although internal strain relaxation exists in any non-Bravais lattices including Si and SiC, it does not play a dominant role in the instability of Si. The difference between Si and SiC originates from additional effect of chemical ordering in β-SiC, i.e., the atomic size difference between Si and C atoms and the chemical preference of mixed bonds. The atomic size difference in β-SiC is found to be essential for the

amorphization process under compression. Physically, the size difference of the two atoms inside a primitive cell changes the response of local strain, and as a result, the atomic size effect significantly changes the elastic constants of C_{11}, C_{22} and C_{44}. With the atomic size disparity suppressed, the instability mechanism of β-SiC under compression would change from shear to tetragonal shear, and the structural response of β-SiC would change from solid-state amorphization to polymorphic phase transformation. Therefore, the atomic size difference is a crucial factor in the amorphization of binary materials, which has already been noticed in experiments[106].

Finally, we have carried out a preliminary study of the crystalline/amorphous interface in SiC in Chapter 7. We have shown the feasibility of using atomistic simulations to analyze the interface structure and bonding. We have also estimated the work of adhesion of the interface model.

We end this conclusion by pointing out the general implications of this thesis work. We have shown the practical feasibility of modeling mechanical behavior of homogeneous crystals under stress. We have demonstrated that the stability criteria based on the stiffness coefficients are correct for hydrostatic loadings, and the combined approach of the elastic stability analysis and the MD simulations are capable to provide a comprehensive understanding of the elastic instabilities and unstable structural responses of crystals. Most significantly, we have illustrated that well-defined manipulation of interatomic interactions can lead to new insights into complex problems that are otherwise almost inaccessible by usual means of simulation or experiments.

8.2 Discussions and Future Work

In this thesis, we have presented results of our investigations of β-SiC which combine MD simulations and elastic stability analysis. This work constitutes the first systematic study of the mechanical behavior of β-SiC under stress. It has obtained an important understanding of the fundamental problems associated with the ideal crystal strength of β-SiC. The results obtained in this thesis will be useful for further investigation of the structural and mechanical behavior of the SiC system under com-

plicated loading situations such as in a fiber reinforced matrix composite material. Also, the results will help future studies to investigate the mechanical stability and structural transition of β-SiC crystals with structural defects such as point defects, impurities and interfaces. The defected materials are of practical importance and interest in the sense that any man-made materials have more or less defects in the structure.

As pointed out previously, the roles played by defects in the structural transition of a crystal are open for study, especially in the context of elastic stability analysis. It deserves extensive future study. The difficulty of this study will be to develop an effective method to calculate elastic constants in an inhomogeneous system. Local region with defects can have very different elastic behavior from that of defect-free regions. Under an external loading, the instability criteria could be violated first in the local region. Thus, it is crucial to be able to characterize the local elastic constants. Methodologies of calculating local elastic constants have been proposed and applied in crystals with grain boundaries[114][115]. If the methodologies can be extended to crystals with defects in general, similar elastic stability analysis combined with molecular dynamics simulations can be applied to study the elastic stability and structural response of defected crystals so that the roles of defects in the structural transitions can be explored.

In our tension study of β-SiC, the process of crack nucleation is due to lattice decohesion as the spinodal instability is violated. While this study has focused on the initiation of cracks in β-SiC, another fundamental and important problem is regarding the inherent strength and deformability of a crystal with pre-existing crack tips. Under an external stress, the existing cracks will propagate at a critical point. It is essential to study the response of crack tips and to understand how the crack tip behavior is affected by various conditions such as temperatures. An atomistic study combining molecular dynamics simulations and elastic dislocation analysis[126] has been performed for iron[38][127], where brittle to ductile transition is observed at high temperature. Similar methodology can be applied to β-SiC with incorporation of the newly formulated dislocation nucleation theory based on the Peierls

framework[128][124]. Such study will focus on the competition between decohesion and shear break down at the crack tip and investigate the crystal fracture toughness. One needs notice that in studying the brittle to ductile transition of materials, additional difficulty exists for simulations of covalent materials since dislocations do not move easily in covalent materials as they do in metallic materials. Recently, Bulatov et al. have developed a novel method to study dislocation motion in Si[46]. Similar method could be applied to study β-SiC in the future.

In this thesis, our crystalline-amorphous SiC interface model has set up an initial stage to study the challenging problem of interfacial mechanical behavior, which could eventually help to understand the performance of fiber-matrix composite materials in the future. With the constructed interface model, not only can one study the correlation between the interfacial structure and bonding, one can also investigate the correlation between the structure and fracture behavior of bimaterial interfaces[122]. The fracture behavior of an interface is characterized by the fracture toughness K_c or the critical energy release rate G_c. Compared to the fracture problem within an elastically homogeneous media, additional complexities arise for interface fracture problem due to shearing of crack surfaces caused by modulus mismatch[129]. Thus, for interface crack problem, the separate modes of tensile and shear cannot be defined unambiguously. A concept termed *phase angle of loading* ψ is introduced to measure the mixture of shear and tensile opening experienced by the interface crack surface[130]. When a crack is propagating along an interface, the elastic mismatch causes a superposition of a degree of rotation on a stress state by a pure tensile loading. And the phase angle of loading will depend on the rotational displacement as well as the elastic coefficients which can be calculated in terms of two dimensionless Dundurs' parameters[130]. Consequently, one must specify both G and ψ in describing interfacial crack tip opening. The K, G and ψ are important parameters that are used to establish criteria for the maximum interfacial toughness. Combining these criteria with the monolithic fiber toughness of β-SiC (can be obtained from the study mentioned in last paragraph), one is able to investigate the toughness of the fiber-matrix composite, which is a subject which deserves extensive future work.

Appendix A

Derivation of Forces, Stresses and Elastic Constants for Tersoff Potential Function

Let U be the total potential energy of the system; α, β, γ and ϵ stand for the three Cartesian coordinate components x,y or z; i,j,k, l or a, b ... label specific atoms.

Tersoff's potential can be written as:

$$U = \sum_i U_i = \frac{1}{2}\sum_{i\neq j} V_{ij} \tag{A.1}$$

$$V_{ij} = f_c(r_{ij})f_R(r_{ij}) + f_c(r_{ij})b_{ij}f_A(r_{ij}) = V_{ij}^{(2)} + V_{ij}^{(3)} \tag{A.2}$$

$$f_R(r_{ij}) = A_{ij}\exp(-\lambda_{ij}r_{ij}) \tag{A.3}$$

$$f_A(r_{ij}) = -B_{ij}\exp(-\mu_{ij}r_{ij}) \tag{A.4}$$

$$b_{ij} = \chi_{ij}(1+z_{ij}^{n_i})^{-1/2n_i} \tag{A.5}$$

$$z_{ij} = \beta_i\zeta_{ij} = \sum_{k(\neq i,j)} f_c(r_{ik})\beta_i g(\theta_{ijk}) \tag{A.6}$$

$$g(\theta_{ijk}) = 1 + c_i^2/d_i^2 - c_i^2/[d_i^2 + (h_i - \cos\theta_{ijk})^2] \tag{A.7}$$

$$f_c(r_{ij}) = \begin{cases} 1 & r_{ij} < R_{ij} \\ \frac{1}{2} + \frac{1}{2}\cos\left[\frac{\pi(r_{ij}-R_{ij})}{S_{ij}-R_{ij}}\right] & R_{ij} < r_{ij} < S_{ij} \\ 0 & r_{ij} > S_{ij} \end{cases} \tag{A.8}$$

For convenience, in the formulae presented above, we call i an *central atom*, j an *neighbor atom* of i, and k an *environmental atom* of ij pair. Both j and k atoms are within cut-off distance from i atom. Most terms are either constant or only dependent on pair distance r_{ij}. The only many-body term is b_{ij}. $V_{ij}^{(2)}$ only depends on pair distance r_{ij} while $V_{ij}^{(3)}$ depends on distances r_{ij}, r_{ik} and r_{jk} in each ijk triplet of atoms. All notations defined above will be used in the following derivations of forces, stresses(or pressure) and elastic constants.

A.1 Forces

The basic formula of force calculation for any potential energy can be written as:

$$\vec{F}_i = -\frac{\partial U}{\partial \vec{r}_i}, \ or \ \ F_{i\alpha} = -\frac{\partial U}{\partial r_{i\alpha}} \tag{A.9}$$

For Tersoff's potential, the force on atom a can be written as:

$$\vec{F}_a \ = \ -\frac{1}{2} \cdot \frac{\partial}{\partial \vec{r}_a} [\sum_{j(\neq a)} V_{aj} + \sum_{i(\neq a)} V_{ia} + \sum_{i(\neq a)} \sum_{j(\neq i,a)} V_{ij}] \tag{A.10}$$

This calculation is nontrivial compared to other empirical potential functions. The difficulty comes from the many-body term z_{ij} in the potential. The calculation can be very inefficient if not handled properly. Our approach to calculate forces is as follows. Three levels of *do loops* are used. The first *do loop* goes through all the atoms in the system and every atom will have a chance to become *central atom* i sequentially. When *central atom* i is specified, the second level *do loop* are performed twice. For the first time, it goes through all of its neighbors and calculate the many-body term z_{ij}. For the second time, it goes through all of its neighbors and every neighbor will have a chance to become *neighbor atom* j. When such a ij pair is specified, the third *do loop* goes through all the other neighbors exclusive of j and everyone of them will have a chance to become *environmental atom* k of ij pair. Force calculations will be performed for each ijk triplet of atoms thus chosen. For each triplet, we simultaneously calculate forces $\vec{F}_i^c$ on i, $\vec{F}_j^n$ on j and $\vec{F}_k^e$ on k. We can think that

$\vec{F}_i^c$ is the force on i when i acts as a *central atom*, $\vec{F}_j^n$ is the force on j when j acts as a *neighbor atom* and $\vec{F}_k^e$ is the force on k when k acts as an *environmental atom*. Inside each triplet, the three atoms play different roles and each get part of its force calculated. Eventually every atom has equal chances to play the role of *central atom* or *neighbor atom* or *environmental atom*. As shown in Equation (A.10), the first term gives the force on a when it plays the role of *central atom*; the second term gives the force on a when it plays the role of *neighbor atom* and the third term gives the force on a when it plays the role of *environmental atom*. And the sum of the three forces gives the total force on atom a. So only after all the three *do loops* finished, can one get the complete forces on each atom. Also it should be remembered that all forces are many-body terms because of its dependence of z_{ij} which is always calculated before force calculations performed. Now we derive the formulae to calculate $\vec{F}_i^c$, $\vec{F}_j^n$ and $\vec{F}_k^e$ for each ijk triplet:

$$F_{i\alpha}^c = -\frac{1}{2}\cdot\frac{\partial V_{ij}}{\partial r_{i\alpha}} = -\frac{1}{2}[\frac{\partial V_{ij}}{\partial r_{ij}}\cdot\frac{r_{ij\alpha}}{r_{ij}} + \frac{\partial V_{ij}}{\partial r_{ik}}\cdot\frac{r_{ik\alpha}}{r_{ik}}] \tag{A.11}$$

$$F_{j\alpha}^n = -\frac{1}{2}\cdot\frac{\partial V_{ij}}{\partial r_{j\alpha}} = -\frac{1}{2}[\frac{\partial V_{ij}}{\partial r_{ji}}\cdot\frac{r_{ji\alpha}}{r_{ji}} + \frac{\partial V_{ij}}{\partial r_{jk}}\cdot\frac{r_{jk\alpha}}{r_{jk}}] \tag{A.12}$$

$$F_{k\alpha}^e = -\frac{1}{2}\cdot\frac{\partial V_{ij}}{\partial r_{k\alpha}} = -\frac{1}{2}[\frac{\partial V_{ij}}{\partial r_{ik}}\cdot\frac{r_{ki\alpha}}{r_{ik}} + \frac{\partial V_{ij}}{\partial r_{jk}}\cdot\frac{r_{kj\alpha}}{r_{jk}}] \tag{A.13}$$

A.2 Stresses

Atomic stresses can be calculated by [34]:

$$\sigma_{\alpha\beta} = \frac{1}{V}[\sum_i m_i v_{i\alpha} v_{i\beta} - \frac{1}{2}\sum_{i\neq j}\frac{\partial U}{\partial r_{ij}}\cdot\frac{r_{ij\alpha}r_{ij\beta}}{r_{ij}}] \tag{A.14}$$

Where the first term is called kinetic term and the second is called Virial term $\sigma'_{\alpha\beta}$. Since:

$$\frac{\partial U}{\partial r_{ij}} = \frac{1}{2}[\frac{\partial V_{ij}}{\partial r_{ij}} + \frac{\partial V_{ji}}{\partial r_{ij}}] + \frac{1}{2}\sum_{k(\neq i,j)}[\frac{\partial V_{ik}}{\partial r_{ij}} + \frac{\partial V_{ki}}{\partial r_{ij}} + \frac{\partial V_{jk}}{\partial r_{ij}} + \frac{\partial V_{kj}}{\partial r_{ij}}] \tag{A.15}$$

We obtain:

$$\begin{aligned}\sigma'_{\alpha\beta} &= -\frac{1}{2}\cdot\frac{1}{V}\sum_{i\neq j}\frac{\partial U}{\partial r_{ij}}\cdot\frac{r_{ij\alpha}r_{ij\beta}}{r_{ij}} \\ &= -\frac{1}{4V}\sum_{i\neq j}[\frac{\partial V_{ij}}{\partial r_{ij}}+\frac{\partial V_{ji}}{\partial r_{ij}}+\sum_{k(\neq i,j)}(\frac{\partial V_{ik}}{\partial r_{ij}}+\frac{\partial V_{ki}}{\partial r_{ij}}+\frac{\partial V_{jk}}{\partial r_{ij}}+\frac{\partial V_{kj}}{\partial r_{ij}})]\frac{r_{ij\alpha}r_{ij\beta}}{r_{ij}} \quad \text{(A.16)}\end{aligned}$$

By rearranging dummy indices, we obtain:

$$\sigma'_{\alpha\beta} = -\frac{1}{2V}\sum_{i\neq j}\{\frac{\partial V_{ij}}{\partial r_{ij}}\cdot\frac{r_{ij\alpha}r_{ij\beta}}{r_{ij}}+\sum_{k(\neq i,j)}[\frac{\partial V_{ij}}{\partial r_{ik}}\cdot\frac{r_{ik\alpha}r_{ik\beta}}{r_{ik}}+\frac{\partial V_{ij}}{\partial r_{jk}}\cdot\frac{r_{jk\alpha}r_{jk\beta}}{r_{jk}}]\} \quad \text{(A.17)}$$

A.3 Elastic Constants

Elastic constants are calculated by fluctuation formulae [34]. From this formulae, elastic constant consists of three terms, i.e., *kinetic term* $C^k_{\alpha\beta\gamma\epsilon}$, *fluctuation term* $C^f_{\alpha\beta\gamma\epsilon}$ and *Born term* $C^B_{\alpha\beta\gamma\epsilon}$. For cubic system, it's easily shown that for any potential function the formulae can be written as:

$$\begin{aligned}C_{\alpha\beta\gamma\epsilon} &= \frac{l_0}{l}\cdot[-\frac{V}{k_BT}\cdot\delta(\sigma_{\alpha\beta}\sigma_{\gamma\epsilon})+\frac{2Nk_BT}{V}\cdot(\delta_{\alpha\epsilon}\delta_{\beta\gamma}+\delta_{\alpha\gamma}\delta_{\beta\epsilon}) \\ &\quad +<\frac{1}{V}\sum_{i<j}\sum_{k<l}[\frac{\partial^2U}{\partial r_{ij}\partial r_{kl}}-\frac{\partial U}{\partial r_{ij}}\cdot\frac{\delta_{ik}\delta_{jl}}{r_{ij}}]\frac{r_{ij\alpha}r_{ij\beta}r_{kl\gamma}r_{kl\epsilon}}{r_{ij}r_{kl}}>] \quad \text{(A.18)}\end{aligned}$$

where bracket <> represents the ensemble average; $\delta_{\alpha\epsilon}$'s are the Kronecker functions and $\delta(AB) =< AB > - < A >< B >$. For Tersoff's potential:

$$\begin{aligned}C^B_{\alpha\beta\gamma\epsilon} &= <\frac{1}{V}\sum_{i<j}\sum_{k<l}[\frac{\partial^2U}{\partial r_{ij}\partial r_{kl}}-\frac{\partial U}{\partial r_{ij}}\cdot\frac{\delta_{ik}\delta_{jl}}{r_{ij}}]\frac{r_{ij\alpha}r_{ij\beta}r_{kl\gamma}r_{kl\epsilon}}{r_{ij}r_{kl}}> \\ &= <\frac{1}{V}\cdot\frac{1}{2}\sum_{i\neq j}[\frac{1}{2}\sum_{k\neq l}\frac{\partial^2U}{\partial r_{ij}\partial r_{kl}}\cdot\frac{r_{ij\alpha}r_{ij\beta}r_{kl\gamma}r_{kl\epsilon}}{r_{ij}r_{kl}}-\frac{\partial U}{\partial r_{ij}}\cdot\frac{r_{ij\alpha}r_{ij\beta}r_{ij\gamma}r_{ij\epsilon}}{r^3_{ij}}]> \\ &= <\frac{1}{V}C^B_1>-<\frac{1}{V}C^B_2> \quad \text{(A.19)}\end{aligned}$$

Where use Equation (A.15), we can easily obtain the second term above:

$$\begin{aligned} C_2^B &= \frac{1}{2}\sum_{i\neq j}\frac{\partial U}{\partial r_{ij}}\cdot\frac{r_{ij\alpha}r_{ij\beta}r_{ij\gamma}r_{ij\epsilon}}{r_{ij}^3} \\ &= \frac{1}{2}\sum_{i\neq j}\frac{\partial V_{ij}}{\partial r_{ij}}\cdot\frac{r_{ij\alpha}r_{ij\beta}r_{ij\gamma}r_{ij\epsilon}}{r_{ij}^3}+ \\ &\quad \frac{1}{2}\sum_{i(\neq j)}\sum_{k(\neq i,j)}[\frac{\partial V_{ij}}{\partial r_{ik}}\cdot\frac{r_{ik\alpha}r_{ik\beta}r_{ik\gamma}r_{ik\epsilon}}{r_{ik}^3}+\frac{\partial V_{ij}}{\partial r_{jk}}\cdot\frac{r_{jk\alpha}r_{jk\beta}r_{jk\gamma}r_{jk\epsilon}}{r_{jk}^3}] \end{aligned} \quad (A.20)$$

We can obtain:

$$\begin{aligned} C_1^B &= \frac{1}{4}\sum_{i\neq j}\sum_{k\neq l}\frac{\partial^2 U}{\partial r_{ij}\partial r_{kl}}\cdot\frac{r_{ij\alpha}r_{ij\beta}r_{kl\gamma}r_{kl\epsilon}}{r_{ij}r_{kl}} \\ &= \frac{1}{2}\sum_{i\neq j}\frac{\partial^2 U}{\partial r_{ij}^2}\cdot\frac{r_{ij\alpha}r_{ij\beta}r_{ij\gamma}r_{ij\epsilon}}{r_{ij}^2}+\frac{1}{4}\sum_{i\neq j}\sum_{l\neq m(l,m\neq i,j)}\frac{\partial^2 U}{\partial r_{ij}\partial r_{lm}}\cdot\frac{r_{ij\alpha}r_{ij\beta}r_{lm\gamma}r_{lm\epsilon}}{r_{ij}r_{lm}}+ \\ &\quad \frac{1}{2}\sum_{i\neq j}\sum_{l(\neq i,j)}[\frac{\partial^2 U}{\partial r_{ij}\partial r_{il}}\cdot\frac{r_{ij\alpha}r_{ij\beta}r_{il\gamma}r_{il\epsilon}}{r_{ij}r_{il}}+\frac{\partial^2 U}{\partial r_{ij}\partial r_{jl}}\cdot\frac{r_{ij\alpha}r_{ij\beta}r_{jl\gamma}r_{jl\epsilon}}{r_{ij}r_{jl}}] \end{aligned} \quad (A.21)$$

Since

$$\begin{aligned} \frac{\partial^2 U}{\partial r_{ij}\partial r_{il}} &= \frac{1}{2}\{\frac{\partial^2 V_{ij}}{\partial r_{ij}\partial r_{il}}+\frac{\partial^2 V_{ji}}{\partial r_{ij}\partial r_{il}}+\sum_{k(\neq i,j)}[\frac{\partial^2 V_{ik}}{\partial r_{ij}\partial r_{il}}+\frac{\partial^2 V_{ki}}{\partial r_{ij}\partial r_{il}}]+\frac{\partial^2 V_{jl}}{\partial r_{ij}\partial r_{il}}+\frac{\partial^2 V_{lj}}{\partial r_{ij}\partial r_{il}}\} \\ \frac{\partial^2 U}{\partial r_{ij}\partial r_{jl}} &= \frac{1}{2}\{\frac{\partial^2 V_{ij}}{\partial r_{ij}\partial r_{jl}}+\frac{\partial^2 V_{ji}}{\partial r_{ij}\partial r_{jl}}+\sum_{k(\neq i,j)}[\frac{\partial^2 V_{jk}}{\partial r_{ij}\partial r_{jl}}+\frac{\partial^2 V_{kj}}{\partial r_{ij}\partial r_{jl}}]+\frac{\partial^2 V_{il}}{\partial r_{ij}\partial r_{jl}}+\frac{\partial^2 V_{li}}{\partial r_{ij}\partial r_{jl}}\} \\ \frac{\partial^2 U}{\partial r_{ij}^2} &= \frac{1}{2}\{\frac{\partial^2 V_{ij}}{\partial r_{ij}^2}+\frac{\partial^2 V_{ji}}{\partial r_{ij}^2}+\sum_{k(\neq i,j)}[\frac{\partial^2 V_{ik}}{\partial r_{ij}^2}+\frac{\partial^2 V_{ki}}{\partial r_{ij}^2}+\frac{\partial^2 V_{jk}}{\partial r_{ij}^2}+\frac{\partial^2 V_{kj}}{\partial r_{ij}^2}]\} \end{aligned} \quad (A.22)$$

We can obtain:

$$\begin{aligned} C_1^B &= \frac{1}{2}\sum_{i\neq j}\{\frac{\partial^2 V_{ij}}{\partial r_{ij}^2}\cdot\frac{r_{ij\alpha}r_{ij\beta}r_{ij\gamma}r_{ij\epsilon}}{r_{ij}^2} \\ &\quad +\sum_{k(\neq i,j)}[\frac{\partial^2 V_{ij}}{\partial r_{ik}^2}\cdot\frac{r_{ik\alpha}r_{ik\beta}r_{ik\gamma}r_{ik\epsilon}}{r_{ik}^2}+\frac{\partial^2 V_{ij}}{\partial r_{jk}^2}\cdot\frac{r_{jk\alpha}r_{jk\beta}r_{jk\gamma}r_{jk\epsilon}}{r_{jk}^2} \\ &\quad +\frac{\partial^2 V_{ij}}{\partial r_{ij}\partial r_{ik}}\cdot\frac{r_{ij\alpha}r_{ij\beta}r_{ik\gamma}r_{ik\epsilon}+r_{ik\alpha}r_{ik\beta}r_{ij\gamma}r_{ij\epsilon}}{r_{ij}r_{ik}}+\frac{\partial^2 V_{ij}}{\partial r_{ij}r_{jk}}\cdot\frac{r_{ij\alpha}r_{ij\beta}r_{jk\gamma}r_{jk\epsilon}+r_{jk\alpha}r_{jk\beta}r_{ij\gamma}r_{ij\epsilon}}{r_{ij}r_{jk}} \\ &\quad +\frac{\partial^2 V_{ij}}{\partial r_{ik}\partial r_{jk}}\cdot\frac{r_{ik\alpha}r_{ik\beta}r_{jk\gamma}r_{jk\epsilon}+r_{jk\alpha}r_{jk\beta}r_{ik\gamma}r_{ik\epsilon}}{r_{ik}r_{jk}}+\sum_{l\neq i,j,k}(\frac{\partial^2 V_{ij}}{\partial r_{ik}\partial r_{il}}\cdot\frac{r_{ik\alpha}r_{ik\beta}r_{il\gamma}r_{il\epsilon}}{r_{ik}r_{il}} \end{aligned}$$

$$+\frac{\partial^2 V_{ij}}{\partial r_{jk}\partial r_{jl}}\cdot\frac{r_{jk\alpha}r_{jk\beta}r_{jl\gamma}r_{jl\epsilon}}{r_{jk}r_{jl}}+\frac{\partial^2 V_{ij}}{\partial r_{ik}\partial r_{jl}}\cdot\frac{r_{ik\alpha}r_{ik\beta}r_{jl\gamma}r_{jl\epsilon}+r_{jl\alpha}r_{jl\beta}r_{ik\gamma}r_{ik\epsilon}}{r_{ik}r_{jl}})]\} \tag{A.23}$$

If we use Voigt's notation, C_{11}, C_{12} and C_{44} are:

$$C_{11} = \frac{l_0}{l}\cdot[-\frac{V}{k_BT}\cdot\delta(\sigma_{xx}\sigma_{xx})+\frac{4Nk_BT}{V}+<\frac{1}{V}C_{11}^B>] \tag{A.24}$$

$$C_{12} = \frac{l_0}{l}\cdot[-\frac{V}{k_BT}\cdot\delta(\sigma_{xx}\sigma_{yy})+<\frac{1}{V}C_{12}^B>] \tag{A.25}$$

$$C_{44} = \frac{l_0}{l}\cdot[-\frac{V}{k_BT}\cdot\delta(\sigma_{yz}\sigma_{yz})+\frac{2Nk_BT}{V}+<\frac{1}{V}C_{44}^B>] \tag{A.26}$$

state or explain how one obtain C_{11}^B, C_{12}^B and C_{44}^B from C_1^B and C_2^B. where

$$\begin{aligned}C_{11}^B = {} & \frac{1}{2}\sum_{i\neq j}\{(\frac{\partial^2 V_{ij}}{\partial r_{ij}^2}-\frac{\partial V_{ij}}{\partial r_{ij}}\cdot\frac{1}{r_{ij}})\frac{x_{ij}^4}{r_{ij}^2}\\ & +\sum_{k(\neq i,j)}[(\frac{\partial^2 V_{ij}}{\partial r_{ik}^2}-\frac{\partial V_{ij}}{\partial r_{ik}}\cdot\frac{1}{r_{ik}})\frac{x_{ik}^4}{r_{ik}^2}+(\frac{\partial^2 V_{ij}}{\partial r_{jk}^2}-\frac{\partial V_{ij}}{\partial r_{jk}}\cdot\frac{1}{r_{jk}})\frac{x_{jk}^4}{r_{jk}^2}+\frac{\partial^2 V_{ij}}{\partial r_{ij}\partial r_{ik}}\cdot\frac{x_{ij}^2x_{ik}^2}{r_{ij}r_{ik}}\\ & +\frac{\partial^2 V_{ij}}{\partial r_{ij}r_{jk}}\cdot\frac{x_{ij}^2x_{jk}^2}{r_{ij}r_{jk}}+\frac{\partial^2 V_{ij}}{\partial r_{ik}\partial r_{jk}}\cdot\frac{2x_{ik}^2x_{jk}^2}{r_{ik}r_{jk}}+\sum_{l\neq i,j,k}(\frac{\partial^2 V_{ij}}{\partial r_{ik}\partial r_{il}}\cdot\frac{x_{ik}^2x_{il}^2}{r_{ik}r_{il}}\\ & +\frac{\partial^2 V_{ij}}{\partial r_{jk}\partial r_{jl}}\cdot\frac{x_{jk}^2x_{jl}^2}{r_{jk}r_{jl}}+\frac{\partial^2 V_{ij}}{\partial r_{ik}\partial r_{jl}}\cdot\frac{2x_{ik}^2x_{jl}^2}{r_{ik}r_{jl}})]\}\end{aligned} \tag{A.27}$$

$$\begin{aligned}C_{12}^B = {} & \frac{1}{2}\sum_{i\neq j}\{(\frac{\partial^2 V_{ij}}{\partial r_{ij}^2}-\frac{\partial V_{ij}}{\partial r_{ij}}\cdot\frac{1}{r_{ij}})\frac{x_{ij}^2y_{ij}^2}{r_{ij}^2}\\ & +\sum_{k(\neq i,j)}[(\frac{\partial^2 V_{ij}}{\partial r_{ik}^2}-\frac{\partial V_{ij}}{\partial r_{ik}}\cdot\frac{1}{r_{ik}})\frac{x_{ik}^2y_{ik}^2}{r_{ik}^2}+(\frac{\partial^2 V_{ij}}{\partial r_{jk}^2}-\frac{\partial V_{ij}}{\partial r_{jk}}\cdot\frac{1}{r_{jk}})\frac{x_{jk}^2y_{jk}^2}{r_{jk}^2}+\frac{\partial^2 V_{ij}}{\partial r_{ij}\partial r_{ik}}\cdot\frac{x_{ij}^2y_{ik}^2}{r_{ij}r_{ik}}\\ & +\frac{\partial^2 V_{ij}}{\partial r_{ij}r_{jk}}\cdot\frac{x_{ij}^2y_{jk}^2}{r_{ij}r_{jk}}+\frac{\partial^2 V_{ij}}{\partial r_{ik}\partial r_{jk}}\cdot\frac{(x_{ik}^2y_{jk}^2+x_{jk}^2y_{ik}^2)}{r_{ik}r_{jk}}+\sum_{l(\neq i,j,k)}(\frac{\partial^2 V_{ij}}{\partial r_{ik}\partial r_{il}}\cdot\frac{x_{ik}^2y_{il}^2}{r_{ik}r_{il}}\\ & +\frac{\partial^2 V_{ij}}{\partial r_{jk}\partial r_{jl}}\cdot\frac{x_{jk}^2y_{jl}^2}{r_{jk}r_{jl}}+\frac{\partial^2 V_{ij}}{\partial r_{ik}\partial r_{jl}}\cdot\frac{x_{ik}^2y_{jl}^2+x_{jl}^2y_{ik}^2}{r_{ik}r_{jl}})]\}\end{aligned} \tag{A.28}$$

$$\begin{aligned}C_{44}^B = {} & \frac{1}{2}\sum_{i\neq j}\{(\frac{\partial^2 V_{ij}}{\partial r_{ij}^2}-\frac{\partial V_{ij}}{\partial r_{ij}}\cdot\frac{1}{r_{ij}})\frac{x_{ij}^2y_{ij}^2}{r_{ij}^2}\\ & +\sum_{k(\neq i,j)}[(\frac{\partial^2 V_{ij}}{\partial r_{ik}^2}-\frac{\partial V_{ij}}{\partial r_{ik}}\cdot\frac{1}{r_{ik}})\frac{x_{ik}^2y_{ik}^2}{r_{ik}^2}+(\frac{\partial^2 V_{ij}}{\partial r_{jk}^2}-\frac{\partial V_{ij}}{\partial r_{jk}}\cdot\frac{1}{r_{jk}})\frac{x_{jk}^2y_{jk}^2}{r_{jk}^2}+\frac{\partial^2 V_{ij}}{\partial r_{ij}\partial r_{ik}}\cdot\frac{x_{ij}y_{ij}x_{ik}y_{ik}}{r_{ij}r_{ik}}\end{aligned}$$

$$+\frac{\partial^2 V_{ij}}{\partial r_{ij} r_{jk}} \cdot \frac{x_{ij} y_{ij} x_{jk} y_{jk}}{r_{ij} r_{jk}} + \frac{\partial^2 V_{ij}}{\partial r_{ik} \partial r_{jk}} \cdot \frac{2 x_{ik} y_{ik} x_{jk} y_{jk}}{r_{ik} r_{jk}} + \sum_{l(\neq i,j,k)} \left(\frac{\partial^2 V_{ij}}{\partial r_{ik} \partial r_{il}} \cdot \frac{x_{ik} y_{ik} x_{il} y_{il}}{r_{ik} r_{il}} \right.$$

$$\left. + \frac{\partial^2 V_{ij}}{\partial r_{jk} \partial r_{jl}} \cdot \frac{x_{jk} y_{jk} x_{jl} y_{jl}}{r_{jk} r_{jl}} + \frac{\partial^2 V_{ij}}{\partial r_{ik} \partial r_{jl}} \cdot \frac{2 x_{ik} y_{ik} x_{jl} y_{jl}}{r_{ik} r_{jl}} \right)] \} \tag{A.29}$$

Up to now, we have worked out the formulae of forces, stresses and elastic constants for Tersoff's potential.

Appendix B

Derivation of Detailed Terms Used in Appendix A

B.1 Terms Used in First Derivatives

$$\begin{aligned}
\frac{\partial V_{ij}}{\partial r_{ij}} &= f_c'[A\exp(-\lambda_{ij}r_{ij}) - Bb_{ij}\exp(-\mu_{ij}r_{ij})] \\
&\quad + f_c[-A\lambda_{ij}\exp(-\lambda_{ij}r_{ij}) + Bb_{ij}\mu_{ij}\exp(-\mu_{ij}r_{ij})] \\
&\quad - f_c B\exp(-\mu_{ij}r_{ij})\cdot\frac{\partial b_{ij}}{\partial r_{ij}} \qquad \text{(B.1)} \\
\frac{\partial V_{ij}}{\partial r_{ik}} &= -f_c B\exp(-\mu_{ij}r_{ij})\cdot\frac{\partial b_{ij}}{\partial r_{ik}} \qquad \text{(B.2)} \\
\frac{\partial V_{ij}}{\partial r_{jk}} &= -f_c B\exp(-\mu_{ij}r_{ij})\cdot\frac{\partial b_{ij}}{\partial r_{jk}} \qquad \text{(B.3)}
\end{aligned}$$

Where

$$\begin{aligned}
f_c' &= -\frac{\pi}{2(S-R)}\sin\frac{\pi(r-R)}{S-R} \qquad \text{(B.4)} \\
\frac{\partial b_{ij}}{\partial r_{ij}} &= \frac{\partial b_{ij}}{\partial z_{ij}}\beta_i\frac{\partial \zeta_{ij}}{\partial r_{ij}};\quad \frac{\partial b_{ij}}{\partial r_{ik}} = \frac{\partial b_{ij}}{\partial z_{ij}}\beta_i\frac{\partial \zeta_{ij}}{\partial r_{ik}};\quad \frac{\partial b_{ij}}{\partial r_{jk}} = \frac{\partial b_{ij}}{\partial z_{ij}}\beta_i\frac{\partial \zeta_{ij}}{\partial r_{jk}} \qquad \text{(B.5)} \\
\frac{\partial b_{ij}}{\partial z_{ij}} &= -\frac{1}{2}\chi_{ij}(1+z_{ij}^{n_i})^{-(1+2n_i)/2n_i}z_{ij}^{n_i-1} \qquad \text{(B.6)} \\
\frac{\partial \zeta_{ij}}{\partial r_{ij}} &= \sum_{k(\neq i,j)} f_c(r_{ik})\cdot\frac{\partial g}{\partial\cos\theta}\cdot\frac{\partial cos\theta}{\partial r_{ij}} \qquad \text{(B.7)}
\end{aligned}$$

$$\frac{\partial \zeta_{ij}}{\partial r_{jk}} = \sum_{k(\neq i,j)} f_c(r_{ik}) \cdot \frac{\partial g}{\partial \cos\theta} \cdot \frac{\partial cos\theta}{\partial r_{jk}} \tag{B.8}$$

$$\frac{\partial \zeta_{ij}}{\partial r_{ik}} = \sum_{k(\neq i,j)} [f_c(r_{ik}) \cdot \frac{\partial g}{\partial \cos\theta} \cdot \frac{\partial cos\theta}{\partial r_{ik}} + f_c'(r_{ik}) g] \tag{B.9}$$

And

$$\frac{\partial g}{\partial \cos\theta} = -\frac{2c_i^2(h_i - \cos\theta)}{[d_i^2 + (h_i - \cos\theta)^2]^2} \tag{B.10}$$

$$\frac{\partial \cos\theta}{\partial r_{ij}} = \frac{1}{r_{ik}} - \frac{cos\theta}{r_{ij}}; \quad \frac{\partial c\upsilon s\theta}{\partial r_{ik}} = \frac{1}{r_{ij}} - \frac{cos\theta}{r_{ik}}; \quad \frac{\partial cos\theta}{\partial r_{jk}} = -\frac{r_{jk}}{r_{ij} r_{ik}} \tag{B.11}$$

B.2 Terms Used in Second Derivatives

$$\begin{aligned}\frac{\partial^2 V_{ij}}{\partial r_{ij}^2} &= f_c''[A\exp(-\lambda_{ij} r_{ij}) - B b_{ij} \exp(-\mu_{ij} r_{ij})] \\ &\quad + 2 f_c'[-A\lambda_{ij} \exp(-\lambda_{ij} r_{ij}) + B b_{ij} \mu_{ij} \exp(-\mu_{ij} r_{ij})] \\ &\quad + f_c[A\lambda_{ij}^2 \exp(-\lambda_{ij} r_{ij}) - B b_{ij} \mu_{ij}^2 \exp(-\mu_{ij} r_{ij})] \\ &\quad + 2(f_c \mu_{ij} - f_c') B \exp(-\mu_{ij} r_{ij}) \frac{\partial b_{ij}}{\partial r_{ij}} - f_c B \exp(-\mu_{ij} r_{ij}) \frac{\partial^2 b_{ij}}{\partial r_{ij}^2}\end{aligned} \tag{B.12}$$

$$\frac{\partial^2 V_{ij}}{\partial r_{ij} \partial r_{ik}} = (f_c \mu_{ij} - f_c') B \exp(-\mu_{ij} r_{ij}) \frac{\partial b_{ij}}{\partial r_{ik}} - f_c B \exp(-\mu_{ij} r_{ij}) \frac{\partial^2 b_{ij}}{\partial r_{ij} \partial r_{ik}} \tag{B.13}$$

$$\frac{\partial^2 V_{ij}}{\partial r_{ij} \partial r_{jk}} = (f_c \mu_{ij} - f_c') B \exp(-\mu_{ij} r_{ij}) \frac{\partial b_{ij}}{\partial r_{jk}} - f_c B \exp(-\mu_{ij} r_{ij}) \frac{\partial^2 b_{ij}}{\partial r_{ij} \partial r_{jk}} \tag{B.14}$$

$$\frac{\partial^2 V_{ij}}{\partial r_{ik}^2} = -f_c B \exp(-\mu_{ij} r_{ij}) \frac{\partial^2 b_{ij}}{\partial r_{ik}^2} \tag{B.15}$$

$$\frac{\partial^2 V_{ij}}{\partial r_{jk}^2} = -f_c B \exp(-\mu_{ij} r_{ij}) \frac{\partial^2 b_{ij}}{\partial r_{jk}^2} \tag{B.16}$$

$$\frac{\partial^2 V_{ij}}{\partial r_{ik} \partial r_{jk}} = -f_c B \exp(-\mu_{ij} r_{ij}) \frac{\partial^2 b_{ij}}{\partial r_{ik} \partial r_{jk}} \tag{B.17}$$

where

$$\frac{\partial^2 b_{ij}}{\partial r_{ij}^2} = \beta_i^2 \frac{\partial^2 b_{ij}}{\partial z_{ij}^2} \cdot (\frac{\partial \zeta_{ij}}{\partial r_{ij}})^2 + \beta_i \frac{\partial b_{ij}}{\partial z_{ij}} \cdot \frac{\partial^2 \zeta_{ij}}{\partial r_{ij}^2} \tag{B.18}$$

$$\frac{\partial^2 b_{ij}}{\partial r_{ik}^2} = \beta_i^2 \frac{\partial^2 b_{ij}}{\partial z_{ij}^2} \cdot (\frac{\partial \zeta_{ij}}{\partial r_{ik}})^2 + \beta_i \frac{\partial b_{ij}}{\partial z_{ij}} \cdot \frac{\partial^2 \zeta_{ij}}{\partial r_{ik}^2} \tag{B.19}$$

$$\frac{\partial^2 b_{ij}}{\partial r_{jk}^2} = \beta_i^2 \frac{\partial^2 b_{ij}}{\partial z_{ij}^2} \cdot (\frac{\partial \zeta_{ij}}{\partial r_{jk}})^2 + \beta_i \frac{\partial b_{ij}}{\partial z_{ij}} \cdot \frac{\partial^2 \zeta_{ij}}{\partial r_{jk}^2} \tag{B.20}$$

$$\frac{\partial^2 b_{ij}}{\partial r_{ij} \partial r_{ik}} = \beta_i^2 \frac{\partial^2 b_{ij}}{\partial z_{ij}^2} \cdot \frac{\partial \zeta_{ij}}{\partial r_{ij}} \cdot \frac{\partial \zeta_{ij}}{\partial r_{ik}} + \beta_i \frac{\partial b_{ij}}{\partial z_{ij}} \cdot \frac{\partial^2 \zeta_{ij}}{\partial r_{ij} \partial r_{ik}} \tag{B.21}$$

$$\frac{\partial^2 b_{ij}}{\partial r_{ij} \partial r_{jk}} = \beta_i^2 \frac{\partial^2 b_{ij}}{\partial z_{ij}^2} \cdot \frac{\partial \zeta_{ij}}{\partial r_{ij}} \cdot \frac{\partial \zeta_{ij}}{\partial r_{jk}} + \beta_i \frac{\partial b_{ij}}{\partial z_{ij}} \cdot \frac{\partial^2 \zeta_{ij}}{\partial r_{ij} \partial r_{jk}} \tag{B.22}$$

$$\frac{\partial^2 b_{ij}}{\partial r_{ik} \partial r_{jk}} = \beta_i^2 \frac{\partial^2 b_{ij}}{\partial z_{ij}^2} \cdot \frac{\partial \zeta_{ij}}{\partial r_{ik}} \cdot \frac{\partial \zeta_{ij}}{\partial r_{jk}} + \beta_i \frac{\partial b_{ij}}{\partial z_{ij}} \cdot \frac{\partial^2 \zeta_{ij}}{\partial r_{ik} \partial r_{jk}} \tag{B.23}$$

$$\frac{\partial^2 b_{ij}}{\partial r_{ik} \partial r_{il}} = \beta_i^2 \frac{\partial^2 b_{ij}}{\partial z_{ij}^2} \cdot \frac{\partial \zeta_{ij}}{\partial r_{ik}} \cdot \frac{\partial \zeta_{ij}}{\partial r_{il}} \tag{B.24}$$

$$\frac{\partial^2 b_{ij}}{\partial r_{jk} \partial r_{jl}} = \beta_i^2 \frac{\partial^2 b_{ij}}{\partial z_{ij}^2} \cdot \frac{\partial \zeta_{ij}}{\partial r_{jk}} \cdot \frac{\partial \zeta_{ij}}{\partial r_{jl}} \tag{B.25}$$

$$\frac{\partial^2 b_{ij}}{\partial r_{ik} \partial r_{jl}} = \beta_i^2 \frac{\partial^2 b_{ij}}{\partial z_{ij}^2} \cdot \frac{\partial \zeta_{ij}}{\partial r_{ik}} \cdot \frac{\partial \zeta_{ij}}{\partial r_{jl}} \tag{B.26}$$

And

$$\frac{\partial^2 b_{ij}}{\partial z_{ij}^2} = \chi_{ij}[\frac{2n_i+1}{4n_i}(1+z_{ij}^{n_i})^{-\frac{1+4n_i}{2n_i}} z_{ij}^{2n_i-2} - \frac{n_i-1}{2}(1+z_{ij}^{n_i})^{-\frac{2n_i+1}{2n_i}} z_{ij}^{n_i-2}] \tag{B.27}$$

$$\frac{\partial^2 \zeta_{ij}}{\partial r_{ij}^2} = \sum_{k(\neq i,j)} f_c(r_{ik})[\frac{\partial^2 g}{\partial(\cos\theta)^2} \cdot (\frac{\partial cos\theta}{\partial r_{ij}})^2 + \frac{\partial g}{\partial \cos\theta} \cdot \frac{\partial^2 cos\theta}{\partial r_{ij}^2}] \tag{B.28}$$

$$\frac{\partial^2 \zeta_{ij}}{\partial r_{jk}^2} = \sum_{k(\neq i,j)} f_c(r_{ik})[\frac{\partial^2 g}{\partial(\cos\theta)^2} \cdot (\frac{\partial cos\theta}{\partial r_{jk}})^2 + \frac{\partial g}{\partial \cos\theta} \cdot \frac{\partial^2 cos\theta}{\partial r_{jk}^2}] \tag{B.29}$$

$$\begin{aligned}\frac{\partial^2 \zeta_{ij}}{\partial r_{ik}^2} = \sum_{k(\neq i,j)} \{ & f_c(r_{ik})[\frac{\partial^2 g}{\partial(\cos\theta)^2} \cdot (\frac{\partial cos\theta}{\partial r_{ik}})^2 + \frac{\partial g}{\partial \cos\theta} \cdot \frac{\partial^2 cos\theta}{\partial r_{ik}^2}] \\ & + 2f_c' \frac{\partial g}{\partial \cos\theta} \cdot \frac{\partial \cos\theta}{\partial r_{ik}} + f_c'' g\}\end{aligned} \tag{B.30}$$

$$\begin{aligned}\frac{\partial^2 \zeta_{ij}}{\partial r_{ij} \partial r_{ik}} = \sum_{k(\neq i,j)} \{ & f_c(r_{ik})[\frac{\partial^2 g}{\partial(\cos\theta)^2} \cdot \frac{\partial cos\theta}{\partial r_{ij}} \cdot \frac{\partial \cos\theta}{\partial r_{ik}} + \frac{\partial g}{\partial \cos\theta} \cdot \frac{\partial^2 cos\theta}{\partial r_{ij} \partial r_{ik}}] \\ & + f_c' \frac{\partial g}{\partial \cos\theta} \cdot \frac{\partial cos\theta}{\partial r_{ij}}\}\end{aligned} \tag{B.31}$$

$$\frac{\partial^2 \zeta_{ij}}{\partial r_{ij} \partial r_{jk}} = \sum_{k(\neq i,j)} f_c(r_{ik})[\frac{\partial^2 g}{\partial(\cos\theta)^2} \cdot \frac{\partial cos\theta}{\partial r_{ij}} \cdot \frac{\partial \cos\theta}{\partial r_{jk}} + \frac{\partial g}{\partial \cos\theta} \cdot \frac{\partial^2 cos\theta}{\partial r_{ij} \partial r_{jk}}] \tag{B.32}$$

$$\begin{aligned}\frac{\partial^2 \zeta_{ij}}{\partial r_{ik} \partial r_{jk}} = \sum_{k(\neq i,j)} \{ & f_c(r_{ik})[\frac{\partial^2 g}{\partial(\cos\theta)^2} \cdot \frac{\partial cos\theta}{\partial r_{ik}} \frac{\partial \cos\theta}{\partial r_{jk}} + \frac{\partial g}{\partial \cos\theta} \cdot \frac{\partial^2 cos\theta}{\partial r_{ik} \partial r_{jk}}] \\ & + f_c' \frac{\partial g}{\partial \cos\theta} \cdot \frac{\partial cos\theta}{\partial r_{jk}}\}\end{aligned} \tag{B.33}$$

where

$$\frac{\partial^2 g}{\partial(\cos\theta)^2} = \frac{2c_i^2}{[d_i^2+(\cos\theta-h_i)^2]^2} - \frac{8c_i^2(\cos\theta-h_i)^2}{[d_i^2+(\cos\theta-h_i)^2]^3} \tag{B.34}$$

$$f_c'' = -\frac{\pi^2}{2(S-R)^2}\cos\frac{\pi(r-R)}{S-R} \tag{B.35}$$

$$\frac{\partial^2\cos\theta}{\partial r_{ij}^2} = \frac{2\cos\theta}{r_{ij}^2} - \frac{1}{r_{ij}r_{ik}}; \quad \frac{\partial^2\cos\theta}{\partial r_{ik}^2} = \frac{2\cos\theta}{r_{ik}^2} - \frac{1}{r_{ij}r_{ik}} \tag{B.36}$$

$$\frac{\partial^2\cos\theta}{\partial r_{ij}\partial r_{ik}} = \frac{\cos\theta}{r_{ij}r_{ik}} - \frac{1}{r_{ij}^2} - \frac{1}{r_{ik}^2} \tag{B.37}$$

$$\frac{\partial^2\cos\theta}{\partial r_{ij}\partial r_{jk}} = \frac{r_{jk}}{r_{ij}^2 r_{ik}}; \quad \frac{\partial^2\cos\theta}{\partial r_{ik}\partial r_{jk}} = \frac{r_{jk}}{r_{ik}^2 r_{ij}}; \quad \frac{\partial^2\cos\theta}{\partial r_{jk}^2} = -\frac{1}{r_{ij}r_{ik}} \tag{B.38}$$

Bibliography

[1] *Amorphous and crystalline silicon carbide and related materials: proceedings of the first international conference, Washington DC, December, 1987* (Springer-Verlag, New York, 1989).

[2] *Amorphous and crystalline silicon carbide II recent developments: proceedings of the 2nd International Conference , Santa Clara, CA, Dec., 1988* (Springer-Verlag, New York, 1989).

[3] *Amorphous and crystalline silicon carbide III and other group IV-IV materials: proceedings of the 3rd international conference, Washington DC, April, 1990* (Springer-Verlag, New York, 1992).

[4] *Amorphous and crystalline silicon carbide IV: proceedings of the 4th international conference, Santa Clara, CA, Oct. 1991* (Springer-Verlag, New York, 1992).

[5] *Silicon Carbide - 1973*, edited by R. C. Marshall, J. W. Faust, Jr. and C. E. Ryan, (Univ. of South Calorina, Columbia, 1974).

[6] A. R. Verma and P. Krishna, *Polymorphism and Polytypism in Crystals* (John Wiley & Sons, New York, 1966), pp.103.

[7] *Proceedings of an international conference on Interfacial Phenomena in Composite Materials, Sheffield, UK, 1989*, edited by F. R. Jones.

[8] B. R. Lawn and T. R. Wilshaw, *Fracture of Brittle Solids* (Cambridge University Press, New York, 1975), pp.17.

[9] *Proceedings of the Symposium on Interfacial Phenomena in Composites: Processing, Characterization and Mechanical properties, Newport, RI, June, 1988*, edited by S. Suresh and A. Needelman.

[10] R. Hill, Math. Proc. Camb. Philos. Soc. **77**, 225 (1975).

[11] D. Wallace, *Thermodynamics of Crystal* (John Wiley & Sons, New York,1972).

[12] M. Born, Proc. Camb. Philos. Soc. **36**, 160 (1940).

[13] M. Born and K. Huang, *Dynamical Theory of Crystal Lattices* (Clarendon, Oxford, 1956).

[14] R. Hill and F. Milstein, Phys. Rev. B **15**, 3087 (1977).

[15] J. Wang, S. Yip, S. R. Phillpot, and D. Wolf, Phys. Rev. Lett. **71**, 4182 (1993).

[16] J. Wang, S. Yip, S. R. Phillpot, and D. Wolf, to be published.

[17] J. H. Wang, PhD Thesis, *Atomistic Study of Stress-Induced Unstable Structural Responses of Crystals at Finite Temperatures*, Massachusetts Institute of Technology, January 1993.

[18] J. R. Rice, private communication.

[19] L. L Boyer, Phase Transitions **5**, 1 (1985).

[20] F. Milstein and B. Farber, Phys. Rev. Lett. **44**, 277 (1980).

[21] J. S. Tse and D. D. Klug, Phys. Rev. Lett. **67**, 3559 (1991).

[22] S. M. Foiles, M. I. Baskes and M. S. Daw, Phys. Rev. B **33**, 7983 (1986).

[23] F. Cleri, J. Wang and S. Yip, J. Appl. Phys., in press.

[24] K. Mizushima, S. Yip and E. Kaxiras, Phys. Rev. B **50**, 14952 (1994).

[25] J. Tersoff, Phys. Rev. B **38**, 9902 (1988).

[26] J. Tersoff, Phys. Rev. B **49**, 16349 (1994).

[27] J. Tersoff, Phys. Rev. B **39**, 5566 (1989).

[28] J. M. Haile, *Molecular Dynamics Simulation* (John Wiley & Sons, Inc., New York, 1992).

[29] M. P. Allen and D. J. Tildesley, *Computer Simulation of Liquids* (Clarendon Press, Oxford, 1987).

[30] C. W. Gear, *Numerical Initial Value Problems in Ordinary Differential Equations* (Prentice-Hall, Englewood Cliffs, 1971).

[31] M. Parrinello and A. Rahman, J. Appl. Phys. **52**, 7182 (1981).

[32] J. R. Ray and A. Rahman, J. Chem. Phys. **80**, 4423 (1984).

[33] F. F. Abraham, D. Brodbeck, R. A. Rafey and W. E. Rudge, Phys. Rev. Lett. **73**, 272 (1994).

[34] P. Vashishta, R. K. Kalia, S. W. de Leeuw, D. L. Greewell, A. Nakno, W. Jin, J. Yu, L. Bi and W. Li, Comp. Mat. Sci. **2**, 180 (1994).

[35] J. R. Ray, Comp. Phys. Rept. **8**, 109 (1988).

[36] M. Sprik, R. W. Impey and M. L. Klein, Phys. Rev. B **29**, 4368 (1984).

[37] J. Wang, S. Yip, S. Phillpot, and D. Wolf, J. Alloys and Compounds **194**, 407 (1993).

[38] K. S. Cheung, PhD Thesis, *Atomistic Study of Dislocation Nucleation at a Crack Tip*, Massachusetts Institute of Technology, June 1990.

[39] C. S. G. Cousins, J. Phys. C: Solid State Phys. **11**, 4867 (1978).

[40] C. S. G. Cousins, J. Phys. C: Solid State Phys. **11**, 4881 (1978).

[41] J. F. Lutsko, J. Appl. Phys. **65**, 2991 (1989).

[42] F. H. Stillinger and T. A. Weber, Phys. Rev. B **31**, 5262 (1985).

[43] E. Pearson, T. Takai, T. Halicioglu, and W. A. Tiller, J. Crys. Growth **70**, 33 (1984).

[44] J. R. Ray, M. C. Moody and A. Rahman, Phys. Rev. B **32**, 733 (1985).

[45] H. Balamane, T. Halicioglu, and W. A. Tiller, Phys. Rev. B **46**, 2250 (1992).

[46] V. Bulatov, S. Yip and A. Argon, paper in preparation.

[47] M. I. Baskes, Sandia Report, printed August 1994.

[48] M. Kohyama, S. Kose, M. Kinoshita, and R. Yamamoto, J. Phys. Condensed Matter **2**, 7791 (1990).

[49] J. A. Majewski and P. Vogl, Phys. Rev. B **35**, 9666 (1987).

[50] A. Isik, PhD Thesis, *Molecular Dynamics Simulation of Covalent Materials Using Empirical Tight-binding Method*, Massachusetts Institute of Technology, June 1994.

[51] private communication.

[52] J. Tersoff, Phys. Rev. Lett. **56**, 632 (1986).

[53] J. Tersoff, Phys. Rev. B **27**, 6991 (1988).

[54] J. Tersoff, Phys. Rev. Lett. **61**, 2879 (1988).

[55] D. W. Brenner, Phys. Rev. Lett. **63**, 1022 (1989).

[56] P. C. Kelires, Europhys. Lett. **14**, 43 (1991).

[57] G. C. Abell, Phys. Rev. B **31**, 6184 (1985).

[58] F. Finocchi, G. Galli, M. Parrinello, and C. M. Bertoni, Phys. Rev. Lett. **68**, 3044 (1992).

[59] J. H. Rose and J. R. Smith and F. Guinea and J. Ferrante, Phys. Rev. B **29**, 2963 (1984).

[60] H. Aourag, G. Merad, K. Ghaffour, H. Abid, N. Badi and B. Khelifa, Comp. Mat. Sci. **1**, 78 (1992).

[61] K. J. Chang and M. L. Cohen, Phys. Rev. B **35**, 8196 (1987).

[62] C. Kittel, *Introduction to solid state physics* (Wiley, New York, 1986).

[63] M. T. Yin and M. L. Cohen, Phys. Rev. B **26**, 5668 (1982).

[64] R. Car and M. Parrinello, Phys. Rev. Lett. **55**, 2471 (1985).

[65] Helen M. J. Smith, Proc. Roy. Soc. A**241**, 105 (1948).

[66] D. W. Feldman, J. H. Parker, W. J. Choyke and L. Patrick, Phys. Rev. **173**, 787 (1968); D. W. Feldman, J. H. Parker, W. J. Choyke and L. Patrick, Phys. Rev. **170**, 698 (1968).

[67] E. O. Kane, Phys. Rev. B, **31**, 7865 (1985).

[68] I. V. Aleksandrov, A. F. Goncharov, E. V. Yakovenko and S. M. Stishov, *High Pressure Research: application to earth and planetary sciences*, (American Geophysical Union, Washington, D.C., 1992), pp.409.

[69] M. Yoshida, A. Onodera, M. Ueno, K. Takemura, and O. Shimomura, Phys. Rev. B **48**, 10587 (1993).

[70] K. Strossner and M. Cardona and W. J. Choyke, Sol. Stat. Communi. **63**, 113 (1987).

[71] F. Birch, J. Geophys. Res. **83**, 1257 (1978).

[72] Z. Li and R. C. Bradt, J. Mat. Sci. **21**, 4366 (1986).

[73] Z. Li and R. C. Bradt, J. Mat. Sci. **22**, 2557 (1987).

[74] W. R. L. Lambrecht, B. Segall, M. Methfessel, and M. van Schilfgaarde, Phys. Rev. B **44**, 3685 (1991).

[75] K. S. Cheung, A. Argon and S. Yip, J. Appl. Phys. **69**, 2088 (1991).

[76] S. R. Phillpot, S. Yip and D. Wolf, Computers in Physics **Nov/Dec**, 20 (1989).

[77] B. Rand, in *Interfacial Phenomena in Composite Materials '89*, edited by F. R. Jones.

[78] S. Erkoc, T. Halicioglu and W. A. Tiller, Phys. Stat. Sol. (b) **157**, K23 (1990).

[79] B. N. Oshcherin, Phys. Stat. Sol. (a) **34**, K181 (1976).

[80] S. P. Mehandru and A. B. Anderson, Phys. Rev. B **42**, 9040 (1990).

[81] D. H. Lee and J. D. Joannopoulos, J. Vac. Sci. Technol. **21**, 351 (1982).

[82] C. S. Chang, N. J. Zheng, S. T. Tsong, Y. C. Wang and R. F. Davis, J. Vac. Sci. Technol. B **9**, 681 (1991).

[83] R. Kaplan, Surface Science **215**, 111 (1989).

[84] M. Tang and S. Yip, to be published.

[85] Lawrence, E. Malvern, *Introduction to the mechanics of a continuous medium* (Englewood Cliffs, N. J., Prentice-Hall, 1969).

[86] Z. P. Bazant and L. Cedolin, *Stability of Structures* (Oxford University Press, New York, 1991).

[87] A. Saada, *Elasticity Theory and Applications* (Pergamon Press, New York, 1974).

[88] G. Grimvall, *Thermodynamical Properties of Materials* (North-Holland, New York, 1986).

[89] D. Wolf, J. Jazzack, in *Materials Interface*, Chap.2, edited by D. Wolf and S. Yip, (Champman-Hall, New York, 1992).

[90] K. Huang, Proc. R. Soc. London A **203**, 178 (1950).

[91] L. Landau and E. M. Lifshitz, *Theory of Elasticity* (Pergamon Press, New York, 1986), pp.83; A. E. H. Love, *A Treatise on the Mathematical Theory of Elasticity* (Dover, New York, 1944).

[92] R. Hill and F. Milstein, Phys. Rev. B **15**, 3087 (1977), F. Milstein and R. Hill, J. Mech. Phys. Solids **25**, 457 (1977), idem. ibid. **26**, 213 (1978), idem. ibid **27**, 215 (1979); F. Milstein and R. Hill, Phys. Rev. Lett. **43**, 1411 (1979).

[93] F. Milstein, J. Matr. Sci. **15**, 1071 (1980).

[94] T. H. K. Barron and M. L. Klein, Proc. Phys. Soc. **85**, 523 (1965).

[95] F. McClintock and A. Argon, *Mechanical Behavior of Materials* (Addison-Wesley, Reading, Mass., 1966).

[96] Y. Sun, G. E. Beltz, and J. R. Rice, Mater. Sci. Eng. A**170**, 67 (1993).

[97] W. A. Harrison, *Electronic Structure and the Properties of Solids* (W. H. Freeman and Company, San Francisco, 1980), pp.233.

[98] *Proceedings of the Conference on Solid State Amorphizing Transformations, Los Alamos, New Mexico, 1987*, edited by R. B. Schwartz and W. L. Johnson. [J. Less-Common. Met. **140** (1988).].

[99] E. G. Ponyatovsky and O. I. Barkalov, Mat. Sci. Rept. **8**, 147 (1992), and references therein.

[100] M. B. Kruger and R. Jeanloz, Science **249**, 647 (1990).

[101] L. E. McNeil and M. Grimsditch, Phys. Rev. Lett. **68**, 83 (1992).

[102] G. C. Serghiou, R. R. Winters and W. S. Hammack, Phys. Rev. Lett. **68**, 331 (1992).

[103] R. G. Greene, H. Luo and A. L. Ruoff, Phys. Rev. Lett. **73**, 2476 (1994).

[104] N. Binggeli and J. R. Chelikowsky, Phys. Rev. Lett. **69**, 2220 (1992).

[105] J. S. Tse and D. D. Klug, Phys. Rev. Lett. **67**, 3559 (1991).

[106] H. Inui, H. Mori and H. Fujita, Acta metall. **37**, 1337 (1989).

[107] H. Inui, H. Mori, A. Suzuki and H. Fujita, Philos. Mag. B **65**, 1 (1992).

[108] R. M. Wentzcovitch, M. L. Cohen and P. K. Lam, Phys. Rev. B. **36**, 6058 (1987).

[109] D. Wolf and S. Yip, MRS Bulletin **October**, 21 (1990).

[110] F. F. Abraham, Adv. Phys. **35**, 1 (1986).

[111] S. Yip and S. R. Phillpot, *Dynamical Simulation of Grain Boundaries at Elevated Temperatures*, MRS Bulletin, October, 1990.

[112] J. F. Lutsko and D. Wolf, Scripta. Metall. **22**, 1923 (1988).

[113] J. F. Lutsko, J. Appl. Phys. **64**, 1152 (1988).

[114] M. D. Kluge, D. Wolf, J. F. Lutsko and S. R. Phillpot, J. Appl. Phys. **67**, 2370 (1990).

[115] I. Alber, J. L. Bassani, M. Khantha, V. Vitek and G. J. Wang, Phil. Trans. R. Soc. Lond. A **339**, 555 (1992).

[116] F. H. Stillinger and B. D. Lubachevsky, J. Stat. Phys. **73**, 497 (1993).

[117] C. S. Yoon and J. Megusar, Interface Research, paper submitted.

[118] J. F. Lutsko, D. Wolf, S. Yip, S. R. Phillpot and T. Nguyen, Phys. Rev. B **38**, 11572 (1988).

[119] B. B. Laird and A. D. J. Haymet , Chemical Reviews **92**, 1819 (1992).

[120] M. E. Eberhart, D. P. Clougherty and J. N. Louwen, MRS Bulletin, April issue, 53 (1991).

[121] J. R. Rice, in *Chemistry and Phsics of Fracture*, edited by R. M. Latanision and R. H. Jones (Matinus Nijhoff, Dordrecht, 1987), p.27.

[122] A. G. Evans and M. Rühle, MRS Bulletin, October issue, 46 (1990).

[123] V. Gupta, MRS Bulletin, April, 39 (1994).

[124] J. R. Rice, G. E. Beltz and Y. Sun, in *Topics in Fracture and Fatigue*, A. S. Argon, ed. (Springer-Verlag, Berlin, 1992), p.1.

[125] G. E. Beltz and J. R. Rice, Acta. Met. **40**, s321 (1992).

[126] J. R. Rice and R. Thomson, Phil. Mag. **29**, 73 (1974).

[127] K. S. Cheung and S. Yip, Modelling Simul. Mater. Sci. Eng. **2**, 865 (1994).

[128] J. R. Rice, J. Mech. Phys. Solids **40**, 239 (1992).

[129] J. R. Rice, J. Appl. Mech. **55**, 98 (1988).

[130] *Metal-Ceramic Interfaces*, edited by M. Rühle, A. G. Evans, M. F. Ashby and J. P. Hirth, (Pergamon Press, Oxford, 1990).